UNIVERSITY OF OKLAHOMA

GRADUATE COLLEGE

DYNAMIC DRILLING FLUIDS LOSS AND FILTRATION: IMPACT OF DYNAMIC WELLBORE CONDITIONS AND WELLBORE STRENGTHENING IMPLICATIONS

A DISSERTATION

SUBMITTED TO THE GRADUATE FACULTY

in partial fulfillment of the requirements for the

Degree of

DOCTOR OF PHILOSOPHY

By

CHINEDUM PETER EZEAKACHA
Norman, Oklahoma
2018

DYNAMIC DRILLING FLUIDS LOSS AND FILTRATION: IMPACT OF DYNAMIC WELLBORE CONDITIONS AND WELLBORE STRENGTHENING IMPICATIONS

A DISSERTATION APPROVED FOR THE
MEWBOURNE SCHOOL OF PETROLEUM AND GEOLOGICAL ENGINEERING

BY

Dr. Saeed Salehi, Chair

Dr. Ziho Kang

Dr. Ramadan Ahmed

Dr. Catalin Teodoriu

Dr. Mashhad Fahes

Dedication

I dedicate this PhD dissertation to God, my wife: Mrs. Chioma Delphine Ezeakacha, my parents: Sir and Lady Rufus and Catherine Ezeakacha, and my siblings: Mr. Tobechukwu Patrick Ezeakacha, Dr. Nnaemeka Francis Ezeakacha (PhD), Mr. Chukwuebuka Gabriel Ezeakacha, and Miss Mary-Jacinta Ngozinkechinyere Ezeakacha.

Acknowledgement

I would like to express my deepest gratitude to God Almighty for granting me life and good health of mind and body to complete this PhD program. My profound gratitude and appreciation go to my dissertation direction: Dr. Saeed Salehi (PhD P.E). He took me under his supervision from my first day in graduate school (January 14, 2013), trained me, sponsored me, and put me through hard and smart work. In my toughest times, he was there to lift me up. Dr. Salehi exposed me to several research projects, mentored me to publish 24 papers from my research area and supported me in making over 20 technical presentations at local, national, and international conferences, symposiums, and meetings. Dr. Salehi, I will be forever indebted to you. Thank you very much for everything.

I would like to thank all the members of my dissertation committee for accepting to be in the committee and their time. Beginning with the outside committee member, Dr. Ziho Kang (PhD), your feedbacks on my statistical design and analysis were very useful. Special thanks go to Dr. Ramadan Ahmed (PhD), Dr. Cataline Teodoriu (PhD), and Dr. Mashhad Fahes. The contributions and feedbacks you all gave during my research, particularly during my general exam were extremely valuable.

It was an honor to have worked closely with Mr. Jeff McCaskill at the OU Well Construction and Technology Center (WCTC). You were my go-to personnel during my experiments, especially when the machines broke down and/or a process needs to be adjusted or improved in the lab. Thank you. My gratitude goes to Dr. Carl Sondergeld (PhD) for permitting me to conduct my rock properties measurements, scanning electron microscope imaging, and elemental mapping at the Integrated Core Characterization Center (IC^3). In addition, I am grateful

to Dr. Mark Cutis (PhD), Dr. Ali Tinni (PhD), and Mr. Gary Stowe for their support during my investigations at the IC^3.

I am also grateful to the Mewbourne School of Petroleum and Geological Engineering for granting me scholarships and travel awards to support my studies and research presentations. This acknowledgement is incomplete if I do not recognize Dr. Raj Kiran (PhD). We started this journey together and he provided valuable analytical contributions to my research. I am very grateful. Special mention goes to my friends who played different roles during this period of my study in different capacities: Dr. Asadollah Hayatdavoud (PhD P.E), Chiedozie Ekweribe, Junior Ehigiator, Ugochukwu David Akpakwu, Ogbugo Ananaba, Oluwatobi Olorunsola, Ademide Mabadeje, Rodrigo Rivera, and Dolly Na-Yemeh.

Finally, to my wonderful family to whom this 6 years and PhD dissertation are dedicated to, I love you all and I say thank you for your support in finishing this PhD program. To my wife, Mrs. Chioma Delphine Ezeakacha, thank you for putting up with me through this tough period and having my back. I love you. May God Almighty bless everyone mentioned herein and those not mentioned but have contributed in one way or another. I am grateful.

Thank you all.

Table of Contents

List of Tables

List of Figures

Abstract

Lost circulation (drilling fluid loss) and mud filtration have been investigated over the years because they lead to non-drilling time (NDT) and increase the overall well cost. It is usually the first source of damage to the formation among other processes such as completions, workover, and hydraulic fracturing. There are several field solutions that have been proffered and these are grouped under remedial and preventative solutions. Investigation of drilling fluid loss is mostly done via experimental studies with several types of setups, fluid formulations, and porous media. However, lithology complexities, geothermal and geochemical effects, and other wellbore drilling dynamics continue to push the boundaries to develop better preventative strategies.

In this research, pore and fracture-scale dynamic drilling fluid loss are investigated and the results are used in characterizing filter cake wellbore strengthening. A comprehensive theoretical study was first conducted to provide the technical background required to address the research hypotheses. This was followed by experimental investigations whose results show that temperature, rotary speed, fracture width and orientation, rock permeability and porosity, lost circulation material (LCM) type, and LCM concentration are critical factors that significantly influence dynamic drilling fluid loss and filtration. Scanning electron microscope (SEM) images and elemental maps of selected samples showed near-wellbore pore plugging by granular LCM. Granular and fibrous LCM concentration thresholds were established based on the maximum anticipated operating conditions. The result from testing the filter cake stability (a measure of the filter cake wellbore strengthening process in fractures) was 67% successful.

Statistical design and analysis were used for pre-experimental and post-experimental evaluations. The results revealed the significance of the single and multiple effects of the factors investigated. The empirical models from post-experimental studies showed good predictability

of dynamic fluid loss and filtration with considerable high R^2 values. To enhance the predictability of mud filtration and fill the gaps in an empirical modeling approach, a robust mechanistic model for dynamic drilling fluid filtration was developed and tuned based on laboratory results. The model revealed an average relative error that is less than 5 % in estimating dynamic mud filtration. Geomechanical and in-situ stress implications were investigated. The results showed that the rock permeability and filter cake permeability profiles largely control the changes in wellbore hoop stress profile.

The novelty in this study is in the use of thick-walled cylindrical sandstones, limestones, chalks, and fracture slots to profile dynamic drilling fluid loss and filtration of different fluid designs. Different pressures, temperatures, and drillpipe rotary speeds were combined to simulate dynamic wellbore conditions under which fluid/filtrate loss, filter cake evolution, and filter cake plastering effect can occur. The approaches in the research can be used in drilling fluid design for minimizing fluid loss, wellbore strengthening application, and selection of operating conditions.

Chapter 1: Introduction

1.1 Overview of Drilling Fluid Loss and Filtration

Wellbore stability issues such as lost circulation (drilling fluid loss), wellbore breakout (collapse), and formation fluid influx (kick) are commonly experienced in drilling operations. The economic impact in resolving these challenges as well as the safety concerns are usually high. Typically, the operational mud window (a mud weight selection guide that aids in choosing equivalent circulating densities, ECD) serves as the first line of defense in preventing these issues. When the operational mud window becomes narrower (especially in deep-water drilling and depleted formations), these wellbore stability issues become more difficult to handle. Other challenging environments where these issues are encountered include but not limited to: salt drilling environments, unconsolidated sandstones, naturally fractured carbonate rocks, and shale gas drilling.

While operators and service company's dread these wellbore stability challenges, there is an industry consensus that lost circulation and drilling fluids filtration are among the top ten challenges encountered in deep-water drilling operations (Zamora et al. 2000), leading to non-drilling time (NDT). Lost circulation or drilling fluid loss is the loss of drilling fluid to the formation in an over balanced drilling operation. It has the following disadvantages which include but not limited to: NDT required in curing losses, stuck drillpipe and potential sidetrack, blowout from wellbore ballooning pay zones because of drop in drilling fluid hydrostatic pressure, formation damage in a pay zone, and potential abandonment of rig. The economic impact of drilling fluid loss events on the oil and gas industry is approximately $800 million USD per year. Figure 1.1 reveals that up to 40 % of the NDT recorded for gas-drilled wells in the Gulf of Mexico (GoM) from 1993 to 2003 is related to drilling operations with lost circulation as the highest contributor.

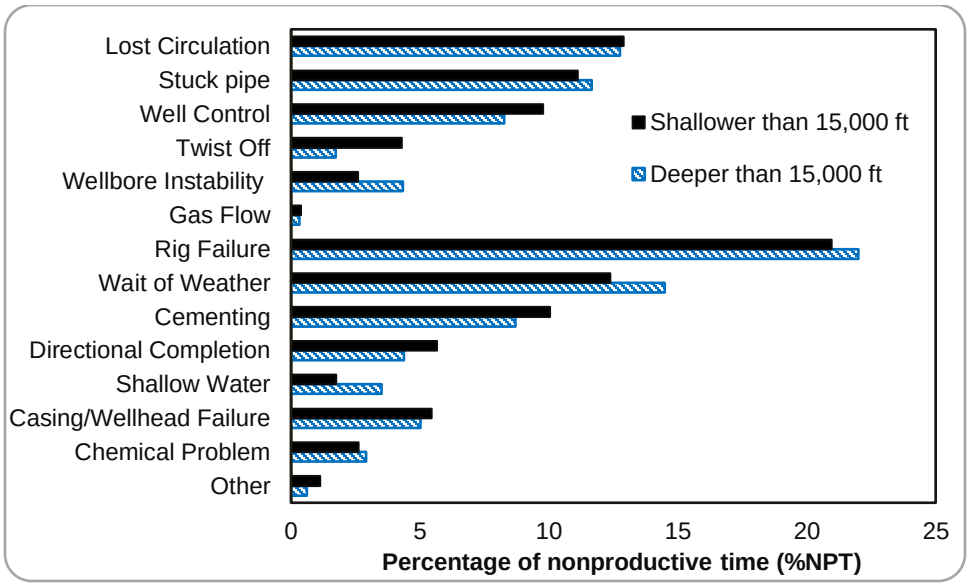

Figure 1.1: Record of gas-drilled wells in the Gulf of Mexico (GoM) from 1993 to 2003 (modified after James K. Dodson 2003)

According to Rosenberg and Gala (2012), one of the notable lost circulation non-productive time (NPT) incidents was from an offshore Veracruz field with a total economic impact of $ 4.78 million USD. This cost was incurred from severe fluid losses more than 2,500 bbl, leading to stuck pipe and costly fishing operations. Ezeakacha (2014) conducted a comparative study and statistical review of lost circulation events in different formations that were combated by casing while drilling (CwD) operation. The study which was based on published reports and papers from several fluid loss events around the world shows that 23 % of these events occurred in the Gulf of Mexico (GoM). Irrespective of the region, Figure 1.3 shows that these events can occur in almost every hydrocarbon bearing lithology. A further review of these field case studies suggested that in one well, a lost circulation interval can be up to 5000 ft, while 48 % of the case studies were between 100 ft to 1000 ft.

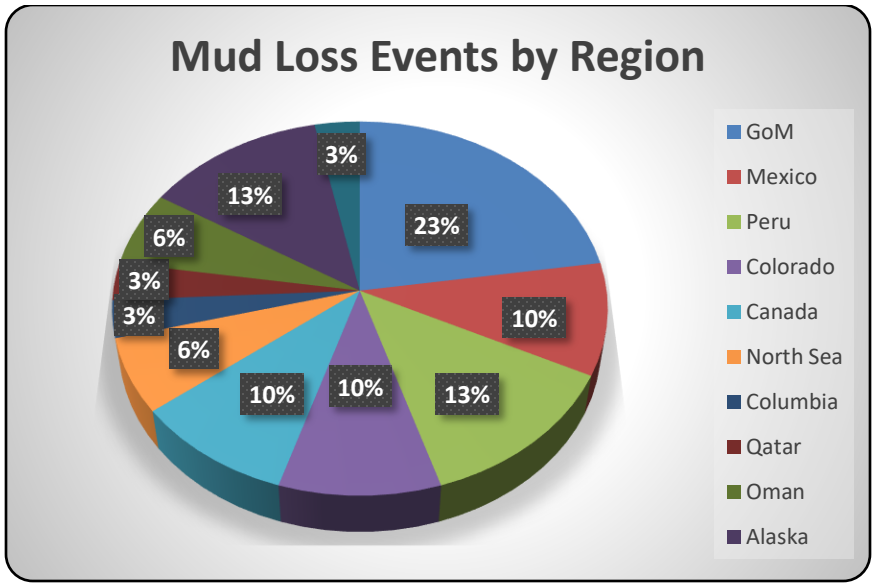

Figure 1.2: Record of fluid loss events in various regions (Ezeakacha 2014)

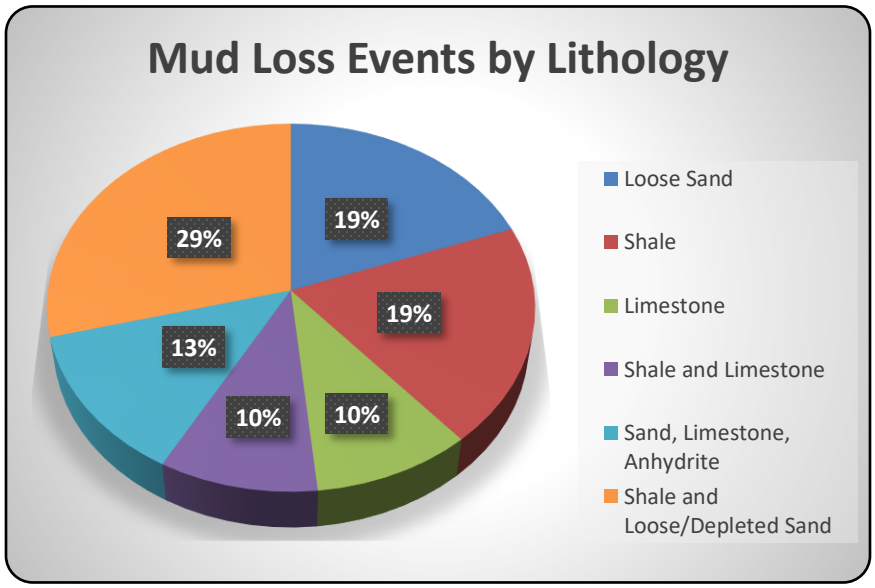

Figure 1.3: Record of fluid loss events in various lithologies (Ezeakacha 2014)

Drilling fluid loss and filtration are complex processes that occur simultaneously in overbalanced drilling. They can result to formation damage in a reservoir section if not controlled. They can also result to wellbore strengthening from the evolution of filter cake if well-sized drilling fluid particles are used. On one hand, formation damage refers to the reduction of the relative permeability of a rock and oil because of the deep invasion of ultra-fine mud particles and filtrate

(Byrne et al. 2015; Bellarby 2009). On the other hand, filter cake wellbore strengthening refers to the evolution of well-sized mud cake particles around the near-wellbore pore throats and fractures to increase the fracture gradient of an interval (Salehi and Kiran 2016). According to the authors, the evolution of a thin and low-permeability filter cake can reduce formation damage from fluid invasion and increase the effective stress around the wellbore.

1.2 Motivation and Research Hypotheses

Fluid loss and filtration during drilling and cementing have been an industry research focus in the past decades. Solutions have been offered from the addition of fluid loss control materials, to use of lost circulation materials (LCM), advanced pills, and other novel technologies such as wellbore strengthening, casing while drilling (CwD) and managed pressure drilling (MPD). However, the dynamics and constantly changing wellbore conditions continue to push the frontier for more research into accurate quantification and mitigation methods for drilling fluid loss and filtration.

In an actual field condition, several factors impact drilling fluid loss and filtration. These include but not limited to: condition of the wellbore fluid flow (static or dynamic), temperature variation, type and composition of drilling fluid, type of lithology, permeability and porosity of rock, rotary speed/eccentricity, pressure, type and concentration of LCM, and mud flow rate. These factors can either have a positive impact by reducing losses or a negative impact by increasing fluid loss. It is unclear which of them is significant, considering that they can have single effects and combined effects (two and three factors). Furthermore, drilling fluid loss and filtration are both complex processes that tend to alter the stress profile of an intact rock during drilling because of filter cake evolution. Combining these factors using theoretical, experimental, statistical, and numerical modeling approaches will provide more reliable information for mitigating losses and

investigating wellbore strengthening. With the forgoing, the following hypotheses have been developed for this study:

1. Dynamic drilling fluid loss and filtration is significantly influenced by up to three factors as single effects and multiple (factor combinations) effects.
2. Wellbore strengthening by filter cake can be quantified from dynamic drilling fluid loss and filtration.

1.3 Research Objectives

In the design and development of drilling fluids, laboratory fluid loss parameters are determined at constant test conditions. In addition, they are determined according to experimental combination of mud additives, rather than a comprehensive approach. Conventional methods of characterizing mud lost circulation with filtration data in field application can be time-consuming, particularly because of the interaction between several factors that impact mud filtration. The following are the specific objectives of this research:

1. Investigate the effects of LCM type, LCM concentration, rotary speed, temperature, and fracture width on dynamic drilling fluid loss and filtration.
2. Characterize pore-scale dynamic drilling fluids filtration and filter cake evolution using ceramic filter tubes and thick-walled cylindrical sandstone and carbonate rocks.
3. Characterize fracture-scale dynamic drilling fluid loss using thick-walled cylindrical fracture slots with varying fracture widths and orientations.
4. Develop a mathematical model for dynamic drilling fluids filtration in a radial coordinate system and validate the model with the experimental results from this study.

5. Profile hoop stress development and filter cake stability for wellbore strengthening application.

1.4 Research Methods

The workflow that is used in this addressing the study objectives is shown in Figure 1.4. The research methods that have been used are classified into four study approaches and they are:

1. *Theoretical Study*: An updated literature review on drilling fluid loss, filtration, and wellbore strengthening was performed. Field reports, conference proceedings, journal articles, and related technical publications were reviewed. A detailed revision of fluid loss mechanisms, factors affecting fluid loss and filtration, experimental, analytical, and field case studies, as well as gaps in applied solutions were conducted. The outcome of this study approach provided the baseline and roadmap for integrating the experimental/statistical and modeling methods in addressing the research hypotheses.
2. *Statistical Design and Analysis*: In this research, statistical methods were used for pre-experimental and post-experimental investigations. The following methods were used: design of experiments (DoE), hypothesis testing using analysis of variance (ANOVA), and regression analysis.
3. *Laboratory Experiments*: The laboratory experimental methods that were used in this research include: drilling fluid formulation, rheological measurements, particle size distribution (PSD) measurements, and dynamic-radial fluid loss and filtration tests. The post experimental investigations that were conducted on samples of interest are scanning electron microscope (SEM) imaging and energy dispersive X-ray spectroscopy (EDS).
4. *Mathematical Modeling and Geomechanical Investigations*: Existing mathematical models for dynamic fluid filtration were tested with the experimental data. The effects of a

concentric pipe rotation, temperature, and LCM concentration were considered in developing a new mechanistic model which was solved numerically using a commercial software (Matlab^{T}). Furthermore, the hoop stress profiles for different rock samples were predicted using an existing numerical approach and mud filtration/filter cake permeability data for lithology-dependent wellbore strengthening application.

1.5 Scope of Study

In this study, the experimental investigations were conducted with fresh water-based muds (WBM) and the formulations are discussed in detail in section 3.3.1. The experiments were conducted under dynamic (pipe rotation only) condition. Other experimental conditions (minimum and maximum limits) are laboratory-controlled and have been described in section 3.3.3.3.

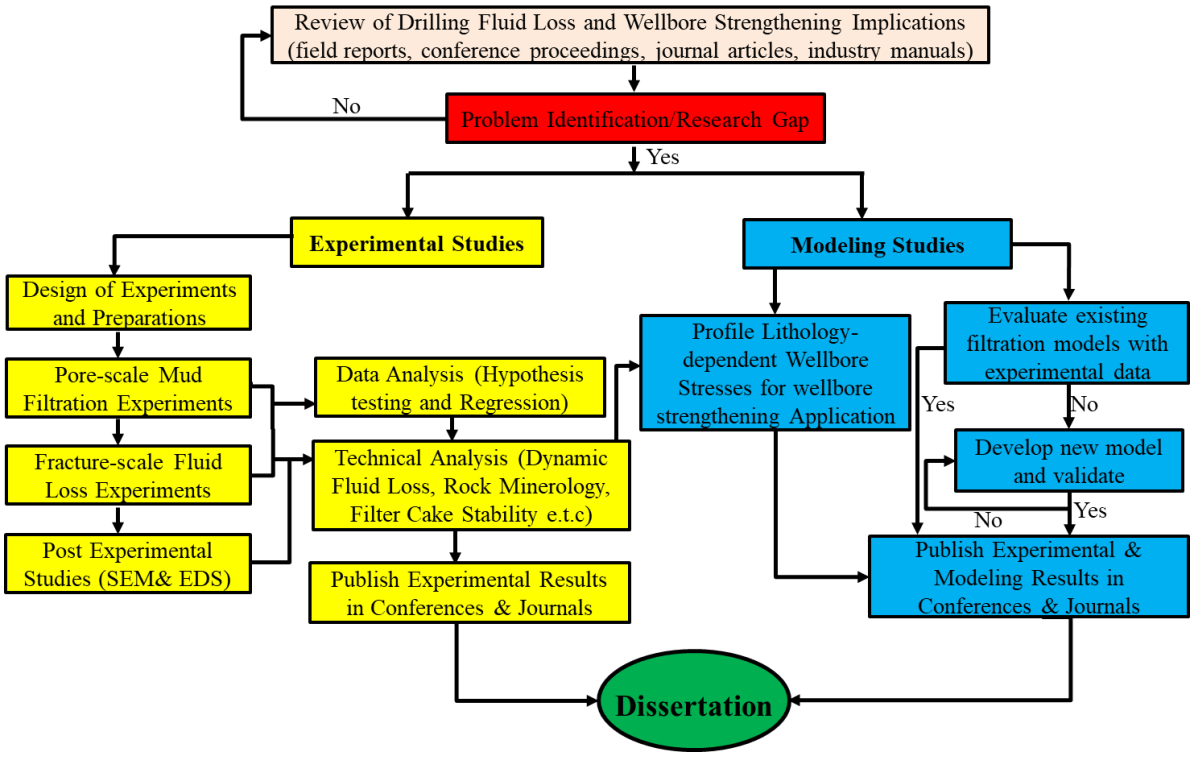

Figure 1.4: Workflow for investigating dynamic drilling fluids loss and filtration.

Chapter 2: Literature Review and Background Study

2.1 Overview

An extensive background study was conducted on drilling fluid loss and mud filtration. Beginning with lost circulation NPT implications highlighted in chapter one, this chapter describes the mechanisms of lost circulation and updated review of applied field solutions and current gaps. The details of filtration mechanisms in aqueous and non-aqueous fluid (NAF) systems are described herein. Next, a critical review of the factors that affect drilling fluid loss and filtration was conducted and documented in this chapter. Among these factors include but no limited to: fracture dimensions, rock minerology (geochemical factor), temperature, LCMs, mud rheology, drill pipe rotation /wellbore geometry.

2.2 Mechanisms of Drilling Fluid Loss

Lost circulation (drilling fluid loss) is defined as the loss of drilling fluid to the formation because of the differential pressure created by the fluid density in an overbalance drilling operation. In technical terms, fluid loss occurs when the drilling mud's ECD exceeds the hoop stress and tensile strength of the rock (Dupriest 2005). Over the years, the types and classifications of lost circulation have been typically defined by the intensity or fluid loss rate to the formation (seepage, partial, server, and total losses). However, these classifications do not provide adequate information on the loss mechanisms, profiles, and suggestive preventative strategies. One way to study the mechanisms of fluid loss and their profiles is to characterize the porous media through which lost circulation events occur. Ghalambor et al. (2014) classified fluid loss mechanisms based on the fluid loss porous media and these include: losses to pore throats, losses to induced or natural fractures, and losses to vugs and carverns. Figure 2.1 shows a wellbore schematic that describes the three fluid loss mechanisms.

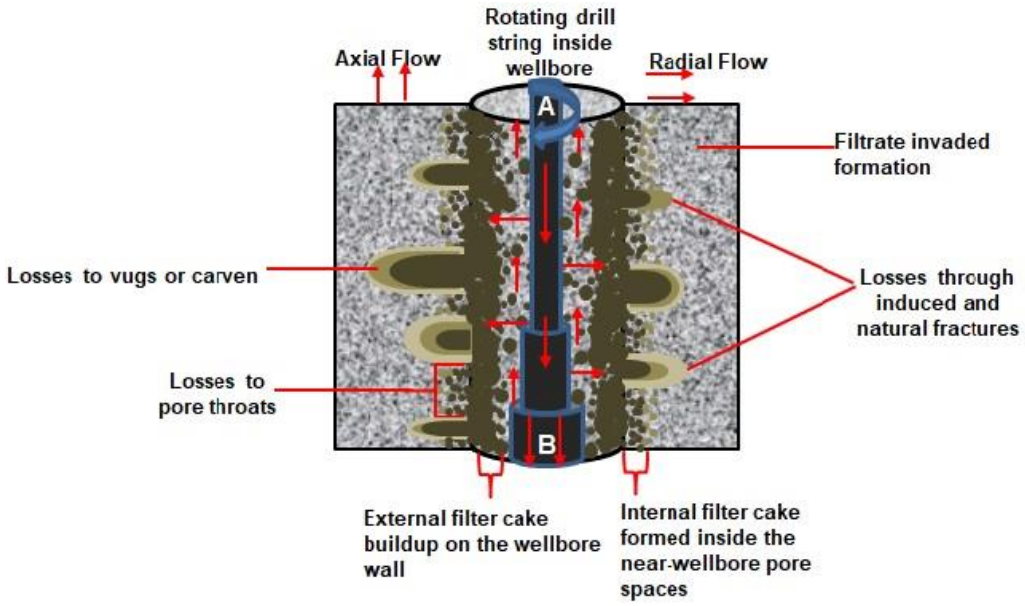

Figure 2.1: Wellbore schematic for lost circulation, mud filtration, and filter cake evolution in dynamic condition (modified after Ezeakacha and Salehi 2018).

Another important look at drilling fluid loss mechanism is that it can occur under two wellbore fluid conditions that vary more in the loss rates. As shown in Figure 2.1, the rate at which fluid particles are transported in the radial and axial directions can vary, based on the fluid particles flow condition, shape, and size. In the first condition (static fluid loss), there is no drilling fluid circulation in the wellbore, and fluid particle migration to the external filter cake surface is not impeded. The growth of the external filter cake tends to decrease the fluid and filtrate invasion rate. The second condition (dynamic fluid loss) occurs during fluid circulation and/or drillpipe rotation. The major difference between the static and dynamic fluid loss conditions is that the drilling fluid shearing action and helical flow condition along the wellbore wall in the latter overcomes the inertia condition of static fluid loss. Thus, the accumulation of drilling fluid particles and cuttings at the external filter cake and wellbore wall is impeded. In some cases, fluid particles and rock cuttings can be broken down further as they flow back to the surface because of pipe rotation and eccentricity. This is commonly observed in casing while drilling/drilling with liner applications (Ezeakacha 2014; Salehi et al. 2013; Rosenberg and Gala 2012).

Dynamic fluid loss condition is usually of interest because it accounts for up to 75 % of the total lost circulation time (Allen et al. 1991). Figure 2.2 shows that the fluid loss rate decreases because the fluid shearing action at any given depth declines as the drill bit progresses deeper. The authors claimed that the fluid shearing action is influenced by the pipe diameter, mud flow rate, and flow condition (laminar or turbulent) of the fluid. The flow condition at the bit is typically turbulent because of the jet impact force from the nozzles. The rapid flow along the drill collars tends to reduce over time as the fluid travel upwards. Along the drillpipe section, the shearing action is controlled by the laminar flow regime.

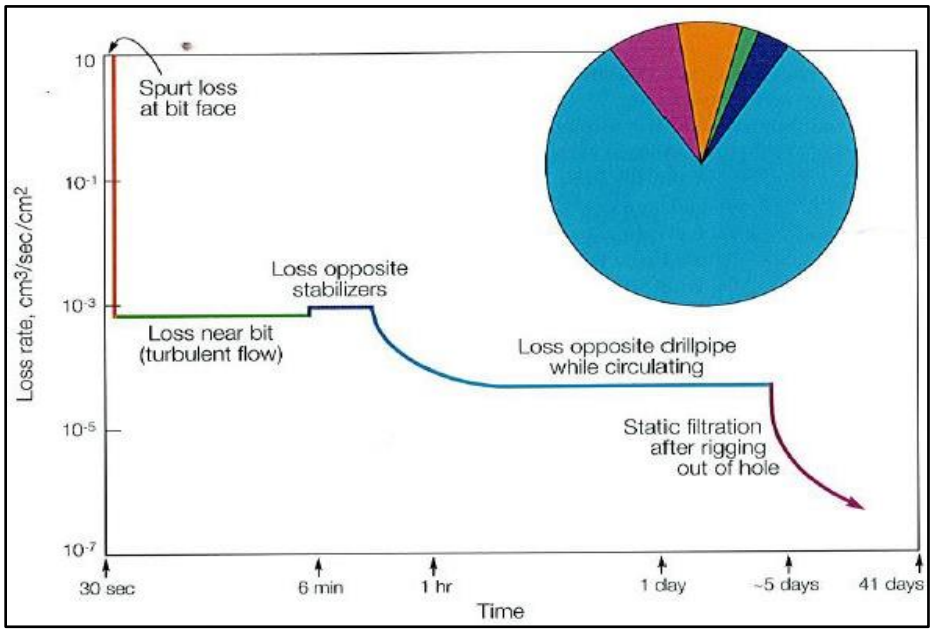

Figure 2.2: Lost circulation rate into permeable formation (Allen et al. 1991).

2.3 Drilling Fluid Loss and Filtration in Fractures (Induced and Natural Fractures)

Drilling fluid loss and filtration in fractures are typically classified with respect to the fracture type (natural fractures and drilling induced fractures). Losses through natural fractures occur in vugular and cavernous formations such as limestone, dolomite, and interbedded wellbore ballooning zones. Over the years, the lubrication theory has been used to predicate fluid loss in natural fractures, but

it does not account for pore throat losses (Ghalambor et al. 2014). The authors used this theory's fundamental equation (2.1), yield Power law rheological model, and numerical approach to determine the fluid loss through a 500 µm natural fracture width. They also determined the fluid loss rate using equation 2.2, and Figure 2.3 shows the result and plot of fluid loss through the fracture. The authors suggested that fracture width is critical to fluid loss, and that fluid loss stopped increasing because of the rheological properties of the fluid.

$$\frac{\partial(wv)}{\partial r} + \frac{1}{r}(wv) + \frac{\partial w}{\partial t} \quad \text{..... (2.1)}$$

$$q_{loss} = 2\pi r_w w_w v_w \quad \text{..... (2.2)}$$

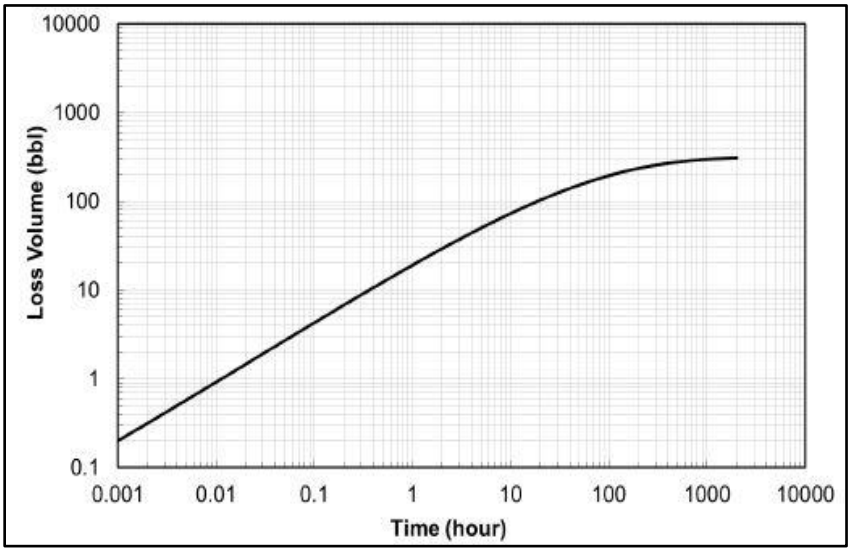

Figure 2.3: Fluid loss versus time for 500 µm natural fracture (Ghalambor et al. 2014).

Losses through drilling induced do not behave linearly like losses through natural fractures (Majidi et al. 2011). Rather, they are more sensitive to ECD variations, and can easily propagate if not sealed effectively. Fluid loss through an induced fracture takes place when the ECD exceeds the fracture gradient and tensile strength of a rock (Dupriest 2005). At the early development stages of an induced fracture, if the fluid inside and at the tip of the induced fracture contains well-sized fluid particles, it forms an external cake inside the fracture. This allows the development of more

external filter cake layers through compaction, over the fracture volume, and out to the wellbore wall open to the wellbore fluid. During this time, drilling fluid filtration can occur from the external filter cake within the fracture mouth and along the fracture length, through to the internal filter cake at the pore spaces surrounding the fracture. However, the changing wellbore dynamics (increase in mud flowrate, ECD, rotary speed, and bottomhole pressure) can increase the differential pressure across the wellbore wall. This results in the rupture of the two filter cake regions (external and internal filter cake); thus, permitting further fluid loss, fracture widening, and fracture elongation.

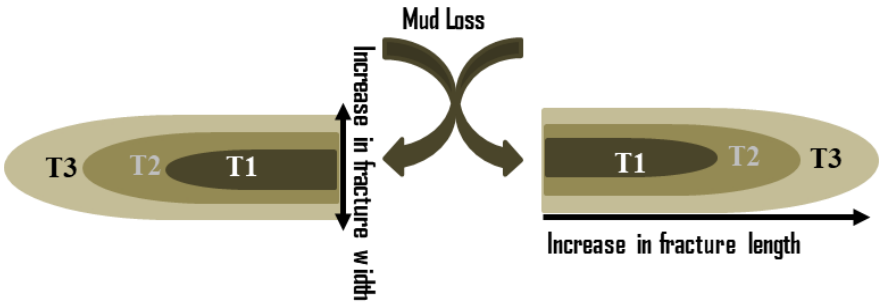

Figure 2.4: 2-D schematic showing the changes in fracture dimension over time with fluid loss.

Figure 2.4 shows that the fracture length, width, and aperture will increase over time because of the continuous rupture of the filter cake because of the dynamic wellbore conditions. Thus, it is important to seal an induced fracture before it propagates beyond containment. One of the ways to achieve this is to seal the maximum expected fracture width. Wang et al. (2016) referred to this as the critical sealing width. The authors used the hydraulic fracturing analytical theory to determine the spurt loss for a fast sealing LCM fluid, required to seal a critical induced fracture width. To avoid fracture widening while forming a stable filter cake bridge, the authors concluded that the spurt volume should be less or equal to the maximum allowable fluid loss volume into the fracture. Furthermore, Majidi et al. (2011) used an analytical approach and parameters such as fluid rheological properties, fracture parameters, and operational conditions to quantify fluid losses in

induced fractures. Their sensitivity analysis revealed that an induced facture width and rate of fracture propagation depends on the net differential pressure across the fracture and stiffness of the fracture. They also suggested that drilling fluid rheological profile impacts fracture propagation. The authors concluded that a high viscosity fluid can impede fracture propagation by partially sealing and isolating the fracture mouth from the wellbore fluid pressure.

A considerable number of experimental studies have been performed to quantify the fracture sealing efficiency of filter cakes from different LCM fluid formulations (Ezeakacha and Salehi 2018; Jeennakorn et al. 2017; Alsaba 2015; Salehi et al. 2015; Guo et al. 2014; Nwaoji et al. 2013; Hettema et al. 2007; Aston et al. 2004;). AlAwad and Fattah (2017) used shredded car tires as fracture sealing material in an experimental study. They modified the cell of a high pressure high temperature filter press to house fractured core samples (disk shape) in a static-linear filtration experiment. The authors recorded 25 cm^3 cumulative loss at 200 psi differential and 176^oF. After establishing the seal on the 0.12inch fracture width, pressure was increased to 900 psi and they recorded no filtrate loss. They concluded that the material can seal the fracture dimension investigated and preventing further losses. Wang et al. (2016) developed what they referred to as a "fast-sealing LCM". They used a static-linear permeability plugging test (PPT) apparatus to test the performance of this material and concluded that the fast-sealing LCM could seal fracture apertures between 200 µm to 1000 µm. Furthermore, Chellappah et al. (2015) used a combination of in-house walnut shell and marble to form a wellbore strengthening fluid. The particle size distribution (PSD) of the walnut shell was between 600 µm and 2000 µm, while the marble PSD was up to 800 µm. They tested this combination in a stress cage formulation and applied the recipe on fracture slots up to 0.19inch width using a PPT setup at 1500 psi. The authors recorded low fluid loss values between 22 cm^3 and 28 cm^3 with the recipe. However, without the marble, they

recorded over 250 cm^3. Although, the walnut shell is suitable for sealing fractures, the authors noted the importance of the background marble PSD. They suggested that the marble served to increase the interstitial packing within the small voids left by the walnut shell particles; thus, forming a more stable seal with the fracture.

In addition to these experimental studies, it is worthy to understand the creation and propagation mechanism of induced fractures in a wellbore field condition. This knowledge provides additional information on how to increase the fracture gradient and prevent further losses. The fracture pressure gradient is one of the main components of an operational mud window. Identifying the depth at which a casing is set, and the number of required casing strings are governed by a major key factor which is the fracture pressure gradient (Nygaard and Salehi 2011). There are three main tests that can be conducted to estimate the fracture gradient. They are typically referred to as the formation strength tests (FST), and they include: formation integrity test (FIT), leak-off test (LOT), and extended leak-off test (XLOT) (Alberty and McLean 2014). The major difference between the FIT and LOT is that in FIT, the formation is not fractured while in LOT, the formation is fractured at a pressure referred to the as the fracture gradient. The XLOT is a LOT repeated in two or more cycles to obtain more accurate data of fracture pressure. Breure et al. (2016) described a field case where they successfully deployed an LCM remedial squeeze to a severely fractured zone with vuggy pores. A formation integrity test (FIT) performed after each squeeze revealed that an increase (0.7ppg) in the fracture gradient had been achieved by the LCM mud cake wellbore strengthening process.

To corroborate the positive effect of filter cake evolution in fractures, Cook et al. (2016) studied the mechanical performance of a thick and thin external filter cake on a narrow and wide fracture opening respectively. The result of their study revealed that the thin filter cake would

move more rapidly into the fracture than the thick filter cake, in response to a differential pressure increase. This process increases the viscous resistance of the filter cake bridge within the fracture. For the thick filter cake, a crack tends to propagate upwards from the fracture mouth while the thin filter cake experiences tensile failure. Guo et al. (2014) also used various rock block experimental apparatus tests to confirm the effectiveness of filter cake in sealing induced fractures. Their study emphasized on the importance of LCM and particle size distribution in fracture sealing. They concluded that these two parameters are critical for sealing fracture widths that are greater than 1000 μm.

2.4 Applied Field Solutions to Drilling Fluid Loss and Current Gaps

There are several applied field solutions ranging from using plugging materials in a single treatment, to combining more than one type of lost circulation material (LCM), wellbore strengthening approaches, managed pressure drilling, and casing while drilling technology. The use of LCMs can be broadly categorized into remedial treatment (after a lost circulation event) and preventative treatment (in anticipation of a lost circulation zone). Other solutions can also be classified as either preventative solution or remedial solution, depending on the time of application, nature, and severity of loss event.

2.4.1 Remedial Treatment

Remedial treatment can be defined as any treatment method that is applied to cure fluid loss after a loss event has occurred. Typically, conventional LCMs are used for this type of treatment. They can be described as physically suspended mud particles that are categorized based on their physical appearance and/or properties into as fibrous, flaky, and granular, or a blend of all three (Canson 1985; White 1956; Howard and Scott 1951). Remedial treatment entails constant addition of conventional LCMs to the drilling fluid to reduce the losses. In a severe event such as losses to

vugs and carvens, LCMs are pumped in as concentrated pills and/or as sweeps to cure the losses (Fidan et al. 2004; Morita et al. 1990; Messenger 1981). They can also be pumped in as chemically activated cross-linked pills (Caughron et al. 2002; Bruton et al. 2001), deformable-viscous-cohesive (DVC) materials (Wang 2011; Whitfill 2008; Traugott et al. 2007), high concentration sand slurry mixtures (Saasen et al. 2011; Saasen et al. 2004), cross-linked cement (Mata and Veiga 2004), and nanocomposite materials and gel (Nwaoji et al. 2013; Lecolier et al. 2005). The current gap in this treatment method as the name suggests is that it is corrective measure, and a form of damage control.

2.4.2 Preventative Treatment

Preventative treatment is any method that is used in combating drilling fluid loss when the loss zone is known or anticipated. Per Whitfill (2008), the primary objective of a preventative treatment is to strengthen the wellbore. For instance, the pore pressure of an adjacent non-producing zone can be too close (1 ppg or less) to the fracture gradient of an already produced formation that is currently being drilled through. The goal in this scenario is to formulate a preventative drilling fluid recipe in a way that the fracturing pressure of the depleted zone is increased, while avoiding potential collapse and/or kick from the nearby adjacent zone. This process is usually referred to as wellbore strengthening. Salehi (2012) defined wellbore strengthening as a variety of approach that gives room for drilling a wellbore or an interval of interest with an increased fracturing pressure. Previous experimental, analytical, and field case studies have revealed that wellbore strengthening can be achieved through several techniques (Alberty and Yao 2018; Kiran and Salehi; Wang et al. 2016; Ezeakacha et al. 2016; Dorman et al. 2015; Contreras et al. 2014; Salehi and Nygaard 2011; Dupriest et al. 2008; Alberty and McLean 2004; Morita et al. 1990).

Some of the techniques include but not limited to: increasing the near wellbore hoop stress by having plugs of strong solid particles in short fractures, mud cake plastering around the wellbore, and increasing the fracture initiation pressure by minimizing leak off point value. Irrespective of the technique, wellbore strengthening has proven to be successfully used globally for drilling many oil and gas wells. Notably used for drilling through produced formations with their characteristic depleted pore pressure and fracture gradient. It's important to understand and quantify the mechanisms and frontier of preventative treatments. Using well-sized LCM particles in low concentration (preventative treatment) is more effective than using double the concentration in a remedial treatment (Guo et al. 2014). However, one of the current gaps in this solution is that to a certain degree, the average pore size distribution and expected fracture dimensions of the rocks dictates the type, size, and/or combination of LCMs to add for effective fluid loss reduction and wellbore strengthening. In real-time drilling operations, it is often difficult, if not impossible, to predict the actual pore size distribution and/or fracture geometry. This makes it quite difficult to design an optimum preventative drilling fluid recipe with the right particle sizes for mitigating losses.

2.4.3 Casing while Drilling (CwD) Solution

Casing while Drilling (CwD) can be described as the simultaneous drilling and casing of a well, using standard oil field casing as the drill string for providing torque, and a casing drilling assembly which is usually a top drive rig system. This technological solution is used in combating complete lost circulation (no-return) zones in a single trip with minimal connections (Espinosa et al. 2017; Kiran and Salehi 2016; Munoz et al. 2016; Velmurugan et al. 2015; Ezeakacha 2014; Salehi et al. 2013; Rosenberg and Gala 2012; Karimi et al. 2011; Warren et al. 2004). Filter cake plastering effect have been attributed to the increase in wellbore fracturing pressure and successful wellbore

strengthening observed in casing drilling applications. This phenomenon is defined as the smearing of drilling fluid solids to the wellbore wall and induced fractures, creating a thin and firm filter cake. As shown in Figure 2.5, this phenomenon is linked to the small annular clearance and constant rotation of the casing in contact with the wellbore. Some other factors such as mud weight, equivalent circulating density (ECD), flowrate, and fluid PSD also contribute to the plastering effect.

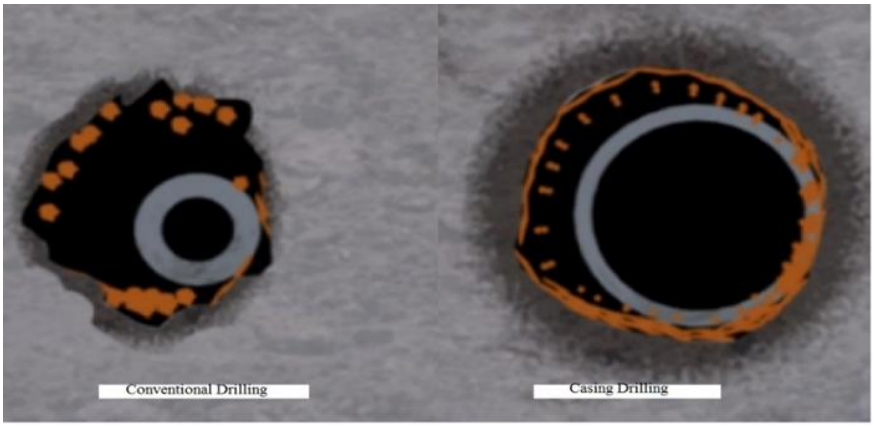

Figure 2.5: **Wellbore stability improvement by CwD compared to conventional drilling (Karimi et al. 2011)**

Alsaba (2015) referred to CwD and use of expandable liners as mechanical solutions under the remedial treatment approach. This is true but not in all cases, and it is supported by a comparative case by case field study for casing/liner while drilling operations used in lost circulation events (Ezeakacha 2014). The author discovered that up to 60% of the field cases had initially identified the lost circulation zones and their severity. Thus, CwD can be referred to as a contingent plan (remedial solution), where conventional drilling proves abortive. In some exceptional cases however, CwD is planned as a preventative treatment, especially with the use of LCMs for wellbore strengthening purposes. This has been deployed particularly for drilling through depleted sections or a very narrow operational mud window interval. Some of the major gaps, challenges, and considerations for CwD includes but not limited to: high cost and logistics, torque and drag

model (for deviated well profiles), cyclic fatigue model, proper stabilization to optimize inclination, and proper centralization for correct standoff during wellbore cementing operation.

2.4.4 Managed Pressure Drilling (MPD)

The international association of drilling contractors (IADC) subcommittee for underbalanced and balanced pressure drilling defines managed pressure drilling (MPD) as a flexible drilling process that can be used to specifically monitor and control the annular pressure profile of a well. By monitoring and controlling the annular wellbore profile, MPD methods may use a closed loop or pressurized mud return technique, downhole pumps, and/or alterative mechanical devices (Haghshenas et al. 2008). MPD methods are used in situations where conventional and unconventional LCM application and other mitigation procedures fail or are too expensive. Like CwD, MPD can also be used to drill very narrow operational mud window sections, where the risk of total lost circulation, formation fluid influx, and wellbore collapse are imminent. Haghshenas et al. (2008) classified MPD methods into: constant bottom hole pressure method (CBHP), pressurized mud cap drilling (PMCD), and Dual Gradient Drilling (DGD).

There have been several case studies and histories reported with respect to successful MPD operations (Haq et al. 2016; Ta Quo et al. 2016; Mashaal et al. 2013). These studies suggest that MPD solution is a viable option for mitigating lost circulation. If a loss zone is anticipated, it can be termed as a preventative mechanical solution. In addition, it can be synergized with CwD for future applications. However, one of the gaps and challenges with MPD is in the logistics and additional rig components such as the rotating control device (RCD). Also, availability of sea water makes MPD a more viable option for tackling total losses in offshore drilling rather than onshore drilling.

2.5 Filtration Mechanisms in Aqueous and Non-Aqueous Fluid (NAF) Fluid Systems

There are three major classifications of drilling fluids and these are: aqueous fluid system, non-aqueous fluid system, and aerated fluid system. The first two are typically used in overbalanced drilling, while aerated fluid system is usually employed in underbalanced drilling operations. Drilling fluid loss occurs in an overbalanced drilling operation. Thus, the focus in this subsection will be on the first two fluid systems. The primary difference between aqueous and non-aqueous fluid systems is the base fluid. While an aqueous fluid system can have fresh water or sea water as the base fluid, non-aqueous fluid (NAF) systems use either diesel, synthetic oil, or mineral oil as the base fluid. Aqueous fluid systems are generally referred to as water-based muds (WBM). The base fluid in each of these fluid systems play a key role in controlling their filtration mechanism, profile, and intensity. Both fluid systems have similar filtration mechanisms especially at the preliminary stages of fluid loss and filtration.

2.5.1 Filtration Mechanism in Aqueous Fluid System

The first stage of drilling fluid loss (WBM) occurs when the rock is exposed by the drill bit to the drilling fluid with a differential pressure. This is known to as “high-energy spurt loss” and it is usually measured in 10 seconds during pore-scale laboratory fluid loss experiments. In the second stage (mud filtration), constant differential pressure across the wellbore wall tends to force ultra-fine solids and filtrate to invade the external filter cake and pores of the rock in what is known as “low-energy, steady state fluid invasion”. This is usually collected for 30 minutes during a pore-scale laboratory fluid loss experiment. The detailed mechanism of these two fluid loss stages will be explained in the next two paragraphs. Before this, it is worthy to mention that this two-stage process (high-energy spurt loss and low-energy steady state fluid invasion) is not always in this order for all fluid loss processes, because they can be influenced by other fluid loss variables.

Recently, Ezeakacha and Salehi (2018) studied the dynamic filtration mechanisms and profiles of various WBM recipes on different rock samples. They used thick-walled cylindrical rocks from various lithologies and discovered that some experiments did not reveal the typical "high-energy spurt loss" before the "low-energy steady state fluid invasion". Instead, a delay was observed which was immediately followed by the "low-energy steady state fluid invasion". The authors referred to this observation as the fluid/filtrate loss breakthrough time. They defined it as the time taken before a significant fluid loss value is observed after attaining experimental conditions (differential pressure, temperature, and rotary speed). They likened this observation to the typical spurt loss time (10 seconds) in the low temperature low pressure filter press tests with filter papers. The authors concluded that the fluid loss breakthrough time in rocks is largely influenced by rock permeability, porosity, bridging solid cluster mechanism, rotary speed, and temperature.

Within the first stage of mud filtration, rock exposure by the drilling bit tends to create induced fractures in the maximum horizontal stress direction. Prior to their propagation, the initial fracture width can be as small as the surrounding average pore throat diameter. Fluid is lost through these fractures and wellbore pore throats because of differential pressure. During this time, an internal filter cake can be formed from the accumulation of mud particles that plug the near-wellbore pore throats and newly induced fractures. This leads to wellbore stabilization or filter cake wellbore strengthening. Wellbore strengthening by filter cake occurs when drilling fluid particles are driven by a potential to penetrate and deposit in and around the wellbore wall, thus forming a low-permeability internal filter cake that increases the fracture gradient (Kiran and Salehi 2016; Cook et al. 2016; Farahani et al. 2014). Jilani et al. (2002) claimed that the internal filter cake buildup within the pore throats is favored by differential pressures around 300 psi. The

authors concluded that fluid particles will migrate freely through the pore constrictions at low pressures (100-200 psi). They also noted that pressures up to 700 psi will fragment the internal filter cake or enlarge the pore throat walls because of particle-pore friction. But this is also dependent on the type and morphology of the drilling fluids additives (particularly LCMs) used.

The mechanism of bridging solids cluster is very critical for internal filter cake evolution as it dictates the stability of the bridge that must be formed to prevent subsequent ultra-fine solids and filtrate influx (Khan et al. 2016; Civan 2007). Ezeakacha et al. (2017) supported this claim by defining particle-particle interlocking and particle-pore interlocking as the cohesive interaction between various mud particles, formation fines, and pore throat surface because of the difference in material roughness, irregularity, and surface area. The authors attributed the reduction in mud filtration to these two mechanisms using scanning electron microscope (SEM) images of cores and LCMs to corroborate mud filtrate experimental results. Furthermore, the plasticity of the low-permeability internal filter cake assists in reducing the near-wellbore permeability and isolating the formation fluid from further damage. In addition, the pressure of the newly invaded mud depends on the formation pressure; thus, the internal filter cake will tend to lower the formation pore pressure increase behind it after building up (Cook et al. 2016).

After the evolution of the internal filter cake, drilling fluid filtration commences as the second stage of fluid loss. This process allows mud filtrate and ultra-fine particles to invade the rock through the external filter cake that is been developed (Jiao and Sharma 1994). The external filter cake is the visible filter cake region that develops from the accumulation of various mud particle sizes on the wellbore wall, and it is in direct contact with the wellbore fluid. The fluid drag effect causes the external filter cake to undergo compaction by allowing the smaller particles to penetrate deeper through it (Tien et al. 1997). The authors suggested that larger-sized particles first

form the base of the external filter cake. However, the elevated drag potential that drives all the fluid particles to the cake surface deposits smaller particles faster. At some point within dynamic filtration, drilling fluids particle migration to the external filter cake and erosion rates become the same. This makes the external filter cake a heterogeneous material, comprising of various particle sizes at the formation face, while permitting only small particles to be exposed to the wellbore fluid flow path (Wang et al. 2016; Elkatatny et al. 2013). Cook et al. (2016) suggested that the average external filter cake thickness from water-based muds (WBM) is usually between 0.05 inches and 0.5 inches, depending on the operating conditions and porous media.

2.5.2 Filtration Mechanism in Non-Aqueous Fluid (NAF) System

The filtration mechanisms described for aqueous fluid system typically applies to NAF system. In general, NAF's have been recognized with distinctive benefits such as thin-impermeable filter cake, improved lubricity, enhanced shale stability, rheological stability at elevated temperature, and tolerance to some contamination. For instance, increasing the overbalance pressure across a very thin oil-based-filter cake causes the deformation of brine droplets in the mud brine phase, and this reduces the external filter cake's permeability (Allen et al. 1991). However, the authors suggested that if the emulsion droplets in an oil-based mud (OBM) breaks down, with the brine droplets coalescing, brine can also invade the formation. Warner and Rathmell (1997) determined the controlling mechanism of filtration rate in OBM by invading rock samples with OBM filtrate. The authors concluded that the OBM filter cake controls the pressure profile between the mud and rock sample; thus, controlling the filtrate invasion radial length. In addition, because of the low fluid loss from OBM's, the filter cakes from this mud system are usually thinner compared to those from WBM's (Cook et al. 2016). Furthermore, the characterization of filter cake compressive strength (yield stress), carried out by Cerasi et al. (2001), revealed a wide range of yield stress

values (10^3-10^5pa). The authors suggested that the magnitude of this property is weaker in an OBM compared to a WBM, and this conclusion is supported by Figure 2.6.

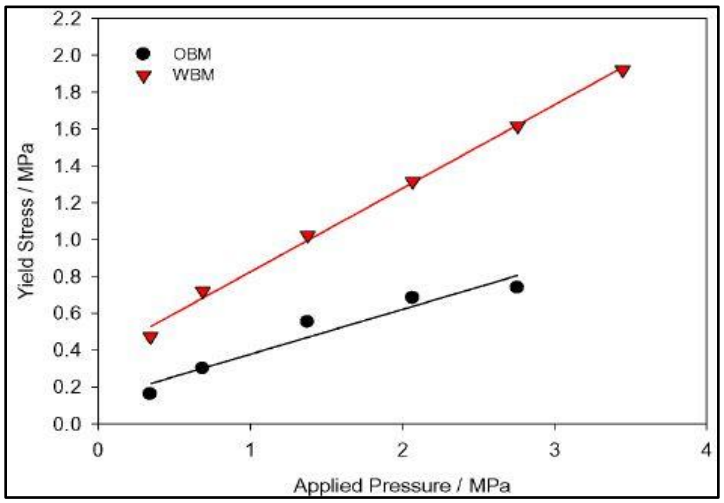

Figure 2.6: Filter cake yield stress from 13.3ppg OBM and 12ppg WBM (Cook et al. 2016).

An OBM recipe that is carefully formulated with LCM for field application will reduce fluid loss and enhance the filter cake properties. However, low-permeability filter cake from OBM filtration can also be an issue for filter cake wellbore strengthening especially in fractures. OBM's prevent effective leak-off and have lower fracture propagation and reopening pressure compared to WBM (Morita et al.1990). This is partly because the weighting material and emulsion droplets are the main filter cake components, and they play little to no role in the mechanical bridging of fractures. To solve this challenge, Brege et al. (2010) discovered that by changing the wettability of an OBM filter cake, from oil-wet to water-wet, the filter cake permeability will be enhanced. The authors developed a spotting fluid treatment that could improve the effectiveness of a water-based LCM pill used in OBM's. Their results showed that this treatment can improve the carrier fluid's capability to hold the LCM; thus, altering the wettability of an OBM filter cake from oil-wet to water-wet. They concluded that this will promote the healing of fractures and ultimately increase the fracture propagating pressure (wellbore strengthening).

2.6 Critical Review of Factors Affecting Drilling Fluid Loss and Mud Filtration

The complexity of drilling fluid loss and filtration goes beyond the frontiers of the mechanisms that have been discussed. In a field scenario, there are several factors that can complicate fluid loss and filtration. These factors have been classified into operational (control) factors and pre-existing factors. The operational factors are variables that are within the design and control limits of operators and service companies. These factors can be determined before drilling and can be controlled within drilling or mud loss/filtration events. They include but not limited to: type of fluid, fluid weight, fluid rheology, type of LCM, concentration/combination of LCM, fluid flow rate, rotary speed, eccentricity, and tripping speed. The pre-existing factors are variables that are typically uncontrollable. They can be referred to as "mother nature" factors, and they include but not limited to: temperature increase with depth, fracture height, fracture width or aperture, fracture length, type and composition rock, rock permeability, rock porosity, and rock fluid interaction.

2.6.1 Review of Lost Circulation Material's (LCM) and Particle Size Distribution (PSD)

Lost circulation materials (LCMs) are drilling fluid additives that are used to primarily mitigate lost circulation into fractures and highly porous media. Applying an LCM to a drilling fluid has significant effects on the quality and composition of a filter cake. Previous studies on the microstructure and composition of the external filter have shown that approximately 60% or more of the filter cake, developed from an LCM blended mud is composed of the LCM solids used. Thus, classification of these materials is critical as it helps to determine which type and combinations can result in effective fluid loss reduction and filter cake evolution. Alsaba (2015) reclassified LCMs into eight categories based on their appearance and application. These are: 1). granular LCM type (calcium carbonate, graphite, gilsonite, bentonite, perlite), 2). flaky LCM type (flaked calcium carbonate, cottonseed hull, and corn cobs), 3). fibrous materials (cellulose fiber,

saw dust, mineral fiber, and Cedar fiber), 4). acid/water soluble LCMs (calcium carbonate and mineral fiber), 5). LCM mixture, 6). High fluid LCM squeeze, 7). swellable/hydratable LCM, 8). nanoparticles (NP) LCM (iron hydroxide, silica, and calcium carbonate). The author described in detail the differences between these LCM types and combinations.

Table 2.1: Evolution of particle size distribution (PSD) and LCM selection criteria

Literature	Type of Study	Porous Media	Outcome
Andreasen and Anderson (1930)	Ideal Parking Theory (IPT)	Pore Throat	Packing Density, x = 0.5
Bo et al. (1965)	PSD for glad Beads	Pore Throat	Packing Density, x = 1
Abrams (1977)	2-rule for LCM selection	Pore Throat	Median particle size ≥ 1/3 mean target pore size
		Pore Throat	Concentration ≥ 5% volume
Smith et al (1996) and Hands et al. (1998)	D_{90} Rule for LCM PSD	Pore Throat	90% particle size = pore size
Dicks et al. (2000)	Revised IPT	Pore Throat	Packing Density, x = 0.5
Vickers et al. (2006)	5-rule for LCM PSD	Pore Throat	D90 = largest pore throat
		Pore Throat	D75 < 2/3 the largest pore throat
		Pore Throat	D50 ≥ 1/3 of the mean pore throat
		Pore Throat	D25 = 1/7 the mean pore throat
		Pore Throat	D10 > smallest pore throat
Whitefill (2008)	LCM PSD rule for fracture	Fracture	D_{50} = fracture width
Chellappah and Aston (2012)	Revised IPT	Pore Throat	Packing Density, x = 0.25 to 1.25
Ezeakacha (2014)	Revised IPT	Pore Throat	Packing Density, x = 1
Alsaba (2015)	LCM PSD rule for fracture	Fracture	D_{50} ≥ 3/10 of fracture width
			D90 ≥ 6/5 of fracture width
Ezeakacha (2018)	LCM selection rule based on operating conditions	Sandstone, Limestone, Chalk	For temp. ≤ 200°F, rotary speed ≤ 70 RPM, permeability ≤ 105 mD, and porosity ≤ 23% $CaCO_3$ concentration ≥ 55 lb/bbl
		Fracture	For fracture width ≤ 2000 µm, temperature ≤ 220°F, and rotary speed ≤ 110 rpm: 2.4 % ≤ Cedar fiber concentration volume ≤ 14 %

Adding LCMs in mud formulations can influence the PSD of the wellbore fluid, and enhance filter cake properties such as thickness, cohesion, and tightness (Kiran and Salehi 2016). Table 2.1 summarizes the evolution and research progress made in drilling fluid PSD and LCM selection

criteria. Drilling fluid particle size distribution (PSD) can be defined as the spatial distribution of various size particles within a drilling fluid system, and their potential for plugging target pore throat diameters or fracture widths in a rock (Ezeakacha and Salehi 2018). During drilling, wellbore conditions are dynamic, and these conditions tend to alter the PSD of LCMs before they reach the target pore throat or fracture opening. For instance, LCMs have temperature limits beyond which they start to degrade, and this reduces their pore and fracture plugging potential. This is one of the gaps that have not been addressed in most previous studies. In addition, the gelling material used in preparing drilling fluid plays a critical role in LCM agglomeration and packing with. Furthermore, the studies in Table 2.1 whose LCM/PSD criteria are for pore-scale invasion have only considered average pore throat diameter. This result from this dissertation shows that the PSD/LCM selection criteria for pore-scale invasion in Indiana limestone and Austin chalk should consider porosity, permeability, average pore throat diameter, and internal natural fractures/solution channels. While the LCM/PSD selection criterial for sandstones largely depends on permeability and average pore throat diameter.

Following the advancements in drilling fluids PSD analyses and packing theory development, it is worthy to note that unimodal and bimodal fluid PSD patterns can exist. Considering an incremental PSD plot, a unimodal PSD shows only one obvious peak, depicting the mean size distribution of fluid particles. An example of a unimodal PSD is the red PSD curve in Figure 2.7. Some fluids with irregular size distribution of particles or particles that are not completely dispersed in the fluid exhibit the bimodal PSD. This PSD profile (shown by the remaining four curves in Figure 2.7) exhibit more than one peak, usually two. In some cases, some of the peaks are not completely obvious (like the green curve in Figure 2.7). In this figure, one of

the three levels of what is believed to be the theoretical mechanism of wellbore strengthening in casing while drilling is the combined LCM and cutting PSD.

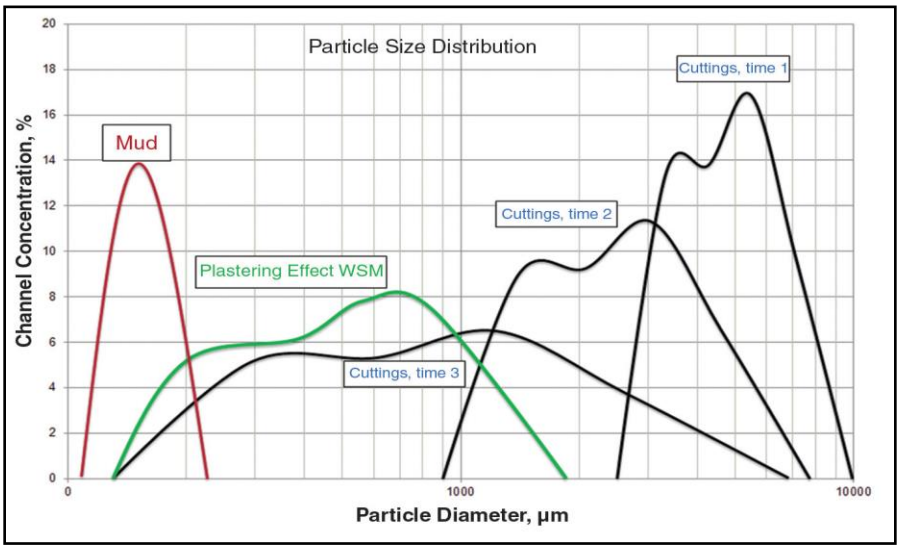

Figure 2.7: Custom blends of LCM creates the best condition for plastering effect CwD (Courtesy: Weatherford)

Irrespective of a fluids' PSD profile, it is important to have a general idea of matching fluid particles to pore throat sizes. Thus, wellbore drilling fluid particles can be categorized as follows: particles smaller than the average pore throat diameter, particles much greater than the average pore throat diameter, and particles with sizes equal to or nearly equivalent to the average pore throat diameter. Mud particles that are smaller than the average pore throat diameter and ultra-fine particles have greater potential for migrating further into the formation. If these particles migrate in high concentration, but have poor particle packing mechanism, they cause formation damage. Research shows that the shape, morphology, and size distribution of wellbore fluid particles have strong impact on particle packing mechanism (Ezeakacha et al. 2017; Chellappah et al. 2012). Therefore, fluid particles with strong agglomeration will form a rigid internal filter cake region around the near-wellbore pore spaces and fracture openings. This will prevent further formation damage while increasing the near wellbore hoop stress. In addition, the morphology of particles can be analyzed using the sphericity and roundness chart by Powers (1953). Particles that are

greater than a target average pore throat diameter may not completely partake in forming an internal filter cake but will act as external filter cake material (Loeppke et al. 1990).

2.6.2 Review of Drilling Fluid Rheological Effect

Drilling fluid rheology is an important operational factor that affects drilling fluid loss and filtration. Drilling fluid rheological profile impacts fracture propagation, and a high viscosity fluid can impede fracture propagation by partially sealing the fracture mouth from the wellbore fluid pressure (Majidi et al. 2011). The four common types of drilling fluids rheological models include: Newtonian model, Bingham plastic model, Power law model, and Herschel Bulkley model. Some of the studies that have highlighted the importance of mud viscosity in reducing losses through fractures have been discussed in section 2.3. In addition to these, Sanfillippo et al. (1997) performed an analytical study on fluid loss through a non-deformable fracture. The authors considered a compressible Newtonian fluid and obtained an approximate analytical relationship between time and fluid loss volume. The authors did not consider the muds plugging effect in their model but concluded that fluid loss seized after some time because of the plugging effect. In another study, Lietard et al. (2004) considered a Bingham plastic fluid and developed a model for fluid loss through a non-deformable fracture. Their model was used to generate curves for mud invasion radius versus time. The authors suggested that fluid loss stopped because of the mud rheology. They attributed this to the formation of a stable plug by the Bingham plastic fluid within the entire fracture channel. Thus, mud invasion and propagation stop at a certain distance from the wellbore wall.

The importance of using a realistic non-Newtonian model to estimate fluid loss cannot be overemphasized (Verga et al. 2000). The authors also used a Bingham plastic fluid to model and estimate fracture aperture with fluid loss data. Lavrov and Tronvoll (2004) incorporated a Power

law fluid model for estimating fluid loss in fractured systems. Figure 2.8 and Figure 2.9 shows the behavior of two Power law fluids compared to a Newtonian fluid model in relation to fluid loss. The authors chose consistency index values to bring the rheological profiles in Figure 2.8 (a) close, over a wide range of shear rates. This also reflects in similar fluid loss profiles observed in Figure 2.8 (b).

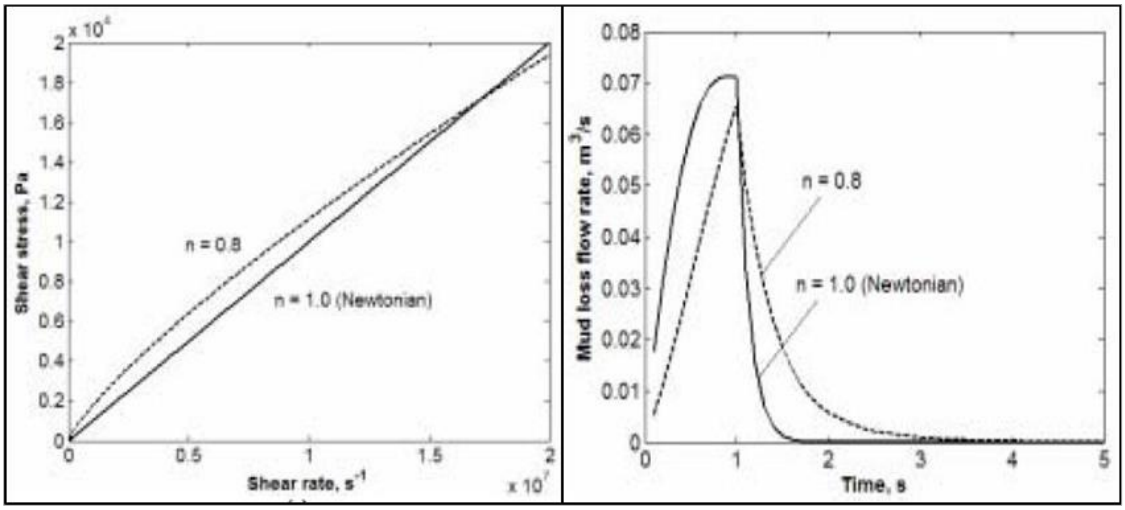

a **b**

Figure 2.8: Mud rheology and loss rate profiles for n = 1, k= 0.001 Pa.s and n = 0.8, k = 0.028 Pa.s$^{0.8}$ (Lavrov and Tronvoll 2004)

The slope of the Newtonian fluid in Figure 2.9 (a) shows that it exhibits a more viscous behavior compared to the Power law fluid. The initial fluid loss profile shows a sharp rise and peak, followed by a quick decline. For the Power law fluid which showed a less viscous profile, the initial fluid loss mechanism (Figure 2.9 b) showed an instantaneous-steady loss rate, followed by a 90^{o} decline in loss rate. The difference in their viscous behavior is displayed in the loss profiles. Increasing the consistency index of a Power law fluid decreases the slope in the loss rate profile. The authors stated that although the mud rheology impacts the initial fluid loss mechanism, it did not affect the total fluid loss volume, which they found to be equal. They assumed a wellbore strengthening scenario where the fracture propagating pressure was above the wellbore pressure. Thus, at some

point during fluid loss, the fluids with different rheological model will come to equilibrium, and the pressure in the wellbore is the same with the pressure in fracture.

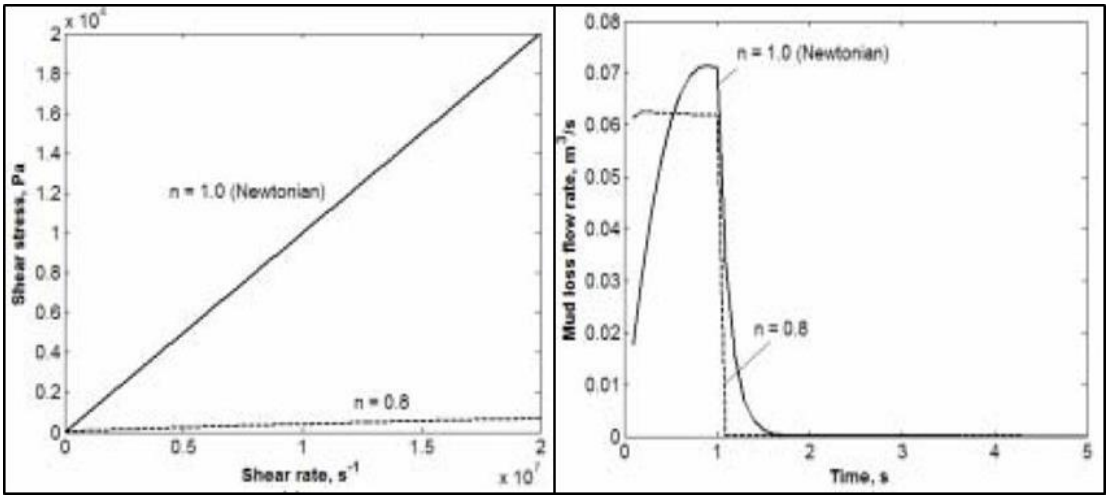

a **b**

Figure 2.9: Mud rheology and loss rate profile for n = 1, k= 0.001 Pa.s and n = 0.8, k = 0.001 Pa.s$^{0.8}$ (Lavrov and Tronvoll 2004)

The impact of fluid rheology at the initial stages of fluid loss is also supported by the numerical study conducted by Sun and Huang (2015). They employed a piecewise rheological model that incorporates yield stress and Power law. The authors suggested that at lower shear rates, the fluids in Figure 2.10 (a) will exhibit similar rheology. But with an increase in shear rate, such profile diverges, and is evident in the profile of fluid invasion radius. Figure 2.10 (b) shows fluid invasion radius over time at high shear rate for different values of flow index. The figure reveals that at the initial mud invasion stage, the fluid invasion radius is impacted by the flow index. However, the invasion radii increasingly converge overtime. Thus, given the same differential pressure, the authors concluded that fluid invasion diameter becomes less sensitive to fluid rheology over time. Their model also suggested that high shear rheology is critical in controlling fluid loss since it takes effect at the initial stages of fluid loss.

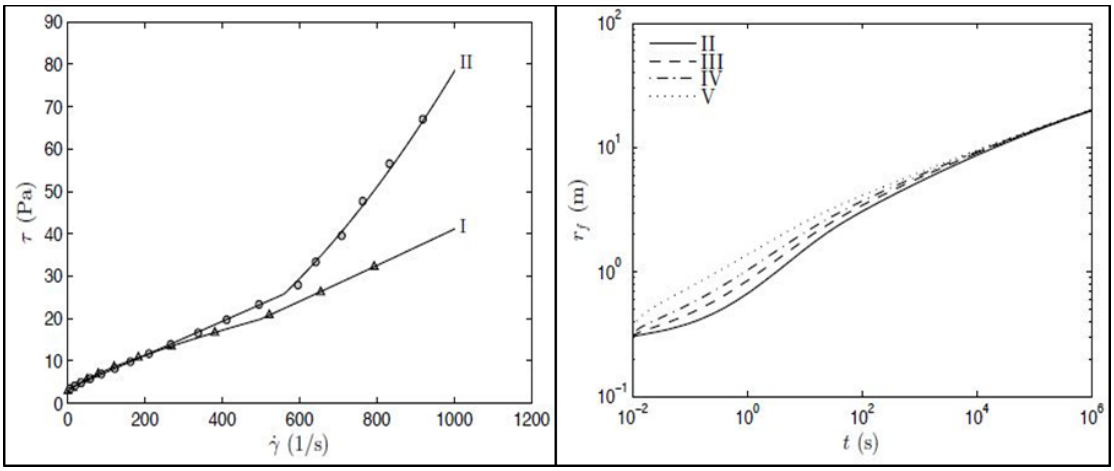

a **b**

Figure 2.10: Shear stress vs. shear rate showing strong deviation as shear rate increases (a) and invasion radius vs. time where case V (n = 0.7) and case II (n= 1.9) (b) (Sun and Huang 2015)

2.6.3 Review of Rotary Speed, Flow Rate, and Wellbore Geometry

Two crucial factors to consider during dynamic fluid loss is the rotational effect of the drillpipe and mud flow rate. These control factors are particularly important because dynamic fluid loss condition accounts for up to 75% of total drilling fluids loss time as shown in Figure 2.2 (Allen et al. 1991). Thus, it is important to understand the effects of changing wellbore dynamic conditions such as drill pipe rotation and flow rate. Several studies have been conducted on mud hydraulics in relation to drillpipe rotation, annular pressure drop (ECD), and wellbore geometry (Ahmed and Miska 2008; Hemphill and Ravi 2005; Ooms and Kampman 2000; Bailey and Paden 1997). Most of these studies agree that there is a relationship between drillpipe rotation and ECD, which will generally impact drilling fluid loss and filtration. According to Ahmed and Miska (2008), the effects of pipe rotation on annular pressure loss is influenced by the flow regime, eccentricity, diameter ratio, and fluid properties (rheology and density). Along the drillpipe section, the shearing action of the mud from pipe rotation and flowrate is controlled by the laminar flow regime (Allen et al. 1991). This results in reduced annular pressure loss effect compared to the bottomhole.

However, an increase in the annular pressure loss and ECD can still exist along the drillpipe section because of Taylor vortices and irregular secondary flows from the lateral drillstring rotation (Ahmed and Miska 2008). The authors suggested that these flows occur because of centrifugal and shear instabilities. In their study, they investigated the effect of drillpipe rotation on a yield Power law fluid in a concentric and eccentric wellbore geometries. They reported shear thinning effect and inertial effect as two major flow phenomena that impacts a change in annular pressure loss with drillpipe rotation. The shear thinning effect is dominant in a concentric or slightly eccentric flow, and annular pressure loss is generally reduced as pipe rotation increases. The inertial effect is dominant in eccentric and/or irregular wellbore geometries, even at low pipe rotation. In the case of high flow rate and Reynolds number, the inertia effect also dominates the shear thinning effect. In both cases (eccentric geometry and high flow rate), the annular pressure drop is increased which leads to an increase in lost circulation and mud filtration.

Hemphill and Ravi (2005) developed an engineering approach for calculating drillpipe rotational effect on concentric wellbore fluid flow. Their approach assumed a Herschel Buckley fluid model. Figure 2.11 shows that the annular rotational velocities decreased as the gap between the drillpipe and wellbore wall increased. The authors concluded that at lower rotary speeds, annular pressure drop and ECD can be lowered. This is because of the reduced wall shear stress and shear thinning behavior of non-Newtonian fluid. However, beyond a certain rotary speed, increased drillpipe rotation will raise ECD and subsequently fluid loss. They also concluded that drillpipe rotational effect was most pronounced when the mud flow rate and axial pressure drop is lowest.

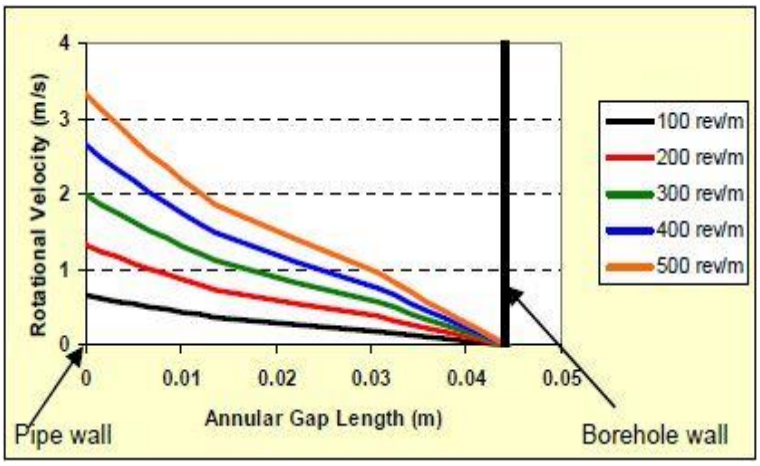

Figure 2.11: **Annular rotational velocities at different rotary speeds, without axial rotation (Hemphill and Ravi 2005)**

The wellbore geometry is also a contributing factor which supports drilling fluids plastering effect that reduces drilling fluid loss and filtration (Figure 2.5). A comparative study showed that up to 90% of successful casing while drilling or drilling with liner operations had a casing-wellbore ratio between 0.7 and 0.85 (Ezeakacha 2014). The studies by Kiran and Salehi (2016) and Salehi et al. (2013) also support this finding. Casing to wellbore ratio below 0.7 may not assist in fracture healing because of insufficient contact between the casing/liner and wellbore wall. Ratios above 0.85 tend to induce longer fractures whose growth may be difficult to arrest and/or take longer time to seal.

The fundamental principle of drillpipe rotation in relation to fluid rheology can be described from the concept of the concentric cylindrical viscometer. This also provides knowledge on the wall shear stresses (outer wall of drillpipe and wellbore wall) and their impact on depositing and eroding the external filter cake particles during drilling fluids filtration. The Searle system (rotating bob and stationary cup) and Couette type system (stationary bob and rotating cup) are the two common viscometry systems (Steffe 1996**)**. Most of the commonly used concentric cylinder viscometers are of the Searle-type system. Figure 2.12 shows a concentric cylinder system with a

bob that is recessed at the top and bottom to minimize end effect. The basic assumptions in deriving the governing equations are: laminar and steady state flow, incompressible fluid, constant temperature, no slip at instrument boundaries, negligible end effects, no bob eccentricity.

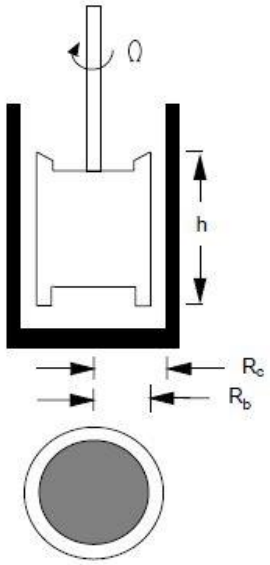

Figure 2.12: Concentric cylinder schematic (based in DIN 53018) (Steffe 1996)

When the bob rotates at a constant speed with a constant angular velocity (Ω), the opposing torque (M) is measured from the shear stress (τ) exerted on the bob by the fluid, and a force balance yields equation (2.3).

$$M = 2\pi h \tau r^2 \quad \text{..... (2.3)}$$

where h is the effective height of the bob, r is any radius between R_c (radius of cup) and R_b (radius of bob). Rearranging equation (2.3) and solving for shear stress, it can be observed that the shear stress tends to decrease from the bob towards the wall and it is maximum when $r = R_b$ as shown in equation (2.4).

$$\tau_b = \frac{M}{2\pi h R_b^2} \quad \text{..... (2.4)}$$

For the shear rate in very narrow gaps, where R_b/R_c is greater than 0.99, the curvature can be neglected, and shear stress will be the same as that of a parallel plate. Thus, the shear rate is given as:

$$\gamma(R_b) = \frac{\Omega_b R_{avg}}{R_c - R_b} \quad \text{(2.5)}$$

R_{avg} is the average of R_b and R_c. For intermediate gap where $G = R_b/R_c$ is greater than 0.5 but less than 0.99, the shear rates at the bob and cup wall are given in equations 2.6 and 2.7. In this equation, n is the flow behavior index of the fluid. Most viscometers and wellbore geometries are within this ratio.

$$\gamma(R_b) = \frac{2\Omega_b}{n\left(1 - G^{\frac{2}{n}}\right)} \quad \text{(2.6)}$$

$$\gamma(R_c) = \frac{-2\Omega_b}{n\left(1 - G^{\frac{-2}{n}}\right)} \quad \text{(2.7)}$$

2.6.4 Review of Geochemical and Lithology Effect

The geochemical factors that impact drilling fluid loss can be referred to as some of the pre-existing factors such as lithology type, rock mineralogical composition, permeability, and porosity. Lithology is a term that is often used to describe the solid portion of a rock; i.e., the gross physical characteristics of a rock and its mineral compositions. The type of lithology is an important variable that influences drilling fluid loss, invasion rates, and filter cake evolution. Hydrocarbon bearing lithologies can be simply classified into clastic rocks (sandstone, shale, and shaly sands) and carbonate rocks (limestone, dolomite, and chalk). The underlying difference between these rocks is in their geochemical composition and mineralogy. While sandstones are largely made up of quartz and feldspar, carbonates are heavily composed of carbonate minerals most of which are calcite. The grain structure, orientation, and cementation are also distinguishing features between

these rocks. The grain structure in sandstones has been influenced overtime by the physical weathering and sedimentation process. Their pores are often interconnected, and quartz is the primary cementing material in most sandstones. In unconsolidated sands or loose sands, the quartz cementation is usually weak (Churcher et al. 1991).

The pore structure in carbonate rocks is largely influenced by chemical dissolution, secondary solutions, and recrystallization of fossil fragments from which their grains are formed. For instance, the petrographic study that was conducted by Churcher et al. (1991) revealed that high-permeability Indiana limestones experienced more chemical weathering during the sedimentary process. This weathering process, secondary solution, and recrystallization resulted into the creation of natural cavities, fractures, and vuggy pores within this limestone. In addition, most carbonate rocks are found to be strongly cemented by calcite, and their grains can be crystalline or granular. Their pores may be highly interconnected and may not be interconnected. However, the presence of vuggy pores and natural fractures existing in carbonate rocks makes them susceptible to high fluid loss and filtration.

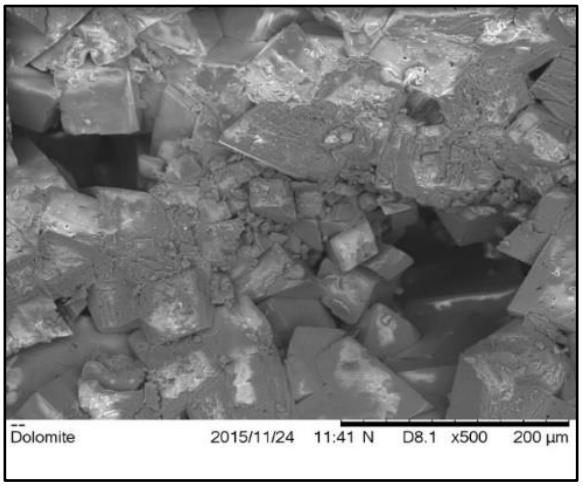

Figure 2.13: Scanning electron microscope (SEM) image of a Silurian dolomite sample

The morphology in Figure 2.13 shows two large vuggy pores, and the particles appear to be crystalline and tightly packed. While cementation describes the compactness of rock particles, the tortuosity of these rocks is also considered to influence mud and filtrate flow through the rocks. Tortuosity is a term that is commonly used to describe the ease of a fluid flow path, and it's often linked to the permeability and porosity of a formation. Some experimental results from this study have shown that high-permeability formations experience high fluid loss, regardless of the cementation. In addition, low-permeability Austin chalk is prone to high fluid loss because of high porosity and as well as poor cementation. Unconsolidated and loose sandstones are also candidates for high fluid loss events because of their poor quartz cementation.

2.6.5 Review of Temperature Effect

Temperature is one of the critical pre-existing factors that affects fluid loss and filtration. One of the primary focus in this study is to quantify the effect of temperature on dynamic fluid loss and filtration. Loeppke et al. (1990) reported that most of the conventional LCMs used in their roller oven test would start degrading at 200^{o}F. The authors concluded that fibrous LCMs such as wood fibers would degrade permanently at 400^{o}F. A recent study has shown that an increase in temperature (120^{o}F to 220^{o}F) can significantly increase dynamic filtrate loss in homogenous ceramic filter tubes up to 40% (Ezeakacha and Salehi 2018). This is based on a 95% confidence interval from experimental and statistical analysis. Preliminary experiments have been conducted on water base mud systems for different temperatures. Figure 2.14 also shows that the two highest mud filtration values were at 220^{o}F, notwithstanding the average pore throat diameter or type of LCM used. This is one of the plots from a recently conducted dynamic fluid loss study at varying temperatures.

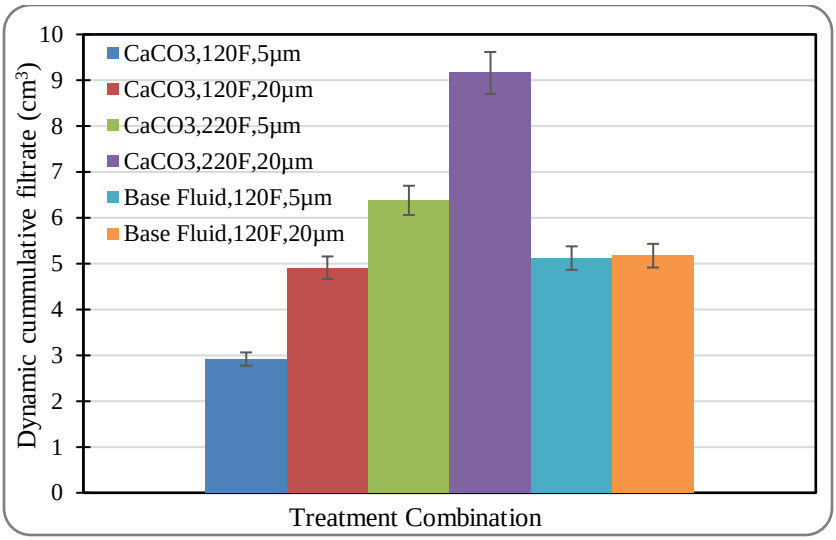

Figure 2.14: Dynamic cumulative filtrate from an LCM and non-LCM fluid after 30minutes (Ezeakacha and Salehi 2018)

Chapter 3: Statistical Design and Analysis and Laboratory Experimental Methods

3.1 Overview

This chapter contains a detailed description of the statistical and laboratory experimental approaches used in this research. The statistical design and analysis will be discussed first, beginning with the pre-experimental considerations (design of experiments and development of hypotheses) and concluding with the post-experimental evaluations which are analysis of variance (ANOVA) and regression analysis. After discussing the statistical methods, the experimental methods will be discussed extensively. The details in this section will cover the materials selection and compositions, types of experiments conducted, experimental devices and setups, and experimental procedures.

3.2 Statistical Design and Analysis

Statistical design and analysis are generally referred to techniques used in conducting research and analyzing data with the aim of drawing specific conclusions based on the measurements and observations. According to Montgomery (2013), there are four eras' in modern evolution of statistical design and analysis. The agricultural era was the first and was led by Sir Ronald A. Fisher (1920s and early 1930). The three fundamental principles of experimental design (replication, randomization, and blocking), factorial design, and analysis of variance (ANOVA) were developed in this era. The second era was the industry era (from the 1950's) led by George box, and the response surface method (RSM) was developed in this era (Box and Wison 1951). Genichi Taguchi led the third era (from late 1970's) and developed what is commonly referred to as the Taguchi design or robust parameter design (Taguchi 1991; Taguchi and Wu 1980). The fourth era included a revised general interest in statistical design and data analysis. In addition,

computer software's and program languages such as SAS, JMP Pro, and R have been developed within this era.

In this study, statistical design and analyses were performed. Dynamic drilling fluid loss and filtration is been investigated and the factors that affect this process have been detailed in section 2.6. Experimental design methods and hypothesis testing can be used in quantifying the effects of operational (control) factors and pre-existing factors on dynamic drilling fluid loss and filtration. Other statistical methods such as linear and multiple regression as well as forecasting can be used as predictive tools for estimating drilling fluid loss and filtration.

3.2.1 Design of Experiments (DoE)

Design of experiments are techniques that are used to achieve desired parameters, and determine optimum design/composition, while minimizing the error and trials (Montgomery 2013; Menezes et al. 2009). It is a scientifically structured method that helps experimenters to identify which independent variable(s) may influence the dependent variable(s) of a process or system. Per Montgomery (2013), statistical design of experiment can be referred to as the process of planning an experiment such that the appropriate data will be generated and analyzed by statistical methods, leading to objective and valid conclusions. Experimental design and analysis can be grouped into two major aspects usually referred to as the "art" and the "math". The "art" entails having a well-grounded background knowledge of the process or system to be studied, and appropriate factors (controlled and uncontrolled) to be investigated. The "math" involves running the appropriate statistical tests and analyses and interpreting the results accurately.

Design of experiments have been applied in oil and gas research. Some of the applications have been briefly highlighted. Greaves et al. (1989) used a 2^k (2^3: two levels and three factors)

factorial DoE for in-situ combustion applications. Chu (1990) used factorial DoE to estimate the performance of steam flooding in terms of oil recovery, cumulative steam-oil ratio, and project life. White et al. (2001) used experimental design analysis to identify and estimate significant geological parameters. Yahia and Khayat (2001) used a factorial DoE (2^3) to investigate the interaction of high-range water reducer and anti-washout admixture for a high-performance cement grout. Ibeh (2007) investigated changes in the rheological properties of oil-based muds (OBM) in HPHT conditions. The author used a series of factorial DoE's and other post-experimental evaluations to determine the effects of temperature and pressure on the fluid's viscosity.

Menezes et al. (2010) used the response surface method (RSM) to study drilling fluids rheological behavior. The authors claimed that most drilling fluids rheological parameters are determined at constant test condition(s), and according to the combination of raw materials experimentally, rather than a comprehensive approach. They concluded that conventional methods of optimizing drilling fluids rheology can be time-consuming and does not reveal an optimum particularly because of interaction effect between the different components. Awoleke et al. (2012) conducted experimental studies on fracture conductivity using 2^6 factorial DoE and analysis. Ezeakacha and Salehi (2018) used 2^3 single replicate experiments to investigate the effects of LCM type, pore throat diameter, and temperature on dynamic mud filtration. They used the percentage contribution method described by Montgomery (2013) to determine the least influential factor, then used the resultant values from this factor as the replicate of the experiments. Figure 3.1 shows the general guidelines for a DoE.

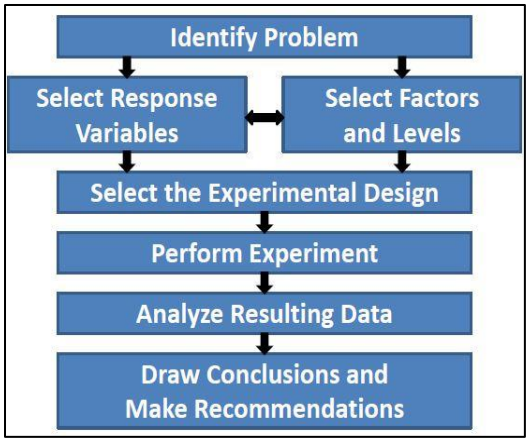

Figure 3.1: Flow chat guideline for experimental design (Montgomery 2013)

3.2.1.1 Design of Experiments (DoE) for Stage One

From the general guideline, several DoE's were developed for this research and the experiments are grouped into three stages, based on the porous media. The first stage of experiments was performed on 10 µm ceramic filter tubes. Dynamic mud filtrate was considered the as the response variable, and the following independent factors were selected: rotary speed, granular LCM concentration, and temperature. These factors were chosen primarily because of their impact on dynamic drilling fluid loss and filtration which have been detailed in chapter two. In this first stage, a special type of factorial DoE was used in selecting the experiments to run. This is called 2^k DoE ("k" factors and 2 levels of low and high). It is defined as a factorial DoE approach that allows the experimenter to shift independent variables (factors) from their lowest levels to their highest levels and determine their individual (single effects) and combined (interaction effects) significances (magnitude and direction) on a process. One of the advantages for choosing this DoE approach for this research is because of the time required to conduct one experiment and high equipment and material cost required to perform the study. Figure 3.2 is a pictorial representation of the DoE, factors, and their interactions. Unlike the classical experiment design (which allows one-factor-multilevel investigation at a time while keeping other independent variables constant), this approach

allows for more than one factor to be evaluated. Although, the level is limited to 2, the overall significances of the factors considered are still determined. Thus, the 2^k DoE can be referred to as a "screening type" DoE approach and can be used for pilot-scale tests.

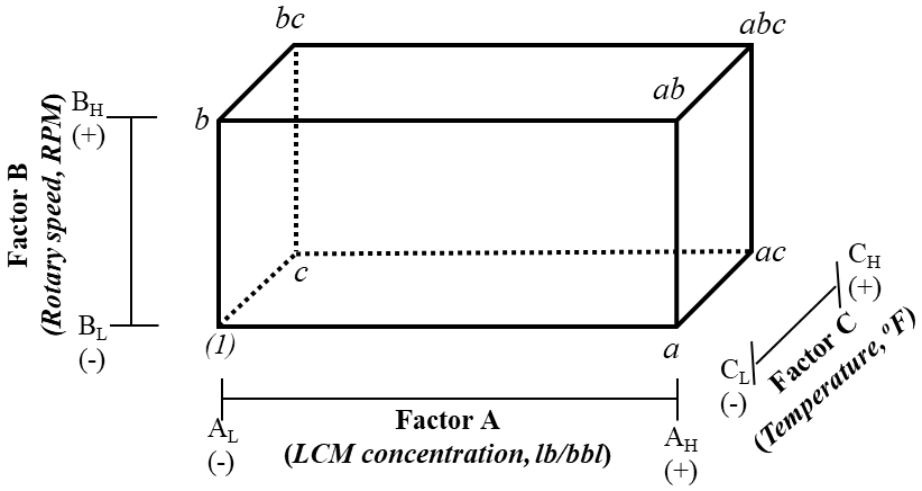

Figure 3.2: Customized 2^3 design of experiment (DoE) for hypothesis testing of factors affecting dynamic drilling fluid filtration using thick-walled cylindrical porous media.

Table 3.1 shows the values that were selected for each factor. In selecting the granular LCM concentration range, previous literatures have suggested between 20 lb/bbl to 80 lb/bbl (Aston et al. 2004; Alsaba 2015). In addition, an industry expert suggested that as formation hardness increases from the Gulf of Mexico (GoM) upwards to Wyoming, granular LCM concentration typically reduces in the order of: 70-80 lb/bbl in the GoM, 40-50 lb/bbl in Texas, and 20-30 lb/bbl in Wyoming. The rotary speed range was selected from a fluid loss data base (Ezeakacha 2014), preliminary tests, and industry expert recommendations. The fluid loss data base had similar pipe and wellbore geometry, compared to the experimental setup used in this research. In addition, Steffe's (1996) method was used to obtain the corresponding shear rate (sec^{-1}), considering the pipe and wellbore geometry used in this study. The results were comparable to those obtained from field studies having similar pipe-wellbore geometry.

Table 3.1: 2^3 factorial design of experiment for 10 microns ceramic filter tubes

Factors	Notation	Low level (-)	High level (+)
LCM concentration	A	30 lb/bbl	80 lb/bbl
Rotary speed	B	30 rpm	110 rpm
Temperature	C	120°F	220°F

Table 3.2: 2^3 experimental design for stage one (ceramic filter tubes)

LCM Conc.	Temperature (°F)	120	220
30 lb/bbl $CaCO_3$	Rotary Speed 1 (30 rpm)	T 1	T 3
	Rotary Speed 2 (110 rpm)	T 2	T 4
80 lb/bbl $CaCO_3$	Rotary Speed 1 (30 rpm)	T 5	T 7
	Rotary Speed 2 (110 rpm)	T 6	T 8

In selecting the temperature range, a temperature and rheological stability study of the WBM recipes were conducted. It was determined that the high level for temperature variable is 220°F, beyond which the WBM begins to become unstable. Hence, 220°F was chosen as the high level for temperature to establish the fluid loss control and pore plugging limits of the recipes used. 120°F was chosen as the low level because of the approximate surface return line temperature of drilling fluid. Table 3.2 shows the number of experiments performed in stage one. 8 experiments (T1 to T8) with repetitions (T9 to T16) were performed, which makes it a total of 16 experiments conducted in the first stage. 12 preliminary experiments with 5 µm and 20 µm ceramic filter tubes were conducted before the main tests in stage one.

3.2.1.2 Design of Experiments (DoE) for Stage Two

The results from the first stage of experiments informed the decision on how to design the experiments for the second stage. This will be explained in section 5.3.11. The second stage of experiments was performed on actual rock samples. Stage two experiments are further divided into

two phases. The first phase of experiments was performed at a reduced temperature (120^{o}F) and moderate rotary speed (70 rpm) which were held constant. The following rocks were tested: Michigan sandstone, Buff Berea sandstone, Upper Grey sandstone, Bandera Brown sandstone, Indiana limestone 1 (2.4 mD), Indiana limestone 2 (70 mD), and Austin chalk.

Table 3.3: Experimental design for the first phase of experiments within stage two

Lithology	Base Fluid (without LCM)	Sample 2 (55 lb/bbl calcium carbonate)
Michigan sandstone	T 17	T 23
Bandera Brown sandstone	T 18	T 24
Upper Grey sandstone	T 19	T 25
Indiana limestone 1 (2.4 mD)	T 20	T 26
Indiana limestone 2 (70 mD)	T 21	T 27
Austin Chalk	T 22	T 28

Table 3.3 shows the experimental combinations and tests performed in this first phase. The primary goal for conducting these experiments was to establish the pore plugging and plastering effect of a well-sized granular LCM fluid at operating conditions that tend not to exacerbate fluid loss and filtration. Furthermore, the reduced operating conditions allows for better understanding of lithology complexities on dynamic mud filtration. 12 experiments (T 17 to T 28) were conducted in the first phase of stage two experiments.

The second phase of experiments in stage two was performed at a constant elevated temperature (220^{o}F) on selected rock samples (Michigan sandstone, Buff Berea sandstone, Upper Grey sandstone, 70 mD Indiana limestone, and Austin chalk). Dynamic mud filtrate was considered the as the response variable, and the following independent factors were selected: rotary speed and granular LCM concentration. A full factorial DoE (3^2: two factors three levels) which is shown in Table 3.4 was used to design and determine the experiments to perform in this

phase. This is a statistical method that is used to design and account for all possible experimental combinations (depending on material availability, cost, and desired technical outcome), for which there are two or more independent variables having two or more discrete levels. The primary goal for using this design on the rocks is to estimate dynamic mud filtration as a function of granular LCM concentration and rotary speed using regression analysis. In the second phase of stage two experiments, 9 experiments were performed for each rock sample (45 experiments for 5 lithologies: T 29 to T 73). Thus, for this second stage of experiments on the rocks, a total of 57 experiments were performed and each experiment required not less than 2 hours to complete.

Table 3.4: 3^2 experimental design for the second phase of experiments within stage two

Rotary Speed/LCM conc.	30 lb/bbl	55 lb/bbl	80 lb/bbl
30 RPM	R1C1	R1C2	R1C3
70 RPM	R2C1	R2C2	R2C3
110 RPM	R3C1	R3C2	R3C3

3.2.1.3 Design of Experiments (DoE) for Stage Three

The third stage of experiments was designed to investigate dynamic drilling fluid loss through fractures. Table 3.5 shows a two factor three levels (3^2) DoE for investigating the relationship between dynamic-radial fluid loss, vertical fracture widths, and Cedar fiber LCM concentrations. The nomenclature "FW1C1" means fracture width 1 LCM concentration 1. Table 3.6 shows another two factor three levels (3^2) DoE for investigating the relationship between dynamic-radial fluid loss, various orientations of fracture width, and Cedar fiber LCM concentrations. The nomenclature "FO1C1" means fracture orientation 1 LCM concentration 1. The fracture widths were selected because they fall within the range of induced fracture widths observed with image logs (Barton et al. 1997). Moreover, previous investigations have tested similar fracture width slots

in disk shape (Wang et al. 2016; Alsaba 2015). Three concentrations of Cedar fiber were chosen from preliminary experiments and a previous study by Alsaba et al. (2014). A total of 20 experiments (T 74 to T 93) were conducted in this stage including the screening tests. In general, a total of 105 dynamic fluid loss/filtration experiments were conducted in this study.

Table 3.5: 3^2 experimental design and combination for vertical fracture widths and Cedar fiber LCM concentrations

Vertical fracture width/LCM concentration	5 lb/bbl	15 lb/bbl	30 lb/bbl
500 µm	FW1C1 (T 74)	FW1C2 (T 75)	FW1C3 (T 76)
1000 µm	FW2C1 (T 77)	FW2C2 (T 78)	FW2C3 (T 79)
2000 µm	FW3C1 (T 80)	FW3C2 (T 81)	FW3C3 (T 82)

Table 3.6: 3^2 experimental design and combination for various orientations and Cedar fiber LCM concentrations

Fracture orientation/LCM concentration	5 lb/bbl	15 lb/bbl	30 lb/bbl
Two vertical fractures (FW = 500 µm, FH = 10000 µm)	FO1C1 (T 83)	FO1C2 (T 84)	FO1C3 (T 85)
One vertical fracture (FW = 1000 µm, FH = 10000 µm)	FO2C1 (T 86)	FO2C2 (T 87)	FO2C3 (T 88)
One horizontal fracture (FW = 10000 µm, FH = 1000 µm)	FO3C1 (T 89)	FO3C2 (T 90)	FO3C3 (T 91)

3.2.2 Hypothesis Tests Using Analysis of Variance (ANOVA)

The second statistical design and analysis method used in this research is analysis of variance (ANOVA). These was applied to the data from the first stage of experiments. ANOVA is a statistical approach developed by Ronald Fisher and used to analyze the variances among group means (Fisher 1966). This is used to compare the means between groups and determine whether

any of these means are significantly different from others. ANOVA is divided into two groups: one-way ANOVA and two-way ANOVA. The primary difference between these two is that in one-way ANOVA, only one factor (independent variable) with multiple levels is investigated. In a two-way ANOVA, two or more factors having multiple levels are investigated.

In statistical analysis, when comparing more than two means (one by one for example using the t-test), the probability of type I error increases. Thus, one of the advantages of conducting ANOVA is that it reduces the probability of type I error. Type I error is referred to as the probability of rejecting a null hypothesis when it is true. A null hypothesis is considered a "no effect" hypothesis. Another advantage of ANOVA is that it reduces the amounts of comparisons between levels while determining the significance of the factor and their levels. To perform ANOVA, the right questions must be asked, and proper hypotheses developed. The following set of hypotheses were developed for characterizing dynamic drilling fluid filtration:

1. Calcium carbonate LCM Conc. (A) Hypothesis

   H_o: $\tau_{LCM1} = \tau_{LCM2} = 0$

   H_I: $\tau_i \neq 0$ *for at least one i where i is the calcium carbonate LCM concentration with 2 levels: 30 lb/bbl and 80 lb/bbl. The concentration range was selected base on previous studies (Aston et al. 2004; Alsaba 2015), preliminary studies, and industry expert recommendation.*

2. Rotary Speed (B) Hypothesis

   H_o: $\beta_{RS1} = \beta_{RS2} = 0$

   H_I: $\beta_j \neq 0$ *for at least one j where j is the rotary speed with 2 levels: 30 RPM and 110 RPM. The rotary speed range was selected from a fluid loss data base (Ezeakacha 2014), preliminary studies, and comparable rotary speed values from Steffe's (1996) method.*

3. Temperature (C) Hypothesis

   H_o: $\Upsilon_{T1} = \Upsilon_{T2} = 0$

   H_I: $\Upsilon_k \neq 0$ *for at least one k where k is temperature with 2 levels: 120°F and 220°F. The temperature range was selected from preliminary studies that were used to characterize the temperature-dependent rheological stability of a water-based mud.*

4. Calcium carbonate LCM Conc. and Rotary Speed (AB) Interaction Hypothesis

   H_o: $(\tau\beta)_{ij} = 0$

   H_I: $(\tau\beta)_{ij} \neq 0$ *for at least one i or j.*

5. Calcium carbonate LCM Conc. and Temperature (AC) Interaction Hypothesis

   H_o: $(\tau\Upsilon)_{ik} = 0$

   H_I: $(\tau\Upsilon)_{ik} \neq 0$ *for at least one i or k.*

6. Rotary Speed and Temperature (BC)Interaction Hypothesis

   H_o: $(\beta\Upsilon)_{jk} = 0$

   H_I: $(\beta\Upsilon)_{jk} \neq 0$ *for at least one j or k.*

7. Calcium carbonate LCM Conc., Rotary Speed, & Temperature (ABC) Interaction Hypothesis

   H_o: $(\tau\beta\Upsilon)_{ijk} = 0$

   H_I: $(\tau\beta\Upsilon)_{ijk} \neq 0$ *for at least one i, j or k.*

ANOVA was conducted on the results from the ceramic filter tube experiments based on a 95% confidence interval (CI). Conclusions were drawn regarding the single and interaction (combined) effects of the factors affecting dynamic drilling fluid filtration. One of the important considerations that enables the complete evaluation of ANOVA is that each experiment must be replicated (Fisher 1966). Without replication, there is no estimate of error within the treatments or levels (no sum squared error), the degree of freedom error is zero, and there is no mean squared error. Therefore,

the F-test cannot be performed, and it is impossible to obtain the p-values to determine the significance of factors and their combined effects (interactions).

According to Montgomery (2013), there are three assumptions that must be satisfied. These were used to check the adequacy of the ANOVA performed in this study and they are: normality assumption, independence assumption, and constant variance assumption. The normality assumption suggests that a normal probability plot of the residuals of the data looks like a sample from a normal distribution which is centered at zero. More sampling data can be collected to improve the normality assumption. The independence assumption suggests that a plot of the residuals versus the run order reveals random data and no detectable pattern in the data. Randomization can be done to improve this assumption. The constant variance assumption suggests low variability between the residuals when plotted against the levels. The factors are meant to affect the response and not the variability in the response. A balanced DoE is one way to ensure that this assumption is satisfied. These three assumptions were checked, and their outcomes are reported in section 5.2.2.3.

3.2.3 Regression Analysis

The third statistical design and analysis approach used in this study is regression. Regression analysis was performed using the data from dynamic mud filtration in rocks (second stage) and dynamic fluid loss in vertical fractures (third stage). After performing the experiments and analyzing the fluid loss profiles, regression analysis was conducted on the results from these experiments. Regression analysis is a mathematical approach that is used to show the relationship between a dependent variable and independent variable(s) (Montgomery 2013). Regression can be linear (a response variable that is dependent on one factor) or multiple (a response variable that is dependent on more than one factor). From the mathematical relationship, regression can be used

as a predictive tool to predict a dependent variable from a range of independent variable(s). There are four components that are used in performing and evaluating a regression: the regression hypothesis, ANOVA table, the R^2/adjusted R^2 values, and the coefficient(s) of factors. The following regression hypotheses have been developed according the porous media, for the stage two and stage three experiments whose complete data were successfully generated:

1. Buff Berea SS Regression Hypothesis

   H_o: Dynamic mud filtration in Buff Berea sandstone cannot be explained by changes in rotary speed and calcium carbonate LCM concentration.

   H_I: Dynamic mud filtration in Buff Berea sandstone can be explained by changes in rotary speed and calcium carbonate LCM concentration.

2. Michigan SS Regression Hypothesis

   H_o: Dynamic mud filtration in Michigan sandstone cannot be explained by changes in rotary speed and calcium carbonate LCM concentration.

   H_I: Dynamic mud filtration in Michigan sandstone can be explained by changes in rotary speed and calcium carbonate LCM concentration.

3. Upper Grey SS Regression Hypothesis

   H_o: Dynamic mud filtration in Upper Grey sandstone cannot be explained by changes in rotary speed and calcium carbonate LCM concentration.

   H_I: Dynamic mud filtration in Upper Grey sandstone can be explained by changes in rotary speed and calcium carbonate LCM concentration.

4. Indiana limestone Regression Hypothesis

   H_o: Dynamic mud filtration in Indiana limestone cannot be explained by changes in rotary speed and calcium carbonate LCM concentration.

H_1: Dynamic mud filtration in Indiana limestone can be explained by changes in rotary speed and calcium carbonate LCM concentration.

5. Austin chalk Regression Hypothesis

   H_o: Dynamic mud filtration in Austin chalk cannot be explained by changes in rotary speed and calcium carbonate LCM concentration.

   H_1: Dynamic mud filtration in Austin chalk can be explained by changes in rotary speed and calcium carbonate LCM concentration.

6. Vertical Fracture Width Hypothesis

   H_o: Regression model does not explain the relationship between dynamic fluid loss, vertical fracture width, and Cedar fiber LCM concentration.

   H_1: Regression model explains the relationship between dynamic fluid loss, vertical fracture width, and Cedar fiber LCM concentration.

Like the hypothesis testing with ANOVA, all the regressions parameters were evaluated with a 95% confidence interval. In some cases, the confidence interval was reduced to 90% for further evaluation of the regression results. Other details of the regression analysis such as the ANOVA table, R^2/adjusted R^2 values, and coefficient of factors have been discussed in subsection 5.3.11.

3.3 Experimental Methods and Laboratory Procedures

Drilling fluid loss and filtration are typically characterized with laboratory experimental methods. In this section, the materials selection and compositions, types of experiments conducted, experimental devices and setups, and experimental procedures will be discussed.

3.3.1 Drilling Fluid Design and Material Selection

Drilling fluid design is one of the critical factors to consider for successful fluid loss reduction and wellbore strengthening by filter cake. Several types of LCMs can be used as single or combined treatments with other drilling fluid additives to formulate preventative fluid recipes. In this research, the drilling fluids were formulated according to the porous media being investigated. Water-based mud (WBM) was selected and the mud formulations are in Table 3.7, Table 3.8, and Table 3.9. The recipes in Table 3.7 and Table 3.8 were designed to characterize pore-scale dynamic mud filtration in ceramic filter tubes (stage one) and different lithologies (stage two). The recipe in Table 3.7 was compared with sample 2 in Table 3.8 for reduced temperature (120^{o}F) and moderate rotary speed (70 rpm) conditions in different lithologies (stage two). Samples 1 and 3 (Table 3.8) were used in stage one while samples 1, 2, and 3 were used in stage two for elevated constant temperature (220^{o}F) and varying rotary speed conditions (30, 70, and 110 rpm's).

Table 3.7: Water-based mud design without LCM.

Additive	lb/bbl	% by weight	% by volume
Water	306.1	66.2	87.5
Gel (Bentonite)	20.0	4.3	2.4
Caustic Soda	0.5	0.1	0.1
Lignite	4.0	0.9	0.8
Desco	4.0	0.9	0.7
Barite	128.6	27.8	8.6

Calcium carbonate was selected as the granular LCM. Ezeakacha and Salehi (2018) stated that the various levels of fine, medium, and coarse calcium carbonate are not significant in reducing dynamic mud filtration. The authors based this conclusion on a 95% confidence interval (CI) from a series of dynamic-linear mud filtration experiments. Therefore, sized calcium carbonate with a

D_{50} of 72.75µm was chosen. Although, calcium carbonate's PSD tends to change (decrease) when pumped downhole in an actual field condition, it's often the most commercially used granular LCM because of its accessibility and cost (Berg 2013). In addition, it is classified as an acid-soluble LCM which can be dissolved readily in hydrochloric acid during completion (Alsaba 2015).

Three concentrations of calcium carbonate were chosen based on the recommendation from Aston et al. (2004). The concentrations of samples 2 and 3 satisfies Abrams' (1977) second rule for selecting LCM for pore throat plugging. This rule suggests that to achieve effective pore bridging, LCM concentration should be at least 5% by volume of the total solids in a drilling fluid. The author had a second rule which states that the median particle size of an LCM should be equal to or slightly more than 1/3 of the mean target pore diameter. This implies that for effective particle bridging, the D_{50} of the bridging material should be slightly greater or equal to the mean pore size distribution of the porous media. All the mud additives were selected based on field reports.

The drilling fluid recipes in Table 3.9 were formulated to characterize dynamic fluid loss in fractures (stage three). Three concentrations of Cedar fiber were chosen after preliminary experiments and considering a previous study by Alsaba et al. (2014). The PSD of Cedar fiber was measured, and sieve analysis was performed. The results showed that 63.8 % of particles were equal to or greater than 500 µm, which is one of the fracture widths being investigated. This condition satisfies Whitfill's (2008) PSD criteria for this fracture width (D_{50} should be equal to the fracture width). In addition, the condition also satisfies Alsaba's (2015) PSD criteria which suggests that D_{50} should be greater or equal to 3/10 of the fracture width. In all the 6 recipes, barite was used to weigh up the fluids to 11 lb/gal (ppg).

Table 3.8: Water-based mud design with calcium carbonate LCM.

Fluid Additives	Sample 1 (30 lb/bbl)			Sample 2 (55 lb/bbl)			Sample 3 (80 lb/bbl)		
	lb/bbl	% wt.	% vol	lb/bbl	% wt.	% vol	lb/bbl	% wt.	% vol
Water	300.88	65.00	85.97	296.51	64.10	84.72	292.15	63.20	83.47
Gel (Bentonite)	20.00	4.32	2.38	20.00	4.32	2.38	20.00	4.33	2.38
Caustic Soda	0.50	0.11	0.09	0.50	0.11	0.09	0.50	0.11	0.09
Lignite	4.00	0.86	0.76	4.00	0.86	0.76	4.00	0.87	0.76
Desco	4.00	0.86	0.71	4.00	0.86	0.71	4.00	0.87	0.71
Calcium carbonate	30.00	6.48	3.17	55.00	11.89	5.82	80.00	17.31	8.47
Barite	103.48	22.36	6.91	82.55	17.85	5.51	61.61	13.33	4.11

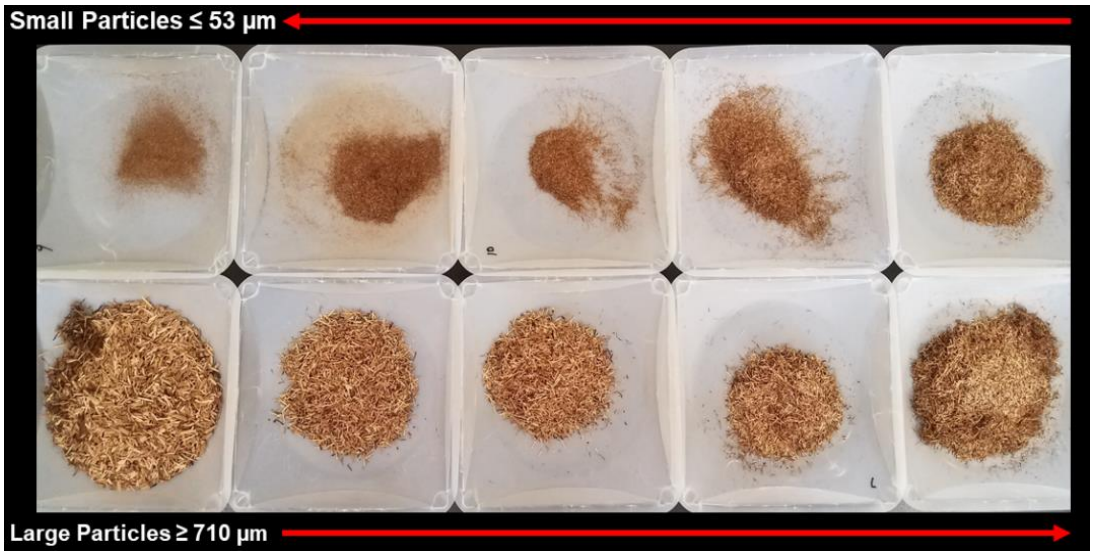

Figure 3.3: Sieve analysis showing different particles sizes of Cedar fiber.

Table 3.9: Water-based mud design with Cedar fiber LCM.

Fluid Additives	Sample 4 (5 lb/bbl)			Sample 5 (15 lb/bbl)			Sample 6 (30 lb/bbl)		
	lb/bbl	% wt.	% vol	lb/bbl	% wt.	% vol	lb/bbl	% wt.	% vol
Water	296.75	64.05	84.79	278.01	59.99	79.43	249.91	53.90	71.40
Gel (Bentonite)	20.00	4.32	2.38	20.00	4.32	2.38	20.00	4.31	2.38
Caustic Soda	0.50	0.11	0.09	0.50	0.11	0.09	0.50	0.11	0.09
Lignite	4.00	0.86	0.76	4.00	0.86	0.76	4.00	0.86	0.76
Desco	4.00	0.86	0.71	4.00	0.86	0.71	4.00	0.86	0.71
Fiber	5.00	1.08	2.38	15.00	3.24	7.14	30.00	6.47	14.29
Barite	133.04	28.72	8.88	141.91	30.62	9.47	155.21	33.48	10.36

3.3.2 Porous Media Selection and Design

In the study of drilling fluid loss, porous media characterization is important because it can provide adequate information on mud loss profiles and suggestive preventative strategies. In most laboratory drilling fluids investigations, ceramic filter disks, tubes, and filter papers are commonly used as the porous media. Some studies have used sandstone core samples in disk shape and these are cored to fit the boundary conditions of dynamic-linear high temperature high pressure (HTHP) filter press and permeability plugging test (PPT) apparatus (Ezeakacha et al. 2017; Salehi et al. 2015; Salehi et al. 2014). Others have modified the HTHP and low temperature low pressure (LTLP) filter press to accommodate longer core and slot samples in disk shape (Jeennakorn et al. 2017; AlAwad and Fattah 2017; Alsaba 2015). The porous media selection and design were carried out based on the stages the dynamic fluid loss and filtration experiments were divided into. Ceramic filter tubes were selected as the porous media for first stage. 10 µm average pore throat diameter was chosen because there is no significant difference between the dynamic mud filtration data obtained from 5 µm and 20 µm tubes (Ezeakacha and Salehi 2018). Figure 3.4 shows one of

the filter tubes that were used. Usually, ceramic filter tubes are classified by average pore throat size (i.e. the average minimum pore diameter). As shown in Table 3.10, they are normally measured in microns (µm). It should be noted that this property is not the same as permeability. The permeability of a porous material (rock samples in this study) is the measure or degree of fluid flow through the porous media, when subjected to differential pressure. It is measured in Darcy or millidarcy (md).

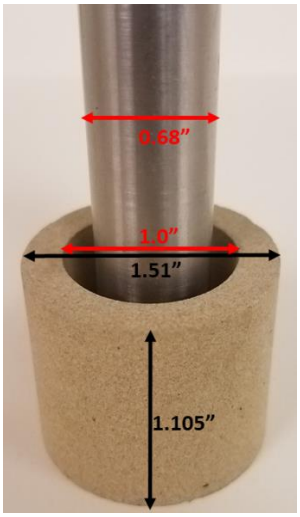

Figure 3.4: 10µm ceramic filter tube with rotating shaft at the center

Table 3.10: Mean pore throat specification for ceramic filter disks (Courtesy: Ofite Instrument)

Mean Pore Throat (µm)		Permeability (Darcy)	
New (Mercury)	Old (Air)	New (Mercury)	Old (Air)
10	3	775 mD	400 mD
12	5	850 mD	750 mD
20	10	3 D	2 D
40	20	8 D	5 D
50	35	15 D	10 D
55	60	20 D	20 D
120	90	40 D	100 D
160	150	--	180 D
250	190	--	--

The second stage of experiments were performed on thick-walled cylindrical rock samples from different lithologies. The rock samples include: Michigan sandstone, Buff Berea sandstone, Upper Grey sandstone, Indiana limestone, and Austin chalk. Figure 3.5 and Figure 3.6 shows the

sandstone and carbonate rock samples used in the second stage of the experimental studies. For each thick-walled cylindrical core sample, a 1.0-inch coring bit was used to core through a 4 x 4 x 6 core block, making the inner diameter. This was followed by a 1.5-inch coring bit which cored the outer diameter. A saw was used to slice the core into a height of 1.1 inches.

Figure 3.5: Thick-walled cylindrical sandstone lithologies (left to right)): Buff Berea sandstones, Michigan sandstones, Bandera Brown sandstones, and Upper Grey sandstones

Figure 3.6: Thick-walled cylindrical carbonate lithologies (left to right): 2.4 mD Indiana limestone 1, 70 mD Indiana limestone 2, and Austin chalk

Table 3.11 shows the intrinsic rock properties of the samples. The sandstones are composed of feldspar and quartz from physical weathering process and sedimentation (Churcher et al. 1991) and their pore throats are often connected (Tavanaei and Salehi 2015). Quartz is the primary cementing material most sandstones. Elemental maps from this study reveal a high concentration of Aluminum and Silicon with some traces of Potassium and Zinc in the sandstones. Indiana limestone and Austin chalk are carbonate rocks that are primarily composed of calcite. Their pore structures and grains are influenced by chemical dissolution and recrystallization of fossil fragments. Indiana limestone grains can be crystalline or granular and they have strong calcite cementation. The pores of Indiana limestone are not often interconnected like most sandstone rocks. Austin chalk is a soft milky-white porous rock whose high porosity often compensates for

its low permeability. It a depleted formation that lies above the Eagle Ford shale in Texas. The elemental maps obtained in this study for both carbonate rocks revealed the presence of Ytterbium (Yb) in addition to Calcium as the primary elements of the grains. Ytterbium is a rare earth element that is soft, ductile, and malleable. The concentration of this element in Austin chalk was much higher compared to Indiana limestone. This observation can partially explain the weak grain cementation in Austin chalk.

Table 3.11: Rock properties

Lithology	Formation	Brine Perm. (mD)	Porosity (%)
Buff Berea sandstone	Kansas	350	18.50
Upper Grey sandstone	Kipton	105	17.65
Michigan sandstone	NA	350	19.44
Bandera Brown sandstone	Kansas	7	22.98
Indiana limestone 1	Bedford	2.4	14.23
Indiana limestone 2	Bedford	70	16.21
Austin chalk	Edwards Plateau	3	31.99

One of the primary reasons for selecting these rocks is to characterize the mud filtration profiles of the lithologies they represent. In addition, the experimental results would address the dominance of primary rock properties (permeability and porosity) and filter cake evolution for wellbore strengthening application. According to Salehi and Kiran (2016), a positive change in the effective wellbore stress can occur when a permeable wellbore is exposed to a low-permeability filter cake. Furthermore, the dynamic fluid filtration modeling approach can be extended to other rocks with similar properties by conducting further experiments.

The third stage of the experiments were performed on thick-walled cylindrical fracture slots with different fracture widths and orientations (Figure 3.7). Different fracture widths and

orientations were simulated with the slots. These widths were selected because they fall within the range of induced fracture widths observed with image logs (Barton et al. 1997). Moreover, previous investigations have tested similar fracture width slots in disk shape (Wang et al. 2016; Alsaba 2015). The slots in this study were custom-made from stainless steel in two parts: the top part which has no opening and bottom parts which had the fracture openings (widths and orientation). The full slot dimensions (outer diameter, inner diameter, and height) are 1.5 inches, 1.0 inch, and 1.1 inches respectively. These dimensions are boundary conditions set by the core holder in the drilling simulator.

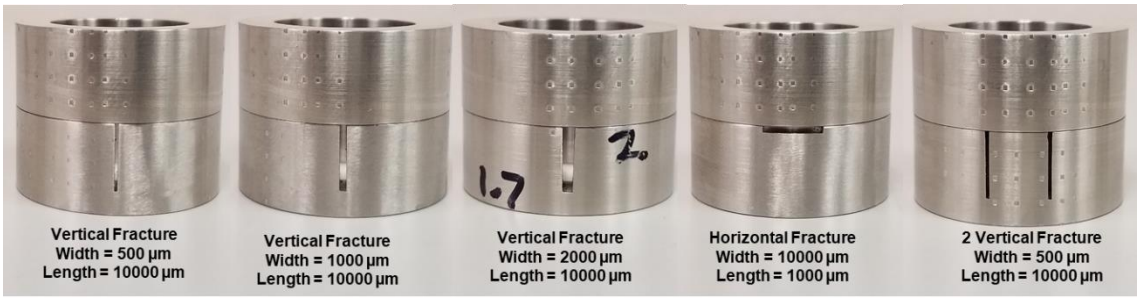

Figure 3.7: Thick-walled cylindrical slots of varying fracture widths and orientations

3.3.3 Types of Experiments, Devices/Setups, and Procedures

3.3.3.1 Particle Size Distribution (PSD)

The PSD's of the drilling fluids used in this study were measured. The $CaCO_3$ fluids (samples 1, 2, and 3) were measured at the National Oilwell Varco fluids control laboratory with the PSD analyzer shown in Figure 3.8 (a). The left section of the machine is used to measure the PSD of granular dry materials (dry PSD), while the right section of the machines measures the PSD of the materials that are well-mixed with fluids (wet PSD). To measure the PSD of a sample, 3 to 4 drops of the sample is placed into the open section below the red arrow. The machine is setup and

engaged to analyze the PSD, and the results are displayed on machines software. The results are exported to PDF files which are plotted in an excel for comparison.

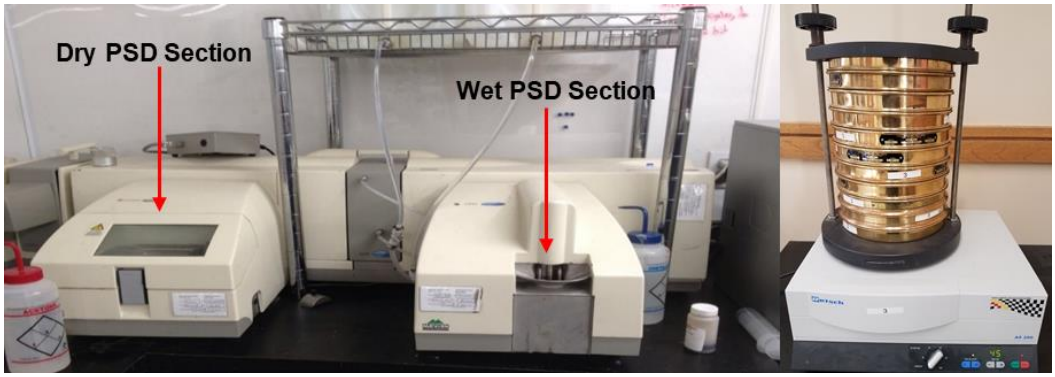

a **b**

Figure 3.8: Malvern 2000 mastersizer laser diffraction PSD analyzer (a) and sieve analyzer (b)

The PSD of the Cedar fiber used in the research was measured with a sieve analyzer in Figure 3.8 (b) because the dry PSD analyzer section in Figure 3.8 (a) could not handle the fiber particle sizes. When setting up the sieve analyzer, about 5 lbs of dry Cedar fiber is placed on the topmost sieve. The analyzer is then engaged by a constant vibration for 45 minutes. This forces the particles to sieve through 10 different sieve trays and particles are shown in Figure 3.3.

3.3.3.2 Drilling Fluids Rheology

Drilling fluids rheology is an important parameter that affects fluid loss and filtration. After mixing all the samples, their rheological investigation was carried out according to API recommended practice (API 13 B-1 2003) with an M3600 automatic viscometer (Figure 3.9). The viscometer was programed to profile drilling fluid rheological parameters (shear stress, shear rate, apparent viscosity, dial reading, and temperature) every 30 seconds, and up to 212^{o}F. WBM viscosity typically decreases as temperature increases because the gelling property of bentonite in a WBM is impacted at elevated temperature. A decrease in viscosity can impair the plastering and

strengthening ability of a drilling fluid. Thus, it is important to establish the limits of the recipes used in this study. After rheological study, dynamic fluid/filtration is performed.

Figure 3.9: M3600 automatic viscometer

3.3.3.3 Dynamic Drilling Fluid Loss and Filtration

A drilling simulator was used to perform the dynamic fluid loss and filtration tests. Besides the experimental factors and levels discussed in section 3.2.1, Table 3.12 shows other constant parameters that were used in the experiments, while Table 3.13 shows some of the API recommended conditions (AP 13 B-1 2003) from which the test parameters in this research were selected.

Table 3.12: Other dynamic drilling fluid loss factors.

Constant Factors	Values
Mud Weight	11 ppg
Porous Media	According to DoE
Rotary Speed	According to DoE
Temperature	According to DoE
Back Pressure	100 psi
Cell Pressure	200 or 300 psi

Table 3.13: Recommended minimum back pressure for fluid loss testing (API 13 B-1 2003)

Test temperature		Vapour pressure		Minimum back pressure	
°C	°F	kPa	psi	kPa	psi
100	212	101	14,7	690	100
120	250	207	30	690	100
150	300	462	67	690	100
Limit of "normal" field testing					
175	350	932	135	1 104	160
200	400	1 704	247	1 898	275
230	450	2 912	422	3 105	450

Figure 3.10 shows the experimental setup sequence for one test. During the setup for one experiment, the porous media and 350 cm^3 of any sample are well secured in the drilling simulator using the sequence. An experiment is divided into three phases. At the beginning of an experiment (first phase), the fluid in the cell is agitated by the rotating shaft at a reduced speed (≈30 rpm), while the heating jacket heats up the cell. The reduced rotation is used to prevent particles from settling during the temperature ramp-up. During this time, the back-pressure knob is opened to flow in 100 psi. If it's a high temperature test, the cell pressure knob is opened to gradually flow in about 30 psi when the temperature reaches approximately 200^{o}F. This is done to prevent the

fluid from starting to boil within the cell, while maintaining a higher back pressure to prevent creating the differential pressure during the heating and agitation stage (first phase).

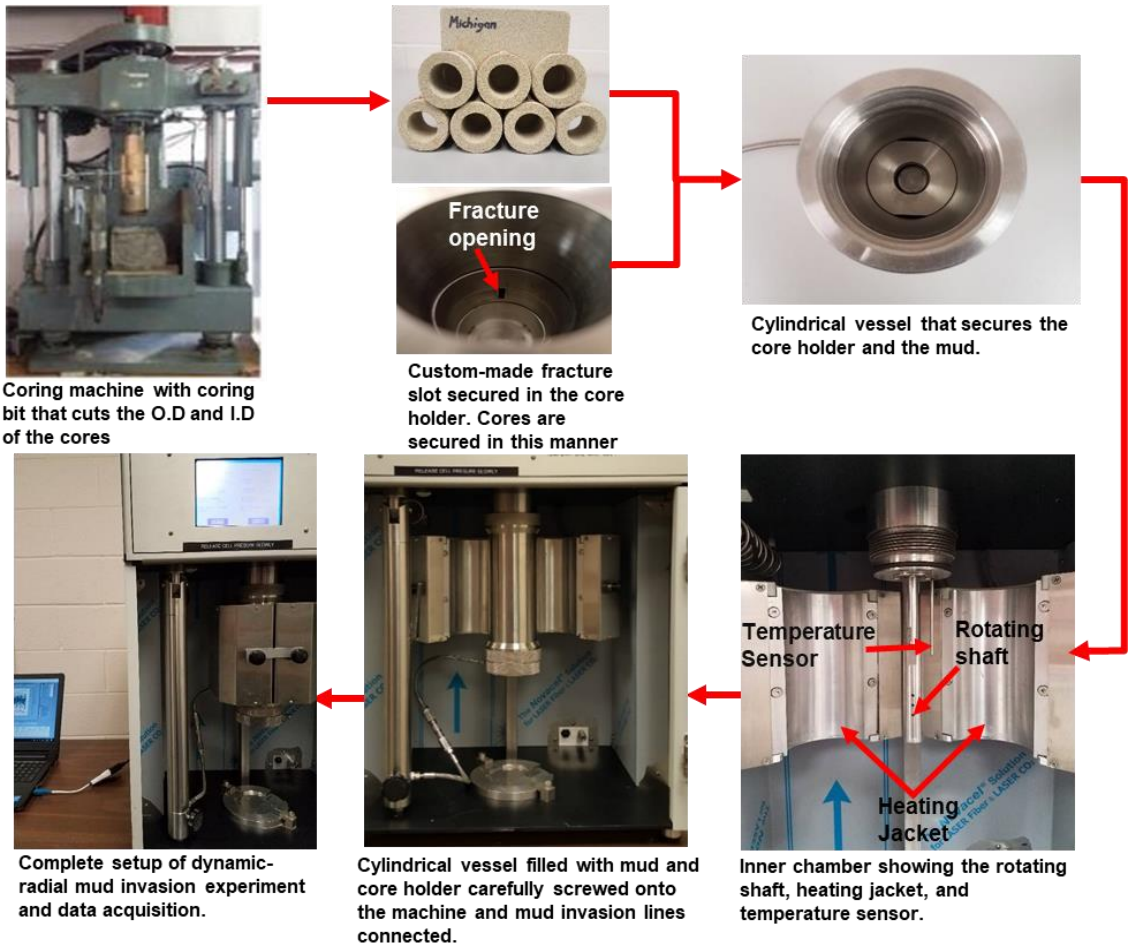

Figure 3.10: Workflow for the experimental setup of dynamic-radial drilling fluid loss and filtration

When the fluid in the cell attains 115^{o}F or 215^{o}F (±5^{o}F from the set point), the cell pressure knob is turned to flow in the complete overbalance pressure into the cell until it exceeds the back pressure to create the differential pressure (second phase). In a normal overbalanced drilling operation, a minimum static overbalanced pressure of 150 - 300 psi is required to prevent formation fluid influx (Drilling Manual 2015; Rehm et al. 2012; Jahn et al. 2008). Thus, the differential pressure for the first and second stage experiments were 300 psi and 100 psi respectively. 100 psi differential was used for the second stage experiments because preliminary experiments showed

that most of the rocks would break inside the core holder at higher differential pressures, rendering the experiments incomplete. This was attributed to their heterogeneity, composition, and possibly weak cementation. Although, the Indian limestone samples were the only exception which is a testament to its strong calcite cementation, a differential pressure of 100 psi was used for all the experiments in this stage for consistency.

The second phase of the third stage experiments was conducted in two pressure regimes: In the first pressure regime (PR_1), 200 psi differential pressure is created in the cell after which 30 minutes mud filtration time was allowed. After 30 minutes, the second pressure regime (PR_2) is established by doubling the differential pressure and allowing it for additional 5 minutes. The second phase of the third stage experiments (dynamic fluid loss collection) was conducted in this manner for two purposes. The first was to establish the formation of a filter cake at the operating conditions and investigate possible mud filtrate invasion through the filter cake within 30 minutes. The second reason is to check for the stability of the filter cakes that would been developed in the fractures at the same operating conditions. In this study, the term "filter cake stability" is used to describe the ability of a filter cake formed in a fracture to resist an increase in differential pressure from 200 psi to 400 psi (at 110 rpm and 220^{o}F) and not rupture. After setting up each experiment, the machine is programmed to collect experimental data (temperature, pressures, rotary speed, torque, and fluid/filtrate loss) every five seconds. The third phase is cooling the system and disengaging the cell for post experimental investigation.

3.3.3.4 Post-Experimental Investigations

Two post-experimental studies were carried out on selected core samples. Scanning electron microscope (SEM) imaging and energy-dispersive X-ray spectroscopy (EDS) were used for the

microscopic study and elemental mapping of the near-wellbore pore throats respectively. Some researchers have used different microscopic imaging techniques for qualitative investigation of both internal and external filter cake evolution in pore throats and fractures (Ezeakacha et al. 2017; Fakhreldin 2010; Al Otaibi et al. 2008). Figure 3.11 shows three core samples from which the SEM images are taken, and elemental mapping performed. The samples were carefully cut out so that the surface to be investigated is not contaminated. The figure also shows the placement of a sample before image capturing. Prior to performing the SEM and EDS imaging, the samples in their wet state (after mud filtration experiments) were vacuum dried and preserved in desiccators. This was done to prevent potential atmospheric interaction that may compromise the composition of the particles. After vacuum drying each sample, the external filter cake was carefully detached without scratching or physically defacing the inner diameter of samples.

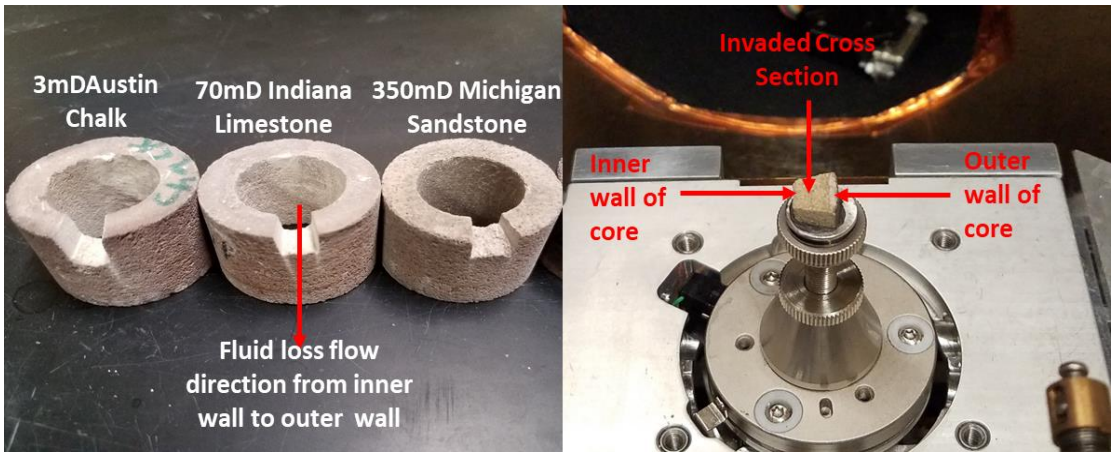

Figure 3.11: Dry core samples from which SEM and EDS samples are prepared (left) and sample placement inside the machine for SEM and EDS analyses (right).

Chapter 4: Mathematical Modeling and Geomechanical Studies

4.1 Overview of Mathematical Modeling of Drilling fluid Filtration

Mud filtration occurs when filter cake develops inside the near-wellbore pore throats and on the wellbore wall. It takes place whether a wellbore fluid condition is in static or dynamic mode. Analytical studies have been conducted and previous models have been developed to estimate filtration rate, invasion radius, filter cake permeability, and filter cake thickness (Ling et al. 2015; Farahani et al. 2014; Civan 1994, 1996). These models have been developed for either of the following systems: static-linear filtration system, dynamic-linear filtration system, static-radial filtration system, and dynamic-radial filtration system. The difference in static and dynamic conditions have been described in section 2.2. A filtration system is linear if the mud filtrate is collected in the axial direction through the porous media in response to differential pressure. A radial filtration system is described by mud filtrate flow through the sides of the porous media in the radial direction. Each of the models have been reviewed briefly and a mechanistic model was developed, solved, and validated with the experimental data from this study.

4.1.1 Filtrate Invasion Radius and Filtration (Ling et al. 2015)

The authors developed a model for estimating the radius of invasion for water-based muds. Figure 4.1 shows a radial wellbore and reservoir. Equation 4.1 shows the position of any filtrate saturation in a radial reservoir system at any time.

$$r_{sf} = \sqrt{\frac{tq_{f-av}}{\pi h \emptyset}\left(\frac{df_f}{dS_f}\right)_{Sf}} \quad \text{..... (4.1)}$$

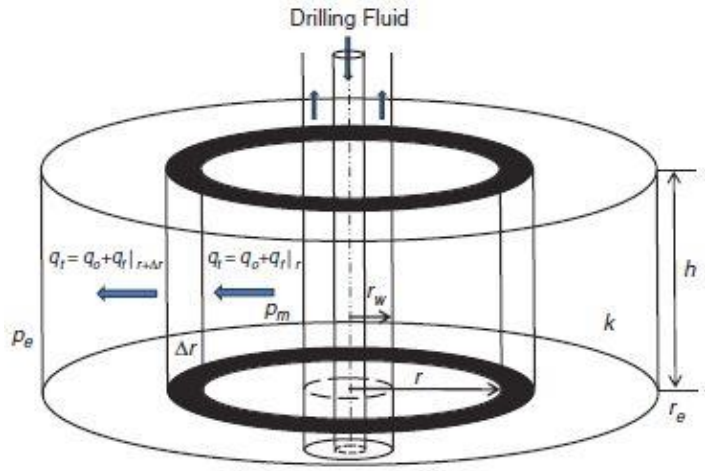

Figure 4.1: Control volume with a circular reservoir and well in center (Ling et al. 2015)

where t is time (hours), $q_{f\text{-}av}$ is average filtrate invasion rate (bbl/hr), h is pay thickness (ft), Φ is formation porosity (%), f_f is the filtrate fraction, and S_f is the filtrate saturation. For negligible capillary pressure, the filtrate fraction is given in equation 4.2. In this equation, k_{ro} is the relative permeability to oil (mD), k_{rf} is the relative permeability to filtrate, μ_o is oil viscosity (cp), and μ_f is the filtrate viscosity (cp).

$$\boldsymbol{f_f = \frac{1}{1+\frac{k_{ro}\mu_f}{k_{rf}\mu_o}}} \quad \text{..... (4.2)}$$

In determining the average filtrate invasion rate, the authors used Bourgoyne et al. (1986) static-linear filtration model shown in equation 4.3. In this equation, Q_f is the total filtrate invasion volume (bbl), k_{mc} is the mud cake permeability(mD), A is flow area of filter press (ft^2), Δp_{mc} is the differential pressure across the mud cake (psi), and h_{mc} is the mud cake thickness (ft) given in equation 4.4. *fsc* is the volume fraction of solid in the mud cake and f_{sm} is the volume fraction of solid in the mud.

$$q_{f-invasion} = \frac{dQ_f}{dt} = \frac{0.0011268 k_{mc} A \Delta p_{mc}}{\mu_f h_{mc}} \quad (4.3)$$

$$h_{mc} = \sqrt{\frac{2 k_{mc} \Delta p_{mc}}{\left(\frac{f_{sc}}{f_{sm}} - 1\right)\mu_f}} \sqrt{t} \quad (4.4)$$

Ling et al. (2015) divided mud filtration into two stages: spurt invasion (filter cake evolution) and invasion at constant filter cake thickness. They treated filtrate invasion through filter cake into the rock as a transient flow and calculated filtrate flow rate as shown in equation 4.5. In this equation, k is the reservoir permeability (mD), $\Delta p_{formation}$ is the differential pressure across the formation (psi), C_t is total compressibility, r_w is the wellbore radius (ft), and s is the skin factor.

$$q_{f-invasion} = \frac{kh\Delta p_{formation}}{162.6\mu_f\left(logt + log\frac{k}{\emptyset \mu_f C_t r_w^2} - 3.23 + 0.87s\right)} \quad (4.5)$$

Combining equations 4.3, 4.4, and 4.5 gives the solution to mud filtration during filter cake evolution (equation 4.6) and mud filtration during constant cake thickness (equation 4.7).

$$q_{f-invasion1} = \frac{p_m - p_p}{\frac{\mu_f \sqrt{\frac{2 k_{mc} \Delta p_{mc}}{\left(\frac{f_{sc}}{f_{sm}} - 1\right)\mu_f}} \sqrt{t}}{0.0011268 k_{mc} A} + \frac{162.6\mu_f\left(logt + log\frac{k}{\emptyset \mu_f C_t r_w^2} - 3.23 + 0.87s\right)}{kh}} \quad (4.6)$$

$$q_{f-invasion2} = \frac{p_m - p_p}{\frac{\mu_f h_{mc}}{0.0011268 k_{mc} A} + \frac{162.6\mu_f\left(logt + log\frac{k}{\emptyset \mu_f C_t r_w^2} - 3.23 + 0.87s\right)}{kh}} \quad (4.7)$$

The limitation of this models is that it does not specify the condition of the wellbore fluid. Considering the filter press model used, it can be assumed that the wellbore fluid is in static condition. However, in one of the authors validation studies, the total invasion time was 100 hours which is up to 4 days. Thus, it can be assumed that the well was in both static and dynamic

condition. Considering that mud filtrate invasion is more severe in dynamic condition because of filter cake erosion, their model combined with Bourgoyne et al. (1986) model did not accurately estimate filtrate invasion when validated with the experimental data from this research.

4.1.2 Static-Radial Filtration (Farahani et al. 2014)

In this study, the authors developed equations for profiling mud filtration in a static-radial system. From Darcy's law (SI unit), equations 4.8 and 4.9 were derived. *S* is the volume fraction of solids in the mud. In equation 4.8, *h* is the porous media thickness. Integrating this equation and converting to drilling field units yields equation 4.10. The radius of penetration (r_p) is given in equation 4.11. They also derived equation 4.12 for mud cake thickness. These equations assume constant formation porosity and permeability, as well as negligible particle invasion into the wellbore. Reference permeability is obtained from the analytical solution of static filtration first-step by Chenevert and Dewan (2001).

$$q_f = \frac{(2\pi r)k_f h}{\mu}\frac{dp}{dr} \quad (4.8)$$

$$q_f = q_{loss} \times (1 - S) \quad (4.9)$$

$$q(t) = 4.6 \times 10^{-7} \times \frac{k_f}{\mu} \times \frac{P_m - P_{mc}(t) - p_f}{ln\left(\frac{r_p}{r_w}\right)} \quad (4.10)$$

$$r_p = \sqrt{r_w^2 + \frac{V_{fi}}{\pi \times h \times \emptyset_f}} \quad (4.11)$$

$$T_{mc,i} = T_{mc,i-1} + \frac{V_{s,i} - V_{s,i-1}}{(1 - S - \emptyset_{mc,i}) \times 2\pi h \times (r_w - T_{mc,i-1})} \quad (4.12)$$

4.1.3 Static and Dynamic Filtration in a Linear System (Civan 1994, 1998)

The author developed linear filtration model's systems considering static and dynamic fluid conditions. Figure 4.2 shows a linear mud filtration schematic with filter cake evolution.

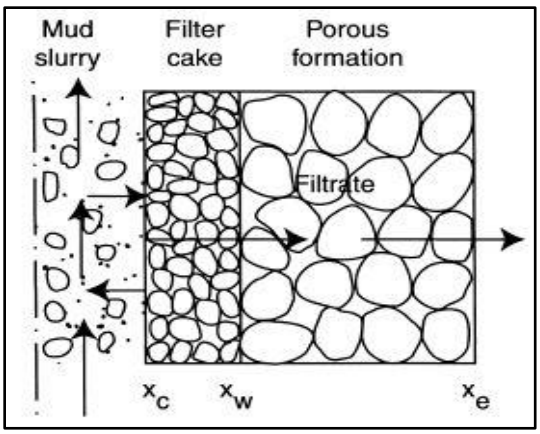

Figure 4.2: Schematic of linear filter cake over a flat surface of a core plug (after Civan ©1999 SPE; reprinted by permission of the Society of Petroleum Engineers)

The complete mathematical derivation can be found in Civan (1998). For dynamic-linear condition, the filtrate flowrate for both Darcy and non-Darcy flows are given in equations 4.13 and 4.14 respectively:

$$q = \frac{\bar{\gamma}}{\bar{\beta}} \quad (4.13)$$

$$q = \frac{\bar{\beta} + \sqrt{\bar{\beta}^2 - 4\bar{\alpha}\bar{\gamma}}}{2\bar{\alpha}} \quad (4.14)$$

Where $\bar{\alpha} = \left(\beta_f L_f + \beta_c \delta\right) \frac{\rho}{a^2}$ (4.15)

$$\bar{\beta} = \left(1 + \frac{K_f \delta}{K_c L_f}\right) \frac{\mu L_f}{a K_f} \quad (4.16)$$

$$\bar{\gamma} = -\left(\frac{q_o \mu L_f}{a K_f} + \frac{\rho \beta_f L_f q_o^2}{a^2}\right) \quad (4.17)$$

To obtain the static-linear filtration model, first integrate equation 4.18 subject to δ = 0 and t = 0. Secondly, rearrange the solution to give equation 4.19.

$$\delta = AQ - \int_0^t B dt \quad (4.18)$$

$$\frac{P_c - P_e}{q} = \left(\frac{\mu L_f}{aK_f} + \frac{\rho \beta_f L_f q}{a^2}\right) + \left(\frac{\mu}{aK_c} + \frac{\rho \beta_c q}{a^2}\right)\delta \quad \text{(4.19)}$$

Equations 4.18 and 4.19 are applicable regardless of whether the flow rate is constant or varying. A plot of $(P_c - P_e)/q$ vs. $\mathcal{S}$ of the experimental data can be used to determine the values of the unknown parameters.

4.1.4 Mechanistic Model for Dynamic-Radial Filtration with Experimental Validation

In this research, a mechanistic model comprising of different aspects was developed for estimating dynamic mud filtration in a radial coordinate system. Figure 4.3 shows the radial wellbore schematic from an experimental porous medium before and after drilling fluid filtration and filter cake evolution. Consider Figure 4.3 (a) prior to filter cake buildup: when differential pressure is created during a fluid loss experiment, the internal filter cake region is formed within the near-wellbore pores throats. This allows the evolution of the external filter cake. The following modeling assumptions have been made:

1. Dynamic condition is created by only drillpipe/shaft rotation (one-dimensional radial flow).
2. Incompressible carrier fluid, particles, and uniform filter cake evolution.
3. Only ultra-fine particles (much smaller than the average pore throat diameter) and filtrate invades the porous media.
4. Negligible rock heterogeneity and mineralogical effect.

The net rate of particle accumulation during filter cake evolution has been previously given by Civan (1994, 1996) in equation 4.20 and the material balance in equation 4.21.

$$R_{ps} = k_d u_c c_p - k_e(\tau_s - \tau_{cr}) \quad \text{(4.20)}$$

$$-dr_c/dt = \frac{k_d u_c c_p - k_e(\tau_s - \tau_{cr})}{(1-\emptyset_c)\rho_p} \quad \text{(4.21)}$$

Equation 4.21 can be rewritten as equation 4.22 after substituting the radial volumetric flux (u_c) at the external filter cake surface.

$$-\frac{d(r_c/r_w)}{dt} = A\frac{q}{r_c/r_w} - B \qquad 0 \le r_c/r_w \le 1 \quad \text{(4.22)}$$

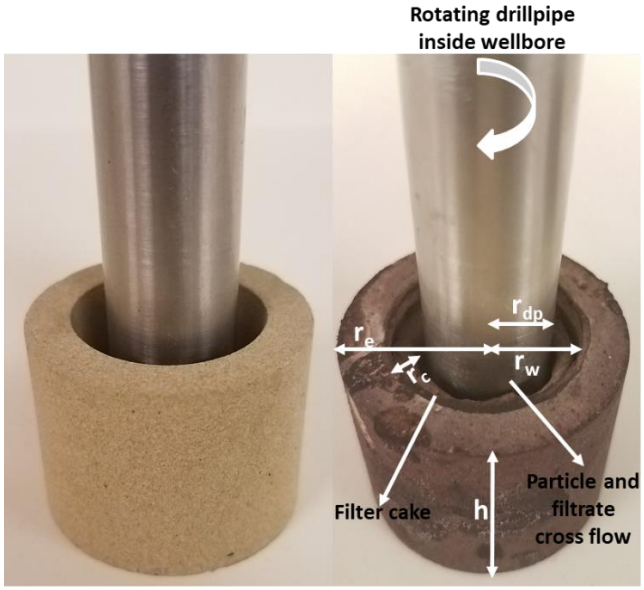

a **b**

Figure 4.3: Dynamic-radial mud filtration schematic before filter cake evolution ((left) and after filter cake evolution (right) in a porous media

The complete derivations are in the Appendix A where parameters A and B have been identified. The first three parameters on the right-hand side of equation 4.20 (before the negative sign) accounts for the deposition of fluid particles to form the external filter cake. The second three parameters on the right-hand side of equation 4.20 (after the negative sign) accounts for the erosion of fluid particles. One of the main factors that was considered in deriving this model is the rotary speed and drillpipe/wellbore geometry. This is because the inertia condition of the fluid in the wellbore is overcome by the hydrodynamic condition from mud circulation and/or drillpipe

rotation. In addition, part of the results from the statistical hypothesis test shows that an increase in the rotary speed (from 30 rpm to 110 rpm) can significantly increases dynamic-radial filtration by more than 5% based on a 95% confidence interval. During dynamic mud filtration, the slurry tangential stress (τ_{sts}) exceeds the critical shear stress (τ_{cr}) for filter cake particles to be eroded. Considering the impact of pipe rotation on the external filter cake erosion and mud filtration, the slurry tangential stress is given as:

$$\tau_{sts} = k\left(\frac{\pi RS}{15n\left(1-G^{-2/n}\right)}\right)^{n} \quad \text{(4.23)}$$

where $G = {}^{r_{dp}}/_{r_c}, \ for\ 0.5 \leq {}^{r_{dp}}/_{r_c} \leq 0.9$ (4.24)

Equations 4.23 and 4.24 also accounts for pipe eccentricity and pipe/wellbore-filter cake geometry. The shear rate component in equation 4.23 will change if the conditions in equation 4.24 changes. However, for the rotating shaft and wellbore geometry used in this study, the conditions are valid. In addition to rotary speed, the temperature of the wellbore and fluid is another factor that can exacerbate drilling fluids filtration. Ezeakacha and Salehi (2018) showed that increasing the temperature of a WBM (with calcium carbonate) from 120^{o}F to 220^{o}F can significantly increase dynamic-radial mud filtration by 40%. In this modeling approach, the impact of temperature on dynamic filtration is accounted from the fluid's experimental n and k values in equation 4.23 at the specified temperature. These values are temperature-dependent and are obtained from the viscosity profile of the drilling fluid. Furthermore, the LCM concentration is accounted for in the n and k values which will vary according to LCM addition. It should be noted that only the n and k values obtained at the desired temperature should be inputted in the model for accuracy.

To account for the radial coordinator flow, the Forchheimer's (1901) equation for radial flow of mud is used as shown in equation 4.25. Combining equation 4.25 with the radial volumetric flux at the external filter cake surface gives equation 4.26. The porous media (rock and filter cake) complexities such as permeability and porosity are accounted for in equations 4.26 and 4.27.

$$-\frac{\partial p}{\partial r} = \frac{\mu}{K}u + \beta_i \rho u^2 \quad \text{(4.25)}$$

$$-\frac{\partial p}{\partial r} = \frac{\mu}{2\pi h K}\frac{q}{r} + \frac{\beta_i \rho}{2\pi h^2}\left(\frac{q}{r}\right)^2 \quad \text{(4.26)}$$

Where β is the inertial flow coefficient for the rock or filter cake and per Liu et al. (1995), it is given as: $\beta_i = \frac{2.92\times10^4 T_{f/c}}{\emptyset_{f/c} K_{f/c}}$ (4.27)

In equation 4.27, $T_{f/c}$ means tortuosity of formation or filter cake. The same goes for the porosity and permeability symbols (please check the Greek symbols). Integrating equation 4.26 for conditions before and during external filter evolution and combining the solutions will yield equation 4.28 for non-Darcy drilling fluid filtrate flow rate.

$$q = \frac{-\beta+\sqrt{\beta^2-4\alpha\gamma}}{2\alpha} \quad \text{(4.28)}$$

Equations 4.22 to 4.28 and A.17 - A.19 in the Appendix A are solved numerically in a computational software (Matlab^T) using the Rung-Kutta 6th order method. The cumulative dynamic filtrate invasion profiles were predicted for different core samples and operating conditions.

It should be noted that this model is developed for radial flow as a function of only the slurry tangential stress. This is because of the experimental results that were used to validate the model is limited to only pipe rotation. However, in field condition, dynamic filtration occurs

mostly because of the helical flow condition of the fluid (slurry axial shear stress from flow rate and slurry tangential shear stress from drill pipe rotation). To account for this, the slurry resultant shear stress is used (see equation 4.29).

$$\tau_{srs} = \sqrt{\tau_{sts}^2 + \tau_{sas}^2} \quad (4.29)$$

The slurry tangential shear stress is provided in equation 4.23 and the slurry tangential shear rate from this equation is

$$\gamma_{str} \frac{\pi RS}{15n\left(1-G^{-2/n}\right)} \quad (4.30)$$

The slurry axial shear stress can be written as:

$$\tau_{sas} = (k\gamma_{srr}^{n-1})\gamma_{sar} \quad (4.31)$$

While the slurry resultant shear rate (γ_{srr}) is written as:

$$\tau_{srs} = \sqrt{\gamma_{str}^2 + \gamma_{sar}^2} \quad (4.32)$$

Ahmed and Miska (2008) provided the equation for the slurry axial shear rate as shown in equation 4.33.

$$\gamma_{sar} \frac{2n+1}{3n} \times \frac{\overline{Vel_{ann}}}{D_h} \quad (4.33)$$

The hydraulic diameter (D_h) is given as:

$$D_h = D_w - D_{dp} \quad (4.34)$$

While the mean annular velocity ($\overline{Vel_{ann}}$) which is a function of mud flow rate and annular area is given as:

$$\overline{Vel_{ann}} = \frac{Q}{A_{ann}} \quad (4.35)$$

Equation 4.36 is used to obtain the annular area as follows:

$$A_{ann} = \frac{\pi}{4}\left(D_w^2 - D_{dp}^2\right) \quad (4.36)$$

Equations 4.29 to 4.36, 4.22 to 4.28, and A.17 - A.19 in the Appendix A were coded and solved numerically in a computational software (Matlab^{T}) using the Rung-Kutta 6th order method. The results are discussed in section 6.1.5.

4.2 Geomechanical Studies and In-situ Stress Complications

Drilling fluids loss through induced fractures occur because the ECD exceeds the effective tangential (hoop) stress and the tensile strength of the rock. Figure 4.4 is a schematic showing two wellbore mechanical failures (shear and tensile failure) in a vertical wellbore assuming a normal faulting regime. The shear failure otherwise known as wellbore collapse occurs when the ECD goes below the shear failure gradient in the operational mud window. This occurs in the direction of the minimum horizontal stress and causes the wellbore to collapse. On the other hand, drilling induced fracture occurs in the maximum horizontal stress direction. Dupriest (2005) defined the concept of fracture closure stress (FCS) in a fluid loss process and suggested that a fracture is opened when the wellbore differential pressure is high enough to surpass the sum of the stress holding the closed rock and the tensile strength of the rock. The author defined the closing stress to be equal to the mud pressure needed to open the fracture. Reduced fluid density and ECD will permit an open fracture to close; thus, reducing fluid loss. Alberty and McLean (2004) developed the stress cage model based on linear elastic fracture mechanics. They concluded that there is an increase in the hoop stress around the wellbore wall which strengthens the wellbore, if an open fracture is effectively plugged.

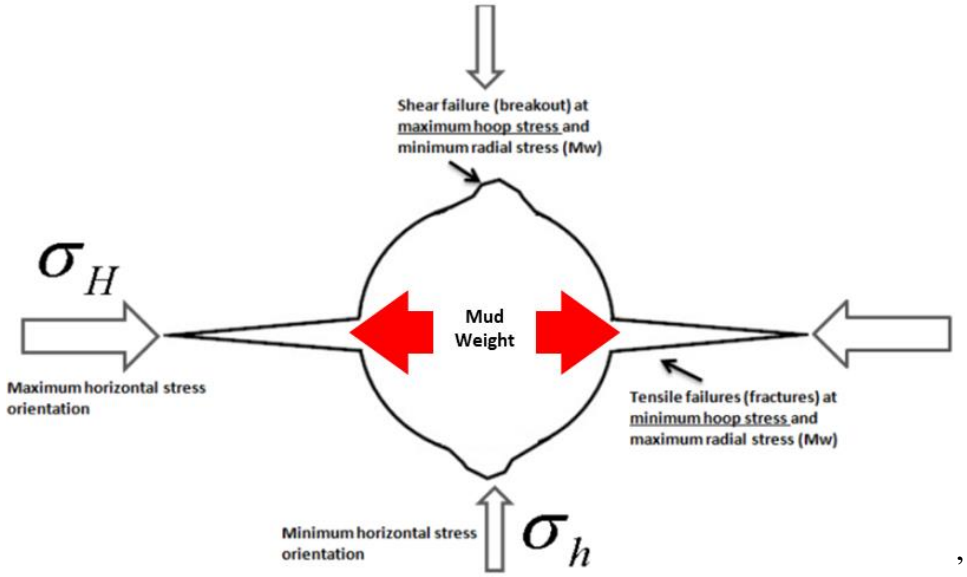

Figure 4.4: Tensile and shear failure for vertical wellbore. Courtesy: Dr. Saeed Salehi (PhD, P.E)

Wellbore strengthening can be described as a variety of approaches that allows for drilling a wellbore or an interval of interest with an increased fracturing pressure (Salehi 2012). The author developed a finite-element simulation for modeling fracture initiation, propagation, and sealing. They author concluded that hoop stress restoration to a value not greater than its theoretical ideal value, is the main mechanism behind wellbore strengthening. Experimental, analytical, and field studies have revealed that wellbore strengthening can be achieved through several techniques (Kiran and Salehi 2016; Dorman et al. 2015; Tran et al. 2011; Salehi and Nygaard 2011; Salehi et al. 2010). One of the primary process that is unique to all the techniques is the redistribution of the near-wellbore stresses when an intact rock is drilled. Prior to drilling, three far field principle stresses exist: vertical stress (σ_v), maximum horizontal stress (σ_H), and minimum horizontal stress (σ_h). Considering a vertical wellbore in a normal faulting regime, these stresses are transformed to the following wellbore stresses during drilling: axial stress (σ_a), radial stress (σ_r), and tangential (hoop) stress (σ_t). The directions of each wellbore stress are shown in Figure 4.5 for an experimental sandstone rock sample.

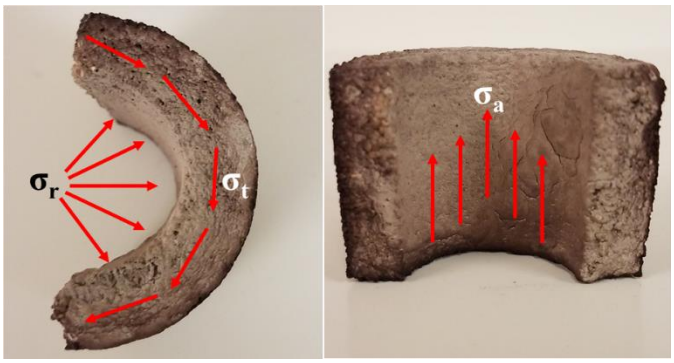

Figure 4.5: Direction of wellbore stresses for a thick-walled cylindrical sandstone sample

In Figure 4.5, the external filter cake can be assumed to be uniformly developed on the inner diameter of the thick-walled cylindrical core. When an intact rock is exposed to drilling fluid, the invasion of mud particles, filtrate, and filter cake evolution is not instantaneous. Rather, it is time-dependent and consequently, the changes in the wellbore stress geometry will be time-dependent. The important components in characterizing wellbore strengthening are the tangential (hoop) stress (σ_t) and radial stress (σ_r). Salehi and Kiran (2016) used a time-dependent poro-elastic model to determine both stresses.

Initially, when there is no filter cake present, the full effect of the differential pressure is completely felt by the rock which leads to maximum flow rate. During external filter cake evolution with time, differential pressure across the external filter cake increases with an increase in the filter cake thickness. This reduces the pressure across the porous media, and subsequently reduces the filtrate flowrate with time. The external filter cake is comprised of various particle sizes (Chenevert and Dewan 2001) and their permeability values are calculated using equations 4.28 and A.17 - A.19 in Appendix A. It can be assumed that the filter cake will transmit the radial stress (σ_r) directly to the wellbore wall without any change in the boundary condition. The solution is based on the study conducted by Chen and Yu (2015). Based on the solution suggested by Cui

et al. (1999), Salehi and Kiran (2016) complied the solution using Laplace's transformation domain. The pore pressure (P), radial stress (σ_r), and hoop stress (σ_θ) can be calculated as follows:

$$P = P_0 + P^{(I)} + P^{(II)} \quad (4.37)$$

$$\sigma_r = -\frac{\sigma_{xx}+\sigma_{yy}}{2} - \left(\sqrt{\left(\frac{\sigma_{xx}-\sigma_{yy}}{2}\right)^2 + {\sigma_{xy}}^2}\right)\cos 2\left(\theta - \left(\frac{1}{2}\tan^{-1}\frac{2\sigma_{xy}}{\sigma_{xx}-\sigma_{yy}}\right)\right) + {\sigma_{rr}}^{(I)} + {\sigma_{rr}}^{(II)} \quad (4.38)$$

$$\sigma_\theta = \frac{\sigma_{xx}+\sigma_{yy}}{2} - \left(\sqrt{\left(\frac{\sigma_{xx}-\sigma_{yy}}{2}\right)^2 + {\sigma_{xy}}^2}\right)\cos 2\left(\theta - \left(\frac{1}{2}\tan^{-1}\frac{2\sigma_{xy}}{\sigma_{xx}-\sigma_{yy}}\right)\right) + {\sigma_{\theta\theta}}^{(I)} + {\sigma_{\theta\theta}}^{(II)} \quad (4.39)$$

In these equations, σ_{xx} is the maximum horizontal stress, σ_{yy} is the minimum horizontal stress, σ_{xy} is the stress perpendicular to the 2-D horizontal plane considered, $P^{(I)}$ and $P^{(II)}$ are pore pressure components dependent on time, $\sigma_{rr}^{(I)}$ and $\sigma_{rr}^{(II)}$ are radial stress component dependent on time, $\sigma_{\theta\theta}^{(I)}$ and $\sigma_{\theta\theta}^{(II)}$ are hoop stress components dependent on time. Using Talbot algorithm (1979) for numerical Laplace inversion method, the above equations are modeled in computational software (Matlab^T) to compare the effect of filter cake evolution on the stresses in the rock samples. These will be discussed in Chapter 6.

Chapter 5: Experimental Results and Discussions

In this chapter, the results of all the experiments that were conducted in this study will be presented. Beginning with drilling fluids rheology and particle size distribution, this chapter will present the rheological profiles of the samples used for the experiments and discuss their temperature-dependent effect on fluid loss and filtration. Next, the experimental results from the stage one experiments on ceramic filter tubes will be presented. The statistical analysis of the results using hypothesis testing and ANOVA will be discussed in detail. The results from the second stage (dynamic filtration with core samples) will be presented. The scientific explanation of the filtration profiles, microscopic analyses, plastering effect, and regression analysis will be detailed. This chapter will also encompass the results and discussions from the third stage of experiments (fluid loss profiles, statistical analysis, and field implications).

5.1 Drilling Fluids Rheology and PSD

5.1.1 Granular ($CaCO_3$) LCM Fluid Rheology

The rheological profiles for the calcium carbonate WBM's are shown in Figure 5.1, Figure 5.3, and Figure 5.3. Figure 5.1 shows the temperature-dependent apparent viscosity profiles for the three $CaCO_3$ WBM's. Apparent viscosity is defined as the viscosity of a fluid at particle time or shear rate. A general observation is that as the LCM concentration increases, the apparent viscosity increases. Temperature is a critical factor that has a more detrimental effect on WBM than OBM. Figure 5.1 shows that for 30 lb/bbl, 55 lb/bbl, and 80 lb/bbl $CaCO_3$ WBM, an increase in temperature from ambient to 120^oF corresponds to a 43%, 49.5%, and 46.5% decrease in apparent viscosity respectively. Furthermore, the percentage decease in apparent viscosity increased to 63.7%, 67.9%, and 66.2% respectively when the temperature increased to approximately 210^oF. 212^oF is the maximum operating temperature limit of the M3600 automatic viscometer.

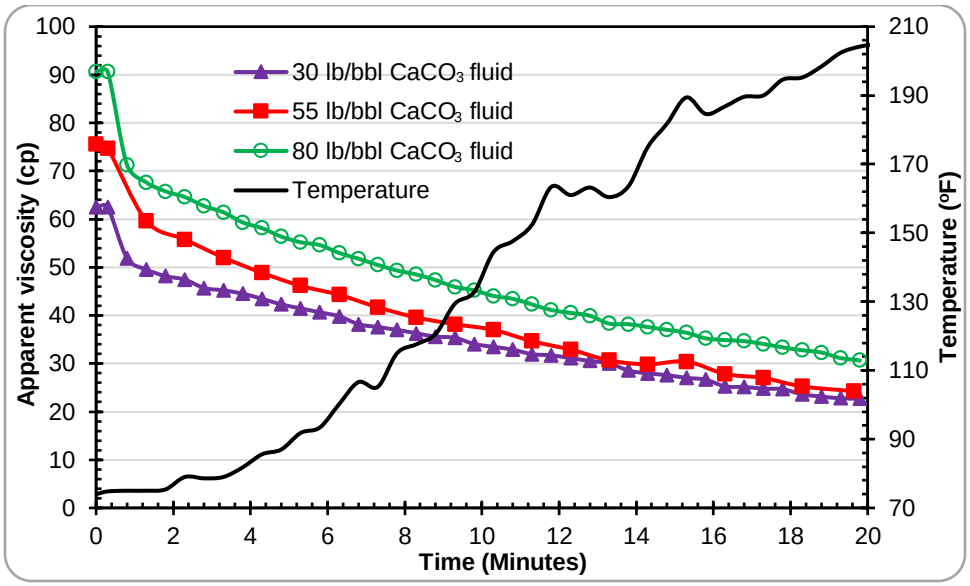

Figure 5.1: Apparent viscosity profiles of $CaCO_3$ LCM fluids vs. temperature at 170.3 sec^{-1}

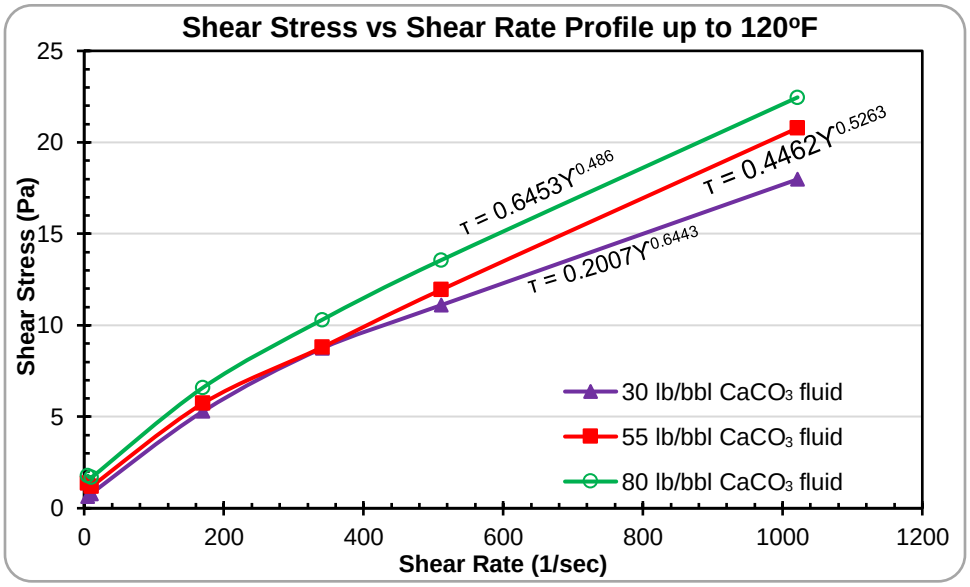

Figure 5.2: Shear stress vs. shear rate profiles of CaCO3 LCM fluids at 120ºF.

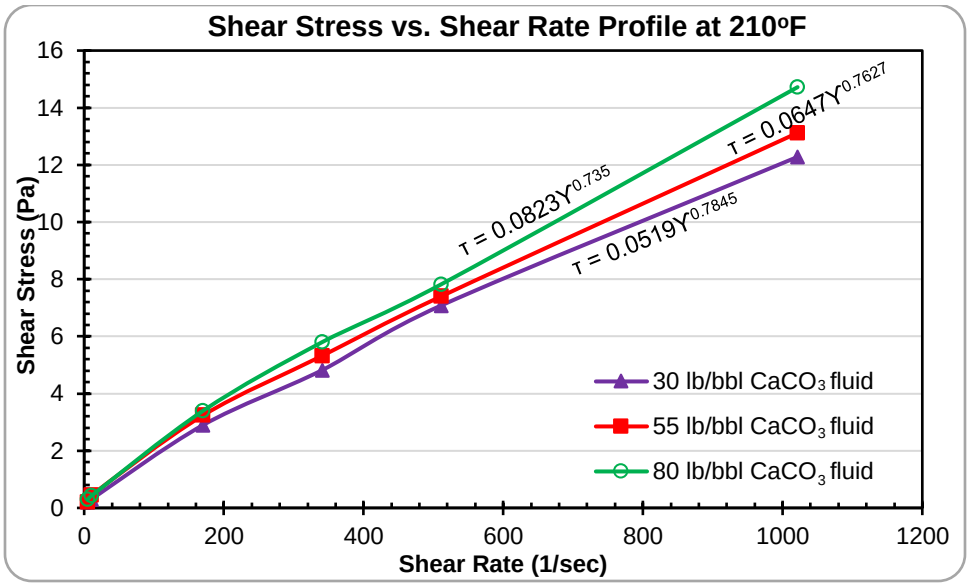

Figure 5.3: Shear stress vs. shear rate profiles of CaCO3 LCM fluids at 210°F.

Figure 5.2 and Figure 5.3 shows the shear stress vs. shear rate plots of all the samples at 120°F and 210°F respectively. Power law equations with consistency indices and flow behavior indices were fitted to each plot. The plots reveal an increase in shear stress as LCM concentration increases. Furthermore, the results show that as the LCM concentration increases, the consistency index increases. This translates to an increase in viscosity. However, the average decrease in the consistency index with an increase in temperature (120°F to 220°F) is up to 82%. Some authors have linked drilling fluids rheology to fluid loss. Sun and Huang (2015) developed a piecewise rheological model which revealed that at the initial stage of mud invasion, the fluid invasion radius is impacted by fluid flow index (n). Furthermore, the analytical study performed by Lavrov and Tronvoll (2004) suggests that a decrease in the consistency index of a Power law fluid can increase the fluid's loss rate, particularly the initial flow rate. Therefore, the rheological profiles obtained are important in characterizing the fluid loss and filtration intensity. In this study, reduction in apparent viscosity and consistency index at elevated temperature makes the fluid samples more susceptible to high loss rate.

5.1.2 Granular LCM Fluid PSD

Figure 5.4 shows the wet PSD of the three $CaCO_3$ WBM samples. The minimum and maximum particle diameters are approximately 0.2 µm and 80 µm respectively. An increase in the bridging agent's concentration had little to no effect on the PSD since it is the same material. However, higher concentrations can form better plugs within the pore throat diameters that are in the PSD range. This is also dependent on other experimental constraints like temperature and rotary speed.

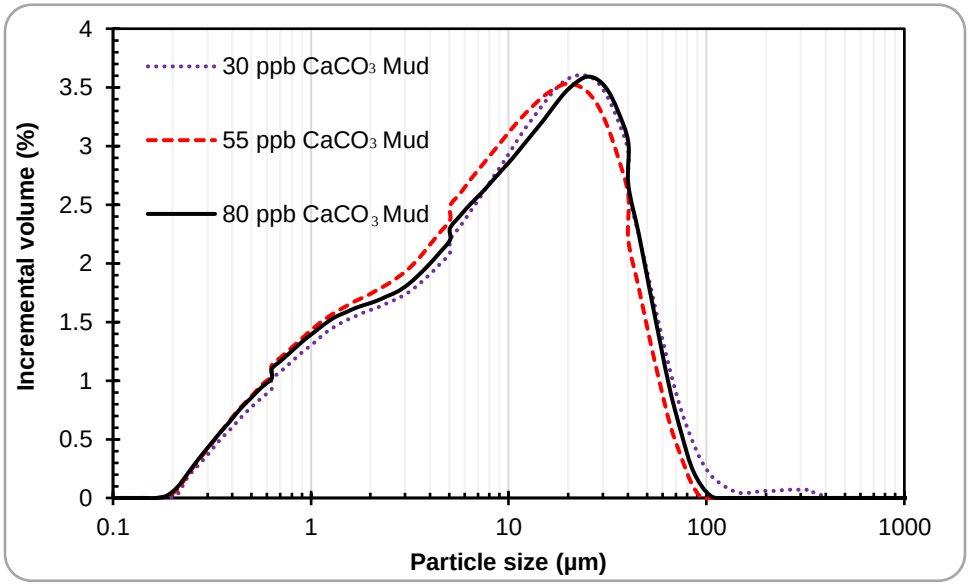

Figure 5.4: Particle size distribution (PSD) of CaCO3 LCM fluid recipes.

5.1.3 Cedar Fiber LCM Fluid Rheology

The shear stress vs. shear rate profiles of the fiber WBM's (5 and 15 lb/bbl) at 200°F are shown in Figure 5.5. The plots were obtained for this temperature because that was the temperature at which the proposed dynamic fluid loss tests (stage three) were conducted. The figure shows that the shear stress increases with an increase in the LCM concentration. In addition, the consistency index of the 5 lb/bbl fiber WBM is lower than the value of the 15 lb/bbl fluid. This implies that the fluid viscosity increases with an increase in LCM concentration, and this is favorable to reducing fluid loss. In the analytical study performed by Ghalambor et al. (2014), the authors attributed fluid loss

reduction through a 500 µm (fracture width) to an increase in viscosity. Thus, it is expected that the 15 lb/bbl fluid will perform better than the 5 lb/bbl fluid by plugging the fractures and reducing more losses. The rheological profile of the 30 lb/bbl fiber WBM was not completely determined because of machine limitation. However, qualitative and visual observation suggests an increase in resistance to flow. This can translate to higher viscosity compared to the first two concentrations, which contributes to reducing losses.

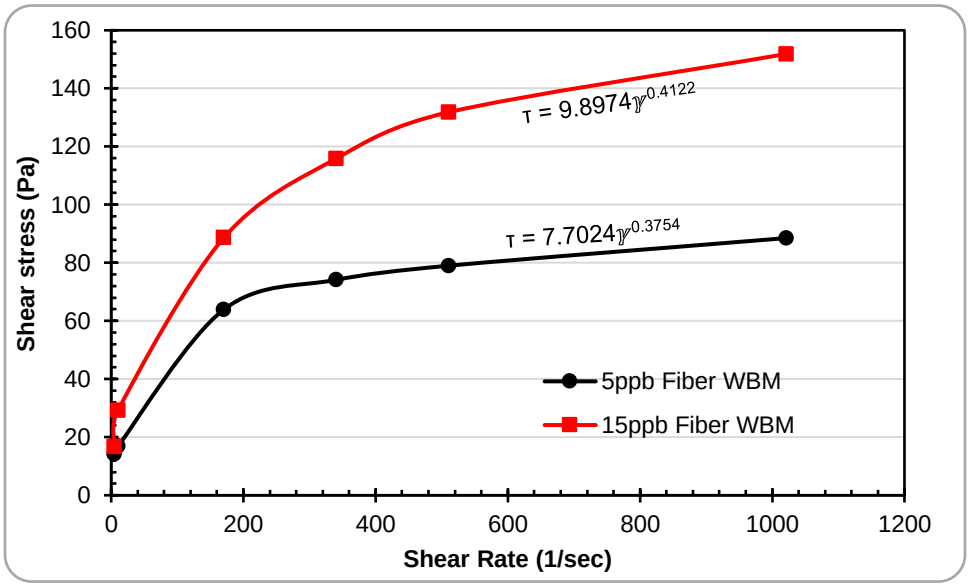

Figure 5.5: shear stress vs. shear rate profiles of Cedar fiber at 200^0F.

5.2 Stage One: Pore-Scale Dynamic Drilling Fluids Filtration (Ceramic Filter Tubes)

5.2.1 Dynamic Drilling Fluid Filtration Profiles

In this subsection, the profiles from the dynamic mud filtration experiments are provided. Each cumulative dynamic filtrate loss profile was plotted against time from zero (after all the experimental conditions have been attained) to 30 minutes (after filtration duration) instead of against the traditional square root of time. This is because the mathematical derivation (by Bourgoyne et al. 1986) which shows cumulative filtrate volume as a function of square root of time was formulated based on Darcy's law applied to static filtration in API filter press. This filter

press uses filter paper as the porous media and there is no material cross-flow. Considering the data collection method (filtrate is collected and measured in a test tube typically after 1 minute, 7.5 minutes, and/or 30 minutes), the author suggested that one way to obtain the spurt invasion is by plotting the cumulative filtrate at these times versus the square root of the times and extrapolating the straight line to zero. Furthermore, the square root of time representation assumes that the filtrate collection after 30 minutes is twice the value after 7.5 minutes. In the field, this method is only used to characterize the filtrate quality of the mud, and twice the value after 7.5 minutes is reported for 30 minutes if the actual value after 30 minutes exceeds the filtrate collector.

Thus, the cumulative filtrate loss versus square root of time plot is only valid for static filtrate conditions, without material cross flow, and for which data collection is limited. Integrating the fundamental Darcy equation for dynamic condition, the author showed cumulative filtrate loss as a function of time. More importantly, the data acquisition system (DAQS) used in this research was able capture the spurt losses and steady state filtration profiles automatically in seconds rather than manually. It is practically not necessary to convert the times to their square root and unimportant to perform extrapolations to estimate spurt loss or 30 minutes cumulative dynamic filtrate loss. Figure 5.6 shows the filtration profiles for the conditions in the graph. Test 1 showed a spurt loss of approximately 0.5 cm^3 before the complete differential pressure was attained. The steady state filtration for this test started after about 5 minutes. For the same conditions, with another filter tube (same pore throat diameter), the repeat of test 1 did not show any spurt loss before or within 10 seconds. A delay in filtration was observed and this phenomenon has been explained by Ezeakacha and Salehi (2018). The steady state filtration for the repeated test began after about 5 minutes and interestingly, both tests exhibited similar profiles with very close end

results. The percentage difference between test 1 and the repeat is 4.8 %. This indicates a good consistency in the experimental conditions and tests.

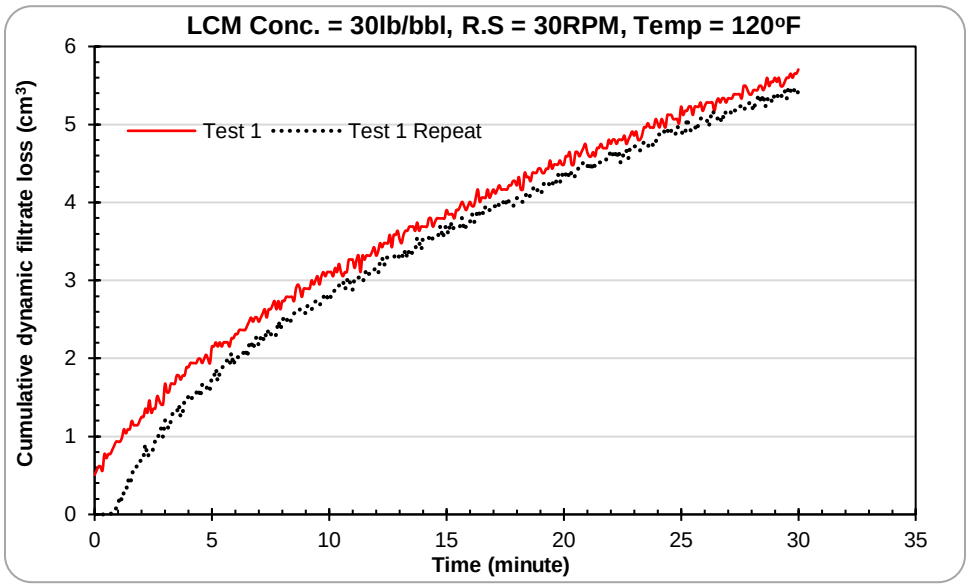

Figure 5.6: Dynamic cumulative filtrate loss profiles for Test 1 and its replicate

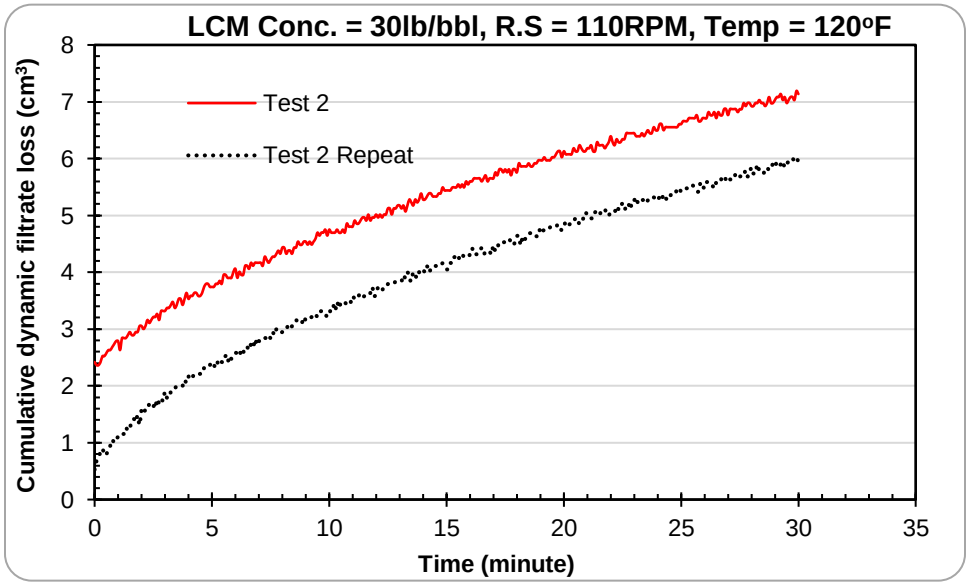

Figure 5.7: Dynamic cumulative filtrate loss profiles for Test 2 and its replicate

Figure 5.7 shows the filtration profiles for the conditions in the graph. Tests 2 and its replicate showed spurt invasions up to 2.365 cm^3 and 0.737 cm^3 respectively. While both tests have the

same experimental conditions, the difference in their spurt is attributed to the fact that two different filter tubes were used. Although, both tubes have the same average pore throat diameter and made from the same material, it is not guaranteed that both experiments will yield the exact same results. However, notice that their steady state profiles are very similar. The percentage difference between test 2 and its replicate is 16.6 %. The difference between the profiles appeared to have been steady throughout the test duration. This is a confirmation of the consistency in the experimental conditions.

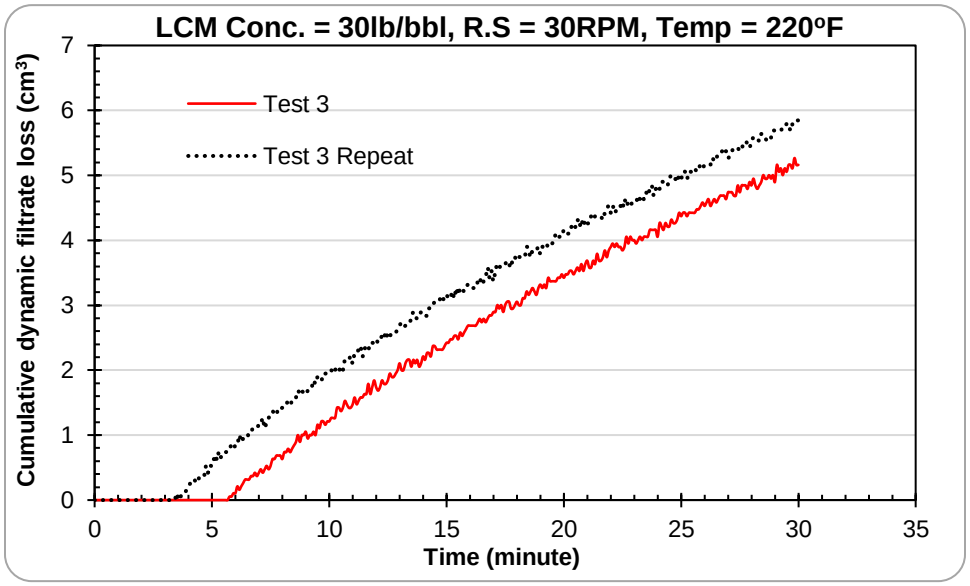

Figure 5.8: Dynamic cumulative filtrate loss profiles for Test 3 and its replicate

Figure 5.8 shows the filtration profiles for the conditions in the graph (Test 3 and its replicate). The filtrate breakthrough times were 5.75 minutes and 3.67 minutes respectively. Although, these delays were observed, the cumulative filtrate values were as high as the numbers obtained in Figure 5.6 and Figure 5.7. Generally, this can be attributed to the low concentration of LCM. Noticeably, the experimental conditions were consistent as this is shown from the parallel profiles from the fluid breakthrough time. The percentage difference between both tests is 11.7 %.

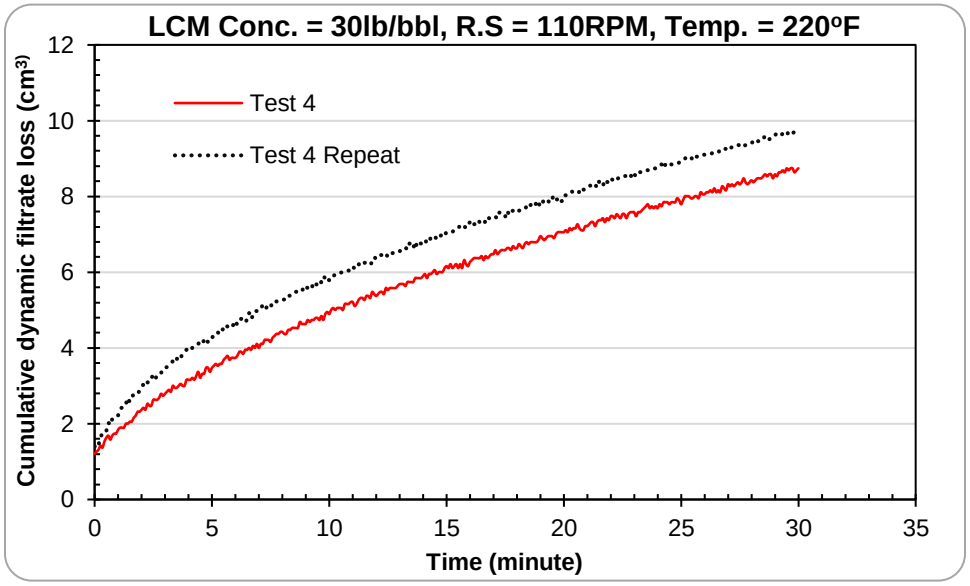

Figure 5.9: Dynamic cumulative filtrate loss profiles for Test 4 and its replicate

Test 4 and its replicate are shown in Figure 5.9. Both tests revealed very similar spurt invasions (1.317 cm^3 and 1.355 cm^3) respectively. The spurt and overall high cumulative dynamic filtrate loss (compared to Figure 5.6, Figure 5.7, and Figure 5.8) is attributed to high rotary speed and temperature. Interestingly, both profiles show similar steady state filtrate invasion profiles. However, a deviation in the profiles can be seen, and this may be linked to the difference in the porous media used. Overall the experimental conditions were consistent and percentage difference in both tests is 9.9 %.

Test 5 and its replicate are shown in Figure 5.10. Spurt invasions were not recorded and the overall low cumulative dynamic filtrate loss (compared to tests 1, 2, 3, and 4) is attributed to the high LCM concentration, low temperature, and low rotary speed. Test 5 showed only 0.005 cm^3 of filtrate, while the repeat showed 2.128 cm^3. The experiment was repeated and a similar profile of little to no filtrate was obtained. The experiment appeared to be the only outlier from

others performed in this stage. However, the effect of an increase in the LCM concentration was strongly indicated.

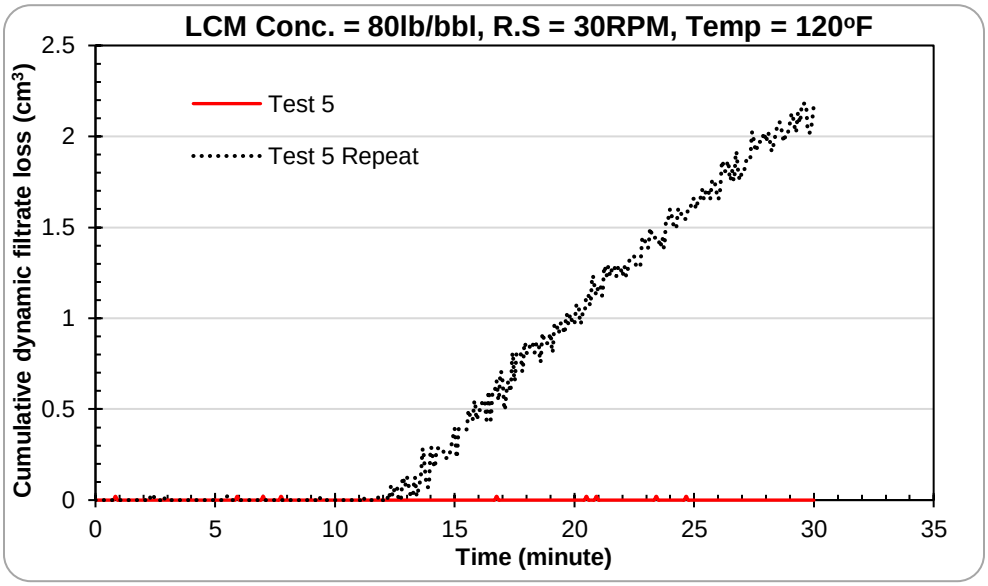

Figure 5.10: Dynamic cumulative filtrate loss profiles for Test 5 and its replicate

Figure 5.11 shows the dynamic filtrate loss profiles for the conditions in test 6 and its replicate. Spurt invasion was not recorded, and for the first 25 minutes, filtrate loss was between 0 and 0.1 cm^3 (0.05 cm^3 on average). It is also noticeable that the profiles are similar, and a significant filtrate collection began towards the end of the experiments. This is a testament to the consistent experimental conditions. However, some form of heterogeneity (two different filter tubes) is evident in the different cumulative filtrate losses. The overall reduced invasion (compared to all the tests in stage one) is attributed to high LCM concentration. It is possible to compare the profiles in Figure 5.11 to the profile in test 5 and argue that at reduced rotary speed (same temperature and LCM concentration), filtrate loss should be lowered compared to high rotary speed. However, recall that the repeat of test 5 and another repeat showed little to no filtrate value, while both tests in Figure 5.11 showed some filtrate value. In general, an increase in the LCM concentration played

a key role in reducing the filtrate loss. The interaction of all these factors and their effects on cumulative dynamic filtrate loss will be explained in detail in section 5.2.2.

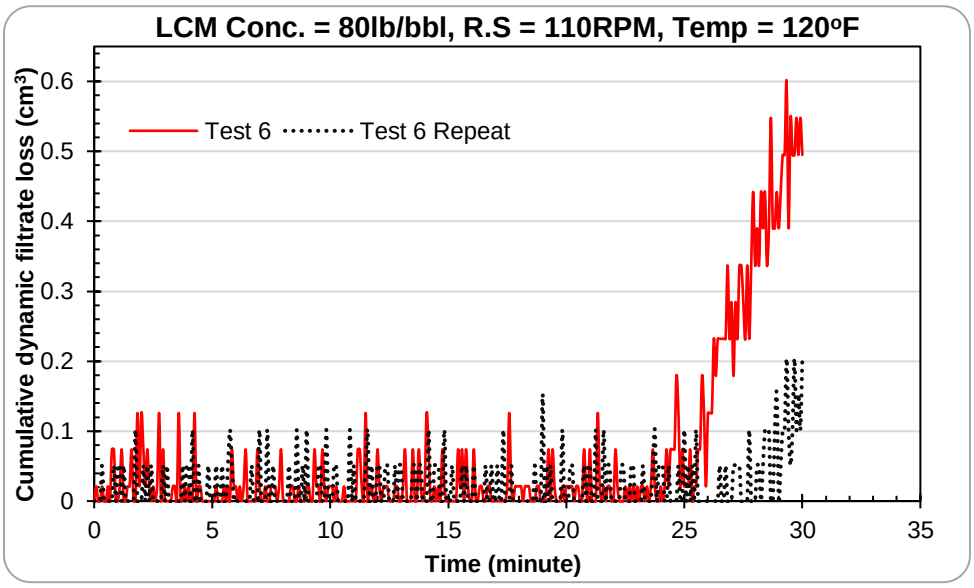

Figure 5.11: Dynamic cumulative filtrate loss profiles for Test 6 and its replicate

Figure 5.12 shows the dynamic filtrate loss profiles for the conditions in test 7 and its replicate. Of all the tests performed in stage one, the tests shown in this figure had the closest profiles. They showed approximately the same filtrate breakthrough time (25 seconds), the same steady state filtration profiles, and very close filtration values. The percentage difference in the cumulative filtrate is 2.5 %. There was no obvious spurt invasion, and this is linked to the high LCM concentration. However, once the filtrate broke through, the effect of elevated temperature controlled the high filtrate loss profile. More details about the interaction of temperature and high LCM concentration is provided in the next section.

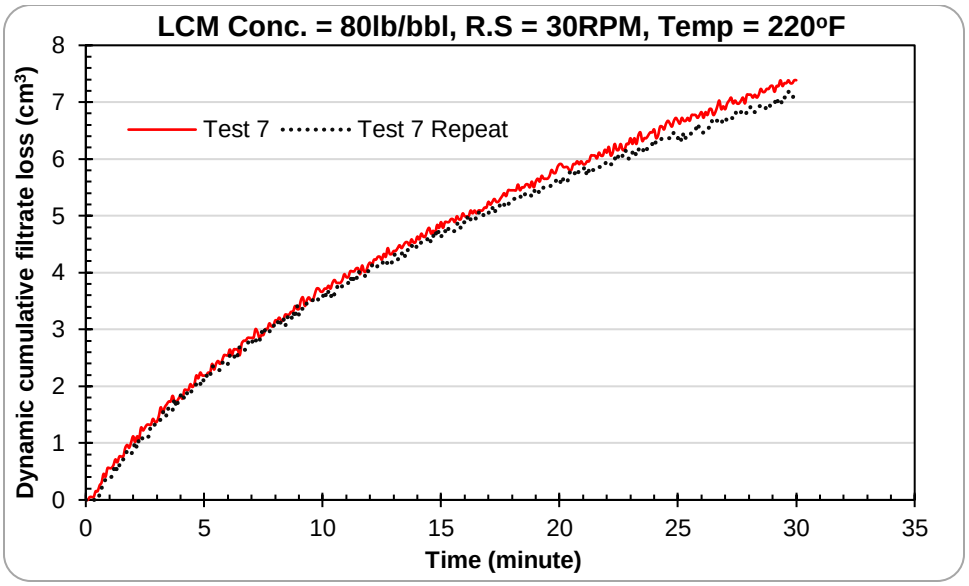

Figure 5.12: Dynamic cumulative filtrate loss profiles for Test 7 and its replicate

Test 8 and its replicate are shown in Figure 5.13. Both tests showed spurt invasions of 1 cm^3 and 0.6 cm^3 respectively. The difference in both values were maintained through the steady state filtration stage. This is also a confirmation of the consistent experimental conditions and different ceramic filter tubes. It is worthy to note that all the tests with high LCM concentration (tests 5, 6, and 7) had no spurt invasion except the tests in Figure 5.13. Also notice that the tests in Figure 5.13 had the highest cumulative dynamic filtrate loss compared to tests 5, 6, and 7 (high LCM concentration tests). This is because of the elevated temperature and rotary speed effect. In general, the tests performed in stage one showed good replications except for test 5. The replicates were performed to obtain some margin of error to perform the statistical analysis. Overall, the percentage differences are low and a testament to the individual ceramic filter tubes used. The steady state filtration profiles of the tests and their replicates showed the consistency in the test conditions used.

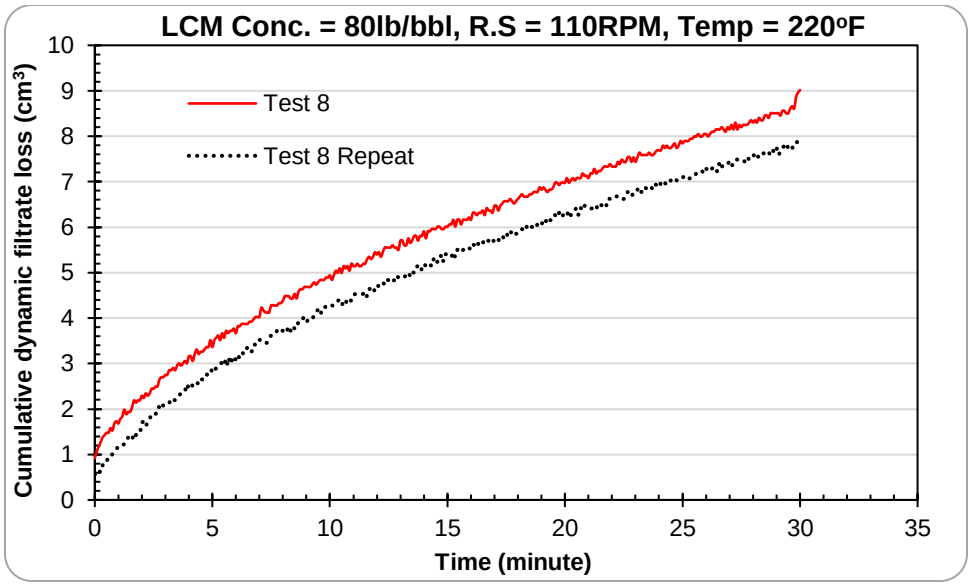

Figure 5.13: Dynamic cumulative filtrate loss profiles for Test 8 and its replicate

5.2.2 Statistical Analysis: Analysis of Variance (ANOVA)

In this subsection of the results, the hypothesis testing results will be presented and in detail. Analysis of Variance (ANOVA) was the testing method used. The F-test was performed, and p-values were obtained as shown in Table 5.1. The sample size of two was used. The F-test is used to test whether there is a variation among group means. The p-value is the probability of finding an observed result when the null hypothesis being tested is true. The hypotheses being tested have been developed in subsection 3.2.2. The test results and discussions are divided into single factor effects and multiple factor effects. Figure 5.14, Figure 5.15, and Figure 5.16 show the single and combined effect plots for all the factors and their interactions. Furthermore, the adequacy of the ANOVA will be confirmed by verifying that the ANOVA meets the three assumptions of normality, independence, and constant variance.

Table 5.1: Analysis of Variance (ANOVA)

Source	SS	DF	MS	F_o	P-value
A	23.34	1	23.34	42.30	0.000187
B	6.71	1	6.71	12.16	0.008237
AB	4.45	1	4.45	8.07	0.021804
C	71.54	1	71.54	129.68	0.000003
AC	34.12	1	34.12	61.84	0.000049
BC	5.30	1	5.30	9.61	0.014679
ABC	0.20	1	0.20	0.36	0.565350
Error	4.41	8	0.55		
Total	150.07	15			

5.2.2.1 Single Factor Effects

Figure 5.14 shows the effect of LCM concentration and its interaction with rotary speed and temperature. Each plot in the figure represents a shift from the low level of LCM concentration (30 lb/bbl) to the high level (80 lb/bbl), at a high or low level of rotary speed and at a high or low level of temperature. The plot AB1C1 represents a decrease in dynamic filtration loss from 11.136 cm^3 to 2.129 cm^3, when LCM concentration increases from 30 lb/bbl to 80 lb/bbl at 30 rpm and 120^{o}F. Plots AB1C1, AB2C1, and AB2C2 reveal a decrease in dynamic filtration loss with an increase in LCM concentration. The increasing profile of plot AB1C2 is attributed to natural experimental error. Moreover, the elevated temperature effect (C2) could have masked the increasing effect of LCM concentration. In general, the single effect of increasing LCM concentration is that dynamic filtration loss decreases. The significance of this decrease is shown in

Table 5.1. The p-value of LCM concentration (A) is less than 0.05. This implies that the null LCM Conc. hypothesis is rejected, with the conclusion that an increase in the LCM concentration from 30 lb/bbl to 80 lb/bbl significantly decreases dynamic filtration loss. The overall effect estimate of increase in LCM concentration is a decrease in dynamic mud filtration by 16%.

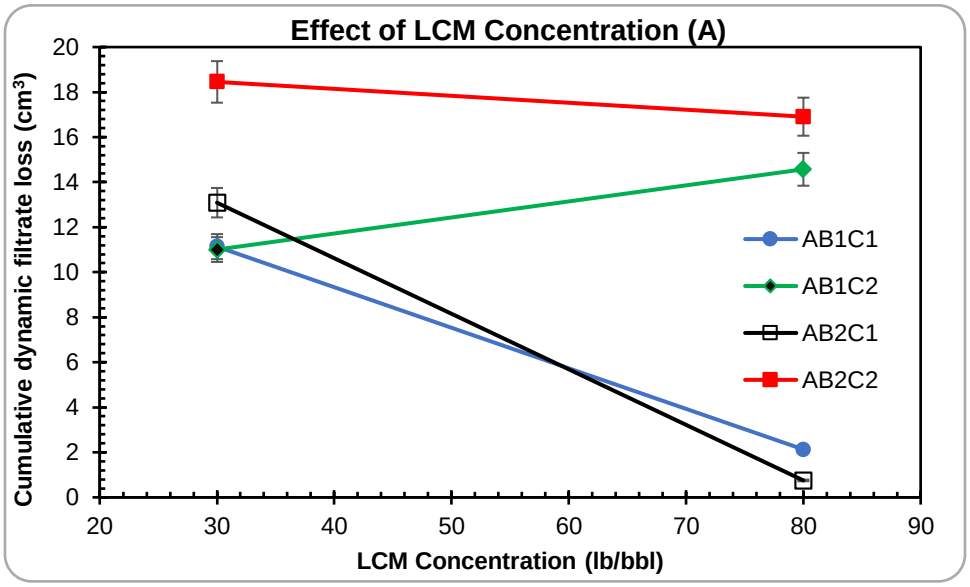

Figure 5.14: Effect of LCM concentration and interaction with rotary speed and temperature.

Figure 5.15 shows the effect of rotary speed and its interaction with LCM concentration and temperature. Each plot represents a shift from the low level of rotary speed (30 rpm) to its high level (110 rpm), at a high or low level of LCM concentration and at a high or low level of temperature. Plots A1BC1, A1BC2, and A2BC2 reveal that an increase in rotary speed tends to increase dynamic mud filtration loss. The effect of high LCM concentration (A2) combined with low temperature (C1) is a plausible mechanism for the slight decreasing trend shown in plot A2BC1. Thus, an increase in rotary speed generally results to an increase in dynamic mud filtration loss. The p-value in

Table 5.1 for rotary speed single effect (B) shows that its impact (increase) on dynamic mud filtration loss is significant because it is less than 0.05. Thus, the null rotary speed hypothesis is rejected with the conclusion that an increase in rotary speed from 30 rpm to 110 rpm significantly increases dynamic mud filtration loss by 5%.

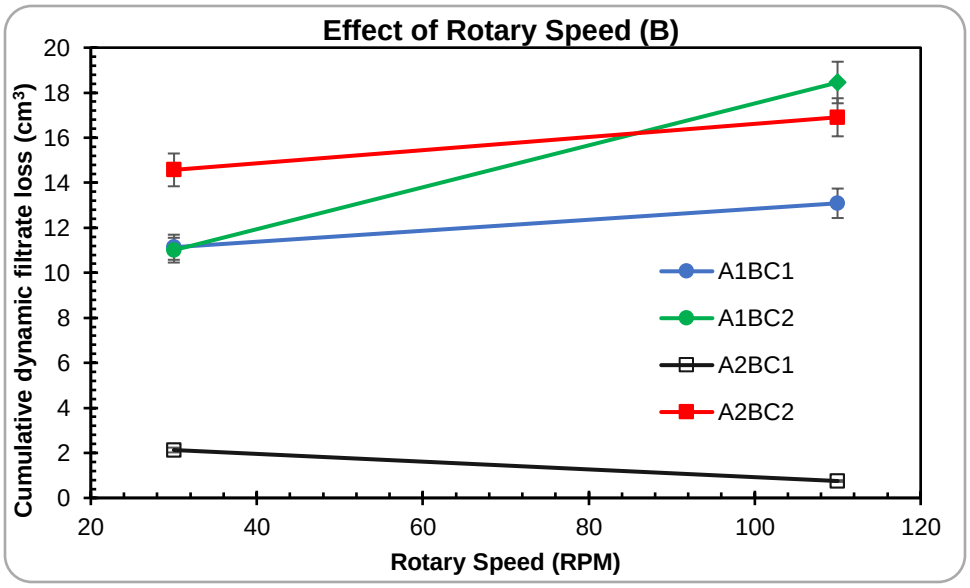

Figure 5.15: Effect of rotary speed and interaction with LCM concentration and temperature.

Figure 5.16 shows the effect of temperature and its interaction with LCM concentration and rotary speed. Each plot depicts a shift from the low level of temperature (120^{o}F) to its high level (220^{o}F), at a high or low level of LCM concentration and at a high or low level of rotary speed. Plots A2B1C, A1B2C, and A2B2C show an increase in dynamic mud filtration loss as temperature increases from 120^{o}F to 220^{o}F. There is no observable change in dynamic mud filtration with an increase in temperature as shown in plot A1B1C. The p-value of temperature (C) in Table 5.1 shows that the impact it has on dynamic mud filtration loss is significant because it is less than 0.05. Therefore,

the null temperature hypothesis is rejected. The overall effect estimate of temperature is an increase in dynamic mud filtration loss by 49.1%.

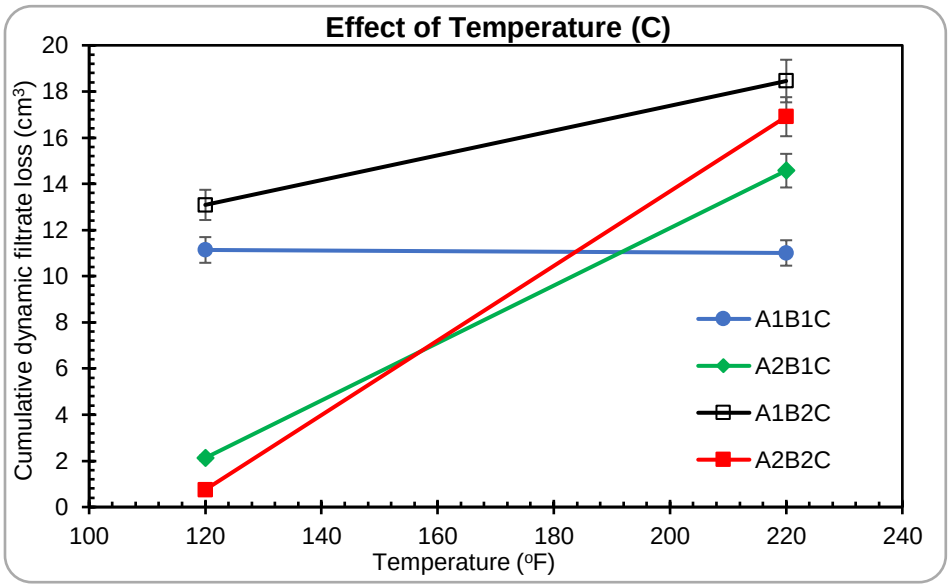

Figure 5.16: Effect of temperature and the interaction with LCM concentration and rotary speed.

All the factors (LCM concentration, rotary speed, and temperature) that have been investigated have shown significant impact on dynamic filtrate loss. The order of their significant single effect (from high to low) is: temperature > LCM concentration > rotary speed. The result from this subsection is critical because it addresses part of the first hypothesis in this study which states that: dynamic drilling fluid loss and filtration is significantly influenced by up to three factors as single effects and multiple (factor combinations) effects. The analysis in subsequent subsection (5.2.2.2) will be used to verify another part of the of the study's first hypothesis

5.2.2.2 Multiple Factor Effects

It is worthy to note that Figure 5.14, Figure 5.15, and Figure 5.16 do not only reveal the singular effects of these factors. They also show their interaction (combined) effects. An interaction effect exists when the effect of one factor on a response varies across the levels of another factor. For

instance, the intersection of plots AB1C1 and AB2C1 in Figure 5.14 indicates that there is an interaction effect between two factors. The intersection of plots AB1C1 (blue) and AB2C1 (black) in Figure 5.14 implies that at low temperature (C1), the effect of increasing the LCM concentration (A) on the decrease in dynamic mud filtration loss is different for the two levels of rotary speed (B) and vice versa. This is called the AB interaction effect. This effect is also seen in the intersection of plots A1BC2 (green) and A2BC2 (red) in Figure 5.15. In this case, it shows that at a high temperature (C2), the effect of increasing rotary speed on dynamic mud filtration varies across the two levels of LCM concentration, and vice versa. It is worthy to mention that the AB interaction effects in Figure 5.14 and Figure 5.15 have decreasing and increasing trends respectively. However, the combined estimate of the interaction effect shows that the interaction of LCM concentration (A) and rotary speed (B) decreases dynamic mud filtrate loss up to 3%. This means that an increase in LCM concentration has a more dominant effect on dynamic mud filtration loss than an increase in rotary speed. The p-value of AB in Table 5.1 is less than 0.05. Therefore, the null LCM concentration-rotary speed interaction hypothesis is rejected, with the conclusion that a combination of the two factors can significantly decrease dynamic mud filtration loss.

Figure 5.16 shows the interaction of rotary speed and temperature (BC) from the intersection of plots A2B1C (green) and A2B2C (red). This BC interaction suggests that at high LCM concentration (A2), the effect of increasing the rotary speed on dynamic mud filtrate loss varies across the two levels of temperature, and vice versa. Furthermore, the BC interaction effect is slightly observed in the intersection of plots A1BC1 (blue) and A1BC2 (green in Figure 5.15). The interpretation of this interaction is that at low LCM concentration (A1), the effect of increasing the rotary speed on dynamic mud filtration loss varies slightly across the two levels of temperature.

The overall estimate of the interaction effect reveals that both factors increased the dynamic mud filtration loss up to 3.6%. The p-value in Table 5.1 for BC interaction is less than 0.05. Therefore, the null rotary speed and temperature interaction hypothesis is rejected, with the conclusion that a combination of the two factors can significantly increase dynamic mud filtration loss.

The interaction of LCM concentration and temperature (AC) is observed in Figure 5.16. The intersection of plots A1B1C (blue) and A2B1C (green) reveal that at low rotary speed (B1), the increasing effect of temperature on dynamic mud filtration varies across the two levels of LCM concentration, and vice versa. In addition, the AC interaction effect is slightly observed with the intersection of AB1C1 and AB1C2 in Figure 5.14. The interpretation of this interaction is that at low rotary speed (B1), the effect of increasing the LCM concentration on dynamic mud filtration loss varies slightly across the two levels of temperature. The overall estimate of the interaction effect shows that dynamic mud filtration loss increased by 23.4%. This means that increase in temperature from 120^{o}F to 220^{o}F has a greater impact on dynamic mud filtration than an increase in calcium carbonate concentration from 30 lb/bbl to 80 lb/bbl. The p-value in Table 5.1 for AC interaction is less than 0.05. Therefore, the null LCM concentration and temperature interaction hypothesis is rejected, with the conclusion that a combination of the two factors significantly increases dynamic mud filtration loss. The p-value for the ABC interaction shows that it is not significant, since it is greater than 0.05.

Based on the analyses performed in this subsection, the order of impact for the two-factor interaction effects on dynamic filtrate loss is: AC (LCM conc./temperature) > BC (rotary speed/temperature) > AB (LCM conc./rotary speed). The result from the single factor effects and multiple factor effects (subsections 5.2.2.1 and 5.2.2.2) completely validates the first hypothesis in this study. A systematic approach was used in carrying out the experiment design, conducting

the actual experiment, acquiring the data, and analyzing the data to validate this research hypothesis (section 1.2).

5.2.2.3 Verification of ANOVA Adequacy

One of the primary objectives for conducting the hypothesis tests using analysis of variance is to determine the magnitude, significance, and order of impact of the factors affecting dynamic mud filtration. However, after determining these, it is important to check that the data used in performing the tests meet certain requirements which allows the ANOVA to be considered adequate. These requirements are assumptions that must be checked, and these have been discussed in section 3.2.2. The results are shown in Figure 5.17, Figure 5.18, and Figure 5.19.

Figure 5.17 shows the normality plot which was used in checking the normality assumption. The R^2 value is greater than 90% and the data appear to be normally distributed. The last point to the right may not be considered as an outlier considering the inherent experimental error that can arise from the different porous media samples used in addition to the sum squared error.

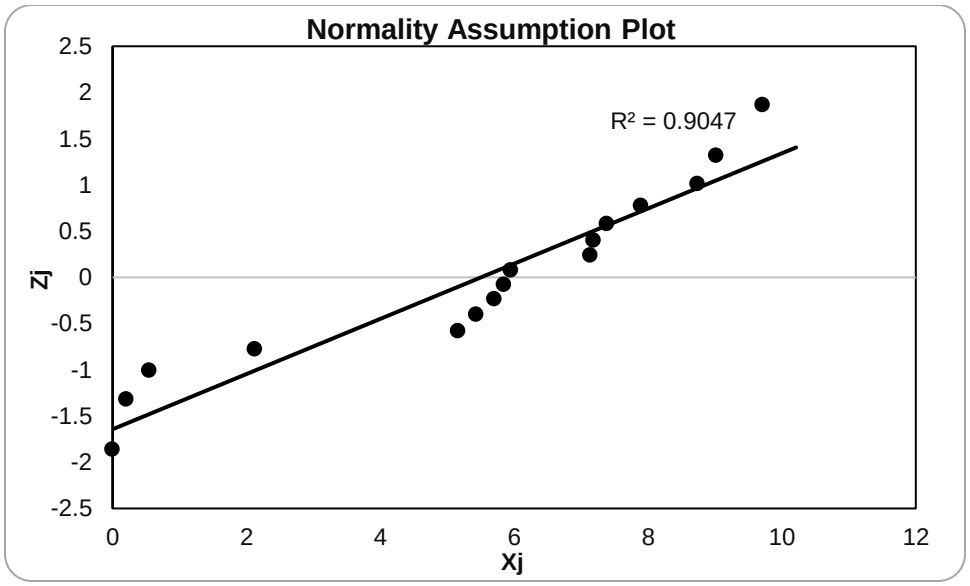

Figure 5.17: Normality plot used in verifying the normality assumption of ANOVA

Figure 5.18 shows the plot used to determine the adequacy of the independent assumption. To fulfil this assumption, a plot of the residuals versus the run order must show randomization of data with no detectable pattern in the plot. Figure 5.18 shows that the data collected are randomized and there is no detectable pattern. Therefore, they are adequate for conducting the hypothesis tests.

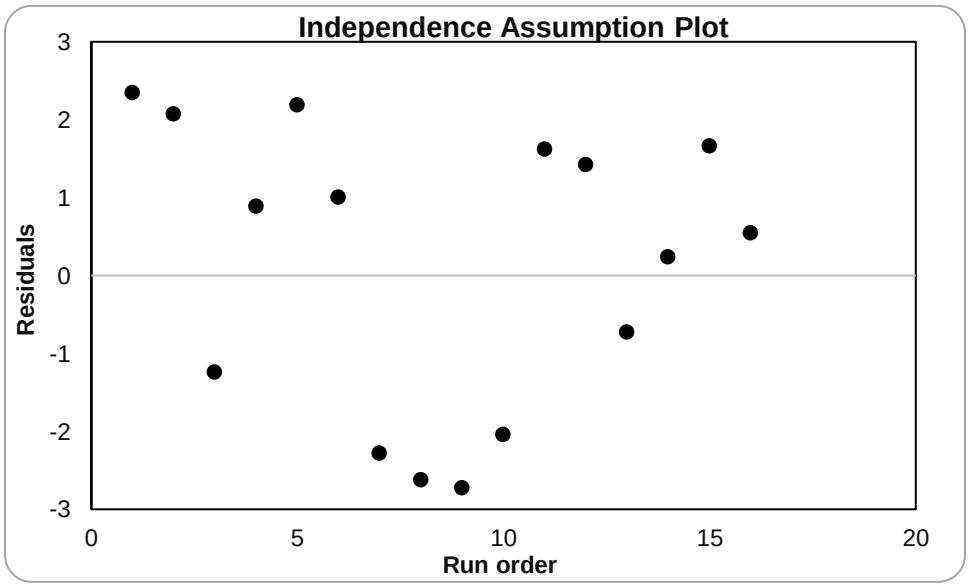

Figure 5.18: Residuals vs. run order plot used in verifying the independence assumption of ANOVA

The constant variance assumption is verified in Figure 5.19. This assumption requires low variability between the residuals. The largest dispersion between residuals is under the predicted filtrate loss value of 1.24 cm^3. Other residuals show nothing unusual and good dispersion. This implies the DoE was balanced and the data obtained are adequate to perform the hypothesis tests using ANOVA.

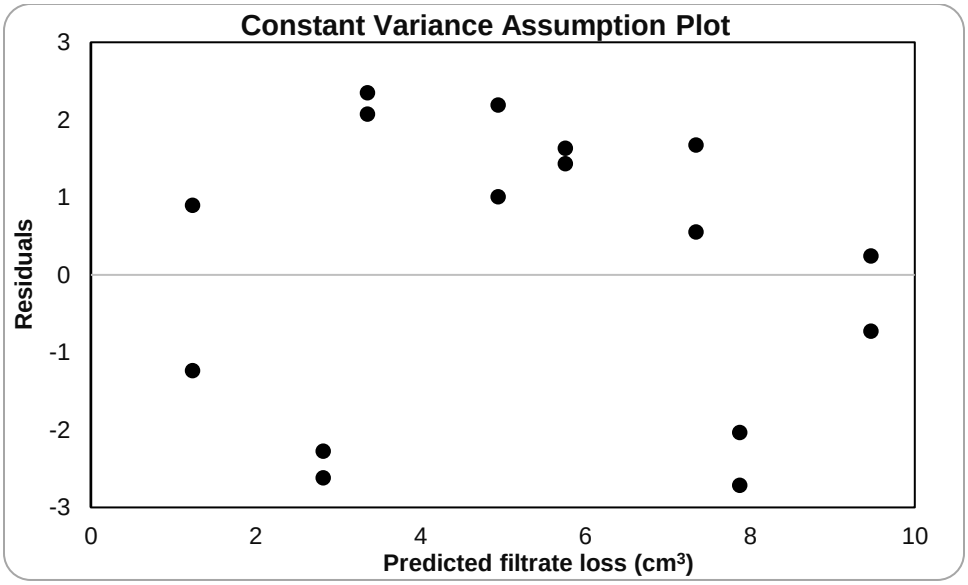

Figure 5.19: Residuals vs. predicted dynamic filtrate loss plot used in verifying the constant variance assumption of ANOVA

5.3 Stage Two: Pore-Scale Dynamic Drilling Fluids Filtration (Different Rocks)

The results from the 57 experiments conducted in stage two are presented in this section. The results from the first phase (12 experiments) are presented from subsection 5.3.1 to 5.3.4. The experiments in this phase were performed at constant conditions (120^oF and 70 rpm) with two different mud recipes (a base fluid without LCM and sample two in Table 3.8). Microscopic evaluations were conducted on selected rock samples from the first phase. The near wellbore plugging effects of the LCM fluid was investigated and reported in section 5.3.5. The results from the second phase (45 experiments) are presented from section 5.3.6 to 5.3.10, while their statistical analyses are presented in subsection 5.3.11. The experiments in the second phase were performed

at 220°F with varying rotary speeds (30, 70, and 110 rpm) and $CaCO_3$ concentrations (30, 55, and 80 lb/bbl).

5.3.1 Dynamic Drilling Fluids Filtration with No LCM Fluid (Phase One)

The dynamic filtrate loss profiles from the experiments with the base fluid are shown in Figure 5.20 for five lithologies. A notable observation is the fluid loss/filtrate breakthrough time. In this study, the breakthrough time is defined as the time taken before a significant fluid loss/filtrate value is recorded after attaining experimental conditions (differential pressure, temperature, and rotary speed). This is similar to the spurt loss time of 10 second recorded in filter press tests with ceramic filter disks and filter papers. The fluid loss/filtrate breakthrough time in rocks is largely influenced by rock permeability, porosity, temperature, rotary speed, bridging solid cluster mechanism, and rock sample heterogeneity. It is worthy to note that for the same experimental conditions, each of the rocks had different filtrate breakthrough times, spurt loss patterns, and cumulative dynamic filtrate loss profiles.

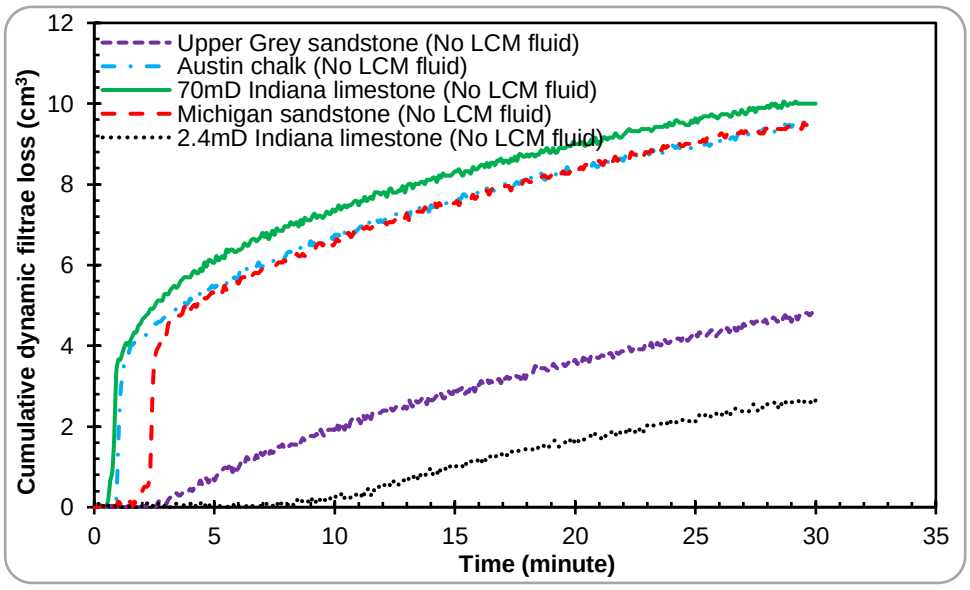

Figure 5.20: Dynamic cumulative filtrate loss profiles from a base fluid (no LCM) on different lithologies at 120°F, 70RPM, and 100 psi

These filtrate loss patterns are controlled by the lithology complexities. Three of the lithologies (70mD Indiana limestone, Michigan sandstone, and Austin chalk) showed spurt invasion (up to 4 cm^3) after filtrate breakthrough followed by steady state filtration. The 70 mD Indiana limestone showed the first spurt invasion (after 45 seconds) and the largest filtrate profile/cumulative value (10.052 cm^3). The spurt invasion in Michigan sandstone was recorded after 1 minute 50 seconds while the spurt invasion in Austin chalk was recorded after 50 seconds. Although, the spurt invasions from these two rocks were approximately 1 minute apart, an interesting observation is that their steady state profiles merged together after 3 minutes 30 seconds with an average difference that is less than 1 % in their profiles and cumulative value.

Upper Grey sandstone and 2.4 mD Indiana limestone did not show spurt invasion but rather began with the steady state mud filtration. The 2.4 mD Indiana limestone had the lowest filtrate value (2.655 cm^3) followed by the Upper Grey sandstone (4.858 cm^3). Considering that the temperature, rotary speed, and bridging solid cluster mechanism (barite) are constant, the only factors that are responsible for the profiles in Figure 5.20 are the porosity, permeability, and heterogeneity of the rocks. Comparing the sandstones, it is obvious that the low permeability of Upper Grey sandstone is responsible for the reduced filtrate loss which is 51.7 % less than the value from Michigan sandstone.

The permeabilities of the Indiana limestones are responsible for the huge gap in their dynamic filtrate loss profiles. Low permeability supports effective particle plugging within the pore throats and tortuous pathways in the rocks. In addition, the tortuosity of these rocks appeals to be a plausible mechanism that affects fluid/filtrate breakthrough time and overall filtrate profile. Tortuosity is used to describe the ease of a fluid flow path, and it's often linked to the permeability of a formation. The order of decrease in dynamic filtrate loss from the highest to lowest is: 70 mD

Indiana limestone > Michigan sandstone > Austin chalk > Upper Grey sandstone > 2.4 mD Indiana limestone. The gap in values between the first three rocks and last two rocks is a testament to the importance of rock permeability and porosity in dynamic fluid loss and filtration.

5.3.2 Dynamic Drilling Fluids Filtration with LCM Fluid (Phase One)

The dynamic filtrate loss profiles from the experiments with the LCM fluid sample 2 are shown in Figure 5.21 for five lithologies. A general observation that the cumulative dynamic filtrate loss for all the rock samples decreased. An interesting observation is that spurt invasion was not recorded and all the experiments with this fluid sample began with the steady state filtration. This observation was particularly noted for 70 mD Indiana limestone, Michigan sandstone, and Austin chalk (compared to the profiles in Figure 5.20 for the same conditions: temperature, rotary speed, pressure, and rock type). Furthermore, the filtrate breakthrough times for these three rocks increased by more than half compared to the times in Figure 5.20. The filtrate breakthrough times for Upper Grey sandstone and 2.4 mD Indiana limestone were also increased.

The practical implication of these observations is that for the experimental conditions, the bridging solid cluster mechanism of $CaCO_3$ combined with barite showed effective internal and external filter cake evolution which contributes to the reduction of particle and mud filtrate cross-flow. The order of decrease in dynamic filtrate loss from the highest to lowest is: 70 mD Indiana limestone > Austin chalk > Michigan sandstone > Upper Grey sandstone > 2.4 mD Indiana limestone. This is similar to the order in the preceding section, with the exception of Austin chalk and Michigan sandstone whose profiles and values were less than 1% different. This is a proof of the consistency in experimental conditions and heterogeneity of the rock samples.

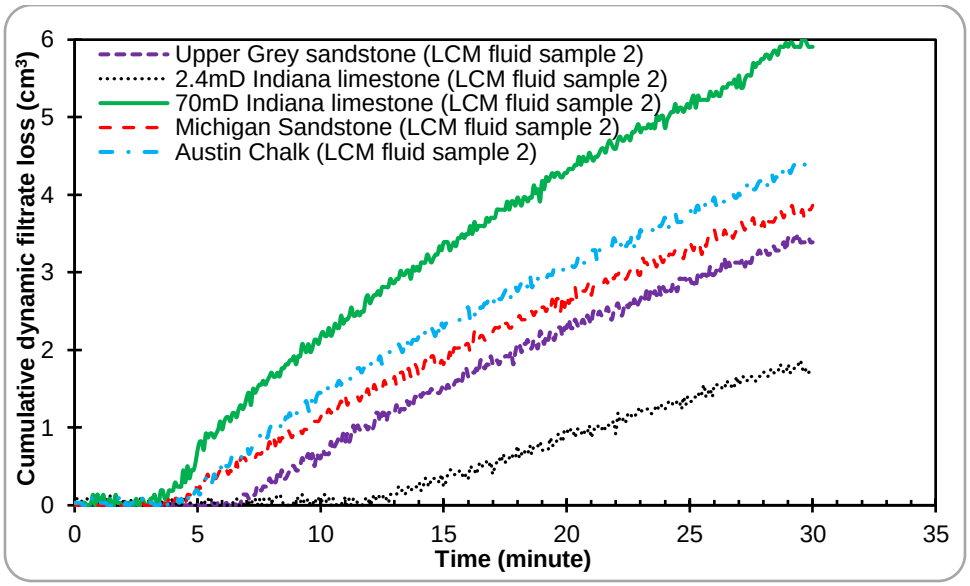

Figure 5.21: Dynamic cumulative filtrate loss profiles from a $CaCO_3$ fluid on different lithologies at 120°F, 70RPM, and 100 psi

The LCM effect is also observed in the difference between the filtrate values from similar lithology. The percentage decrease in dynamic cumulative filtrate loss shifting from high-permeability Michigan sandstone to low-permeability Upper Grey sandstone is 12.3 % (compared to 51.7 % with "no LCM" fluid). The percentage decrease in dynamic cumulative filtrate loss shifting from 70mD Indiana limestone to 2.4 mD Indiana limestone is 68.9 % (compared to 73.5 % with "no LCM" fluid). A petrographic study was conducted by Churcher et al. (1991) to differentiate the low-permeability Indiana limestone (2.4 mD) from the high-permeability Indiana limestone (2.4 mD). The authors claimed that the two factors that distinguishes both rocks are the amount of cementing calcite and degree of oxidation. The 2.4 mD Indiana limestone is highly cemented and this is responsible for its low permeability. The low cumulative filtrate loss values observed in this rock can also be related to poor interconnectivity of the interstitial pore spaces. Therefore, using both fluid formulations, cumulative dynamic filtrate loss is significantly lower in the 2.4 mD Indiana Limestone. This clearly defines the role of limestone rock permeability and heterogeneity in drilling fluid loss and filtration.

The profiles from Austin chalk reveals that it has the third (less than 1 % different from the second) and second highest cumulative filtrate values for the base fluid (no LCM) and LCM fluid respectively. In this study, Austin chalk (3 mD) and 2.4 mD Indiana limestone were the low-permeability carbonate rocks. Using both fluid formulations, the cumulative dynamic filtrate loss values from the 2.4 mD Indiana limestones were significantly lower than the values from the Austin chalk rocks. This difference in dynamic filtrate loss profiles and values lie in their grain structure, orientation, and porosity. The minerology of Austin chalk which consists of interbedded and recrystallized chalks and marls suggests that the pore constrictions are highly connected (31.99 % porosity compared to 14.23 % porosity of 2.4 mD Indiana limestone). The spurt invasion and early filtrate breakthrough with the base fluid also corroborates its high porosity. In addition, Austin chalk is a depleted formation, and a previous field study also showed that it is naturally fractured (Shelkholeslami et al. 1991). Therefore, high porosity, intergranular grain structure, and presence of natural fractures in this rock compensates for its low permeability which results in high fluid loss and filtration.

5.3.3 Comparison of Dynamic Drilling Fluid Filtration from Phase One

In this section, the overall effects of rock permeability, porosity, rock type, homogenous porous media, and LCM are further discussed. Figure 5.22 juxtaposes the results of all cumulative dynamic filtrate losses from the rock samples and a constant pore throat diameter ceramic filter tube. Sample size of two was used which implies that the average of two experiments under the same condition is what is represented in this figure. The figure shows that the lowest amount of filtrate was collected in the 2.4 mD Indiana limestone because of its low permeability and porosity. The 70 mD Indiana limestone had the highest filtrate loss using both fluid formulations. Although, the filtrate losses from the base fluid (no LCM) and LCM-fluid sample 2 experiments in 70 mD

Indiana limestone were 5.5 % and 55.5 % greater than the values from 350 mD Michigan sandstone (highest permeability) respectively, 70 mD is five times less than the permeability of Michigan sandstone. This may not be surprising because of the variation in rock mineralogy, grain network structure, and cementation. The petrographic study carried out by Churcher et al. (1991) suggests that high-permeability Indiana limestones experienced more chemical weathering during the sedimentary process. These weathering processes, secondary solution, and recrystallization resulted into natural cavities, channels, and vuggy pores within this limestone. These features which are absent in sandstones are plausible contributions to the overall high cumulative filtrate loss recorded in the 70 mD Indiana limestone samples.

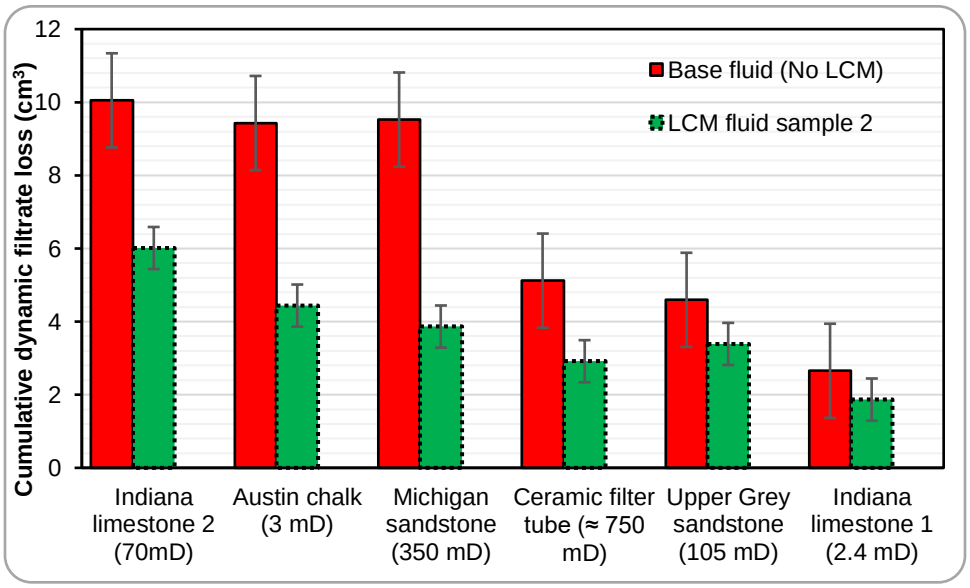

Figure 5.22: General comparison of the cumulative dynamic filtrate losses from the first phase of stage two experiments.

In addition, the invasion rate in the 70 mD Indiana limestone was profiled and the results show that the critical invasion rate did not appear within the 30-minutes of filtrate collection using the two fluid samples. The critical invasion rate is the point at which the rate of fluid particle deposition and erosion rates come to an equilibrium (Tien et al. 1997; Allen et al. 1991). The longer it takes

the critical invasion rate to appear, the more drilling fluid and filtrate are lost to the formation. This pattern was also observed in other high permeability/porosity rocks.

Another important observation in Figure 5.22 is the comparison of the results from the rock samples with ceramic filter tube. The choice of sandstone and carbonate rocks were made to capture a close-to-real field dynamic fluid filtrate profiles and the bridging effects of fluid particles that cover a wide range of permeability in different lithologies. The mineral compositions and pore structures of the actual rocks cannot be compared with a ceramic filter tube. It's important to note that all the first phase experiments in stage two were performed under the same laboratory conditions and procedures. The average pore throat diameter of the ceramic filter tubes whose results are shown in Figure 5.22 is 5μm which is approximately 750 mD according to Table 3.10 (old mercury). As shown in this figure, the values obtained with the ceramic filter tubes is closest to the values from Upper Grey sandstone. But the permeability of Upper Grey sandstone is up to seven times less than the approximated permeability value of the ceramic filter tube. Furthermore, the results from Michigan sandstone and 70 mD Indiana limestone are greater than the results from the filter tubes by up to half. Common industry practice often relies on filtrate loss test results from filter papers and/or ceramic filter discs/tubes. While ceramic filter tubes were used in the stage one experiments to provide the significance and direction of the critical factors affecting mud/filtrate loss, they cannot represent the true porous media complexities in actual rocks during fluid loss and filtration.

The overall effect of using $CaCO_3$ can be quantified further from the data in Figure 5.22. It is worthy to note that there is more variation in the cumulative filtrate loss values from the base fluid (no LCM), while these variations were observed to have been reduced with the LCM fluid sample 2. Statistically, the standard deviation (a measure of variance) of the cumulative filtrate

losses from the base fluid is 3.154, while the standard deviation of the cumulative filtrate losses from the LCM fluid sample 2 is 1.412. This indicates that the proactive use of $CaCO_3$ is approximately twice more effective in controlling dynamic mud filtrate loss in different rock types and permeabilities. Furthermore, the LCM effect on filter cake evolution was more evident in reducing the filtrate losses in high permeability and/or high porosity rocks (Michigan sandstone, 70mD Indiana limestone, and Austin chalk). This observation is supported by Salehi and Kiran (2016). Furthermore, the filtration experiments performed by Dorman et al. (2015) on low-permeability core samples suggests that it is irrelevant to apply the classic bridging theory in designing drilling fluids for low-permeability rocks. They also recommended the use of Nano-particle bridging solids to achieve an effective internal filter cake in low-permeability rocks. Although, the classical bridging theory was not considered in this study, experimental results from phase one stage two shows minimal LCM effect in reducing filtrate loss in low-permeability/low-porosity rocks (2.4 mD Indiana limestone and Upper Grey sandstone). Notwithstanding, this is not completely true for low-permeability/high-porosity Austin chalk. In practical application, rock permeability and porosity should be considered side-by-side in developing a drilling fluid recipe that is geared towards fluid/filtrate loss reduction as well as wellbore strengthening purposes.

5.3.4 Filter Cake Plastering Effect in Sandstone (Phase One)

Drilling fluid plastering is an important property because it reveals the mechanical properties of filter cake and impedes the absolute open hole flow possibilities in a reservoir section. Filter cake plastering effects have been attributed to the increase in wellbore fracturing pressure and successful wellbore strengthening observed in casing while drilling application (Salehi et al. 2013; Rosenberg and Gala 2012). The authors define this phenomenon as the smearing of drilling fluids solids to the wellbore pore throats and fractures, creating a thin and firm external filter cake layer.

In most of the field studies, this phenomenon is attributed to the small annular clearance and constant casing-wellbore contact which helps to repair the wellbore.

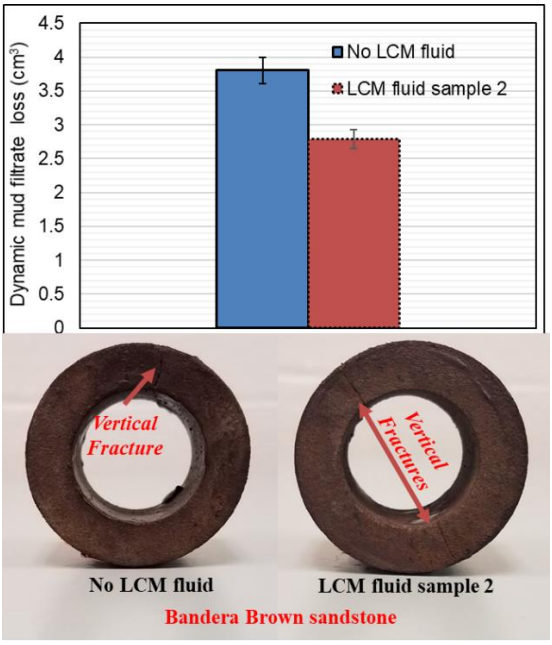

Figure 5.23: Filter cake plastering effects in Bandera Brown sandstone

Figure 5.23 is used to describe filter cake plastering which was observed in Bandera Brown sandstone. During dynamic filtrate loss experiments with this rock, vertical fractures were created unintentionally. First, the base fluid (no LCM) experiment was conducted and one vertical fracture was created. The LCM fluid sample 2 was used to perform the second experiment on another Bandera Brown sample from the same block and two vertical fractures were created. It was expected that the amount of mud filtrate collected after fracture initiation and sealing be more with the two-vertical fracture rock sample. However, the LCM fluid sample 2 showed cumulative filtrate of 2.786 cm^3 with two vertical fractures created in the rock sample. Comparing this value to the base fluid cumulative filtrate (3.803 cm^3) with one vertical fracture, a cautious conclusion that fracture sealing was more effective with the LCM fluid sample 2 can be drawn. This is resulting from the high surface area of active calcium carbonate that enhanced the fluids particle

interaction among themselves and the walls of the fractures.

The filter cake around the wall of the rock samples and inside the fractures has properties that enable them to act as a stable plug to impede subsequent mud and filtrate loss. Those properties include thickness, cohesion, and tightness. LCMs are known for their influence on these filter cake properties. Filter cakes are elastic in nature and can undergo plastic deformation under a shear failure condition. The cohesive property of a filter cake is sometimes referred to as compressive strength, and the primary source of filter cake's cohesive strength is *particle to particle* contact (Cook et al. 2016). Ezeakacha et al. (2017) referred to this as *particle-particle* and *particle-pore interlocking*. Their study revealed that the interlocking effect serves to increase the cohesive strength of the filter cake for resisting the erosive shear stress that is caused by the dynamic circulating drilling fluid. The results and analyses from section 5.3.3 and 5.3.4 are testament to the positive effect of filter cake evolution from an LCM fluid formulation. These, in part, can be used to confirm pore-scale wellbore strengthening from filter cake evolution which is the second hypothesis of this study.

5.3.5 Microscopic Evaluation of Filter Cake Evolution (Phase One)

In this section, scanning electron microscope (SEM) images and elemental maps from energy dispersive X-ray spectroscopy (EDS) are presented. These microscopic evaluations were conducted to verify the near-wellbore pore plugging effect of the LCM fluid sample 2. Three rock samples from the experiments with the LCM fluid sample 2 were investigated and they are: Michigan sandstone, 70 mD Indiana limestone, and Austin chalk. The investigations were conducted on three regions. The first region is the lateral cross-section area that is near the inner diameter of the wellbore (45 μm). The second region is in the middle of the lateral cross-section while the third region is the lateral cross-section area that is close to the outer diameter of the

wellbore. Only the results from the near-wellbore region (first region) are reported in this section because there were no traces of mud particles and key elements of interest in the second and third regions.

5.3.5.1 Microscopic Evaluation of Filter Cake Evolution in Sandstone

Figure 5.24 shows the grey scale SEM images of Michigan sandstone before and after internal filter cake evolution. Figure 5.24 (right) shows particle deposition in the pore throats and a distinction between the sandstone grains and bridging solids. The thick-red arrow pointing downwards indicates the lateral cross-section of filtrate and particle flow from the inner diameter of the sample to the outer diameter. A higher magnification of the grey scale image revealed that the filter cake solids were composed of small and large particles up to 100 µm. It should be noted that the grain morphology and pore structure of Michigan sandstone are contributing factors to effective filter cake evolution. The images suggest good particle-pore and particle-particle interlocking mechanisms. This refers to the cohesive interaction between various filter cake particles and rock grain surface because of the difference in material roughness, irregularity, and surface area (Ezeakacha et al. 2017 and Cook et al. 2016).

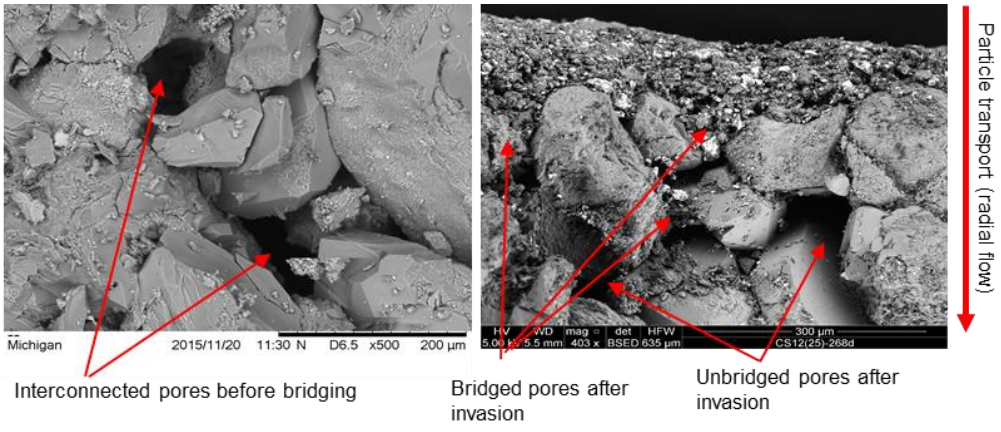

Figure 5.24: Grey scale SEM images before (left) and after (right) filter cake evolution in Michigan sandstone

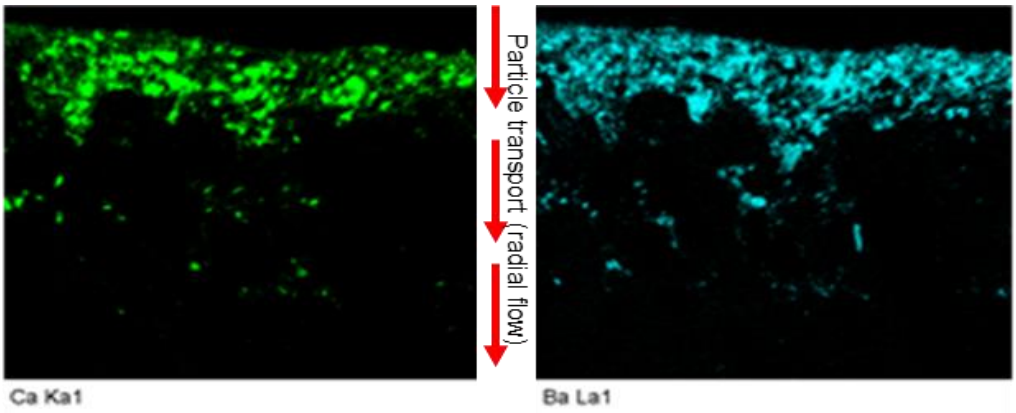

Figure 5.25: Calcium and Barium elemental maps representing bridging solid evolution in Michigan sandstone

In addition to the grey scale SEM images, several elemental maps (Silicon, Carbon, Calcium, Barium, Ytterbium, Sulphur, Iron, Potassium, Aluminum, Zine, and Oxygen) were obtained from the EDS investigation (Appendix B). While some of these elements are typical constituent elements in Michigan sandstone (Silicon and Zine), others such as Calcium and Ytterbium are constituent elements in the carbonate rocks studied. However, the focus is on Calcium and Barium. This is because they are the major constituent elements in the LCM (calcium carbonate, $CaCO_3$) and weighting agent (barite, $BaSO_4$) which makes up to 82.8% of the solids in the filter cake. Moreover, barite does not only serve as a weighting material, it provides additional plugging support by bridging the pore throats of a rock during fluid loss. The elemental maps shown in Figure 5.25 corroborates the grey scale image shown in Figure 5.24 (right). They show an even distribution of Calcium and Barium which appear to be in high concentrations and are a good representation of the bridging solids in the near-wellbore region. Traces of these particles are seen to deplete as the lateral cross-section of investigation increases. The implication is that an effective filter cake was formed at the experimental conditions, preventing further invasion of ultra-fine mud particles and filtrate. This translates to a reduction in the mud/filtrate loss and wellbore strengthening by the filter cake.

5.3.5.2 Microscopic Evaluation of Filter Cake Evolution in Limestone

Figure 5.26 shows the grey scale SEM images of Indiana limestone before and after filter cake evolution with the LCM fluid sample 2. The figure to the right shows small and large bridging particle deposition around the top right section. An unbridged pore can be visually observed from this image. The elemental maps shown in Figure 5.27 (left) indicates spatial distribution of Calcium. It is somewhat difficult to distinguish between the Calcium element from the LCM and the constituent Calcium element from the Indiana limestone grains. However, the Barium elemental map in Figure 5.27 (right) confirms the location and distribution of Calcium from the LCM since both materials were homogenized in the fluid. This location also corresponds to the location on the grey scale image (Figure 5.26) where discrete particles of both calcium carbonate and barite were observed to have been deposited.

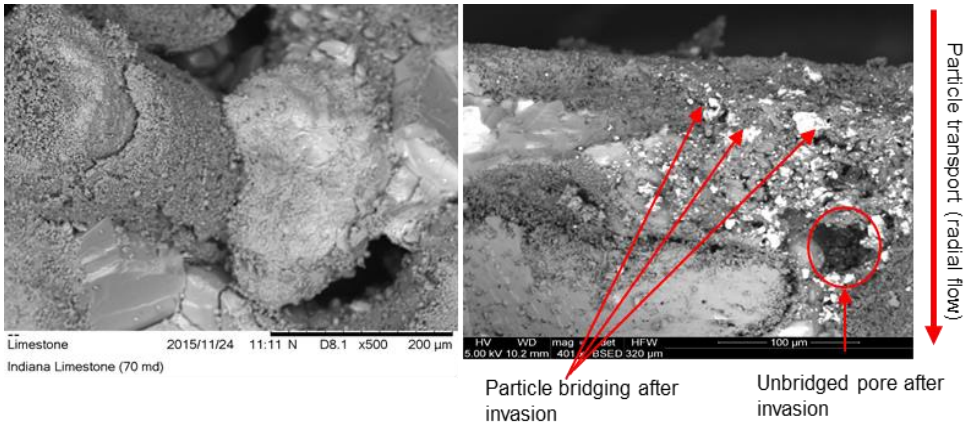

Figure 5.26: Grey scale images before (left) and after (right) filter cake evolution in Indiana limestone

Unlike Michigan sandstone, qualitative observations indicate that filter cake evolution in this rock sample was not completely uniform. This ties back to the minerology of the Indiana limestone. Particle parking and agglomeration appeared not to have been effective; thus, channels within the cake particles and pore throats permitted more filtrate influx. This is a plausible reason for higher dynamic filtrate loss value in this rock compared to Michigan sandstone under the same

experimental conditions. The minerology of Indiana limestone suggests that the pore throats are not often interconnected as sandstones. The dark areas from the Calcium elemental map which do not correspond with the Barium map are thought to be uneven surfaces which may be solution channels or a vuggy pore that have not been bridged.

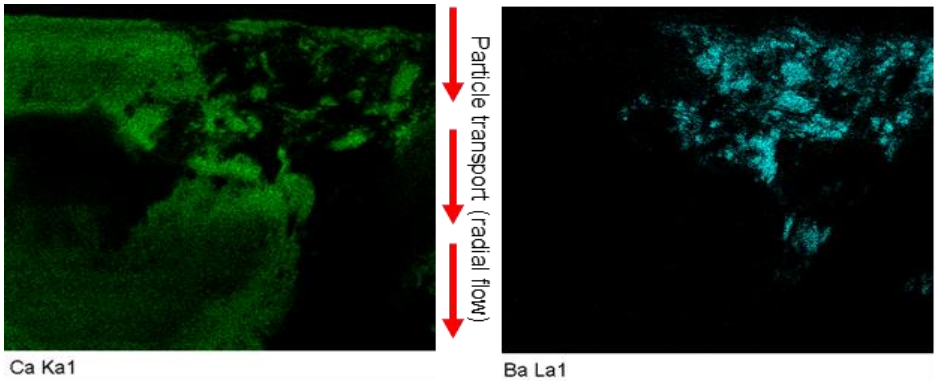

Figure 5.27: Calcium and barium elemental maps representing bridging solid evolution in Indiana limestone

5.3.5.3 Microscopic Evaluation of Filter Cake Evolution in Chalk

The figures in Figure 5.28 are the grey scale SEM images of Austin chalk. The morphology of the rock shows rough and irregular surfaces. The area under investigation revealed uneven distribution of rock grains and bridging solids. Unlike Michigan sandstone and Indiana limestone, the grey scale image after filtrate loss experiment does not clearly reveal particle bridging.

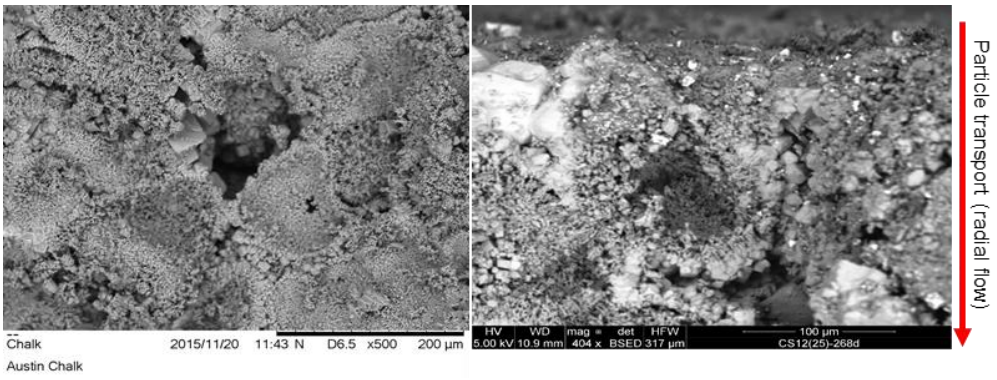

Figure 5.28: Grey scale images before (left) and after (right) filter cake evolution in Austin chalk

The elemental map in Figure 5.29 (left) also shows a combination of the Calcium from the LCM and chalk grains. However, Figure 5.29 (right) reveals two concentration areas of Barium. The high concentration areas are where the cyan color is deep, and particles appear to be large (from top left area down through the right side of a large internal channel). The low concentration areas are depicted by the faint cyan colored dots, sparsely distributed like the Calcium elemental map. These maps show more depth penetration of mud particles in this rock compared to Michigan sandstone and Indiana limestone. Although Austin chalk has low permeability, the penetration depth of particles for the region under investigation is a testament to the high porosity of the rock. Considering that mud particles and key elements (Calcium and Barium) were not observed in region two and three, a cautious conclusion can be made that the penetration depth of particles in Austin chalk is in support of wellbore strengthening by filter cake rather than formation damage. The sum spectrum graphs of all the region ones are shown in Appendix B.

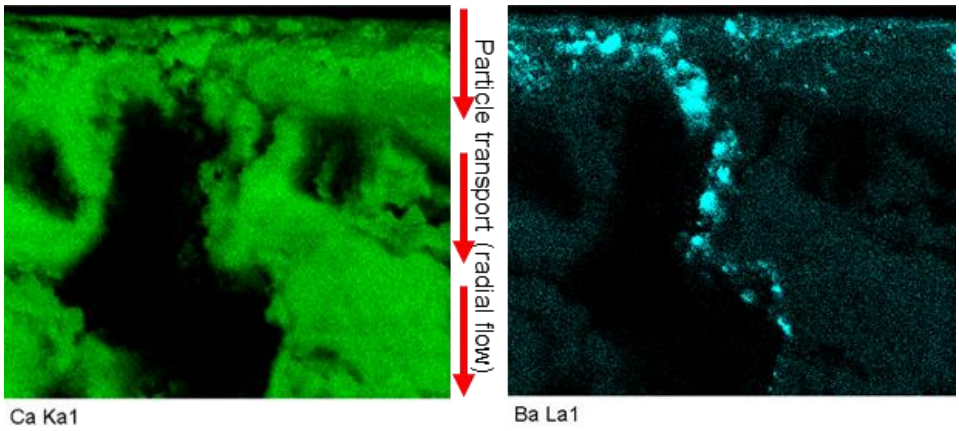

Figure 5.29: Calcium and barium elemental maps representing bridging solid evolution in Austin chalk

5.3.6 Dynamic Drilling Fluids Filtration in Michigan Sandstone (Phase Two)

The dynamic filtrate loss profiles in Michigan sandstone are provided in this section. The permeability and porosity of this sandstone are 350 mD and 19.44 % respectively. The phase two experiments were conducted at different rotary speeds and $CaCO_3$ concentrations. Figure 5.30

shows the filtrate loss profiles in Michigan sandstone when 30 lb/bbl $CaCO_3$ WBM is subjected to different rotary speeds, 220°F, and 100 psi. At 30 and 70 rpm's, spurt invasion was not recorded, and the profiles began with steady state filtration. The cumulative filtrate loss at 30 rpm was greater than the value at 70 rpm by 3.101 cm^3. This can be attributed to the heterogeneity of the rock. The effect of elevated rotary speed is evident in the profile at 110 rpm. 16 cm^3 spurt loss was recorded within the first 30 seconds. The cumulative filtrate loss at this rotary speed was greater than the values at 30 rpm and 70 rpm by 15.77 cm^3 and 18.76 cm^3 respectively. Therefore, with 30 lb/bbl $CaCO_3$ an increase in rotary speed tends to increase dynamic filtrate loss.

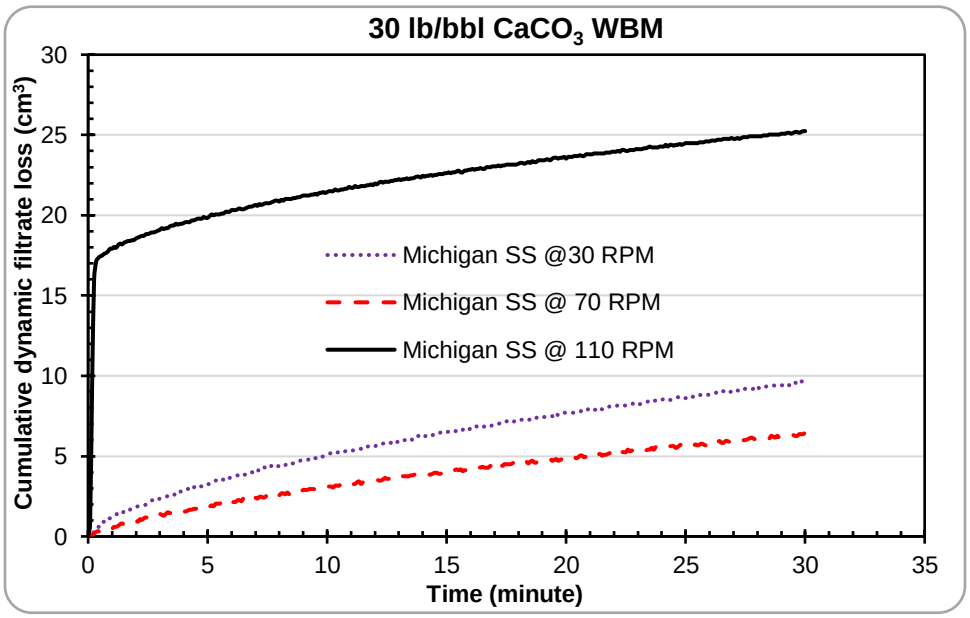

Figure 5.30: Dynamic filtrate loss profiles in Michigan sandstone for 30 lb/bbl $CaCO_3$ WBM

Figure 5.31 shows the filtrate loss profiles in Michigan sandstone when 55 lb/bbl $CaCO_3$ WBM is subjected to different rotary speeds, 220°F, and 100 psi. The filtration profile at 30 rpm had the largest spurt loss (4 cm^3) and cumulative loss (9.148 cm^3). Compared to the same rotary speed in Figure 5.30 with 30 lb/bbl, about the same cumulative filtrate loss (9.469 cm^3) was obtained, except that no significant spurt was not recorded. Therefore, it is possible to infer that at 30 rpm

and other experimental conditions, an increase in $CaCO_3$ from 30 lb/bbl to 55 lb/bbl did not have any effect in reducing dynamic filtrate loss in Michigan sandstone. Going back to Figure 5.31, the filtrate loss profile at 110 rpm showed spurt invasion (2 cm^3) and greater cumulative filtrate loss compared to the value at 70 rpm. This trend was expected. However, considering the profile and greater cumulative filtrate at 30 rpm, compared to the profiles and cumulative filtrates at 70 and 110 rpm's, one plausible explanation is the heterogeneity of the thick-walled cylindrical cores.

Comparing the cumulative values in Figure 5.30 (6.368 cm^3) and Figure 5.31 (6.956 cm^3) at 70 rpm, it is possible to infer that an increase in the $CaCO_3$ from 30 lb/bbl to 55 lb/bbl at the experimental conditions had no effect in reducing dynamic filtrate loss in Michigan sandstone. However, recall that in Figure 5.21, LCM fluid sample 2 (55 lb/bbl $CaCO_3$) was subjected to dynamic mud filtration in Michigan sandstone at 120^{o}F and 70 rpm. The cumulative filtrate loss was 3.865 cm^3 and for the same conditions but elevated temperature (220^{o}F), the filtrate loss was 6.956 cm^3. This implies that temperature significantly increased mud loss and filtrate up to half. This was predicted from the viscosity profiles of the samples in Figure 5.2 and Figure 5.3 where the consistency in index of the LCM fluid sample 2 decreased by 85 % at 210^{o}F. The analytical study performed by Lavrov and Tronvoll (2004) supports this observation (decrease in consistency index of a Power law fluid results to an increase the mud loss rate).

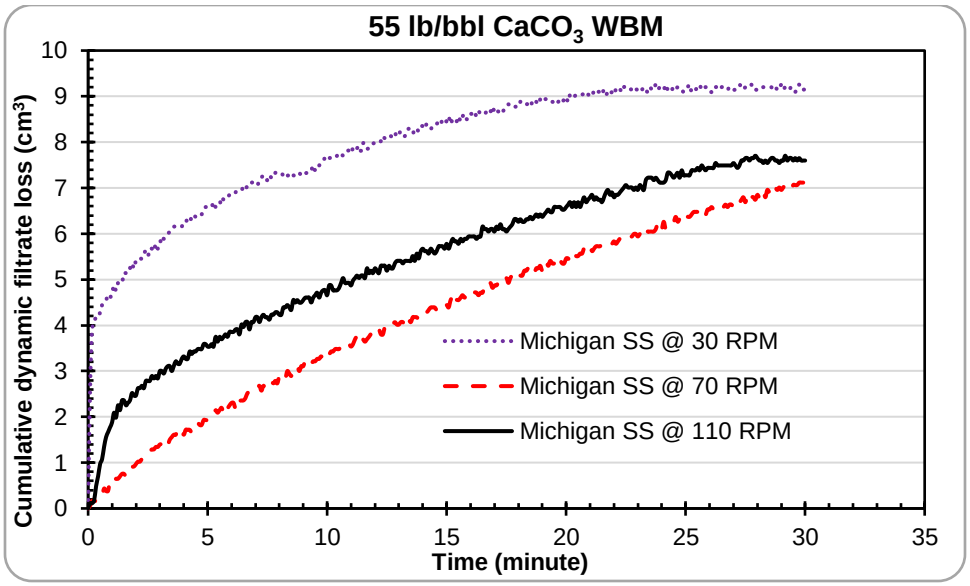

Figure 5.31: Dynamic filtrate loss profiles in Michigan sandstone for 55 lb/bbl $CaCO_3$ WBM

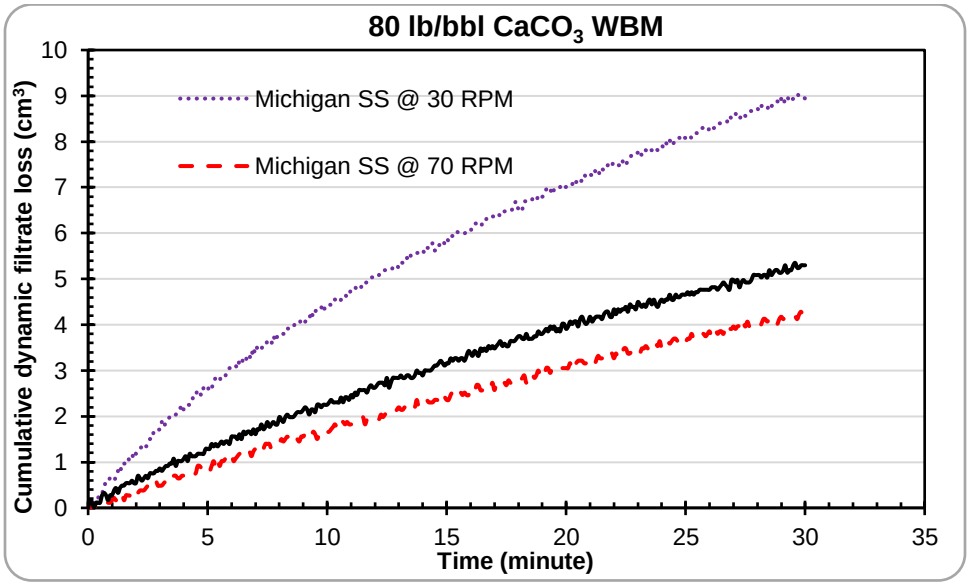

Figure 5.32: Dynamic filtrate loss profiles in Michigan sandstone for 80 lb/bbl $CaCO_3$ WBM

Figure 5.32 shows the filtrate loss profiles in Michigan sandstone when 80 lb/bbl $CaCO_3$ WBM is subjected to different rotary speeds, 220°F, and 100 psi. No spurt invasion was recorded in all the tests which is a positive indication of an increase in LCM concentration. However, the same trend in Figure 5.31 is also observed and the experiment at 30 rpm showed the highest cumulative filtrate loss (8.934 cm^3). The cumulative filtrate loss at 110 rpm (5.245 cm^3) was greater than the value at

70 rpm (4.132 cm^3). This is an indication that an increase in rotary speed tends to increase dynamic filtrate loss. But rock heterogeneity is a plausible explanation for higher losses at 30 rpm in Figure 5.32 as well as Figure 5.31.

The cumulative losses at the same rotary speed (30 rpm) in Figure 5.30 with 30 lb/bbl $CaCO_3$ (9.148 cm^3), Figure 5.31 with 55 lb/bbl $CaCO_3$ (9.469 cm^3), and Figure 5.32 with 80 lb/bbl (8.934 cm3) are compared. A cautious conclusion can be made that at an increase in $CaCO_3$ concentration from 30 lb/bbl to 80 lb/bbl has little to no effect in reducing dynamic drilling fluids filtration in Michigan sandstone at 30 rpm and 220°F. At 70 rpm, the cumulative filtrate losses in Figure 5.30 (6.368 cm^3), Figure 5.31 (6.956 cm^3), and Figure 5.32 (4.132 cm^3) are compared. The results show that an increase in $CaCO_3$ concentration from 30 lb/bbl to 80 lb/bbl tends to decrease dynamic filtrate loss in Michigan sandstone at 70 rpm and 220°F. At 110 rpm, the cumulative filtrate losses in Figure 5.30 (25.239 cm^3), Figure 5.31 (7.598 cm^3), and Figure 5.32 (5.245 cm^3) are compared. The results show that an increase in $CaCO_3$ concentration from 30 lb/bbl to 80 lb/bbl tends to decrease dynamic filtrate loss in Michigan sandstone at 110 rpm, 220°F, and 100 psi.

5.3.7 Dynamic Drilling Fluids Filtration in Buff Berea Sandstone (Phase Two)

The dynamic filtrate loss profiles in Buff Berea sandstone are provided and discussed in this section. The permeability and porosity of this sandstone are 350 mD and 18.5 % respectively. Figure 5.33 shows the filtrate loss profiles in Buff Berea sandstone when 30 lb/bbl $CaCO_3$ WBM is subjected to different rotary speeds and 220°F. The figure clearly shows that as the rotary speed increases, the filtrate loss increases. The trends are similar to those in Figure 5.30 (Michigan sandstone) especially with the large distinction between the profile at 110 rpm (with up to 15 cm^3 spurt loss and more 22 cm^3 cumulative filtrate loss) and the profiles at 30 rpm and 70 rpm.

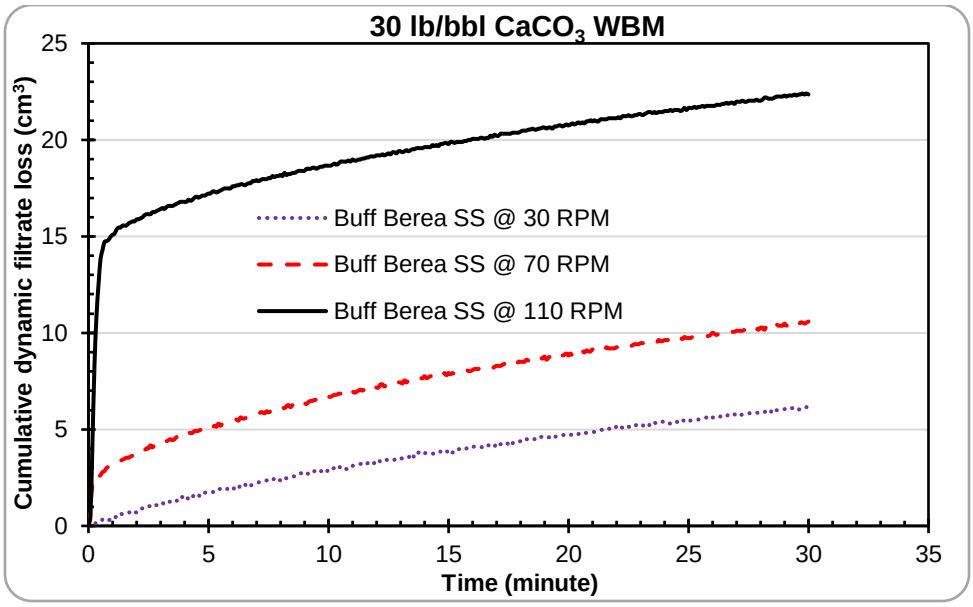

Figure 5.33: Dynamic filtrate loss profiles in Buff Berea sandstone for 30 lb/bbl $CaCO_3$ WBM

Figure 5.34 shows the filtrate loss profiles in Buff Berea sandstone when 55 lb/bbl $CaCO_3$ WBM is subjected to different rotary speeds and 220°F. All the experiments had spurt losses and the experiment at 110 rpm deviated from the trend (increase in filtrate loss with an increase in rotary speed). This experiment had the lowest spurt and filtrate loss. Typically, the spurt invasion tends to detect how much cumulative filtrate will be obtained. Sample heterogeneity has been highlighted as a major factor that affects spurt loss, filtrate breakthrough time, and cumulative filtrate loss. The experiments with the 30 and 70 rpm had spurt losses of 8 cm^3 and 13.74 cm^3 respectively, while their respective cumulative filtrate losses were 16.6 cm^3 and 18 cm^3. Both experiments showed that an increase in rotary speed tends to increase filtrate loss.

It is worthy to note that the steady state filtration of the experiment at 70 rpm appeared to have plateaued after about 17.5 minutes. This implies that the critical invasion rate (the point at which fluid particle deposition and erosion rates on the external filter cake wall come to an equilibrium) described by Tien et al. (1997) and Allen et al. (1991) was attained after 17.5 minutes.

It is often difficult if not impossible to attain the critical invasion rate within 30 minutes. This is also a function of the rock properties and heterogeneity. Comparing the cumulative filtrate losses at the same rotary speed (30 rpm and 70 rpm) in Figure 5.33 and Figure 5.34, it can be observed that dynamic filtrate loss did not decrease with an increase in $CaCO_3$ from 30 lb/bbl to 55 lb/bbl. However, dynamic filtrate loss decreased for the 110 rpm experiments. Figure 5.35 shows dynamic filtrate loss profiles in Buff Berea sandstone when 80 lb/bbl $CaCO_3$ fluid is subjected to different rotary speeds and 220^{o}F. Using this LCM concentration, an increase in rotary speed appeared to have increased dynamic filtrate loss. Spurt invasion and cumulative loss were much worse at 110 rpm.

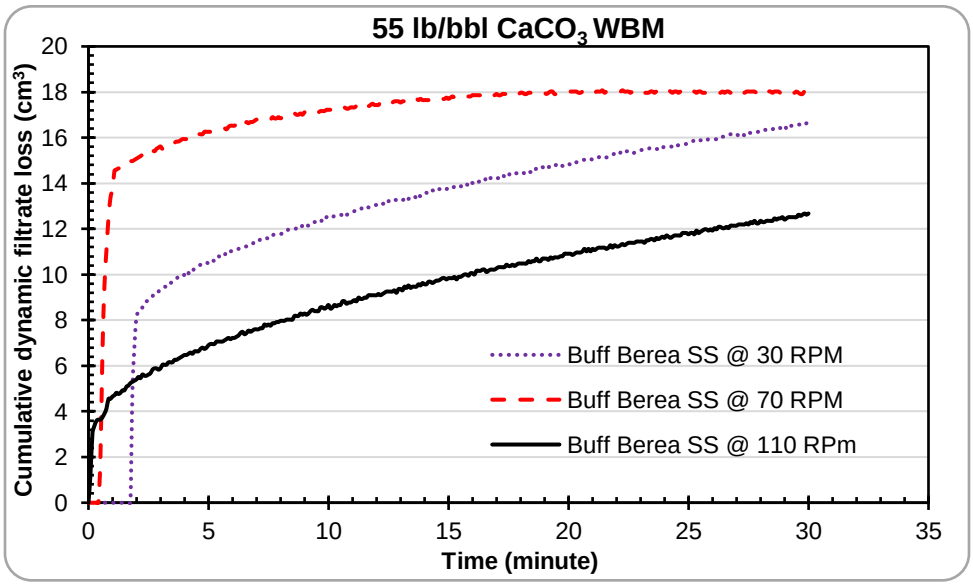

Figure 5.34: Dynamic filtrate loss profiles in Buff Berea sandstone for 55 lb/bbl $CaCO_3$ WBM

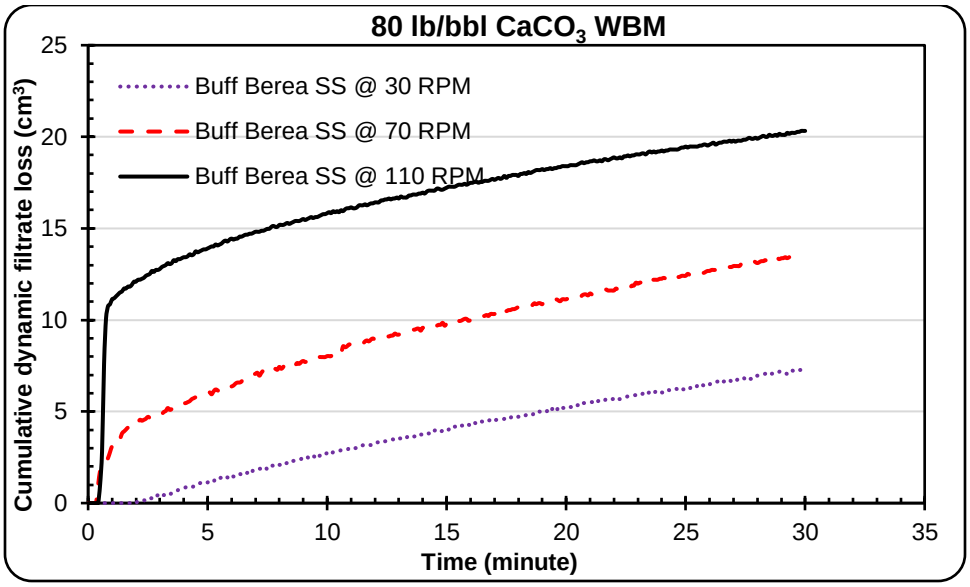

Figure 5.35: Dynamic filtrate loss profiles in Buff Berea sandstone for 80 lb/bbl $CaCO_3$ WBM

Comparing all the figures in this section, an increase in LCM concentration from 30 lb/bbl to 80 lb/bbl did not show a consistent decrease in dynamic filtrate loss at 30 rpm (6.154 cm^3 at 30 lb/bbl LCM, 16.632 cm^3 at 55 lb/bbl LCM, and 7.33 cm^3 at 80 lb/bbl LCM). The same trend is shown at 70 rpm (10.59 cm^3 at 30 lb/bbl LCM, 18 cm^3 at 55 lb/bbl LCM, and 13.47 cm^3 at 80 lb/bbl LCM) and at 110 rpm (22.352 cm^3 at 30 lb/bbl LCM, 12.676 cm^3 at 55 lb/bbl LCM, and 20.268 cm^3 at 80 lb/bbl LCM). Compared to Michigan sandstone, both sandstones have similar permeability, but a much consistent trend (change in filtrate loss with change in LCM concentration at specific rotary speeds) was observed in Michigan sandstone. This clearly shows the difference in the behavior of the two rocks. An increase in temperature also affects mud filtrate loss. Schembre and Kovscek (2005) reported that an increase in temperature causes a repulsion in the total particle to pore interactive forces. This repulsion does not allow filter cake particles to bond effectively with the pore throat walls, wellbore wall, and to themselves; thus, preventing them from forming effective internal and external filter cake layers. This phenomenon appears to have affected Buff Berea sandstone more than Michigan sandstone. For practical purposes and cost effectiveness, an

increase in $CaCO_3$ concentration beyond 55 lb/bbl may not always reduce dynamic fluid loss and filtrate in Buff Berea sandstone at an elevated temperature (220^oF) and varying rotary speeds up 110 rpm.

5.3.8 Dynamic Drilling Fluids Filtration in Upper Grey Sandstone (Phase Two)

The dynamic filtrate loss profiles in Upper Grey sandstone are provided and discussed in this section. The permeability and porosity of this sandstone are 105 mD and 17.65 % respectively. Figure 5.36 shows the filtrate loss profiles in Upper Grey sandstone when 30 lb/bbl $CaCO_3$ WBM is subjected to different rotary speeds and 220^oF. In this figure, the difference between the experiments at 30 rpm and 70 rpm is 0.214 cm^3 with the 30-rpm experiment being higher. The high spurt loss (10.85 cm3) and high cumulative filtrate loss (17.43 cm^3) at 110 rpm is a testament to the observation that an increase in rotary speed results to an increase in dynamic filtrate loss. The results from Upper Grey sandstone (Figure 5.36), Buff Berea sandstone (Figure 5.33), and Michigan sandstone (Figure 5.30) were compared for the same conditions. The comparison showed that dynamic filtrate loss values in Upper Grey sandstone are smaller than the values from Michigan and Buff Berea sandstones. A good explanation for this is that the permeability of Upper Grey sandstone is three times smaller than the permeabilities of Buff Berea and Michigan sandstones. The porosity is also smaller and may have contributed to the reduced filtrate loss.

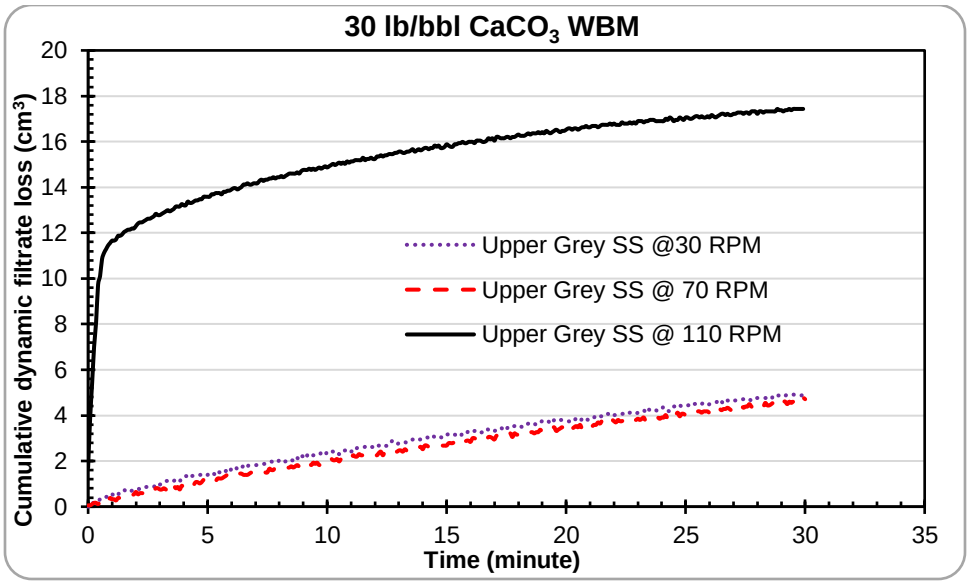

Figure 5.36: Dynamic filtrate loss profiles in Upper Grey sandstone for 30 lb/bbl $CaCO_3$ WBM

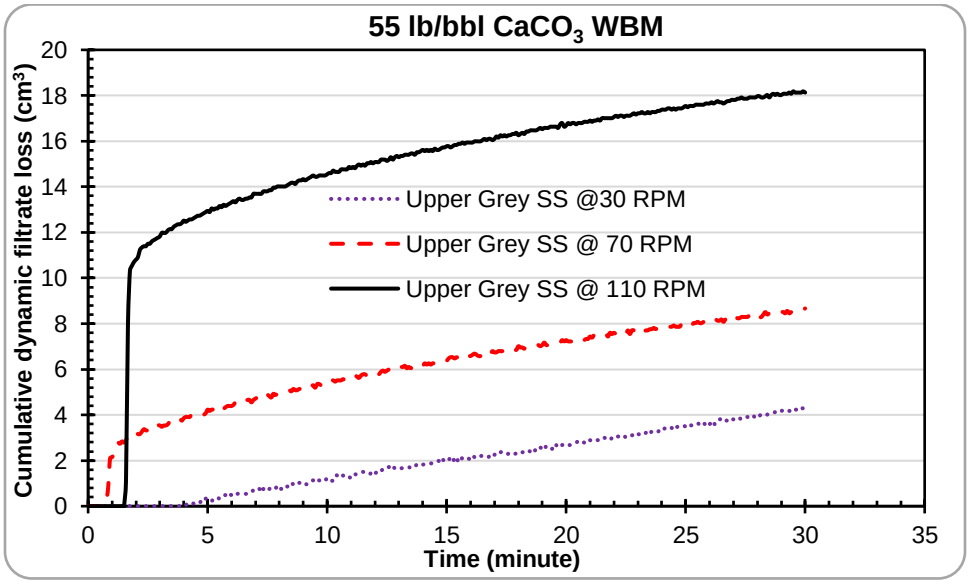

Figure 5.37: Dynamic filtrate loss profiles in Upper Grey sandstone for 55 lb/bbl $CaCO_3$ WBM

Figure 5.37 shows the filtrate loss profiles in Upper Grey sandstone when 55 lb/bbl $CaCO_3$ WBM is subjected to different rotary speeds and 220°F. An increase in the rotary speed corresponded to an increase in dynamic filtrate loss. Spurt losses were recorded for the 70 rpm and 110 rpm tests. The delay in filtrate in filtrate breakthrough compared to Figure 5.36 is attributed to the increase in LCM concentration. However, an increase in the LCM concentration from 30 to 55 lb/bbl did

not decrease cumulative filtrate loss in Upper Grey sandstone on the average. Recall that in Figure 5.21, LCM fluid sample 2 (55 lb/bbl $CaCO_3$) was subjected to dynamic fluid filtration in Upper Grey sandstone at 120^oF and 70 rpm. The cumulative filtrate loss was 3.389 cm^3 and for the same conditions but elevated temperature (220^oF), the filtrate loss was 4.282 cm^3. The temperature increase is the reason behind the increase in filtrate loss for the same conditions. At an elevated temperature, the property of bentonite which enables the material to form a gel is negatively impacted. Thus, particle packing from calcium carbonate and barite is not fully supported because of weak filter cake evolution from a poorly developed gel.

Figure 5.38 shows the filtrate loss profiles in Upper Grey sandstone when 80 lb/bbl $CaCO_3$ WBM is subjected to different rotary speeds and 220^oF. No spurt invasion was recorded in addition to the late filtrate breakthrough times. These are strong indications that the increased LCM concentration had an effect on the dynamic filtrate loss. The difference between the experiments at 30 rpm and 70 rpm is 0.175 cm^3 (with the 30-rpm experiment being higher). This trend is similar to the one in Figure 5.36 for the same rotary speeds. Although, there seem to be little to no difference in the cumulative filtrate loss at these rotary speeds with an increase in LCM concentration, a significant decrease in filtrate loss is shown at 110 rpm with the highest LCM concentration. In general, temperature, rotary speed, sandstone minerology (permeability and porosity), in this order (from high to low) are the controlling factors of dynamic mud loss and filtration in sandstones.

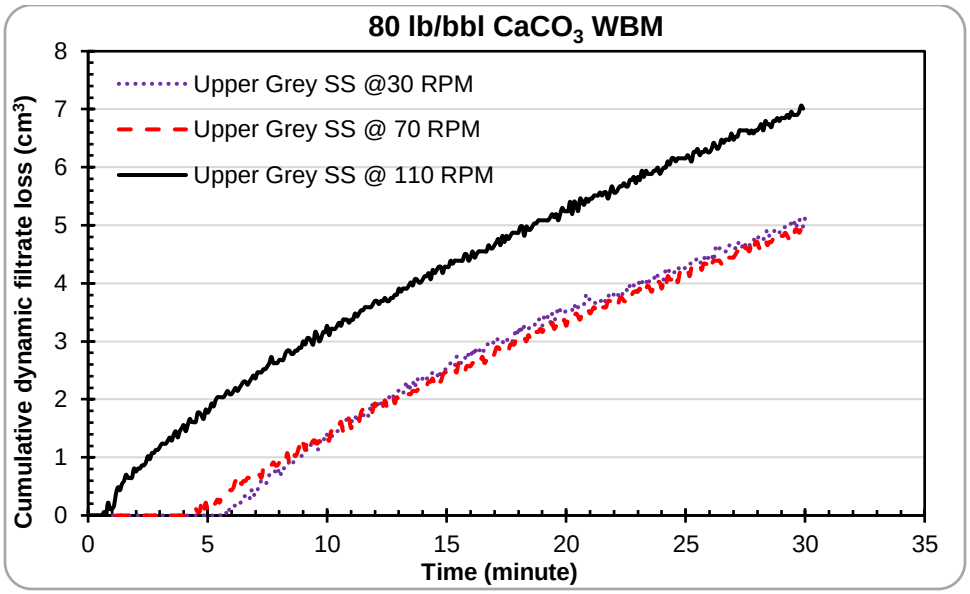

Figure 5.38: Dynamic filtrate loss profiles in Upper Grey sandstone for 80 lb/bbl $CaCO_3$ WBM

5.3.9 Dynamic Drilling Fluids Filtration in 70 mD Indiana Limestone (Phase Two)

In this section, the results from dynamic drilling fluids filtration experiments in Indiana limestone (70 mD) are presented. The porosity of this rock is 16.21 %. The profiles in Figure 5.39 shows that an increase in rotary speed from 30 rpm to 70 rpm results to an increase in cumulative filtrate loss from 12.46 cm^3 to 16.47 cm^3. The little spike in filtrate (experiment at 70 rpm) was because of pressure fluctuation during the test. The experiment at 110 rpm had the lowest filtrate loss (6.154 cm^3) with no significant spurt invasion. It is possible to attribute formation heterogeneity or inherent experiment error to this outcome. However, the same trend is also observed in Figure 5.40 with the 55 lb/bbl LCM WBM. In this figure, an increase in rotary speed from 30 rpm to 70 rpm corresponded to an increase in cumulative filtrate loss from 8.079 cm^3 to 11.019 cm^3, while 5.726 cm^3 was recorded as the cumulative filtrate loss for the 110-rpm experiment. From Figure 5.39 and Figure 5.40, it is observed that an increase in rotary speed beyond 70 rpm does not increase the filtrate loss, and a decrease in cumulative filtrate was recorded for all the rotary speeds, when the LCM concentration increases from 30 lb/bbl to 55 lb/bbl.

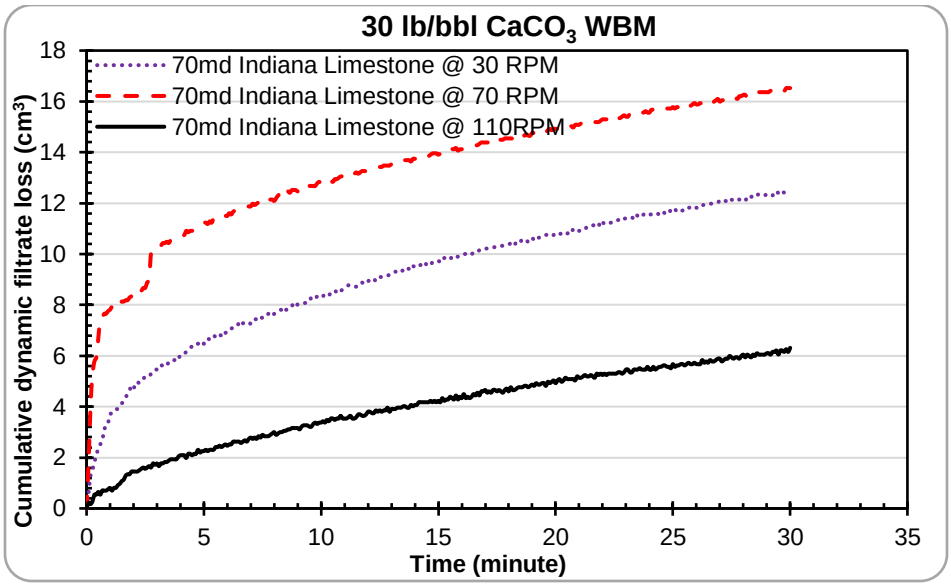

Figure 5.39: Dynamic filtrate loss profiles in Indiana limestone for 30 lb/bbl $CaCO_3$ WBM

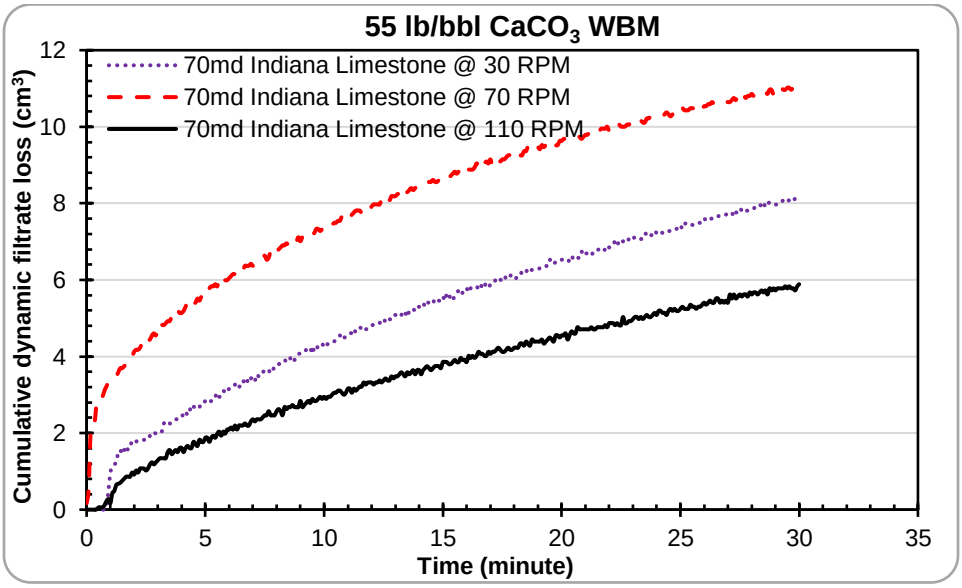

Figure 5.40: Dynamic filtrate loss profiles in Indiana limestone for 55 lb/bbl $CaCO_3$ WBM

Recall that in Figure 5.21, LCM fluid sample 2 (55 lb/bbl $CaCO_3$) was subjected to dynamic fluid filtration in this limestone at 120^{o}F and 70 rpm. The cumulative filtrate loss was 5.908 cm^3 and for the same conditions but elevated temperature (220^{o}F), the filtrate loss was 11.019 cm^3. This result supports the conclusion that an increase in temperature from 120^{o}F to 220^{o}F tends to increase dynamic mud loss and filtrate by up the half its value.

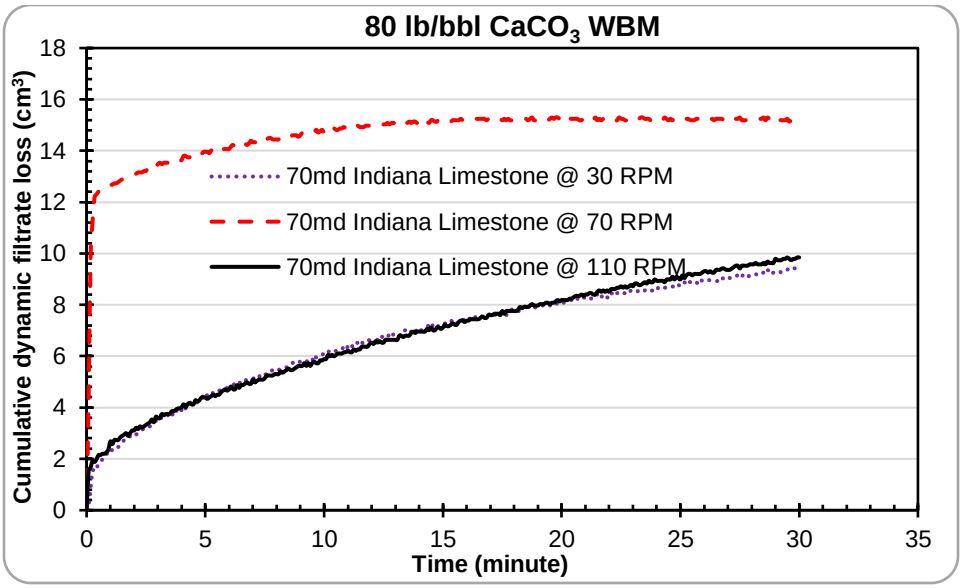

Figure 5.41: Dynamic filtrate loss profiles in Indiana limestone for 80 lb/bbl $CaCO_3$ WBM

Figure 5.41 shows the filtrate loss profile when 70 mD Indiana limestone is exposed to 80 lb/bbl $CaCO_3$ WBM. The experiments at 30 rpm and 110 rpm had almost the same profile while the experiment at 70 rpm showed high spurt loss (12 cm^3) and 15.242 cm^3 cumulative filtrate loss. The critical invasion rate appeared after about 15 minutes in this experiment. In general, an increase in LCM concentration to 80 lb/bbl did not decrease dynamic filtrate loss compared to the results at 55 lb/bbl. The complex minerology of Indian limestone (natural fractures and solution channels) contributes to the inadequate performance of the granular LCM fluid at elevated temperature. Therefore, an increase in the $CaCO_3$ concentration beyond 55 lb/bbl may not always reduce dynamic fluid loss and filtrate in 70 mD Indiana limestone at an elevated temperature (220^oF) and varying rotary speeds up 110 rpm.

5.3.10 Dynamic Drilling Fluids Filtration in Austin Chalk (Phase Two)

The results for dynamic filtrate loss in Austin chalk are presented in this section. In all the experiments, spurt invasion was recorded. Figure 5.42 shows the experiments with 30 lb/bbl of $CaCO_3$ WBM. The 30-rpm experiment showed spurt loss (5.566 cm^3), one vertical fracture

(observed after the experiment), and the cumulative filtrate was 6.421 cm^3. Between the spurt and final filtrate loss, the fracture appeared to have been sealed and only 0.855cm^3 of filtrate was collected. As the rotary speed was increased, the filtrate loss values also increased. The deviation in the 70 rpm was a slight pressure fluctuation after 6 minutes but the experiment was completed without issues. Amongst all the 110 rpm experiments with 30 lb/bbl LCM fluid, it can be observed that only Michigan sandstone, Buff Berea sandstone, and Austin chalk had cumulative losses greater than 22 cm^3. The permeability of both sandstones is up to 100 times more than the permeability of Austin chalk.

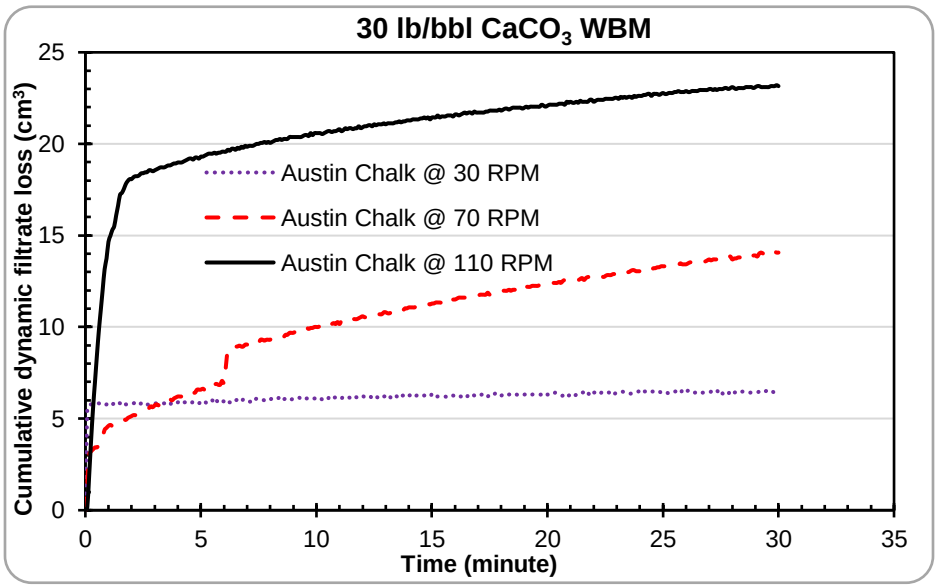

Figure 5.42: Dynamic filtrate loss profiles in Austin chalk for 30 lb/bbl $CaCO_3$ WBM

This implies that Austin chalk's porosity has a greater impact on fluid loss and filtration than its permeability. Figure 5.43 shows the experiments with 55 lb/bbl of $CaCO_3$ WBM. The cumulative filtrate loss at 70 rpm is greater than the value at 30 rpm. However, the cumulative filtrate at 110 rpm is lower than the value at 70 rpm but greater than the value at 30 rpm. This experiment showed spurt invasion and some filtrate loss fluctuations during the early stages. The heterogenous nature of the rock is a major contributing factor the filtrate invasion.

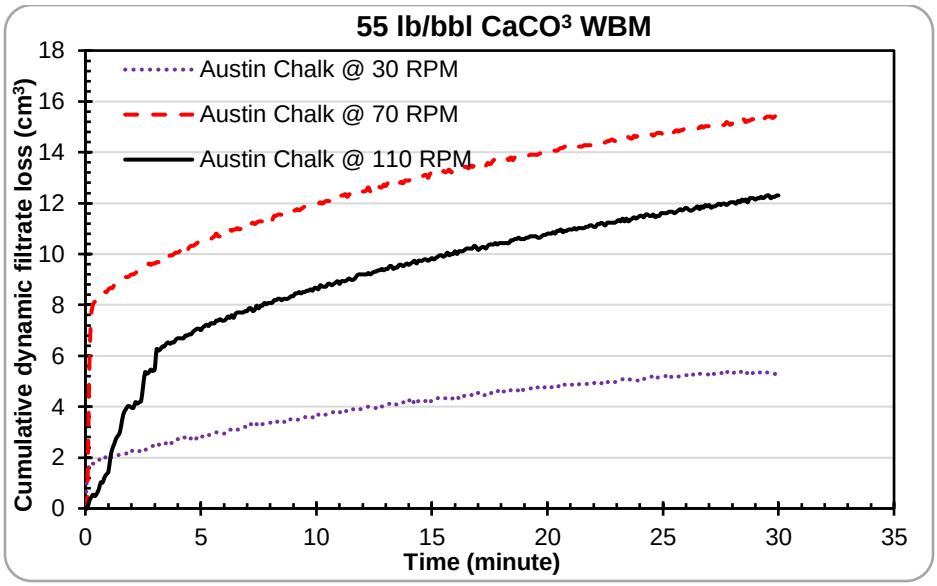

Figure 5.43: Dynamic filtrate loss profiles in Austin chalk for 55 lb/bbl $CaCO_3$ WBM

Figure 5.44 shows the filtration profiles for the 80 lb/bbl LCM WBM. Vertical fractures were created during the experiments with 70 rpm and 110 rpm. The creation of the fractures was unintentional and out of experimental control. In addition, all the experimental conditions that can initiate fractures, if increased, were consistent (rotary speed, mud weight, temperature, and differential pressure). This implies that induced fractures can be easily created in Austin chalk while drilling, compared to other rocks in this study. This confirms the depleted nature of the formation and its susceptibility to high fluid loss and filtration. Comparing the experiments at 70 rpm (median rotary speed) in Figure 5.43 and Figure 5.44, it can be observed that an increase in $CaCO_3$ concentration at elevated temperature does not have any positive effect in reducing filtrate loss in Austin chalk.

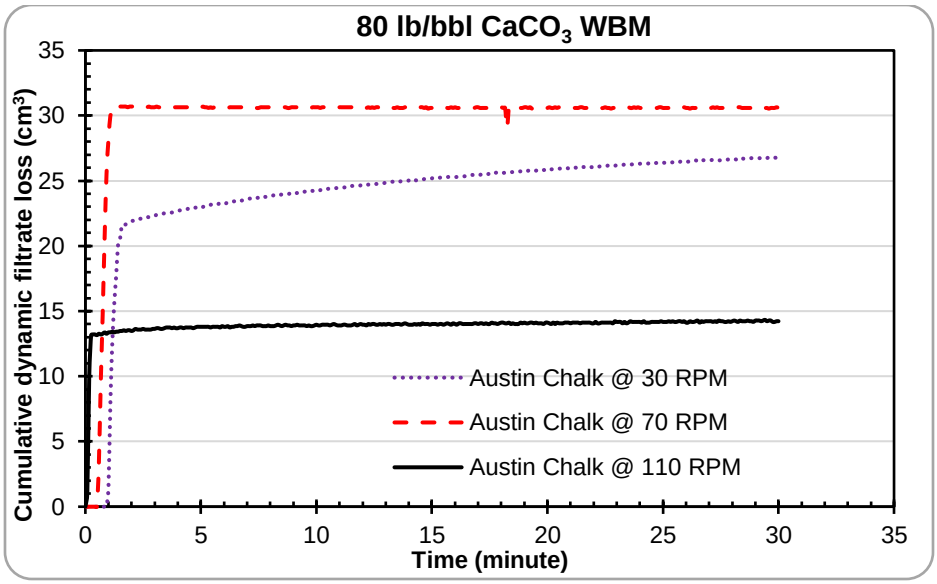

Figure 5.44: Dynamic filtrate loss profiles in Austin chalk for 80 lb/bbl $CaCO_3$ WBM

Combining all the results from stage two experiments (section 5.3.1 to section 5.3.10), it can be concluded that permeability, porosity, possibility of natural fractures/solution channel, and operating conditions (temperature, rotary speed, and pump rate) play important roles in drilling fluid/filtrate invasion. A "one-size-fits-all" type of drilling fluid recipe cannot be used to achieve effective mud cake evolution under changing wellbore conditions. Based on the experimental results, analyses, and operating conditions, a new LCM concentration selection criterion for calcium carbonate was formulated. For temperature less than or equal to 200^{o}F, rotary speed less than or equal to 70 rpm, rock permeability less than or equal to 105 mD, and rock porosity less than or equal to 23 %, the concentration of calcium carbonate should be greater or equal to 55 lb/bbl (5.8 % volume). Above these conditions, an increase in calcium carbonate concentration may not be effective in reducing dynamic fluid/filtrate loss.

5.3.11 Statistical Analysis: Regression Analysis (Phase Two)

One of the primary objectives of conducting the hypothesis tests using analysis of variance is to determine the magnitude, significance, and order of impact of the factors that affect dynamic mud

filtrate loss. The outcome was applied to the design of experiments (DoE) for the stage two experiments (Table 3.4). From the results and material availability, another level was added to the selected factors, making it three levels per factor. The primary objective for adding a third level is to obtain a mathematical relationship between dynamic fluid filtration and the selected factors, using regression analysis. Regression analysis is a mathematical approach that is used to show the relationship between a dependent variable and independent variable(s). It can be linear (a response variable that is dependent on one factor) or multiple (a response variable that is dependent on more than one factor). From the mathematical relationship, regression can be used as a predictive tool to predict a dependent variable from a range of independent variable(s).

All the factors (LCM concentration, rotary speed, and temperature) that were studied from the stage one experiments were significant, based on a 95 % confidence interval. However, LCM concentration and rotary speed were selected for the stage two experiments on the rock samples. One of the primary considerations for selecting these two factors is that in an actual field operation, rotary speed and LCM concentration can be controlled before and during drilling fluid/filtrate loss. In addition, temperature is the most significant factor that increases dynamic fluid filtration, and the experiments on the rocks (stage two) were conducted at the high level of temperature (220^{o}F). Therefore, the regression model that would be developed for dynamic drilling fluid filtration, LCM concentration, and rotary speed will be valid for temperatures up to 220^{o}F and other constant experimental conditions used.

There are four important steps that are taken to perform and evaluate a regression: 1) Develop the regression hypothesis, 2) Obtain the ANOVA table, 3) Evaluate the R^2/adjusted R^2 values, and 4) Evaluate the coefficient(s) of factor(s) and intercept and write down the regression (empirical) model. The appropriate regression hypotheses for the rock samples have been

developed in section 3.2.3. The ANOVA table from a regression analysis is used to determine the significance of the regression. In this case, whether the response variable (cumulative dynamic filtrate loss in rocks) can be explained by the changes in the independent variables ($CaCO_3$ concentration and rotary speed). If the ANOVA table shows that the regression is significant, then the null hypothesis is rejected, and the alternative hypothesis is accepted. Next, the R^2/adjusted R^2 values will be checked to evaluate the predictability of the regression. This is followed by evaluating the coefficient(s) of factor(s) and intercept using their p-values and other technical implications that may have resulted from the experiment. If the regression is not significant (null hypothesis being accepted), there may be no need for steps 3 and 4.

Table 5.2 and Table 5.3 shows the ANOVA table for the Buff Berea sandstone and Michigan sandstone regression analyses respectively. In both tables, the p-values are greater than $\alpha = 0.1$ and $\alpha = 0.05$ for 90 % and 95 % confidence intervals respectively. This means that there is not enough reason to reject the null Buff Berea sandstone regression hypothesis and the null Michigan sandstone regression hypothesis. Therefore, cumulative dynamic filtrate loss in both sandstones cannot be explained by the variations in rotary speed (between 30 rpm to 110 rpm) and $CaCO_3$ concentration (between 30 lb/bbl and 80 lb/bbl). One of the main contributors that led this conclusion is the permeability of both sandstones. The permeability of both sandstones is 350 mD and this is considered high-permeability value compared to other lithologies in this study. Dynamic mud filtrate losses were high even at low rotary speed and high LCM concentration. For instance, in Figure 5.32, the experiment on Michigan sandstone with the highest cumulative filtrate loss was the one performed at 30 rpm, and the fluid contained 80 lb/bbl of $CaCO_3$. Figure 5.33 and Figure 5.34 also show that the dynamic filtrate loss in Buff Berea sandstone did not decrease when the $CaCO_3$ concentration increased (30 lb/bbl to 55 lb/bbl), for the 30 and 70 rpm experiments. In

addition, high $CaCO_3$ concentration was not completely effective at the experimental temperature (220^oF). Therefore, a combination of high rock permeability and elevated temperature are the reasons the regression cannot explain dynamic filtrate loss in Buff Berea and Michigan sandstones from the variations in $CaCO_3$ concentration and rotary speed. Evaluation of R^2/adjusted R^2 and coefficient(s) of factor(s) and intercept was not done since the regressions were not significant.

Table 5.2: Significance of Buff Berea sandstone regression analysis

Source	DF	SS	MS	F_o	P-value
Regression	2	107.26	53.63	2.21	0.19
Residual	6	145.79	24.29		
Total	8	253.05			

Table 5.3: Significance of Michigan sandstone regression analysis

Source	DF	SS	MS	F_o	P-value
Regression	2	104.11	52.05	1.52	0.29
Residual	6	205.97	34.33		
Total	8	310.08			

Table 5.4 shows the ANOVA table for the Upper Grey sandstone regression analysis. Using a 95 % confidence interval (CI), the P-value for the regression analysis is exactly 0.05. That is, the type I error (α) is equal to 0.05. With this P-value, it is possible to reject the null hypothesis and draw the conclusion that dynamic filtrate loss in Upper Grey sandstone can be explained from changes in $CaCO_3$ concentration and rotary speed. However, this conclusion may not be completely definitive since the P-value can be referred to as "borderline P-value", considering the confidence interval (95 %). However, using a 90 % confidence interval (that is, type I error (α) = 0.1), the P-value is less than 0.1. Therefore, the null hypothesis is rejected, and the alternative hypothesis is accepted. This means that dynamic filtrate loss in Upper Grey sandstone can be explained from

the variations in $CaCO_3$ concentration (between 30 lb/bbl to 80 lb/bbl), rotary speed (between 30 rpm and 110 rpm), and other experimental conditions

Table 5.4: Significance of Upper Grey sandstone regression analysis

Source	DF	SS	MS	F_o	P-value
Regression	2	149.27	74.64	4.77	0.05
Residual	6	93.97	15.66		
Total	8	243.24			

The third step used in evaluating a regression component is checking the R^2/adjusted R^2 values. The R^2 value is a number that used to evaluate how much variability that is being explained by the regression. An increase in the R^2 value (towards 100%) translates to more variability being explained by the regression. The predictability of a regression typically increases when the R^2 value increases. The R^2 value for the Upper Grey sandstone regression is 61.4 %, while the adjusted R^2 value is 48.5 %. Although, the regression model is significant, the R^2/adjusted R^2 values show that it's not explaining so much variability. One of the reasons for this is because the regression analysis is a multiple regression that has more two factor and only three levels. Usually, a linear regression with higher treatments (levels) or a multiple regression with higher the treatments (levels) will more than likely reveal higher R^2/adjusted R^2 values. Regardless of the regression type, an increase in the levels translates to an increase in the R^2/adjusted R^2 values (Montgomery 2013). In addition, the variability from the experimental factors, other experimental conditions, and rock heterogeneity are plausible contributions for the R^2/adjusted R^2. As a recommendation, the experimental levels should be increased depending of the availability of experimental materials and cost. This will increase the predictability of the regression model. The fourth step is evaluating the is the coefficients of the factors and intercept of the regression. The coefficients are shown in the empirical model below. In this model, CC is the $CaCO_3$

concentration, RS is the rotary speed, and DFL is dynamic filtrate loss. The intercept is used to describe any other form of variability that may exist or inherent within the experiment. The coefficients of $CaCO_3$ concentration (-0.066) and rotary speed (0.117) are called the partial slopes in the model. For instance, the partial slope (0.117) represents the relationship between dynamic filtrate loss and rotary speed, while holding the $CaCO_3$ concentration constant and vice versa.

$$DFL = 3.777 - 0.066CC + 0.117RS \quad \text{..... (5.1)}$$

Table 5.5: Significance of 70 mD Indiana limestone regression analysis

Source	DF	SS	MS	F_o	P-value
Regression	2	14.16	7.08	0.44	0.66
Residual	6	97.10	16.18		
Total	8	111.27			

Table 5.5 shows the ANOVA table for the 70 mD Indiana limestone regression analysis. Like the Michigan and Buff Berea sandstones, the P-value in this table is greater than $\alpha = 0.1$ and $\alpha = 0.05$ for 90 % and 95 % confidence intervals respectively. This implies that there is not enough reason to reject the null Indiana limestone regression hypothesis. Thus, cumulative dynamic filtrate loss in this limestone cannot be explained by the changes in rotary speed (between 30 rpm to 110 rpm) and $CaCO_3$ concentration (between 30 lb/bbl and 80 lb/bbl). While the permeability of this rock is lower than all the sandstones studied, it is not far-fetched that the main reason for this conclusion is the heterogenous nature of the limestone, which contributed to the experimental results. The regression analysis for Austin chalk was not performed because some of the experiments showed that the rock samples were fractured, and a combination of mud and filtrate were collected.

In general, the models that are developed from a regression analysis are empirical models which are typical based on observations. Given the conditions in this study, an empirical modelling

approach may not be completely sufficient in predicting the cumulative dynamic filtrate loss in rocks or their profiles. Thus, a mechanistic modeling approach was developed, solved, and serves as a better predictive tool than the empirical model (in the case of Upper Grey Sandstone). The results are shown in chapter 6.

5.4 Stage Three: Fracture-Scale Dynamic Drilling Fluids Loss (Fractur Slots)

5.4.1 LCM Type and Concentration Screening

Dynamic fluid loss and filter cake evolution was investigated for various fracture widths. Three sets of experiments were performed: the screening tests, vertical fracture tests, fracture orientation and positioning tests. The screening tests were performed with a 2000 µm to select the best recipe for subsequent tests. Figure 5.45 shows the results from three LCM types and concentrations that were screened. The first type and concentration that was tested was 80 lb/bbl of commercial calcium carbonate (high concentration of granular LCM). The filter cake evolution from this slurry appeared not to be effective. The result revealed spurt invasion up to 28 cm^3 and the filter cake that evolved over the fracture entrance ruptured up to 3 times within 3.3 minutes. This continued until the machine reached its maximum limit for fluid loss collection. The second LCM type and concentration that was tested was 30 lb/bbl of walnut plug. This was selected based on the experiments performed by Alsaba et al. (2014). The result showed that this slurry did not build a stable filter cake over the 2000 µm fracture width and the machine's maximum fluid loss limit was attained in 45 seconds. The third LCM type and concentration that was tested was 30 lb/bbl of Cedar fiber. This was chosen based on the results from preliminary static mud filtration studies and the study performed by Mansour et al. (2018). The result showed that dynamic fluid loss was below the machine's maximum fluid loss limit.

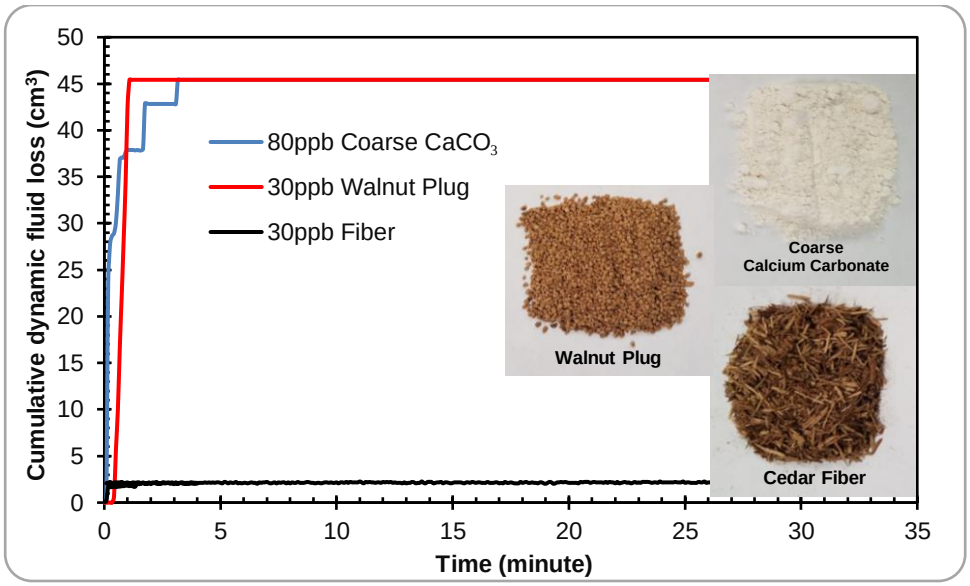

Figure 5.45: LCM screening for dynamic mud invasion in 2000µm fracture width slot

5.4.2 Fracture-Scale Dynamic Fluid Loss Profiles (Vertical Fractures)

The results from the LCM type and concentration screening, material availability, and preliminary studies informed the decision on the recipe and concentrations to use for the second and third set of the fracture fluid loss experiments. The results from the second set of fracture-scale dynamic fluid loss are shown in Figure 5.46, Figure 5.47, and Figure 5.48. The thick blue lines within the graphs (parallel to the vertical axes) represent the two pressure regimes (PR_1 and PR_2) discussed in the methodology (section 3.3.3.3). Between time zero and PR_1, differential pressure (200 psi) was created and stabilized at PR_1. Between PR_1 and PR_2, dynamic fluid filtration was monitored for 30 minutes if a seal has been formed. At PR_2, differential pressure was increased to 400 psi to test the stability of the seal for 5 additional minutes.

5.4.2.1 Dynamic Fluid Loss Profiles in 500 µm Vertical Fracture Width

Figure 5.46 shows the profiles for dynamic fluid loss through a 500 µm vertical fracture. In this figure, the 5 lb/bbl fiber WBM showed the highest fluid loss. Spurt loss (4 cm^3) was recorded after

10 seconds at 37 psi. The spurt value remained constant because of the initial filter cake build up during the spurt loss. At 200 psi (PR_1), the filter cake ruptured, allowing additional 16 cm^3 to flow through the fracture. During the 30 minutes duration, dynamic mud filtration was not observed. The stability of the filter cake was tested after 30 minutes by doubling the differential pressure (PR_2) at the same conditions (220°F and 110 rpm). No further loss was recorded. The same procedure was applied for the 15 lb/bbl fiber WBM experiment and spurt loss (7.5 cm^3) was recorded after 80 seconds at 62 psi. Dynamic fluid loss increased slightly by 0.9 cm^3 at 200 psi and then remained constant. Neither mud filtrate nor further losses were recorded till the end of the experiment. An increase in the fiber LCM concentration from 5 lb/bbl to 15 lb/bbl corresponded to a 58.2 % decrease in dynamic fluid loss through the 500 µm vertical fracture width. The 30 lb/bbl fiber WBM did not show any fluid loss values because the fracture was completely sealed.

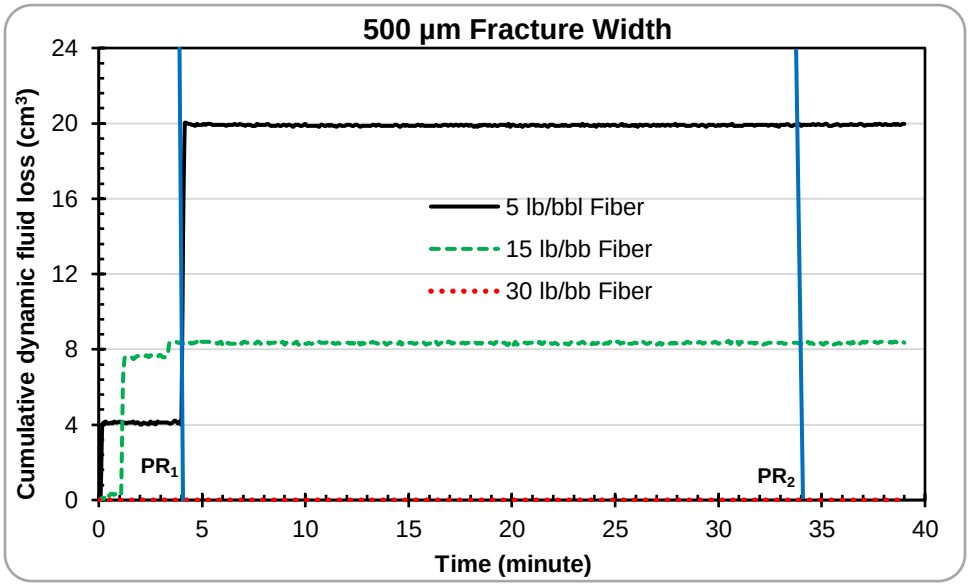

Figure 5.46: Dynamic fluid loss profiles for 500 µm fracture width at 220°F and 110 RPM.

5.4.2.2 Dynamic Fluid Loss Profiles in 1000 µm Vertical Fracture Width

Figure 5.47 shows the dynamic fluid loss profiles through the 1000 µm vertical fracture width. The 5 lb/bbl fiber WBM had the highest dynamic fluid loss with 10 seconds spurt loss (10.21 cm^3) at 27 psi. At 60 psi, dynamic fluid loss increased to 14.33 cm^3 and subsequently to 14.94 cm^3. This value remained constant till the end of the experiment. There was no filtrate loss and the filter cake resisted the increase in differential pressure. With the 15 lb/bbl fiber WBM, spurt loss (5.201 cm^3) was recorded at 34 psi. However, the plot shows slight dynamic mud filtrate loss through the filter cake with a final fluid loss value of 5.861 cm^3. An increase in the Cedar fiber LCM concentration (5 lb/bbl to 15 lb/bbl) showed a 61.3 % decrease in dynamic fluid loss through the 1000 µm vertical fracture width. Using 30 lb/bbl fiber WBM, no fluid loss was recorded within the first pressure regime. The seal that was formed by the filter cake appeared to be effective during this time (between PR_1 and PR_2). But when the differential pressure was doubled, the filter cake ruptured slightly, allowing 1.712 cm^3 of fluid through the fracture.

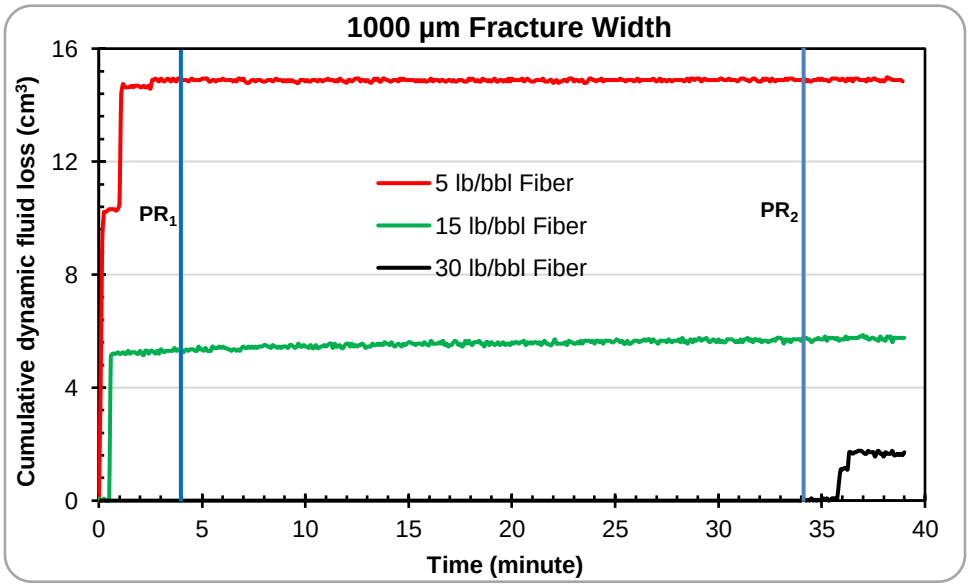

Figure 5.47: Dynamic fluid loss profiles for 1000 µm fracture width at 220°F and 110 RPM.

5.4.2.3 Dynamic Fluid Loss Profiles in 2000 µm Vertical Fracture Width

The dynamic fluid loss profiles through the 2000 µm vertical fracture are shown in Figure 5.48. Using the 5 lb/bbl fiber WBM, spurt loss (3.3 cm^3) was recorded at 21 psi. At 90 psi, dynamic fluid loss increased to 15 cm^3 and remained constant during the 30 minutes duration with no filtrate loss. The filter cake could not resist the increase in differential pressure and at 260 psi, dynamic fluid loss increased to 29.67 cm^3. No further losses were recorded afterwards. Using the 15 lb/bbl fiber WBM, lower spurt loss (2.69 cm^3) was recorded compared to the 1000 µm vertical fracture. However, doubling the differential pressure caused the filter cake over the 2000 µm fracture to rupture, increasing dynamic fluid loss to a final value of 13.33 cm^3. An increase in Cedar fiber LCM concentration (5 lb/bbl to 15 lb/bbl) showed up to 54.7 % decrease in dynamic fluid loss through the 2000 µm vertical fracture. With the 30 lb/bbl fiber WBM, 2.06 cm^3 spurt was recorded and this value remained constant until PR_2. Signs of a rupturing filter cake barrier were somewhat noticeable in the slight increase in dynamic fluid loss from PR_2. However, this was thought to be dynamic mud filtrate in response to the increase in differential pressure.

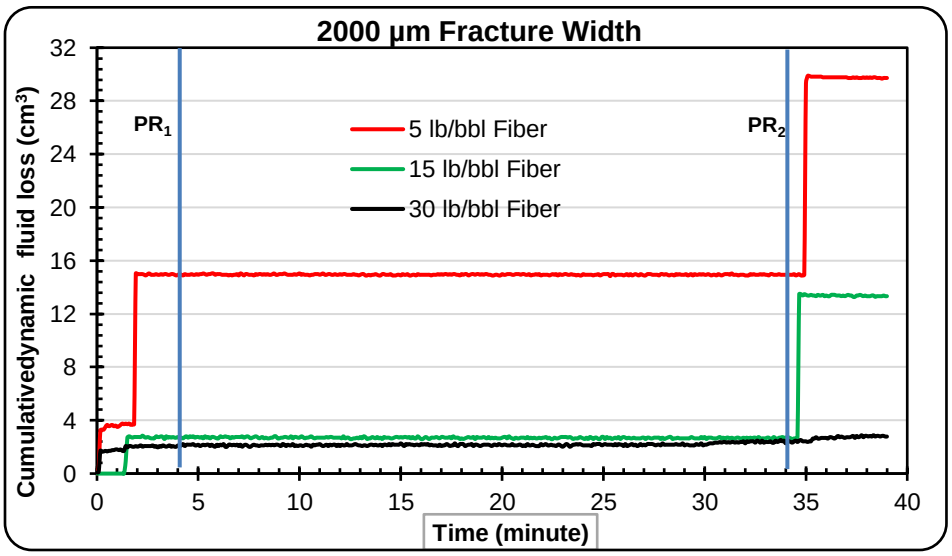

Figure 5.48: Dynamic fluid loss profiles for 2000 µm fracture width at 220°F and 110 RPM.

5.4.2.4 Wellbore Strengthening Implications and Effect of Particle Size Distribution

Following the overall description of the dynamic fluid loss profiles, the results show that as vertical fracture width increases, the amount of differential pressure required to create spurt invasion decreases (specifically true for the 5 lb/bbl fiber WBM). An increase in Cedar fiber LCM concentration can effectively reduce dynamic fluid loss. Increasing the concentration from 5 lb/bbl to 15 lb/bbl revealed an average decrease of 58.1 % dynamic fluid loss over the three vertical fracture widths. In this study, the filter cake stability was tested to demonstrate the impact of filter cake evolution on wellbore strengthening. The term "filter cake stability" has been defined in subsection 3.3.3.3. This is particularly important because it addresses the second hypothesis in this study which states that "wellbore strengthening by filter cake can be quantified from dynamic drilling fluid loss and filtration". After conducting the experiments and testing the stability of the filter cake in each experiment, the results showed 67 % stability of the filter cake (from the LCM fluid) over the three fracture widths that were investigated. This outcome is very important because it implies that filter cake wellbore strengthening in fractures (with widths up to 2000 µm) can be 67 % successful with the proper fluid recipe and at elevated conditions (up to 220^{o}F and 110 rpm).

Furthermore, the particle size distribution (PSD) of the LCM (Cedar fiber) is the primary contributor to forming stable filter cake plugs in the fracture slots. Fiber particles are not spherical, and larger particles are irregular with rough surfaces compared to the smaller particles. In addition, particle orientation to the fracture at the time of fluid loss plays a key role in determining how quickly or slowly a seal is formed over the fracture. For instance, consider that a large fiber particle's height and width are slightly smaller than a vertical fracture slot's height and width. If the particle's orientation (height in the vertical direction) at the time of invasion is parallel to the fracture height, it will pass through the fracture. If the particle's orientation (height in the

horizontal direction) at the time of invasion is perpendicular to the fracture height, it will pass through the fracture. But if the particle's orientation (height in the horizontal direction) is parallel to the fracture width (forming a cross shape with the fracture height), then it may not pass through the fracture. Other orientations such as transverse can also support fracture plugging at the entrance. Figure 5.49 shows the 2000 µm fracture width slot after the experiment with the 15 lb/bbl fiber WBM. Figure 5.49 (a) shows partial sealing on the outer diameter of the slot with extruding filter cake particles. Figure 5.49 (b) shows the inner diameter of the slot with what appears to be an effective filter cake plug. This figure also shows two fiber particles in the transverse direction on the filter cake surface. In addition, finer fiber particles and barite also contributes to filling the voids left by the large particles in the filter cake. Figure 5.49 (c) shows the inner diameter and bottom part of the slot. The fracture opening was the only fluid outlet in response to differential pressure.

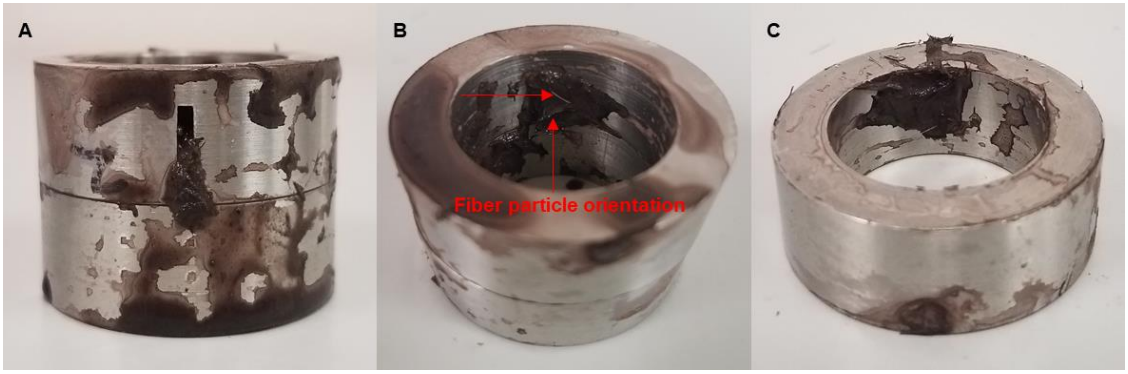

Figure 5.49: Filter cake plastering over the 2000 µm fracture surface after the experiment with the 15 lb/bbl fiber WBM.

5.4.2.5 Statistical Analysis: Regression Analysis

From the DoE in Table 3.5, three levels of each factor were selected primarily to obtain a relationship between dynamic fluid loss and the selected factors using regression analysis. The definition and application of regression analysis have been explained in section 5.3.6. The

regression analysis that was performed on the results from the vertical fracture experiments was based on a 95% confidence interval and is valid for temperatures up to 220^{o}F, rotary speed up to 110 rpm, and other constant experimental conditions used. The vertical fracture regression hypothesis has been developed in section 3.2.3.

The ANOVA table from the regression analysis is used to determine the significance of the vertical fracture regression. Table 5.6 shows the ANOVA for the regression analysis. Based on a 95% confidence interval (CI), the p-value is than 0.05 (i.e type I error, $\alpha = 0.05$). With the forgoing, the null hypothesis is rejected, and the alternative hypothesis is accepted. This implies that dynamic drilling fluid loss can be explained from changes in Cedar fiber LCOM concentration and vertical fracture width. Thus, for Cedar fiber LCM concentration between 5 lb/bbl and 30 lb/bbl, vertical fracture dimensions (width between 500 µm and 2000 µm, height = 10000 µm), and other experimental conditions, dynamic drilling fluid loss can be estimated.

Table 5.6: Significance of the regression analysis

Source	df	SS	MS	F_o	P-value
Regression	2	647.45	323.73	16.84	0.0035
Residual	6	115.31	19.22		
Total	8	762.76			

Table 5.7 shows other statistical data that are used to evaluate the regression model. One of the important components in this table is the R^2 value. The R^2 value is used to determine the proportion of variability that the regression model is explaining. The higher the R^2 value the more variability the regression model is explaining, which increases the predictability. The R^2 value for this regression is 84.9 %. Another important component in Table 5.7 is the adjusted R^2 value. Sometimes, the R^2 value tends to overestimate the impact of the factor(s) affecting a response.

Thus, the adjusted R^2 is used avoid what is referred to as overfitting (i.e. overestimating the importance of the independent variables). Taking into account the adjusted R^2 value (79.8 %), a cautious conclusion can be made that the regression model shows a considerably high predictability of dynamic fluid loss. Furthermore, it is a multiple regression with more than one factor and only three levels. The higher the treatments (levels), the more the R^2 and adjusted R^2 values are expected to increase. Moreover, the variability from the experimental factors and other experimental conditions are plausible mechanisms for the R^2 and adjusted R^2 values. For subsequent experiments, it recommended that the experimental levels be increased to increase the predictability of the regression.

Table 5.7: Other regression statistical data

Regression Statistics	Values
Multiple R	0.921
R Square	0.849
Adjusted R Square	0.798
Standard Error	4.384
Observations	9

Table 5.8 shows the parameters (coefficient of factors) for the regression model. In this table, the intercept is used to account for any form of variability that may have existed within the experiment. Based on a 95 % CI, the p-value for the intercept is less than 0.05. This implies that the intercept influences the model and the prediction of dynamic fluid loss. Therefore, it should not be neglected. The p-value for the fracture width coefficient is not less than 0.05 based on a 95 % CI. This implies that vertical fracture width variation is not significant in explaining dynamic fluid loss. However, it should be noted that this conclusion cannot be fully made if a 90 % CI is

considered because the p-value is exactly 0.10 (two decimal places). Figure 5.50 is used to bolster the conclusion that fracture width is not significant. It is expected that as fracture width increases, dynamic fluid loss increases. However, this was only true for the 30 lb/bbl LCM WBM experiment. For the most part, designing a drilling fluid for a wide range of fracture widths is desirable. Moreover, induced and natural fracture widths cannot be controlled while drilling, and it is often difficult if not impossible to predict in real-time, the fracture dimensions. Thus, it's somewhat beneficial that the model is less sensitive to changes in fracture width (between 500 µm and 2000 µm), while maintaining a good predictability.

The p-value for the Cedar fiber concentration coefficient is less than 0.05 which means that a change in Cedar fiber concentration is significant in estimating dynamic fluid loss. Figure 5.50 also supports this conclusion (cumulative fluid loss decreases as LCM concentration increases for all the fracture widths). Therefore, a new LCM concentration selection criterion for Cedar fiber can be formulated as follows: For fracture width ≤ 2000 µm, temperature ≤ 220°F, and rotary speed ≤ 110 RPM: 2.4% ≥ Cedar fiber volume concentration ≤ 14 %. The empirical model is written in equation 5.2. In this model, DFL is dynamic fluid loss, VFW is vertical fracture width, and CFC is Cedar fiber concentration. The coefficients of fracture width and LCM concentration are referred to as the partial slopes which in each case, represent the relationship between dynamic fluid loss and one of the factors, while holding the other factor constant.

$$DFL\ (cc) = 18.4776 + 0.0045VFW - 0.7790CFC \quad \text{(5.2)}$$

Table 5.8: Regression model parameters

Source	Coefficients	Standard Error	t Stat	P-value
Intercept	18.4776	3.9024	4.7350	0.0032
Fracture width	0.0045	0.0023	1.9212	0.1031
LCM Concentration	-0.7790	0.1422	-5.4771	0.0015

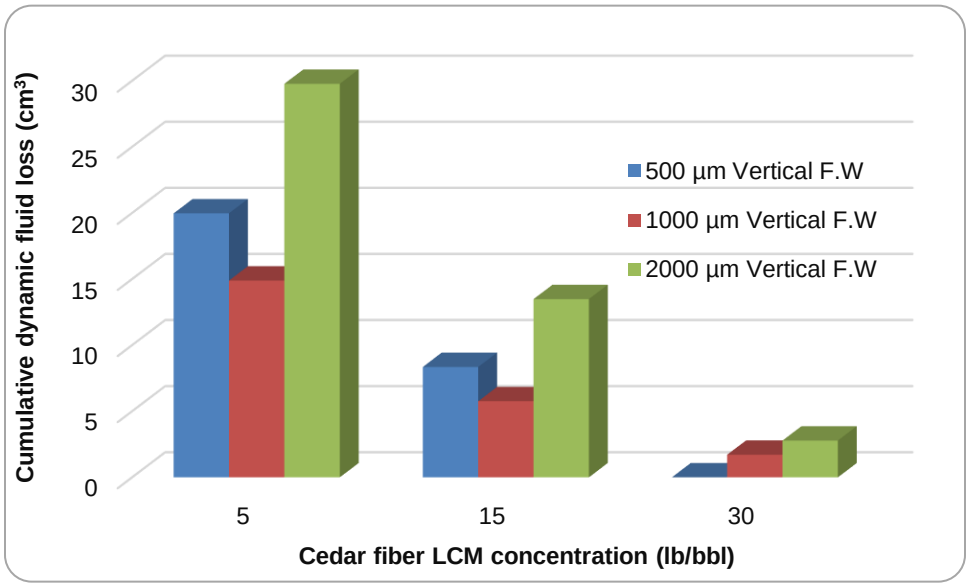

Figure 5.50: Cumulative dynamic fluid loss for vertical fractures of varying widths

5.4.3 Cumulative Dynamic Fluid Loss: Impact of Fracture Orientation

The third set of experiments reported in this section were performed to observe the effect of fracture orientation and change in dimensions. Figure 5.51 shows the cumulative fluid losses through different fracture orientations. In general, an increase in the LCM concentration showed a corresponding decrease in dynamic fluid loss except for the experiment with the 15 lb/bbl Cedar fiber and two 500 µm (FW) vertical fractures. Interestingly, the experiments with the two 500 µm (FW) vertical fractures had the highest fluid losses with the 5 and 15 lb/bbl LCM WBM's. Compared to the one 1000 µm (FW), it would be expected that both experiments yield almost the same cumulative fluid loss values since their combined fracture width is 1000 µm. Also notice that

the experiments with the horizontal fracture had the lowest cumulative dynamic fluid loss compared to the vertical fractures. With the following observations, a cautious inference can be made that fracture positioning and orientation can impact dynamic fluid loss. More experiments are required to further validate these observations. Figure 5.52 shows the complete filter cake plastering after the experiment with the 15 lb/bbl Cedar fiber WBM.

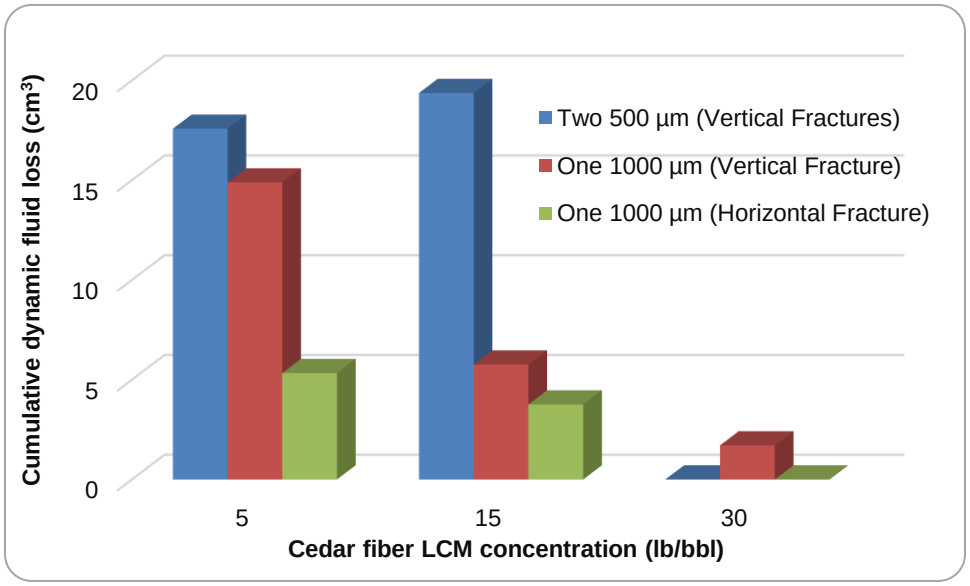

Figure 5.51: Cumulative dynamic fluid loss for one fracture width size with varying orientations.

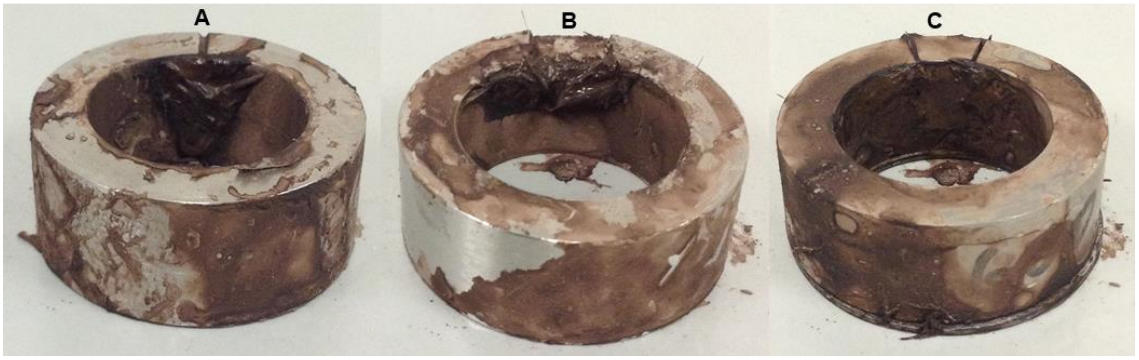

Figure 5.52: Filter cake plastering over (a) one vertical fracture with FW = 1000 µm and FH = 10000 µm; (b) one horizontal fracture with FW = 10000 µm and FH = 1000 µm); and (c) Two vertical fractures with FW = 500 µm and FH = 10000 µm

It worthy to mention that one of the success factors that seems to contribute to the filter cake plastering effect is the rotating shaft - fracture slot geometry. This is related to casing while drilling applications. A comparative study showed that up to 90 % of successful casing while drilling operations had a casing - wellbore ratio between 0.7 and 0.85 (Ezeakacha 2014). The studies by Kiran and Salehi (2016), Kiran (2014), and Salehi et al. (2013) support this finding. The ratio of the rotating shaft to the inner diameter of the slot in this study is 0.68. This value is close to the range reported for filter cake plastering in casing while drilling and proves to support fracture plugging. In addition, the temperature limit in this study did not impair the Cedar fiber's performance unlike calcium carbonate. The roller oven test performed on wood fibers showed that the material degrades permanently at 400^{o}F (Loeppke et al. 1990). For practical purposes, it should be noted that the viscosity of the fiber-based fluids may be a challenge particularly with an increase in fiber concentration. For preventative application, the viscosity of the fiber-based fluid should be profiled with the appropriate apparatus starting with low concentrations (between 5 lb/bbl and 15 lb/bbl). If necessary, higher concentrations up to 30 lb/bbl may be applied for sweep purposes.

Chapter 6: Modeling Results and Discussions

In this chapter, the results from the mathematical modeling and geomechanical studies will be presented. First, the results from the mechanistic model that was developed in section 4.1.4 will be presented in section 6.1. Experimental data from selected experiments were applied to validate the accuracy of the model. After presenting the filtration model results, the geomechanical implications and hoop stress profiles from filter cake evolution, generated from section 4.2 will be discussed in section 6.2

6.1 Mathematical Modeling of Dynamic-Radial Mud Filtration

Different dynamic-radial mud filtration profiles were generated from the model solution. The profiles that were modeled were chosen for different rock types (permeability and porosity), LCM fluid concentrations, and rotary speeds to highlight the efficiency of the model. These profiles were compared and validated with the experimental results. It worthy to mention that the amount of experimental data points is important in substantiating the accuracy of the drilling fluid filtration process and the model used in predicting it. The experimental profiles were generated from 360 dynamic mud filtration data points that were recorded with a data acquisition system (DAQS). In addition, the results from the model's sensitivity analysis will be shown. An example of input data used in modeling dynamic-radial mud filtration is shown in Table 6.1. The input data comprises of experimental conditions and data, model assumptions, and other porous media properties. The parameters which are not in the table, but in the derivation of the model, have been calculated within the model solution. The primary advantage of this model and its solution is that it can be used to develop performance curves of dynamic drilling fluids filtration in different rocks and wellbore conditions for field application.

Table 6.1: Data for modeling dynamic-radial drilling fluid filtration in Buff Berea sandstone

Parameter	Value	Unit
Formation permeability, K_f	0.35	Darcy
Formation porosity, Φ_f	0.185	N/A
Formation tortuosity, T_f	0.7	N/A
Wellbore radius, r_w	1.27	cm
Reservoir radius, r_e	1.91	cm
Radius of drillpipe/rotating shaft, r_{dp}	0.8656	cm
Filter cake radius, r_c	1.1049	cm
Filter cake thickness, δ	0.1651	cm
Filter cake height, h	2.81	cm
Filter cake tortuosity, T_c	0.6	N/A
Filter cake permeability, K_c	0.0009	Darcy
Filter cake porosity, Φ_f	0.4	N/A
filtrate viscosity, μ	0.296	cp
Initial filtrate flow rate, q_o	0.051	cm^3/s
Particle mass density, ρ_p	4.28	g/cc
Particle deposition rate coefficient, k_d	0.00001	N/A
Particle erosion rate coefficient, k_e	0.001	s/cm
Particle mass/carrier fluid volume, C_p	0.5	g/cm^3
Critical shear stress, τ_{cr}	0.5	$dyne/cm^2$
Consistency index, k	0.0823	$dyne/cm^2/s^n$
Flow behavior index, n	0.735	N/A
Drillpipe/shaft rotary speed, RS	70	RPM
Wellbore pressure at the cake surface, P_c	13.61	atm
Formation pressure, P_e	6.804	atm
Temperature, T	220	^oF

6.1.1 Buff Berea Sandstone

The experimental and modeling profiles of dynamic-radial mud filtration in Buff Berea sandstone for the conditions in the plot are shown in Figure 6.1. The slight delay observed on the time axis for the experiment plot is the filtrate breakthrough time which has been described in section 5.3.1. The data in Table 6.1 were used to generate the model plot in Figure 6.1. The model shows very similar profile with the experimental plot. Beginning with the spurt invasion, both plots revealed an approximate spurt loss of 4 cm^3. Interestingly, both plots shown similar steady state filtration profiles with an average relative error that is less than 5 %. Furthermore, the model showed the same cumulative dynamic filtrate loss value as the experimental profile with no error.

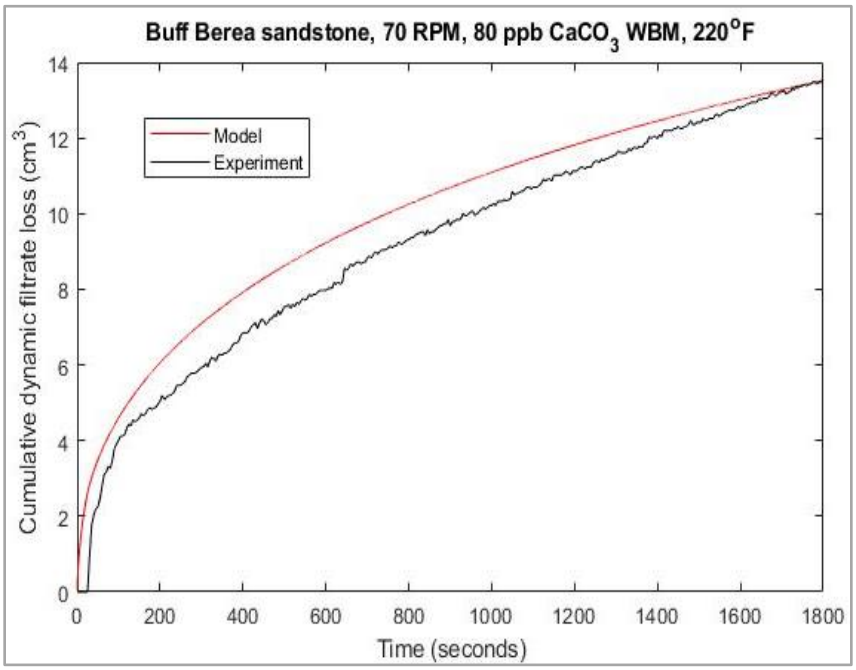

Figure 6.1: Experimental and modeling profiles of 80 ppb $CaCO_3$ WBM filtration in Buff Berea sandstone

From the model profile in Figure 6.1, sensitivity analysis was conducted on rotary speed (Figure 6.2). Keeping other parameters consistent, the results (profiles) show that an increase in rotary speed tends to increase dynamic filtrate loss in Buff Berea sandstone, while a decrease in rotary speed tends to decrease dynamic filtrate loss in this sandstone. The result from this analysis

validates the analytical interpretations and conclusion drawn on the effect of rotary speed on dynamic filtrate loss (Figure 5.15). Furthermore, the cumulative filtrate losses from the sensitive analysis are close to the experimental values (Figure 5.35) with less than 1% relative error.

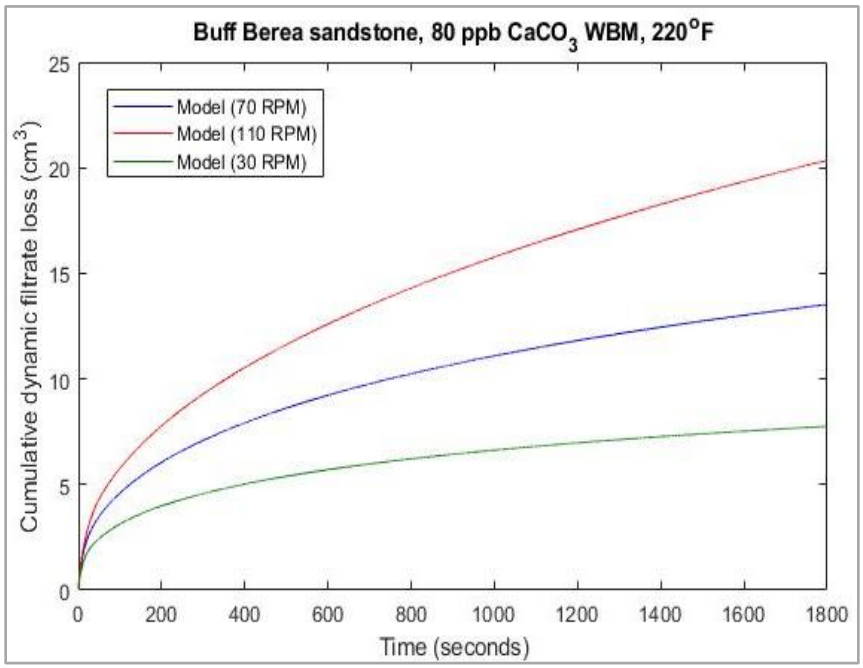

Figure 6.2: Sensitivity analysis of 80 ppb CaCO3 WBM filtration in Buff Berea sandstone.

6.1.2 Michigan Sandstone

The experimental and modeling profiles of dynamic-radial mud filtrate loss in Michigan sandstone for the conditions in the plot are shown in Figure 6.3. The model profile shows more spurt invasion while the experiment seems not to have shown a considerable spurt invasion. The is because the initial flowrate (q_o) is a critical parameter in the model as shown in equation (A.19) in Appendix A. Preliminary results have shown that the model's accuracy in predicting the spurt invasion tends to increase with an increase in the spurt loss recorded during an experiment. This is evident in the profiles shown in Figure 6.1 and Figure 6.3.

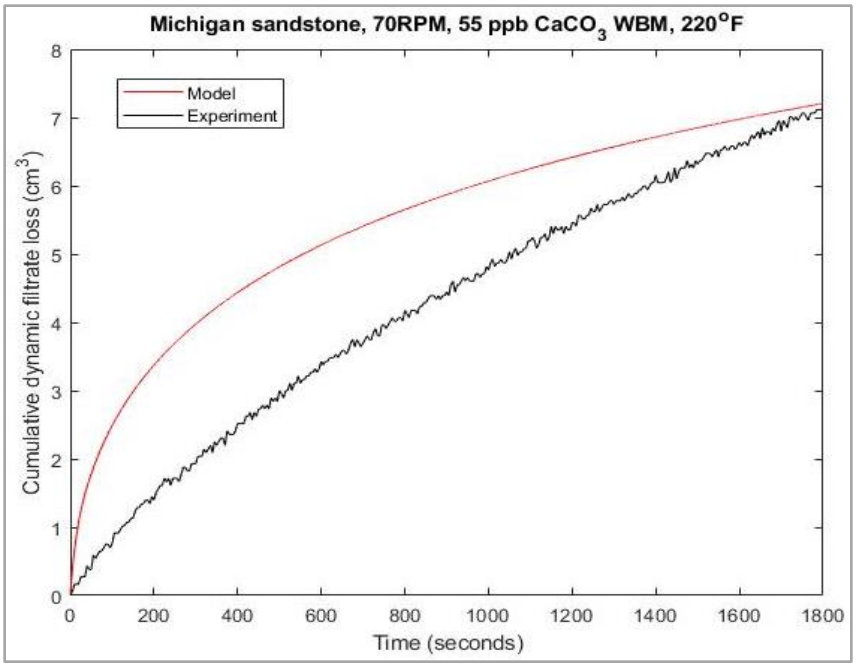

Figure 6.3: Experimental and modeling profiles of 55 ppb $CaCO_3$ WBM filtration in Michigan sandstone

Furthermore, this may be considered a limitation of the model because some of the dynamic-radial mud filtration experiments that have been performed on rock samples have shown little to no spurt losses. While in this case, there was negligible spurt loss, it is possible to conduct another experiment on a separate Michigan sandstone sample from the same core block under the same conditions and obtain a spurt invasion as high as the model prediction. Thus, the model's profile and predicted cumulative dynamic filtrate loss (less than 1.5 % relative error) are considered a good representation of the dynamic-radial fluid filtration in this rock for the conditions. In addition, the rotary speed sensitivity analysis was performed by keeping the other parameters constant. The plots in Figure 6.4 reveal that an increase rotary tends to increase dynamic filtrate loss in Michigan sandstone. The predicted value at 110 rpm is slightly more than the value obtained in the experiment (by 1 cm^3).

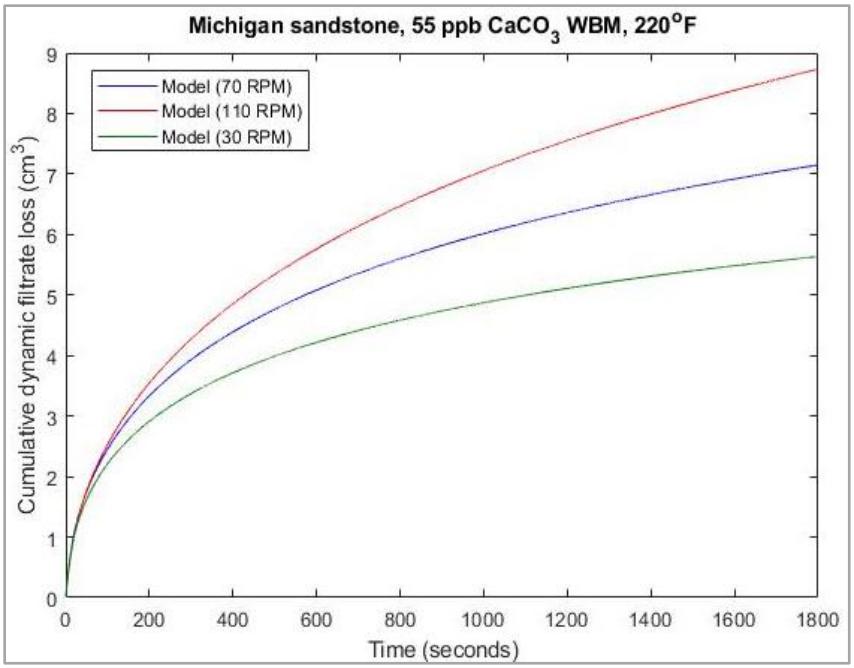

Figure 6.4: Sensitivity analysis of 55 ppb $CaCO_3$ WBM filtration in Michigan sandstone.

6.1.3 Upper Grey Sandstone

The experimental and modeling profiles of dynamic-radial mud filtrate loss in Upper Grey sandstone for the conditions in the plot are shown in Figure 6.5. Both plots show similar spurt loss patterns with the model's spurt loss being more by approximately 1 cm^3. The model and experiment show almost the same steady state filtration patterns and the same cumulative filtrate loss value. The sensitivity analysis results are shown in Figure 6.6 and the same pattern (increase in filtrate loss as rotary speed increases) was observed. Unlike the steep steady state filtration profiles in the high-permeability sandstones (Buff Berea and Michigan), the steady state filtrate profiles in Figure 6.6 tends to confirm lower permeability in Upper grey sandstone compared to Michigan and Buff Berea sandstones. The high spurt invasion can be attributed to the low $CaCO_3$ concentration, elevated rotary speed, and temperature.

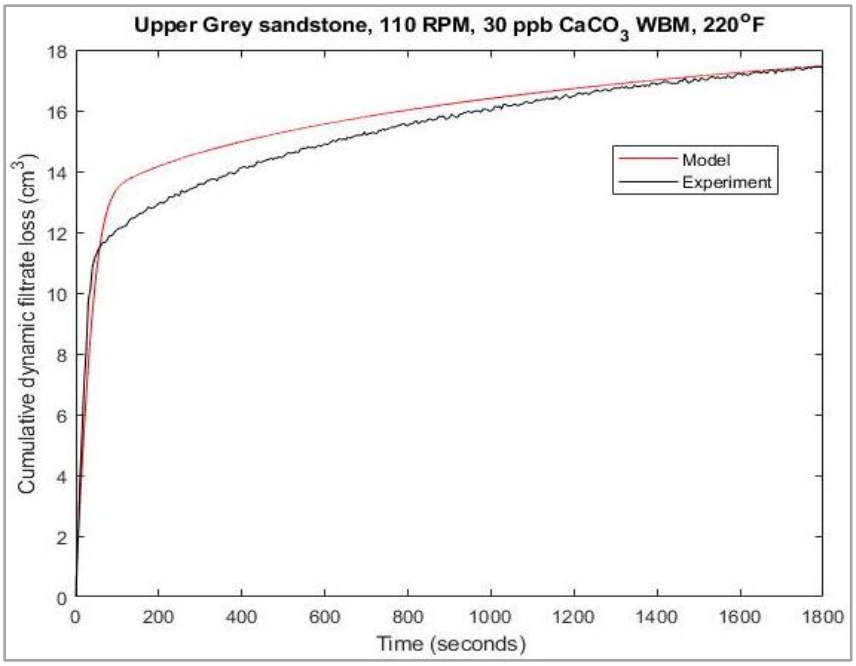

Figure 6.5: Experimental and modeling profiles of 30 ppb $CaCO_3$ WBM filtration in Upper Grey sandstone

In an actual field condition, rock heterogeneity plays a key role in drilling fluid loss and filtration. This has been discussed section 5.3. While the model accounts for individual rock permeability, porosity, and other porous media properties, it does not account for the experimental difference that is typically attributed to the specimen's heterogeneity (negligible rock heterogeneity and mineralogical effect). This is one of the model's assumptions. However, the model and its solution show good predictability of dynamic drilling fluids filtration and good sensitivity to changes in critical parameters such as rotary speed. For future work, it is recommended that more experiments be conducted for the same conditions with rock specimens from the same core block. The experimental results will shed better light on core blocks heterogenous effect while providing additional data that will enhance the model's predictability.

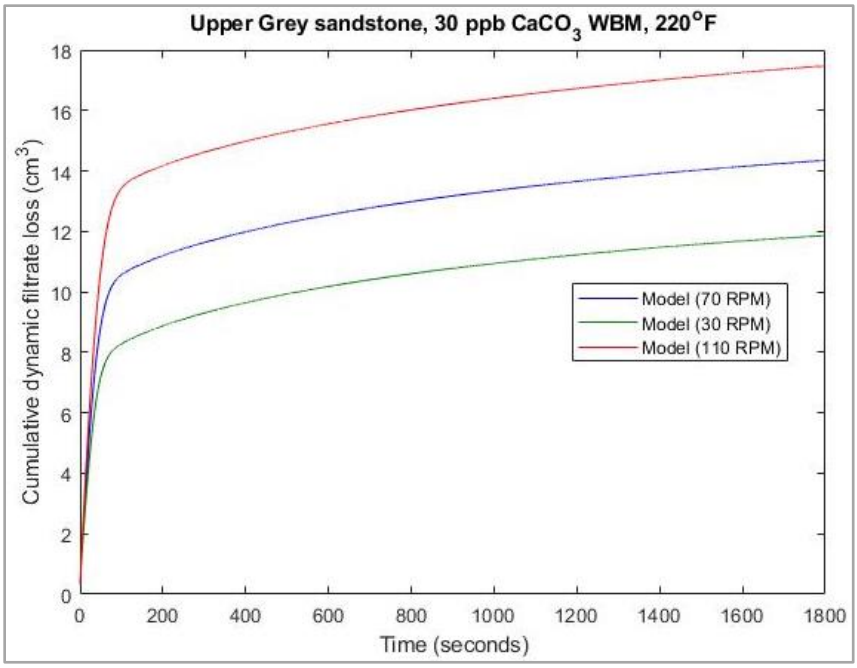

Figure 6.6: Sensitivity analysis of 30 ppb $CaCO_3$ WBM filtration in Upper Grey sandstone.

6.1.4 Indiana Limestone

Figure 6.7 shows the experimental and modeling profiles of dynamic-radial mud filtration in the 70 mD Indiana limestone. It can be observed that the model showed a good prediction of dynamic fluid filtration in this rock. The model's spurt loss was slightly higher (≈1.5 cm^3) but the steady state filtration was like the experimental profile. The model predicted cumulative filtration in this figure with less than 1% relative error. Figure 6.8 shows the rotary speed sensitivity analysis which also confirms that as the rotary speed increases, dynamic-radial mud filtration increases. The result at 30 rpm corresponds to the experimental value in Figure 5.40. Limestone mineralogical properties such as internal cavities, solution channels, and vuggy pores were not accounted for in the model. As a recommendation, additional experimental data from the same limestone blocks and experimental conditions can provide a better pattern for these mineralogical effects on dynamic drilling fluid filtration and its predictability.

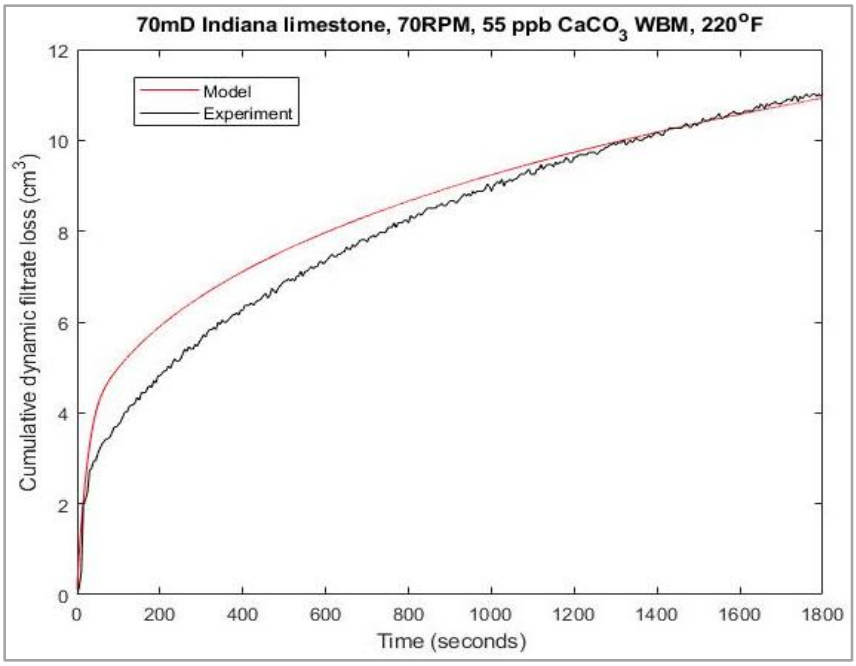

Figure 6.7: Experimental and modeling profiles of 55 ppb $CaCO_3$ WBM filtration in Indiana limestone

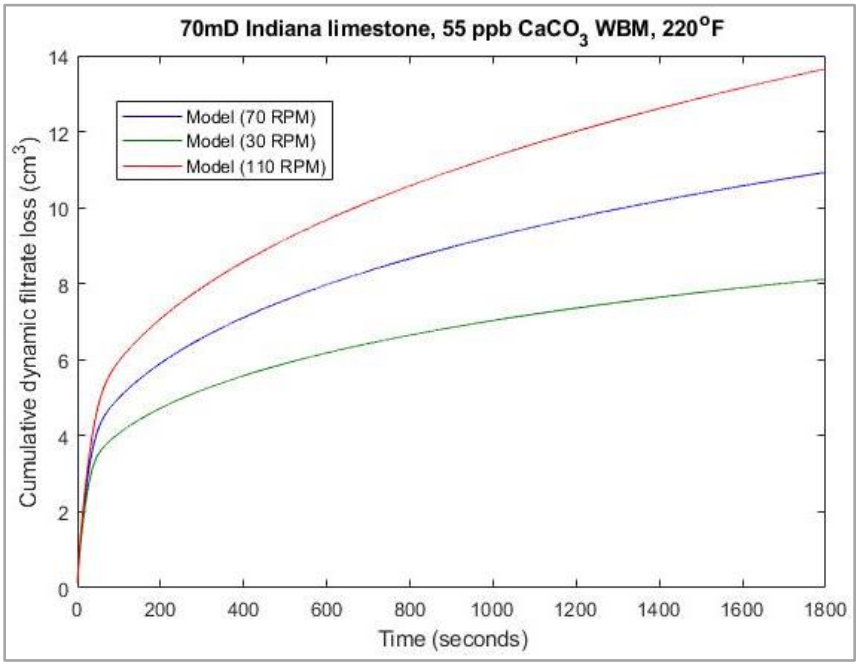

Figure 6.8: Sensitivity analysis of 55 ppb $CaCO_3$ WBM filtration in Indiana limestone

6.1.5 Effect of Axial Flow.

Figure 6.9 shows the modeling profiles of dynamic filtrate loss in Upper Grey sandstone without axial flow and with axial flow. The profile with no axial flow was validated with experimental results (see Figure 6.5). The results in Figure 6.9 show that the axial flow effect from mud flow rate tends to increase dynamic filtrate loss. In addition, the sensitivity analysis conducted on the model with changes in mud flow rate reveals that as the flow rate increase, the cumulative dynamic filtrate loss increases. The flow rate values were selected to match other laboratory-scale data. Since this is a mechanistic model, the challenge of scaling up and/or scaling down is eliminated. Although there is no experimental validation for the axial flow effect, the outcome of this model shows that it can be applied in field operations for predicating dynamic filtrate loss for well-specified operating conditions.

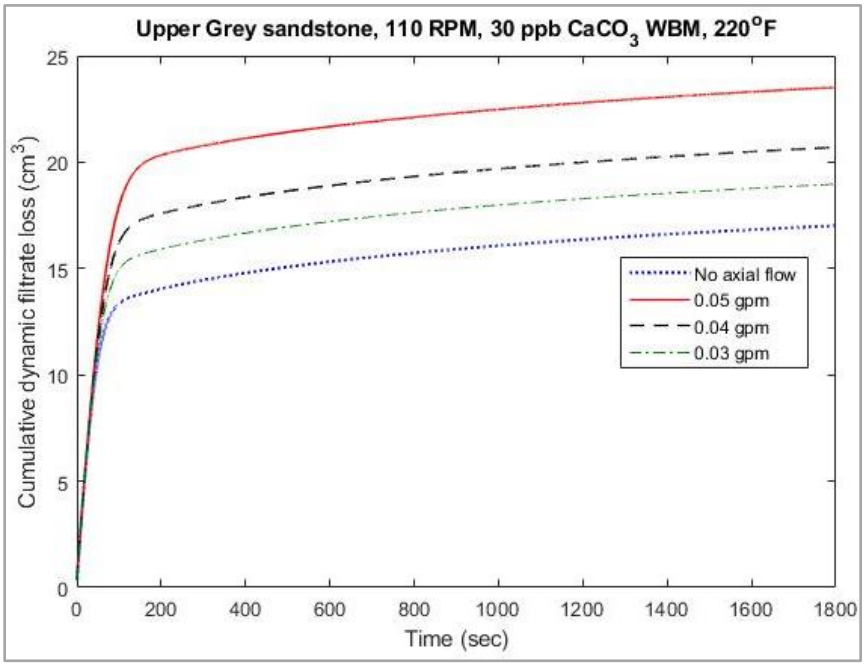

Figure 6.9: Sensitivity analysis to investigate the impact of axial flow

6.2 Wellbore Strengthening from Filter Cake Evolution

Filter cake development on the wellbore wall can be used to estimate wellbore strengthening characteristics in a rock. The analytical model combined with filter cake permeability profile and other filtration data gives an idea about the impact of rock and filter cake properties on increase in wellbore hoop stress. An investigation was carried out to evaluate the hoop stresses in the thick-walled cylindrical carbonate and sandstone rock samples. The 110 rpm experimental data with the lowest filtrate losses in Buff Berea sandstone (55 lb/bbl LCM) and Upper Grey sandstone (80 lb/bbl LCM) were used for hoop stress comparison in sandstone rocks. The 110 rpm experimental data with the lowest filtrate losses in 70 mD Indiana limestone (55 lb/bbl LCM) and Austin chalk (55 lb/bbl) were used for hoop stress comparison in carbonate rocks.

6.2.1 Hoop Stress Profiles in Sandstone Rocks

Buff Berea and Upper Grey sandstones were selected for this investigation because they represent high and low-permeability sandstones respectively. Their hoop stress profiles at an early time of mud and filtrate invasion are shown in Figure 6.10. The results show a higher hoop stress up to 100 % in the maximum horizontal stress direction for the Buff Berea sandstone. This result supports the mechanism of increased wellbore strength by filter cake in highly permeable rocks. Filter cake evolution is a time-dependent process which supports wellbore strengthening. A low-filter cake permeability profile was generated from the Buff Berea sandstone 55 lb/bbl LCM WBM experiment. This permeability profile corroborates the increase in the near-wellbore hoop stress with time. Although, the Upper Grey sandstone 80 lb/bbl LCM WBM experiment had lower cumulative filtrate loss, the filter cake permeability profile was high. This is because there was no spurt loss, late filter cake evolution, and low rock permeability compared to Buff Berea sandstone. The changes in hoop stress profile over time in Upper Grey sandstone was investigated. Figure

6.11 shows that at an early time, the hoop stress around the thick-walled cylindrical core is less because of its low permeability compared to Buff Berea sandstone. However, Figure 6.11 also shows that the hoop stress increased non-uniformly over time because of deposition of fluid particles around the near-wellbore wall and pore throats.

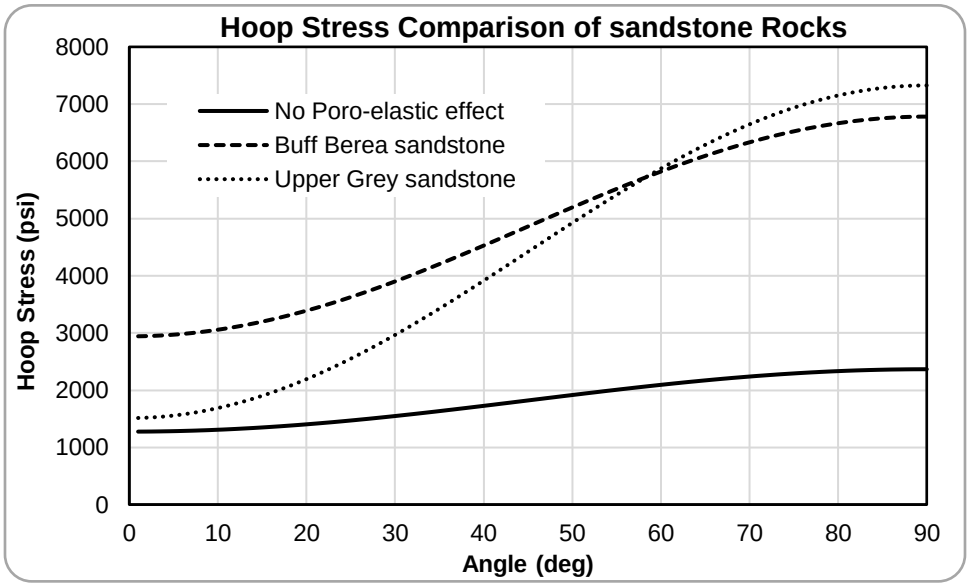

Figure 6.10: Hoop stress profiles around Buff Berea and Upper Grey sandstones

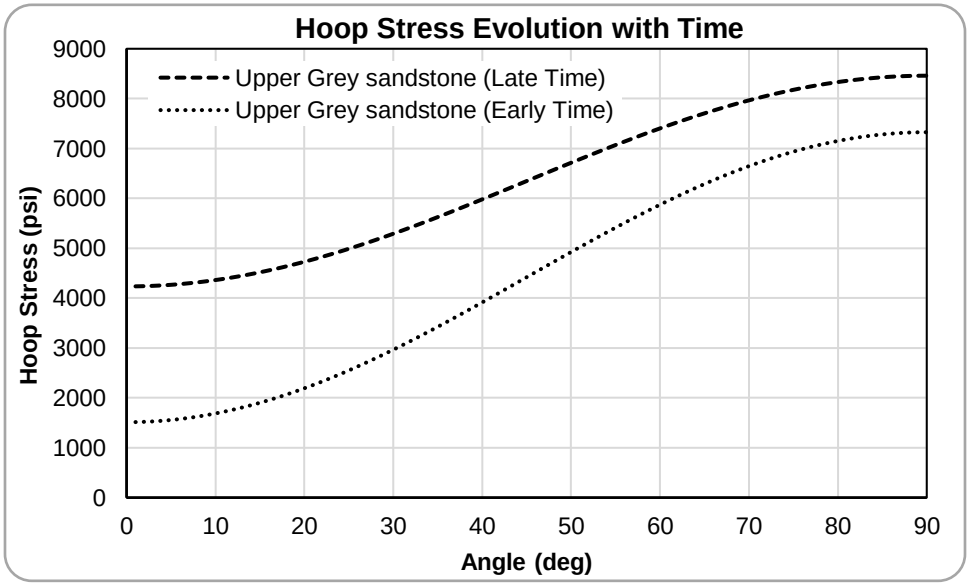

Figure 6.11: Time-dependent hoop stress evolution around Upper Grey sandstone

6.2.2 Hoop Stress Profiles in Carbonate Rocks

Wellbore hoop stress investigations were conducted for the carbonate rocks. Figure 6.12 shows the hoop stress profiles in Austin chalk and Indiana limestone. The figure shows that the hoop stress is higher in Austin chalk by 53 % compared to the limestone. The permeability of Austin chalk is low. However, its porosity (twice the porosity of Indiana limestone) is high. This proves to be a contributing factor that promotes deposition of fluid particle within the near-wellbore pore throats to make up the internal filter cake layer particles that aids rock strengthening. Furthermore, an ultra-low filter cake permeability profile was generated from the Austin chalk experiment with 55 lb/bbl LCM WBM. This is also a plausible contribution to the higher hoop stress profile compared to Indiana limestone with a high filter cake permeability profile.

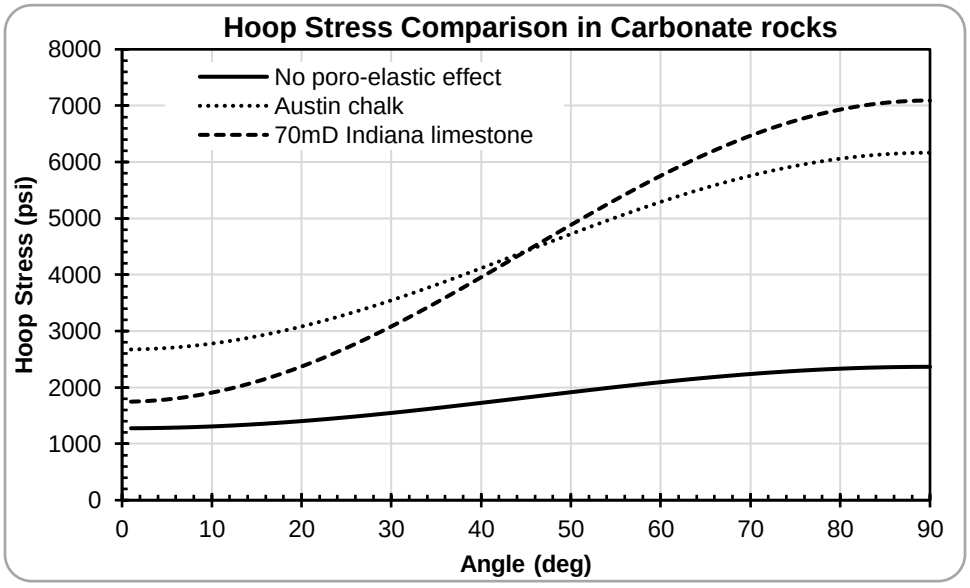

Figure 6.12: Hoop stress profiles around Austin chalk and 70mD Indiana limestone

In addition, the change in hoop stress profile with time was investigated for Indiana limestone. Figure 6.13 shows that as time elapses (up to 30 minutes), more than a 100 % increase in hoop stress in the maximum horizontal stress direction is recorded in Indiana limestone. This means that

as more fluid particles migrate and deposit around the near-wellbore pore throats, they form filter cake that supports wellbore strengthening.

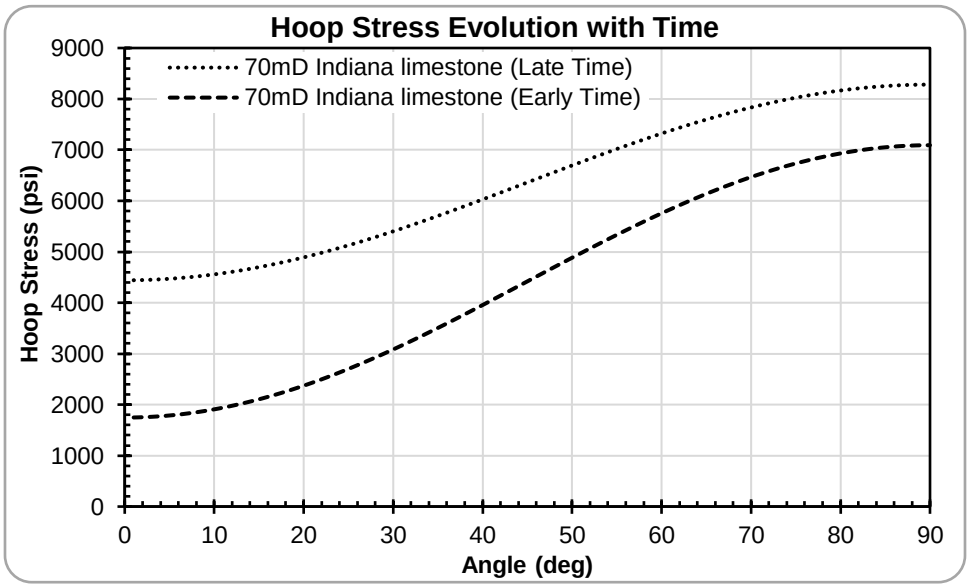

Figure 6.13: Time-dependent hoop stress evolution around 70mD Indiana limestone

Chapter 7: Summary, Conclusions, and Recommendations

7.1 Summary

This dissertation addresses dynamic drilling fluid loss and filtration with respect to dynamic wellbore conditions and implications on wellbore strengthening by filter cake. In this study, two research hypotheses were identified in section 1.2 and were solved using experimental, statistical, and numerical modeling approaches. Statistical design and analysis methods were used to systematically determine experimental runs, analyze the resulting data, and draw conclusions in response to the first research hypothesis. Different WBM formulations were considered, and dynamic fluid/filtrate loss experiments were conducted at different temperatures, pressures, and rotary speeds. Thick-walled cylindrical ceramic materials, sandstone rocks, carbonate rocks, and core slots (with varying fracture widths and orientations) were used to represent dynamic-radial drilling fluid loss and filtration in different porous media. A mechanistic model for predicting dynamic drilling fluid filtrate loss in different rocks and wellbore conditions was developed, solved, and validated with experimental values. Filter cake evolution from pore and fracture-scale drilling fluid invasion were used to estimate hoop stress profiles and filter cake stability for wellbore strengthening applications. The scientific observations and inferences from the experimental and post experimental investigations were used to draw conclusions in response to the second research hypothesis.

For field application, the outcome from this study can be used to generate performance curves of dynamic drilling fluid/filtrate loss for different lithologies, fracture orientation and sizes, and dynamic wellbore conditions. This will save the time and resources required for running fluid loss tests during drilling operations. In addition, it serves to improve the well design process by

providing a methodical approach that helps in selecting preventative recipes and operating conditions that can yield the desired wellbore strengthening outcomes.

7.2 Conclusions

The following conclusions have been drawn based on the results and observations:

1. A robust mechanistic model was developed and tuned based on laboratory data for predicting dynamic-radial mud filtrate in rocks. The model showed good predictability with an average relative error that is less than 5 %. It is recommended to incorporate all the realistic and anticipated wellbore conditions that influences dynamic mud filtration in the model.
2. The sensitivity analysis from the mechanistic model showed that dynamic mud filtrate loss increases as rotary speed increases. This result validates the experimental and statistical interpretations and conclusion drawn on the effect of rotary speed on dynamic mud filtrate loss.
3. An increase in calcium carbonate concentration (30 lb/bbl to 80 lb/bbl) can significantly decrease dynamic mud filtrate loss, while an increase in rotary speed (30 rpm to 110 rpm) and temperature (120^{o}F to 220^{o}F) can significantly increase dynamic mud filtrate loss. These conclusions were drawn from post-experimental analyses (hypothesis testing and ANOVA based on a 95% confidence interval). The order of their significance (from high to low) is: temperature > LCM concentration > rotary speed.
4. Post-experimental analyses showed that the two-factor interaction effects (AB, AC, and BC) have significant impact on dynamic mud filtrate loss. The order of their significance (from high to low) is: AC (LCM concentration/temperature) > BC (rotary speed/temperature) > AB (LCM concentration/rotary speed).

5. WBM rheology is significantly impacted by an increase in temperature, and this increases the susceptibility of mud and filtrate invasion. The degree of impact is largely dependent of the gelling material and type of LCM used in the formulation. For the calcium carbonate WBMs, between 60 % and 67 % reduction in apparent viscosity was recorded when temperature increases (75^{o}F to 210^{o}F). The Cedar fiber WBMs showed good rheological control up to 200^{o}F and maintained good plugging effects up to 220^{o}F.
6. In this study, fluid/filtrate breakthrough time is a delay phenomenon that has been identified to occur during dynamic mud filtration in rocks. The definition and factors influencing it have been detailed in section 5.3.1.
7. The SEM and EDS investigations revealed better uniform filter cake buildup in the near-wellbore pore throats of Michigan sandstone, compared to the limestone and chalk. They also showed typical carbonate rock mineralogical features such as internal fractures, solution channels, and vuggy pores. As a recommendation, the drilling fluids formulation for drilling carbonate rocks should consider a wide range of particle size distribution (PSD) because of these pre-existing features.
8. As a single factor consideration, low formation permeability does not always correlate to low fluid/filtrate loss. This conclusion is drawn from the experimental observations with the Austin chalk formation. Therefore, the permeability and porosity of rocks should be considered side-by-side amongst other factors in designing a preventative drilling fluid recipe.
9. A new LCM concentration selection criterion for calcium carbonate has been proposed based on operating conditions. For temperature $\leq$ 200^{o}F, rotary speed $\leq$ 70 rpm, rock permeability $\leq$ 105 mD, and rock porosity $\leq$ 23 %: Calcium carbonate concentration $\geq$ 55 lb/bbl or $\geq$ 5.8 % volume should be used. This criterion was developed from the experimental results which

revealed that at/below these conditions, 55 lb/bbl calcium carbonate WBM reduced cumulative dynamic mud filtrate loss by more than half compared to a base fluid (no LCM). Above these conditions, an increase in calcium carbonate concentration was not effective in reducing dynamic mud filtrate loss.

10. The cohesive strength of the external filter cakes in all the LCM WBM recipes was enhanced for fluid/filtrate loss reduction in fractures. This is evident in the reduced cumulative dynamic filtrate loss (55 lb/bbl $CaCO_3$ WBM) observed from the Bandera Brown rock experiment with two vertical fractures. An increase in the concentration of Cedar fiber (5 lb/bbl to 15 lb/bbl) revealed 58.1 % average decrease in cumulative dynamic fluid loss over three vertical fracture widths (500, 1000, and 2000 μm).
11. A new LCM concentration selection criterion for Cedar fiber was formulated based on operating conditions. For fracture widths ≤ 2000 μm, temperatures ≤ 220^{o}F, and rotary speeds ≤ 110 rpm: 2.4 % ≤ Cedar fiber volume concentration ≤ 14 %. This criterion is supported by the significance of the experimental and post-experimental analyses which showed good predictability of cumulative dynamic fluid loss.
12. The particle size distribution (PSD) of Cedar fiber and the material's particle orientation to the fracture entrance at the time of invasion are two key factors that impacts the evolution of a stable filter cake seal in fractures. Experimental results also showed that fracture orientation and positioning have considerable impacts on dynamic fluid loss.
13. In this study, the term "filter cake stability" has been defined as the ability of filter cake (formed in a fracture) to resist an increase in differential pressure (from 200 psi to 400 psi, at 110 RPM and 220^{o}F) and not rupture. The result from testing the filter cake stability at operating conditions was 67% successful for the nine cases. This implies that wellbore strengthening by

filter cake evolution in fractures (with widths up to 2000 μm) can be 67% successful with the proper fluid recipe and at elevated conditions (up to 220^{o}F and 110 RPM).

14. In this study, filter cake permeability profiles from the rocks were used in the numerical modeling of wellbore hoop stress instead of hypothetical filter cake profiles used in previous studies. The results showed an increase in hoop stress and better wellbore strengthening effects in Buff Berea sandstone compared to Upper Grey sandstone. For carbonate rock comparison, the numerical modeling results showed an increase in hoop stress and better wellbore strengthening in Austin chalk compared to the Indiana limestone.

7.3 Recommendations

Based on the results and conclusions, recommendations have been made for future work in this area of research. These include but not limited to:

1. The scope of this study limits it to water-based mud (WBM). It is recommended to extend this research effort to non-aqueous drilling fluids (NAF) and possibly aerated drilling fluids. This is because NAF's are recognized for good rheological stability at elevated temperatures, haven identified temperature as a critical factor that increases fluid loss and filtration.
2. Depending on the availability and accessibility, it is recommended to obtain drilling fluids directly from service providers who may be willing to release their field samples and/or recipes.
3. Using the statistical design and analysis approach, it is recommended to introduce multiple levels to the selected factors (depending on material availability and cost). This will increase the predictability of the regression analysis and empirical models.
4. It is recommended to investigate the effect of eccentricity, given that the configuration of the rotating shaft in the drilling simulator allows for a change in eccentricity.

5. For future work, it is recommended to conduct more experiments for the same conditions with rock sample from the same core block. The results will be used to develop a robust pattern for core blocks heterogeneity and rock mineralogical effects which can be used to enhance the mechanistic filtration model's predictability.
6. The experimental work performed in this study can be extended to high temperature conditions (beyond 220^{o}F up to 400^{o}F) for investigating fluid loss in geothermal drilling. In this case, it is recommended to use temperature-resistant gelling materials, temperature-enhanced LCMs, and various shapes of fracture slots.

Nomenclature

Acronyms

CC	Calcium carbonate concentration (*lb/bbl*)
CFC	Cedar fiber concentration (*lb/bbl*)
DF	Degree of freedom (*dimensionless*)
DFL	Dynamic fluid/filtrate loss (cm^3)
FW	Fracture width (*microns*)
FH	Fracture height (*microns*)
LCM	Lost circulation material (*dimensionless*)
ppg	Pounds per gallon
PR_1	Pressure regime 1 (*psi*)
PR_2	Pressure regime 2 (*psi*)
RS	Rotary speed (*RPM*)
WBM	Water based mud (*dimensionless*)

Statistical Design and Analysis Acronyms/Symbols

ANOVA	Analysis of variance
CI	Confidence interval
MS	Mean square
SS	Sum square
F_o	F statistics (F-test)
(1)	Low level of all factors
A	High level of factor A, low level of factors B and C
b	High level of factor B, low level of factors A and C

ab	High level of factors A and B, low level of factor C
c	High level of factor C, low level of factors A and B
ac	High level of factors A and C, low level of factor B
bc	High level of factors B and C, low level of factor A
abc	High level of factors A, B, and C
A	Main effect for factor A ($CaCO_3$ LCM concentration)
B	Main effect for factor B (rotary speed)
AB	Two-order interaction effect of factors A and B (LCM concentration and rotary speed)
C	Main effect of factor C (temperature)
AC	Two-order interaction effect of factors A and C (LCM concentration and temperature)
BC	Two-order interaction effect of factors B and C (rotary speed and temperature)
ABC	Three-order interaction effect of factors A, B, and C (LCM concentration, rotary speed, and temperature)

Other Symbols

A_{ann}	Annular area (cm^2)
c_p	Mass of particles per unit volume of carrier fluid in slurry, (g/cm^3)
D_{dp}	Drillpipe diameter, (cm)
D_h	Hydraulic diameter, (cm)
D_w	Wellbore diameter, (cm)
G	Ratio of the rotating shaft's diameter to the porous medium's inner diameter, (*dimensionless*)

h	Height of formation/cake height (*cm*)
K_f	Formation permeability, (*Darcy*)
K_c	External filter cake permeability, (*Darcy*)
k	Consistency index, ($dynes/cm^2/s^{n'}$)
k_d	Particle deposition rate coefficient (*dimensionless*)
k_e	Particle erosion rate coefficient (*sec/cm*)
n	Flow behavior index, (*dimensionless*)
P_c	Wellbore pressure at the cake surface, (*atm*)
P_e	Formation pressure, (*atm*)
Q	Mud flow rate (cm^3/sec)
q	Filtration rate, (cm^3/sec)
q_o	Initial filtrate flow rate, (cm^3/sec)
R_{ps}	Net mass rate of deposition of particles to form external filter cake, ($g/sec/cm^2$)
r_{dp}	Radius of drillpipe/rotary shaft (*cm*)
r_e	Reservoir radius, (*cm*)
r_c	Filter cake radius, (*cm*)
r_w	Wellbore radius, (*cm*)
T_f	Tortuosity of formation (*dimensionless*)
T_c	Tortuosity of filter cake (*dimensionless*)
u_c	Fluid flux at the cake surface, (*cm/sec*)
$\overline{Vel_{ann}}$	Mean annular velocity, (*cm/sec*)

Greek Symbol

β_i	Inertial flow coefficient, (cm^{-1})

ε_s	Volume mass fraction of solid in the filter cake
δ	Filter cake thickness, (*cm*)
ρ_p	Particle mass density, (g/cm^3)
Φ_c	Filter cake porosity, (*volume fraction*)
Φ_f	Formation porosity, (*volume fraction*)
τ_{cr}	Critical shear stress, ($dynes/cm^2$)
τ_{sts}	Slurry tangential shear stress at the cake surface, ($dynes/cm^2$)
τ_{sas}	Slurry axial shear stress at the cake surface, ($dynes/cm^2$)
τ_{srs}	Slurry resultant shear stress at the cake surface, ($dynes/cm^2$)
μ	Mud filtrate viscosity, (*cp*)
γ_{str}	Slurry tangential shear rate, (sec^{-1})
γ_{sar}	Slurry axial shear rate, (sec^{-1})
γ_{srr}	Slurry resultant shear rate, (sec^{-1})

References

1. Abrams, A. 1977. Mud Design to Minimize Rock Impairment Due to Particle Invasion. *J Pet Technol* **29** (5): 586-592. SPE-5713-PA. http://dx.doi.org/10.2118/5713-PA.

2. Ahmed, R. M. and Miska, S. Z. 2008. Experimental Study and Modeling of Yield Power-Law Fluid Flow in Annuli with Drillpipe Rotation. IADC/SPE Drilling Conference, Orlando, Florida, 4-6 March. IADC/SPE-112604-MS http://dx.doi.org/10.2118/112604-MS.

3. AlAwad, M. N. and Fattah, K. A. 2017. Utilization of Shredded Waste Car Tyres as a Fracture Seal Material (FSM) in Oil and Gas Drilling Operations. *Journal of Petroleum & Environmental Biotechnology*, **08** (02): 21-28. 3DAC8E964440. http://dx.doi.org/10.4172/2157-7463.1000322.

4. Alberty, M. and Yao, Z. 2018. A Practical Method to Monitor Wellbore Strengthening Particle Concentration. IADC/SPE Drilling Conference and Exhibition, Fort Worth Texas, 6-8 March. SPE-189584-MS. http://dx.doi.org/10.2118/189584-MS.

5. Alberty, M. W. and McLean, M. R. 2014. The Use of Modeling to Enhance the Analysis of Formation-Pressure Integrity Tests. *SPE Drill & Compl* **29** (4): 431-437. SPE-167945-PA. http://dx.doi.org/10.2118/167945-PA.

6. Alberty, M. W. and McLean, M. R. 2004. A Physical Model for Stress Cages. SPE Annual Technical Conference and Exhibition, Houston, USA, 26-29 September. SPE-90493-MS. http://dx.doi.org/10.2523/90493-MS.

7. Allen. D., Auzerais, F., Dussan, E. et al. 1991." Invasion Revisited" Oilfield Review.

8. Al Otaibi, M. B., Nasr-El-Din, H. A., and Hill, A. D. 2008. Characteristics and Removal of Filter Cake Formed by Formate-Based Drilling Mud. SPE International Symposium and Exhibition on Formation Damage Control, Lafayette, Louisiana, 13-15 February. SPE-112427-MS. https://doi.org/10.2118/112427-MS.

9. Alsaba, M. T. 2015. *Investigation of Lost Circulation Materials Impact on Fracture Gradient*. PhD Dissertation, Missouri University of Science and Technology, Rolla, Missouri (May 2015). https://scholarsmine.mst.edu/cgi/viewcontent.cgi?article=3439&context=doctoral_dissertations.

10. Alsaba, M. T., Nygaard, R., Saasen, A. et al. 2014. Laboratory Evaluation of Sealing Wide Fractures using Conventional Lost Circulation Materials. SPE Annual Technical Conference and Exhibition, Amsterdam, The Netherlands, 27-29 October. SPE-170576-MS. https://doi.org/10.2118/170576-MS.

11. Andreasen, A. and Andersen, J. 1930. Ueber die Beziehung zwischen Kornabstufung und Zwischenraum in Produkten aus losen Ko¨rnern. Kolloid-Zeitschrift, 217-228.

12. API 13 B-1, *Recommended Practice for Field Testing Water Based-Drilling Fluids*, Third

Edition 2003. Washington, DC: API.

13. Aston, M. S., Alberty, M.W., McLean, M. R. et al. 2004. Drilling Fluids for Wellbore Strengthening. IADC/SPE Drilling Conference, Dallas, Texas, 2-4 March. SPE-87130-MS. http://dx.doi.org/10.2118/87130-MS.

14. Awoleke, O. O., Romero, J. D., Zhu, D. et al. 2012. Experimental investigation of propped fracture conductivity in tight gas reservoirs using factorial design. SPE Hydraulic Fracturing Technology Conference, The Woodland, Texas. 6-8 February. SPE-151963-MS http://dx.doi.org/10.2118/151963-MS.

15. Bailey, W. J. and Peden, J. M. 1997. A Generalized and Consistent Pressure Drop and Flow Regime Transition Model for Drilling Hydraulics Suitable for Slimhole, Underbalanced and Horizontal Wells. SPE/IADC Middle East Drilling Technology Conference, Bahrain, 23-25 November. SPE/IADC-39281. http://dx.doi.org/10.2523/39281-MS.

16. Barton, C. A., Moos, D., Peska, P. et al. 1997. Utilizing Wellbore Image Data to Determine the Complete Stress Tensor: Application to Permeability Anisotropy and Wellbore Stability. *The log analyst*, **38** (06). SPWLA-1997-v38n6a1.

17. Bellarby, J. 2009. *Well Completion Design: Developments in Petroleum Science*, Vol 56. Amsterdam. Elsevier.

18. Berg, D., 2013. Use of Calcium Carbonate as a Drilling Fluid Additive. June 2013, http://www.carmeusena.com/sites/default/files/brochures/milled-limestone/ppt-limestone-oil-gas.pdf (accessed 20 November 2017).

19. Box, G. E. P. and Wislon, K. G. 1951. On the Experimental Attainment of Optimum Conditions." *Journal of the Royal Statistical Society*, B, **13**: 1–45. http://www.jstor.org/stable/2983966.

20. Bourgoyne, T. A., Chenevert, M. E., Millheim, K. K. et al. 1986. Applied Drilling Engineering Volume 2, Richardson Texas. SPE Text Book Series.

21. Brege, J., Chad F. C., Quintero, L. et al. 2010. Improving Wellbore Strengthening Techniques by Altering the Wettability of Non-Aqueous Fluids Lost to Drilling Induced Fractures. 2010 AADE Fluids Conference and Exhibition, Houston, Texas, 6-7 April. AADE-10-DF-HO-43.

22. Bruton, J. R., Ivan, C. D., and Heinz, T. J. 2001. Lost Circulation Control: Evolving Techniques and Strategies to Reduce Downhole Mud Losses. SPE/IADC Drilling Conference, Amsterdam, the Netherlands, 27 February -1 March. SPE-67735-MS. http://dx.doi.org/10.2523/67735-MS.

23. Byrne, M., Zubizarreta, I., and Sorrentino, Y. 2015. The Impact of Formation Damage on Core Quality. SPE European Formation Damage Conference and Exhibition Budapest, Hungary, 3-5 June. SPE-174189-MS. http://dx.doi.org/10.2118/174189-MS.

24. Canson, B. E. 1985. Lost Circulation Treatment for Naturally Fractured, Vugular, orCavernous

Formations. SPE/IADC Drilling Conference, New Orleans, Louisiana, 5-8 March. SPE/IADC 13440. http://dx.doi.org/10.2523/13440-MS.

25. Caughron, D., Renfrow, D., Bruton, J. et al. 2002. Unique Crosslinking Pill in Tandem with Fracture Prediction Model Cures Circulation Losses in Deepwater Gulf of Mexico. IADC/SPE Drilling Conference, Dallas, Texas, USA, 26-28 February. SPE-74518-MS. https://doi.org/10.2523/74518-MS.

26. Cerasi, P., Ladva, H. K., Bradbury, A. J. et al. 2001. Measurement of the Mechanical Properties of Filter Cakes. SPE European Formation Damage and Conference, Hague, The Netherlands, 21-22 May. SPE-68948-MS. http://dx.doi.org/10.2118/68948-MS.

27. Chellappah, K., Kumar, A., and Aston, M. 2015. Drilling Depleted Sands: Challenges Associated with Wellbore Strengthening Fluids. SPE/IADC Drilling Conference and Exhibition, London, United Kingdom. 17-19 March. SPE/IADC-173073-MS. http://dx.doi.org/10.2118/173073-MS.

28. Chellappah, K. and Aston, M., 2012. A New Outlook on the ideal packing Theory of Bridging Solids. SPE International Symposium and Exhibition on formation Damage Control, Lafayette, Louisiana, 15-17 February. SPE 151636-MS. http://dx.doi.org/10.2118/151636-MS.

29. Chen, G. and Yu, L. 2015. Consolidation Around a Tunnel in a General Poroelastic Medium Under Anisotropic Initial Stress *Conditions. Comput. Geotech.*, **66** (2015): 39–52. http://dx.doi.org/10.1016/j.compgeo.2015.01.007.

30. Chenevert, M. E. and Dewan, J. T. 2001. A Model for Filtration of Water-base Mud During Drilling: Determination of Mud Cake Parameters. *Petrophysics* **42** (3): 237-250. SPWLA-2001-v42n3a4.

31. Chu, C. F. 1990. Prediction of Steamflood Performance in Heavy Oil Reservoirs Using Correlations Developed by Factorial Design Method. Presented at the 1990 California Regional Meeting, Ventura, California. 4-6 April. SPE-20020-MS. https://doi.org/10.2118/20020-MS.

32. Churcher, P. L., French, P. R., Shaw, J. C. et al. 1991. Rock Properties of Berea Sandstone, Baker Dolomite, and Indiana Limestone. SPE International Symposium on Oilfield Chemistry, Anaheim, California, 20-22 February. SPE 21044. https://doi.org/10.2523/21044-MS.

33. Civan, F. 2007. *Reservoir Formation Damage*, second edition, Gulf Publishing Company, Waltham, MA, U.S.A, pp: 341-403, pp. 780-782.

34. Civan, F. 1998. Incompressive Cake Filtration: Mechanism, Parameters, and Modeling. *AIChE Journal*, **44** (11): 2379–2387. http://dx.doi.org/10.1002/aic.690441106.

35. Civan, F. 1996. A Multi-Purpose Formation Damage Model. SPE International Symposium and Exhibition on Formation Damage Control, Lafayette, Louisiana, 14-15 February. SPE-31101-MS https://doi.org/10.2118/31101-MS.

36. Civan, F. 1994. A Multi-Phase Mud Filtrate Invasion and Wellbore Filter Cake Formation Model. SPE International Petroleum Conference and Exhibition of Mexico, Veracruz, Mexico, 10-13 October. SPE-28709-MS. https://doi.org/10.2118/28709-MS.

37. Contreras, O., Hareland, G., Husein, M. et al. 2014. Wellbore Strengthening in Sandstones by Means of Nanoparticle-Based Drilling Fluids. SPE Deepwater Drilling and Completions Conference, Galveston Texas, 10-11 September. SPE-170263-MS. http://dx.doi.org/10.2118/170263-MS.

38. Cook, J., Guo, Q., Way, P. et al. 2016. The Role of Filter Cake in Wellbore Strengthening. IADC/SPE Drilling Conference and Exhibition, Fort Worth, Texas, 1-3 March. IADC/SPE-178799-MS. http://dx.doi.org/10.2118/178799-MS.

39. Cui L., Abousleiman, Y., Cheng, H. D. et al. 1999. Time-Dependent Failure Analysis of Inclined Boreholes in Fluid-Saturated Formations. *ASME. J. Energy Resour. Technol*. **121** (1): 31-39. http://dx.doi.org/10.1115/1.2795057.

40. Dorman, J., Lakatos, I. J., Szentes, G. et al. 2015. Mitigation of Formation Damage and Wellbore Instability in Unconventional Reservoirs Using Improved Particle Size Analysis and Design of Drilling Fluids. SPE European Formation Damage Conference and Exhibition, Budapest, Hungary, 3-5 June. SPE 174260-MS. http://dx.doi.org/10.2118/174260-MS.

41. Dupriest, F. E., Smith, M. V., Zeilinger, C. S. et al. 2008. Method to Eliminate Lost Returns and Build Integrity Continuously with High-Filtration-Rate Fluid. SPE/IADC Drilling Conference, Orlando, Florida, USA, 4-6 March. SPE-112656-MS. https://doi.org/10.2118/112656-MS.

42. Dupriest, F. E. 2005. Fracture Closure Stress (FCS) and Lost Returns Practices. SPE/IADC Drilling Conference, Amsterdam, Netherlands, 23-25 February. SPE-92192-MS. https://doi.org/10.2523/92192-MS.

43. Elkatatny, S., Mahmoud, M., and Nasr-El-Din, H. A. 2013. Filter Cake Properties of Water-Based Drilling Fluids Under Static and Dynamic Conditions Using Computed Tomography Scan. *ASME. J. Energy Resour. Technol*, **135** (4): 042201-042201-9. https://doi.org/10.1115/1.4023483.

44. Espinosa, C., Codega, D., Caglieri, A. et al. 2017. Five Years of Drilling with Casing in Argentina and Bolivia. Lessons Learned from the Field. SPE Latin America and Caribbean Petroleum Engineering Conference, Buenos Aires, Argentina, 18-19, May. SPE-185506-MS. https://doi.org/10.2118/185506-MS.

45. Ezeakacha, C. P. and Salehi, S. 2018. Experimental and Statistical Investigation of Drilling Fluids Loss in Porous Media-Part 1. *Journal of Natural Gas Science and Engineering* **51**: 104-115. https://doi.org/10.1016/j.jngse.2017.12.024

46. Ezeakacha, C. P., Salehi, S., and Hayatdavoudi, A. 2017. Experimental Study of Drilling Fluid's Filtration and Mud Cake Evolution in Sandstone Formations. *ASME. J. Energy Resour. Technol*, **139** (2): 022912-022912-8. https://doi.org/10.1115/1.4035425.

47. Ezeakacha, C. P., Salehi, S., Ghalambor, A. et al. 2016. An Integrated Study of Mud Plastering Effect for Reducing Filtrate's Invasion. SPE International Symposium and Exhibition on Formation Damage Control, Lafayette, Louisiana, 26-28 February. SPE 179016-MS. http://dx.doi.org/10.2118/179016-MS.

48. Ezeakacha, C. P. 2014. "*Experimental Investigation of Particle Bridging and Wellbore Strengthening Effects for Casing while Drilling (CwD) Application*." Master's Thesis. University of Louisiana at Lafayette, Lafayette, Louisiana. December 2014. https://pqdtopen.proquest.com/doc/1765654821.html?FMT=ABS.

49. Fakhreldin, Y. E. 2010. Novel Fluid Formulations to Remove Mud Filter-Cake without Affecting Rock Mineralogy. SPE Production and Operations Conference and Exhibition, Tunis, Tunisia, 8-10 June. SPE-136093-MS. https://doi.org/10.2118/136093-MS.

50. Farahani, M., Soleimani, R., Jamshidi, S. et al. 2014. Development of a Dynamic Model for Drilling Fluid's Filtration: Implication to Prevent Formation Damage. SPE International Symposium and Exhibition on formation Damage Control, Lafayette, Louisiana, 26-28 February. SPE-168151-MS. http://dx.doi.org/10.2118/168151-MS.

51. Fidan, E., Babadagli, T., and Kuru, E. 2004. Use of Cement as Lost-Circulation Material: Best Practices. Canadian International Petroleum Conference, Calgary, Alberta, 8-10 June. PETSOC-2004-090. https://doi.org/10.2118/2004-090.

52. Forchheimer, P. 1901. Wasserbewegung durch Boden, Zeitz. Version. Deutsch Ing. 45, 1901, 1782-1788.

53. Fisher, R. A. *The Design of Experiments*. *8th edition*. Hafner Publishing Company, New York (1966).

54. Ghalambor, A., S. Salehi, M. Shahri, et al. 2014. Integrated Workflow for Loss Circulation Prediction. SPE International Symposium and Exhibition for Formation Damage and Control, Lafayette, Louisiana, 26-28 February. SPE-168123-MS. http://dx.doi.org/10.2118/168123-MS.

55. Greaves, M., Dudley, J. W. O. and Field, R. W. 1989. Factorial experiments in in situ combustion. Petroleum Society of Canada Annual Technical Meeting, June 10 - 13, Calgary, Alberta. CIMISPE 90-64. http://dx.doi.org/10.2118/90-64.

56. Guo, Q., Cook, J., Way, P. et al. 2014. A Comprehensive Experimental Study on Wellbore Strengthening. IADC/SPE Drilling Conference and Exhibition, Fort Worth Texas, 4-6 March. IADC/SPE 167957-MS. http://dx.doi.org/10.2118/167957-MS.

57. Haghshenas, A., Paknejad, A., Rehm, B. et al. 2008. *Managed Pressure Drilling*, Gulf Publishing Company, Houston, TX, U.S.A, pp: 1-5.

58. Haq, I., Spriggs, P., Buyers, G. et al. 2016. Managed Pressure, Deep Water Drilling and Logging Under Continuous Reservoir Cross Flow Conditions – A Case History. SPE/IADC Managed Pressure Drilling and Underbalanced Operations Conference and Exhibition,

Galveston Texas, 12-13 April. SPE/IADC-179188-MS. https://doi.org/10.2118/179188-MS.

59. Hemphill, T. and Ravi, K. 2005. Calculation of Drill Pipe Rotation Effects on Axial Flow: An Engineering Approach. SPE Annual Technical Conference and Exhibition, Dallas, Texas, USA, 9-12 October. SPE-97158-MS. http://dx.doi.org/10.2118/97158-MS.

60. Hettema, M., Horsrud, P., Taugbol, K. et al. 2007. Development of an Innovative High-Pressure Testing Device for the Evaluation of Drilling Fluid Systems and Drilling Fluid Additives within Fractured Permeable Zones. Offshore Mediterranean Conference and Exhibition. Ravenna, Italy, 28-30 March. OMC-2007-082. https://www.onepetro.org/conference-paper/OMC-2007-082.

61. Howard, G. C. and Scott, P. P. 1951. An Analysis and the Control of Lost Circulation. *J Pet Technol*, **3** (6): 171-182. https://doi.org/10.2118/951171-g.

62. Ibeh, C.S., 2007. *Investigation on the effects of ultra-high pressure and temperature on the rheological properties of oil-based drilling fluids* (Doctoral dissertation, Texas A&M University). http://oaktrust.library.tamu.edu/handle/1969.1/ETD-TAMU-2569.

63. Jahn, F., Cook, M., and Graham, M. 2008. *Hydrocarbon Exploration & Production*, 2nd Edition. Elsevier Science, Oxford, UK.

64. Jeennakorn, M., Nygaard, R., Nes, O. et al. 2017. Testing Conditions Make a Difference when Testing LCM. *Journal of Natural Gas Science and Engineering* **46**: 375-386. https://doi.org/10.1016/j.jngse.2017.08.003.

65. Jiao, D. and Sharma, M. M. 1994. Mechanism of Cake Buildup in Crossflow Filtration of Colloidal Suspensions. *Journal of Colloid and Interface Science*, **162** (2): 454-462. http://dx.doi.org/10.1006/jcis.1994.1060.

66. Jilani, S. Z., Menouar, H., Al-Majed, A. A. et al. 2002. Effect of Overbalance Pressure on Formation Damage. *Journal of Petroleum Science and Engineering*, **36** (1-2): 97-109. https://doi.org/10.1016/s0920-4105(02)00268-1.

67. Karimi, M., Petrie, S. W., Moellendick, E. et al. 2011. A Review of Casing Drilling Advantages to Reduce Lost Circulation, Augment Wellbore Strengthening, Improve Wellbore Stability, and Mitigate Drilling-induced Formation Damage. SPE/IADC Middle East Drilling Technology Conference and Exhibition, Muscat, Oman, 24-26 October. SPE- 148564-MS. http://dx.doi.org/10.2118/148564-MS.

68. Khan, H., Mirabolghasemi, M., Yang, H. et al. 2016. Comparative Study of Formation Damage due to Straining and Surface Deposition in Porous Media. SPE International Symposium and Exhibition on formation Damage Control, Lafayette, Louisiana, 26-28 February. SPE-178930-MS. http://dx.doi.org/10.2118/178930-MS.

69. Kiran, R. and Salehi, S. 2016. Thermoporoelastic Modeling of Time-Dependent Wellbore Strengthening and Casing Smear. *ASME. J. Energy Resour. Technol* **139** (2): 022903-022903-7. https://doi.org/10.1115/1.4033591

70. Kiran, R., Salehi, S. & Karimi, M., 2014. Finite Element Analysis of Casing Drilling Smearing Effect. SPE Deepwater Drilling and Completions Conference. Galveston Texas, 10-11 September. SPE-170314-MS. http://dx.doi.org/10.2118/170314-MS.

71. Lavrov, A. and Tronvoll, J. 2004. Modeling Mud Loss in Fractured Formations. 11th Abu Dhabi International Petroleum Exhibition and Conference, Abu Dhabi, UAE, 10-13 October. SPE-88700. http://dx.doi.org/10.2118/88700-MS.

72. Lecolier, E., Herzhaft, B., Rousseau, L. et al. 2005. Development of a Nanocomposite Gel for Lost Circulation Treatment. SPE European Formation Damage Conference, Sheveningen, The Netherlands, 25-27 May. SPE-94686- MS. https://doi.org/10.2118/94686-MS.

73. Lietard, O., Kirvelis, R., and Guillot, D. 2004. The Radial Flow Model of Mud Loss into Natural Fractures: Improvements and Field Applications. Unsolicited SPE 88661 received by the SPE office in Richardson Texas, April 17, 2004.

74. Loeppke, G. E., Glowka, D. A., and Wright, E. K., 1990. Design and Evaluation of Lost-Circulation Materials for Severe Environments. *J Pet Technol*, **42** (3): 328-337. SPE-18022-PA. https://doi.org/10.2118/18022-PA.

75. Ling, K., Zhang, H., Shen, Z. et al. 2015. A New Approach to Estimate Invasion Radius of Water-Based-Drilling-Fluid Filtrate to Evaluate Formation Damage Caused by Overbalanced Drilling. *SPE Drilling & Completion*, **30** (01), pp.27–37. http://dx.doi.org/10.2118/168184-PA

76. Liu, X., Civan, F. and Evans, R. D. 1995. Correlation of the Non-Darcy Flow Coefficient. *Journal of Canadian Petroleum Technology*, **34** (10). http://dx.doi.org/10.2118/95-10-05.

77. Majidi, R., Miska, S., and Zhang, J. 2011. Fingerprint of Mud Losses into Natural and Induced Fractures. SPE European Formation Damage Conference, Noordwijk, The Netherlands, 7-11, April. SPE-143854-MS. http://dx.doi.org/10.2118/143854-MS.

78. Mansour, A., Ezeakacha, C. P., Taleghani, A. D. et al. 2017. Smart Lost Circulation Materials for Productive Zones. SPE Annual Technical Conference and Exhibition, San Antonio, Texas, 9-11 October. SPE-187099-MS. http://dx.doi.org/10.2118/187099-MS.

79. Mata, F. and Veiga, M. 2004. Crosslinked Cements Solve Lost Circulation Problems. SPE Annual Technical Conference and Exhibition, Houston, Texas, USA, 26-29 September. SPE-90496-MS. http://dx.doi.org/10.2118/90496-MS.

80. Mashaal, M., Fuller, T., Brown, C. et al. 2013. Managed Pressure Drilling, Casing and Cementing Success in Conventionally Undrillable Wells in Harding Field. SPE Annual Technical Conference and Exhibition, New Orleans, Louisiana. 30th September – 2nd October. SPE 166170-MS. https://doi.org/10.2118/166170-MS.

81. Messenger, J. U. 1981. *Lost Circulation*. PennWell Corp, Tulsa, Oklahoma.

82. Menezes, R. R., Marques, L. N., Campos L. A. et al. 2010. Use of Statistical Design to Study the Influence of CMC on the Rheological Properties of Bentonite Dispersions for Water-based

Drilling Fluids. *Applied Clay Science* **49** (2010): 13-20. https://doi.org/10.1016/j.clay.2010.03.013.

83. Menezes, R. R., Brasileiro, M. I., Gonçalves, W. P. et al. 2009. Statistical design for recycling kaolin processing waste in the manufacturing of mullite-based ceramics. *Materials Research* **12** (2): 201–209. https://doi.org/10.1590/s1516-14392009000200015.

84. Montgomery, D. C. 2013. *Design and Analysis of Experiments*, eight edition, John Wiley and Sons, Inc.

85. Morita, N., Black, A. D., and Fuh, G. F. 1990. Theory of Lost Circulation Pressure. SPE Annual Technical Conference, New Orleans, Louisiana, 23-26 September. SPE-20409-MS. https://doi.org/10.2118/20409-MS.

86. Munoz, G., Dhafeeri, B., and Saggaf, H. 2016. Directional Casing while Drilling Reestablished as Viable Technology in Saudi Arabia. SPE/IADC Middle East Technology Conference and Exhibition, Abu Dhabi UAE, 26-28, January. IADC/SPE-178193-MS. https://doi.org/10.2118/178193-MS.

87. Nwaoji, C., Hareland, G., Husein, M. et al. 2013. Wellbore Strengthening- NanoParticle Drilling Fluid Experimental Design Using Hydraulic Fracture Apparatus. SPE/IADC Drilling Conference, Amsterdam, The Netherlands, 5-7 March. SPE/IADC 163434-MS. http://dx.doi.org/10.2118/163434-MS.

88. Nygaard, R. and Salehi, S. 2011. A Critical Review of Wellbore Strengthening: Physical Model and Field Deployment. American Association of Drilling Engineers. AADE-11-NTCE-24.

89. Ofite Testing Equipment Ceramic Disk Chart. http://www.ofite.com/ceramic-filter-disks. (accessed 10 October 2017).

90. Ooms, G. and Kampman-Reinhartz, B. E. 2000. Influence of Drillpipe Rotation and Eccentricity on Pressure Drop Over Borehole with Newtonian Liquid During Drilling. *SPE Drill & Compl* **15** (04): 249–253. http://dx.doi.org/10.2118/67618-PA.

91. Powers, M. C. 1953. A New Roundness Scale for Sedimentary Particles. *Journal of Sedimentary Research* **23** (2): 117-119. https://doi.org/10.1306/d4269567-2b26-11d7-8648000102c1865d.

92. Rehm, B., Haghshenas, A., Paknejad A. S. et al. 2012. *Underbalanced Drilling: Limits and Extremes*. Gulf Publishing Company, Houston, TX

93. Rosenberg, S. and Gala, D. 2012. Use of Liner Drilling Technology as a Mitigation for Loss Intervals and Hole Instability: A Case Study for Mississippi Cayon. SPE/IADC Drilling Conference, San Diego, California, 6-8 March. IADC/SPE 151181-MS. http://dx.doi.org/10.2118/151181-MS.

94. Saasen, A., Wold, S., Ribesen, B. T. et al. 2011. Permanent Abandonment of a North Sea Well

Using Unconsolidated Well Plugging Material. *SPE Drill & Compl* **26** (3): 371-375. SPE-133446-PA. https://doi.org/10.2118/133446-PA.

95. Saasen, A., Godøy, R., Breivik, D. H. et al. 2004. Concentrated Solid Suspension as an Alternative to Cements for Temporary Abandonment Applications in Oil Wells. SPE Technical Symposium of Saudi Arabia Section, Dhahran, Saudi Arabia, 15-17 May. SPE-SA-34.

96. Salehi, S. and Kiran, R. 2016. Integrated Experimental and Analytical Wellbore Strengthening Solutions by Mud Plastering Effects. *ASME. J. Energy Resour. Technol*. **138** (3): 032904-032904-7. https://doi.org/10.1115/1.4032236.

97. Salehi, S., Ghalambor, A., Saleh, F. K. et al. 2015. Study of Filtrate and Mud Cake Characterization in HPHT: Implications for Formation Damage Control. SPE European Formation Damage Conference and Exhibition, Budapest, Hungary, 3-5 June. SPE 174273-MS. http://dx.doi.org/10.2118/174273-MS.

98. Salehi, S., Hussmann, S., Karimi, M. et al. 2014. Profiling Drilling Fluid's Invasion Using Scanning Electron Microscopy: Implications for Bridging and Wellbore Strengthening Effects. SPE Deepwater Drilling and Completions Conference, Galveston, Texas, 10-11 September. SPE-170315-MS. http://dx.doi.org/10.2118/170315-MS.

99. Salehi, S., Karimi, M., Shahri, M. P. et al. 2013. All in One for All in One for Casing while Drilling Technology: Numerical, Analytical, and Experimental Results and Field Observations. SPE Annual Technical Conference and Exhibition, New Orleans, Louisiana, 30 September-2 October. SPE 166112-MS. http://dx.doi.org/10.2118/166112-MS.

100. Salehi, S. 2012. *Numerical Simulations of Fracture Propagation and Sealing: Implications for Wellbore Strengthening*. PhD Dissertation, Missouri University of Science and Technology, Rolla, Missouri (May 2012). https://scholarsmine.mst.edu/cgi/viewcontent.cgi?article=3367&context=doctoral_dissertations.

101. Salehi, S., and Nygaard, R., 2011. Numerical Study of Fracture Initiation, Propagation, Sealing to Enhance Wellbore Fracture Gradient. 45th US Rock Mechanics/ Geomechanics Symposium, San Francisco California, 26-29 June. ARMA 11-186.

102. Salehi, S., Hareland, G., and Nygaard, R. 2010. Numerical Simulations of Wellbore Stability in Under-Balanced-Drilling Wells. *Journal of Petroleum Science and Engineering* **72** (3–4): 229–235. http://dx.doi.org/10.1016/j.petrol.2010.03.022.

103. Sanfillippo, F., Brignoli, M., Santarelli, F. J. et al. 1997. Characterization of Conductive Fractures While Drilling. SPE European Formation Damage Conference, The Hauge, The Netherlands, 2-3 June. SPE-38177. http://dx.doi.org/10.2118/38177-MS.

104. Schembre, J. M. and Kovscek, A. R. 2005. Mechanism of Formation Damage at Elevated Temperature. *ASME. J. Energy Resour. Technol*, **127** (3): 171-180. http://dx.doi.org/10.1115/1.1924398.

105. Shelkholeslami, B. A., Schlottman, B. W., Seldel, F. A. et al., 1991. Drilling and Production Aspects of Horizontal Wells in the Austin Chalk. *Journal of Petroleum Technology*, **43** (07): 773–779. https://doi.org/10.2118/19825-PA.

106. Steffe, J. F. 1996, *Rheological Methods in Food Process Engineering, second edition*, Freeman Press, East Landing, MI, U.S.A, pp: 156-169.

107. Sun, Y. and Huang, H. 2015. Effect of Rheology on Drilling Mud Loss in a Natural Fracture. 49th US Rock Mechanics/Geomechanics Symposium held in San Francisco, CA, USA, 28 June- 1 July.

108. Talbot, A. 1979. The Accurate Numerical Inversion of Laplace Transformations. *IMA Journal of Applied Mathematics*, **23** (1): 97–120. https://doi.org/10.1093/imamat/23.1.97.

109. Taguchi, G. 1991. *Introduction to Quality Engineering*. Asian Productivity Organization, UNIPUB, White Plains, NY.

110. Taguchi, G. and Wu, Y. 1980. *Introduction to Off-Line Quality Control*, Central Japan Quality Control Association, Nagoya, Japan.

111. Tavanaei, A. and Salehi, S. 2015. Pore Throat and Grain Detection for Rock Sem Images Using Digital Watershed Image Segmentation Algorithm. *Journal of Porous Media*, **18** (5): 507-518. https://doi.org/10.1615/JPorMedia.v18.i5.40

112. Tien, C., Bai, R., and Ramarao, B. V. 1997. Analysis of Cake Growth in Cake Filtration: Effect of Fine Particle Retention. *AIChE Journal* **43** (1): 33-44. https://doi.org/10.1002/aic.690430106.

113. Tran, M.H., Abousleiman, Y., and Nguyen, V. X. 2011. The Effects of Filter-Cake Buildup and Time-Dependent Properties on the Stability of Inclined Wellbores. *SPE Journal* **16** (4): 1010-1028. https://doi.org/10.2118/135893-PA.

114. Traugott, D., Sweatman, R., and Vincent, R. 2007. Increasing the Wellbore Pressure Containment in Gulf of Mexico HP/HT Wells. *SPE Drill & Compl* **22** (01): 16-25. SPE-96420-PA. https://doi.org/10.2118/96420-PA.

115. The Drilling Manual, Fifth Edition, 2015. CRC Press, Boca Raton, FL.

116. Wang, H. M., Savari, S., Whitfill, D. L. et al. 2016. Forming a Seal Independent of Formation Permeability to Prevent Mud Losses—Theory, Lab Tests, and Case Histories. IADC/SPE Drilling Conference and Exhibition, Fort Worth Texas, 1-3 March. IADC/SPE 178790-MS. http://dx.doi.org/10.2118/178790-MS.

117. Wang, H. 2011. Is It Really Possible to Efficiently Form A Strong Seal inside Subterranean Openings without Knowing Their Shape and Size? AADE National Technical Conference and Exhibition, Houston, USA, 12-14 April. AADE-11-NTCE-25.

118. Warner, H. R. and Rathmell, J. J. 1997. Mechanisms Controlling Filtration at the Core Bit

for Oil-Based Muds. *SPE Drilling & Completion*, **12** (02): 111–118. http://dx.doi.org/10.2118/28596-PA.

119. Warren, T., Tessari, R., and Houtchens, B. 2004. Casing Drilling with Retrievable Drilling Assemblies. Offshore Technology Conference, Houston, Texas, USA, 3-6 May. OTC-16564-MS. https://doi.org/10.4043/16564-MS.

120. White, R. J. 1956. *Lost-Circulation Materials and Their Evaluation*. API-56-352. Drilling and Production Practice, New York, New York, USA, 1 January.

121. White, C. D., Willis, B. J., Narayanan, K. et al. 2001. Identifying and estimating significant geologic parameters with experimental design. *SPE Journal*, **6** (03): 311-324. http://dx.doi.org/10.2118/74140-PA.

122. Whitfill, D. 2008. Lost Circulation Material Selection, Particle Size Distribution and Fracture Modeling with Fracture Simulation Software. IADC/SPE Asia Pacific Drilling Technology Conference and Exhibition, Jakarta, Indonesia, 25-27 August. SPE-115039-MS. https://doi.org/10.2118/115039-MS.

123. Velmurugan, N., Mathur, P., and Babu, V. 2015. Particle Size Distribution in Casing Drilling: A Quantitative Analysis. Abu Dhabi International Petroleum Exhibition and Conference, Abu Dhabi UAE, 9-12, May. SPE-177679-MS. https://doi.org/10.2118/177679-MS.

124. Verga, F. M., Carugo, C., Chelini, V. et al. 2000. Detection and Characterization of Fractures in Naturally Fractured Reservoirs. SPE Annual Technical Conference and Exhibition, Dallas, 1-4 October. SPE 63266 Texas http://dx.doi.org/10.2118/63266-MS.

125. Yahia, A. and Khayat K. H. 2011. Experimental Design to Evaluate Interaction of High-Range Water-Reducer and Anti-washout Admixture in High-Performance Cement Grout. *Cement and Concrete Research.* **31** (5): pp. 749-757. http://dx.doi.org/10.1016/s0008-8846(01)00496-3.

126. Zamora, M. and Broussard, M. P. S. 2000. The Top 10 Mud-Related Concerns in Deepwater Drilling Operations. SPE International Petroleum Conference and Exhibition in Mexico, 1-3 February 2000, Villahermosa, Mexico. SPE 59019-MS. https://doi.org/10.2523/59019-MS.

Appendix A: Derivation of Dynamic-Radial Filtration Model

Filter cake material balance is given by (Civan, 1994 and 1996) is:

$$-\epsilon_s \, {dr_c}/{dt} = {R_{ps}}/{\rho_p} \quad \text{(A.1)}$$

The volume mass fraction of solids as a function of porosity is given as:

$$\epsilon_s = 1 - \emptyset_c \quad \text{(A.2)}$$

The net deposition rate of particles to form an external filter cake is given as:

$$R_{ps} = k_d u_c c_p - k_e(\tau_s - \tau_{cr}) \quad \text{(A.3)}$$

Where τ_s is the mud (slurry) shear stress and it is given as:

$$\tau_s = k\left(\frac{\pi RS}{15n\left(1-G^{-2/n}\right)}\right)^n \quad \text{(A.4)}$$

In equation 4, $G = {r_{dp}}/{r_c}$, $for\ 0.5 \le {r_{dp}}/{r_c} \le 0.9$ (A.5)

Substituting equations A.2 and A.3 into A.1 yields

$$-{dr_c}/{dt} = \frac{k_d u_c c_p - k_e(\tau_s - \tau_{cr})}{(1-\emptyset_c)\rho_p} \quad \text{(A.6)}$$

In terms of the filtration rate, the radial volumetric flux at the external cake surface is:

$$u_c = \frac{q}{2\pi h r_c} \quad \text{(A.7)}$$

Substituting equation A.7 into A.6 gives:

$$-\frac{d\left({r_c}/{r_w}\right)}{dt} = A\frac{q}{{r_c}/{r_w}} - B \quad 0 \le {r_c}/{r_w} \le 1 \quad \text{(A.8)}$$

Where $A = \frac{c_p k_d}{(1-\emptyset_c)\rho_p 2\pi h r_w^2}$ (A.9)

and

$$B = \frac{k_e(\tau_s - \tau_{cr})}{(1-\emptyset_c)\rho_p r_w} \quad \text{(A.10)}$$

The Forchheimer's (1901) equation for radial flow of the mud is given as:

$$-\frac{\partial p}{\partial r} = \frac{\mu}{K}u + \beta_i \rho u^2 \text{..... (A.11)}$$

Combining equation A.11 and A.7 yields:

$$-\frac{\partial p}{\partial r} = \frac{\mu}{2\pi hK}\frac{q}{r} + \frac{\beta_i \rho}{2\pi h^2}\left(\frac{q}{r}\right)^2 \text{..... (A.12)}$$

Where β_i is the inertial flow coefficient for the rock or filter cake and per Liu et al. (1995), it is given as: $\beta_i = \frac{2.92\times10^4 T_{f/c}}{\emptyset_{f/c}K_{f/c}}$..... (A.13)

In equation (A.13), $T_{f/c}$ means tortuosity of formation or filter cake. The same goes for the porosity and permeability symbols (please check the Greek symbols). Integrating equation A.12 for conditions before and during evolution of external filter cake results in equation A.13 and A.14 respectively

$$P_c - P_e = \frac{q_o \mu}{2\pi hK_f} ln\left(\frac{r_e}{r_w}\right) + \frac{\beta_f \rho q_o^2}{(2\pi h)^2}\left(\frac{1}{r_w} - \frac{1}{r_e}\right)^2 \text{..... (A.14)}$$

$$P_c - P_e = \frac{q\mu}{2\pi hK_f}\left[ln\left(\frac{r_e}{r_w}\right) + \frac{K_f}{K_c} ln\left(\frac{r_w}{r_c}\right)\right] + \frac{\beta_f \rho q}{(2\pi h)^2}\left[\frac{1}{r_w} - \frac{1}{r_e} + \frac{\beta_c}{\beta_f}\left(\frac{1}{r_w} - \frac{1}{r_e}\right)\right] \text{..... (A.15)}$$

Combining equation A.13 and A.14 yield the following equation for non-Darcy mud filtrate flow rate (Civan 2007)

$$q = \frac{-\beta + \sqrt{\beta^2 - 4\alpha\gamma}}{2\alpha} \text{..... (A.16)}$$

Where $\alpha = \frac{\rho}{(2\pi h)^2}\left[\beta_f\left(\frac{1}{r_w} - \frac{1}{r_e}\right) + \beta_c\left(\frac{1}{r_{w-\delta}} - \frac{1}{r_w}\right)\right]$ ..... (A.17)

$$\beta = \frac{\mu}{2\pi hK_f}\left[ln\left(\frac{r_e}{r_w}\right) + \frac{K_f}{K_c} ln\left(\frac{r_w}{r_w - \delta}\right)\right] \text{..... (A.18)}$$

$$\gamma = -\left[\frac{q_o \mu}{2\pi hK_f} ln\left(\frac{r_e}{r_w}\right) + \frac{\beta_f \rho q_o^2}{(2\pi h)^2}\left(\frac{1}{r_w} - \frac{1}{r_e}\right)\right] \text{..... (A.19)}$$

The input and declarations in Matlab are in the figure below.

```
q(1) = (-B0+sqrt((B0^2)-4*a0*y0))/(2*a0);
%%%%%%%%%%%%%%%%%%%%%%%%%%%%%%%%%%%%%%%%%%%%%%%%%%%%%%%%%%%%%%%%%%%%%%%%%%%%%%%
%% Inputs and Declaration
h = 0.1; % solution stepsize
t = 0:h:1800; % input vector
f=@(delta,dq)((A.*dq/(rw-delta))-B1);
%%%%%%%%%%%%%%%%%%%%%%%%%%%%%%%%%%%
%======Use Runge Kutta to solve the above equations==============
%=================================================================
plot(time(1:18000),Q_final_new(1:18000),'--k')
hold on
x=xlsread('Experimentaldata','sheet1','A1:A1000');
y=xlsread('Experimentaldata','sheet1','B1:B1000');
plot(x,y,'-r')
legend('Model','Experimental')
```

Appendix B: Sum Spectrum Maps of Elements in the Near Wellbore Region One

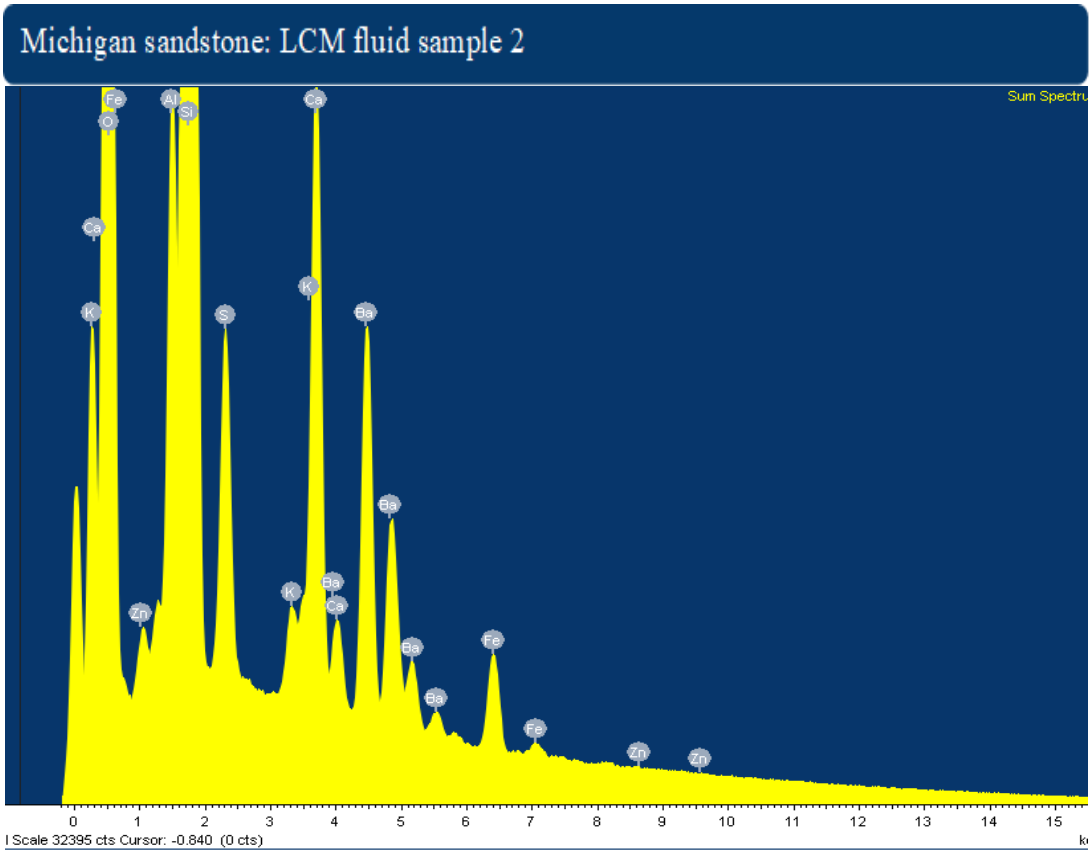

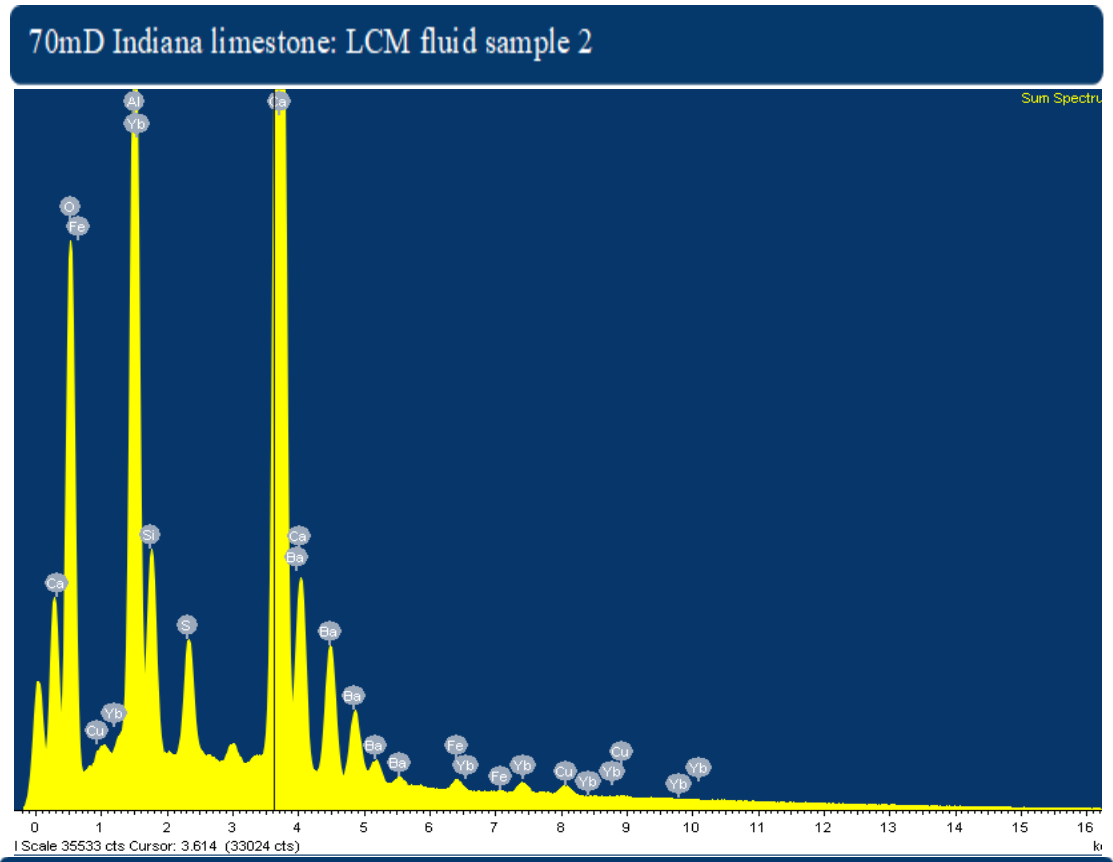
70mD Indiana limestone: LCM fluid sample 2
Sum Spectru
Al
Yb
O
Fe
La
Si
Ca
Ba
S
Cu
0 1 2 3 4 5 6 7 8 9 10 11 12 13 14 15 16
l Scale 35533 cts Cursor: 3.614 (33024 cts)

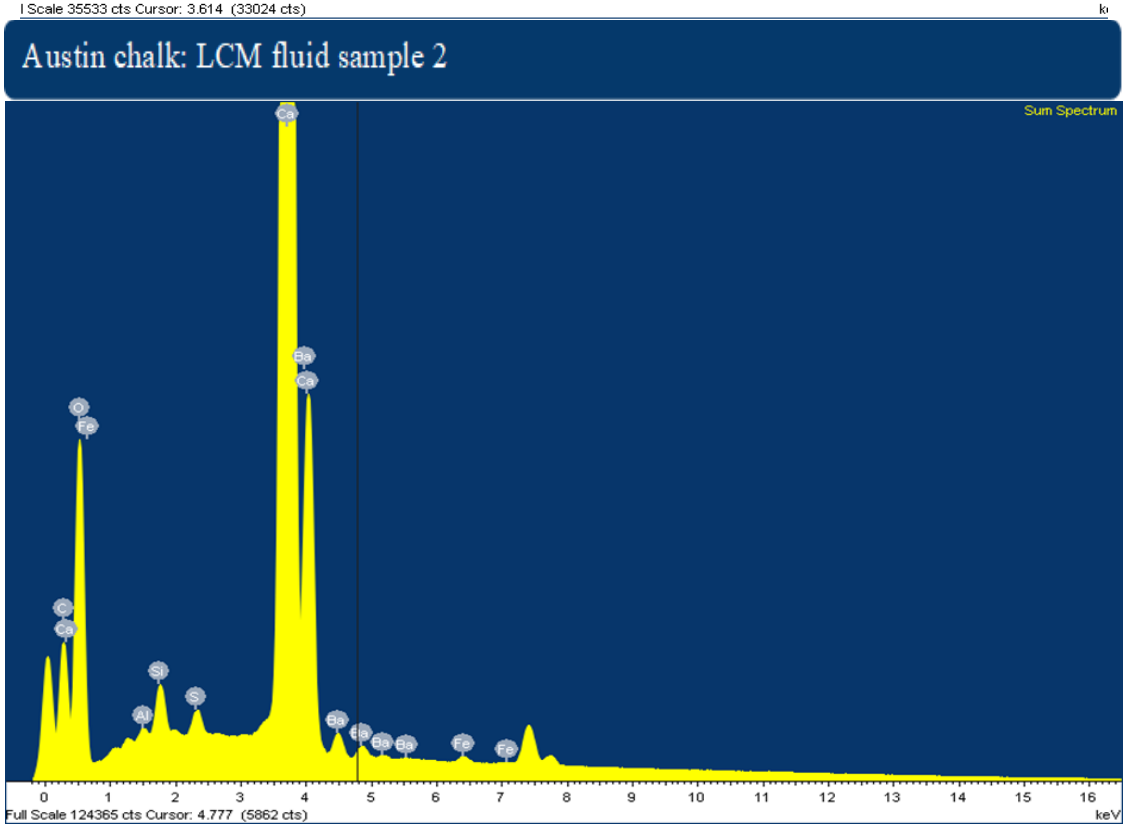
Austin chalk: LCM fluid sample 2
Sum Spectrum
Ca
Ba
O
Fe
C
Si
Al
S
0 1 2 3 4 5 6 7 8 9 10 11 12 13 14 15 16
Full Scale 124365 cts Cursor: 4.777 (5862 cts)
keV

Appendix C: Cumulative Filtrate plots vs Square Root of Time

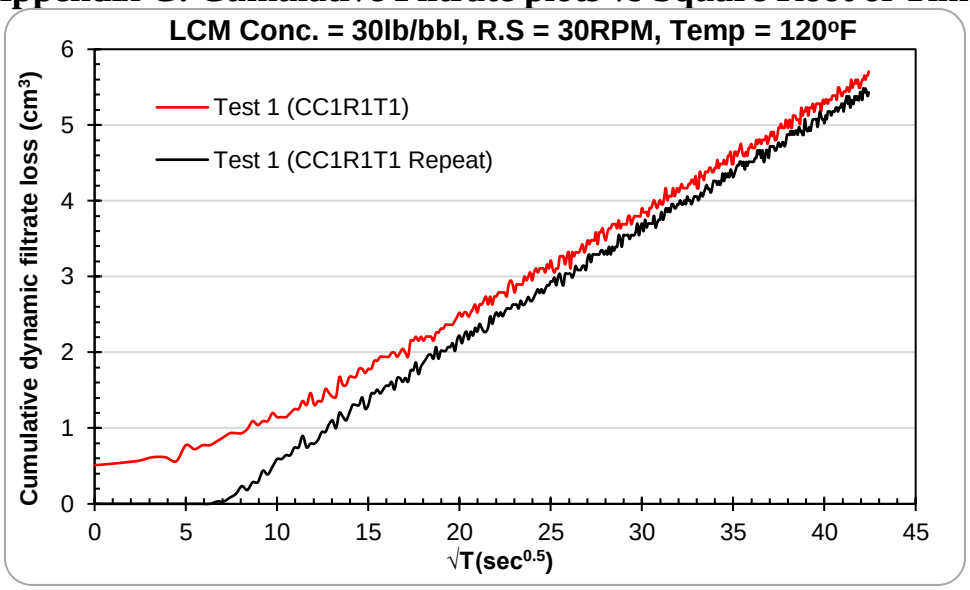

Figure C1: Dynamic cumulative filtrate loss profiles for Test 1 and its replicate

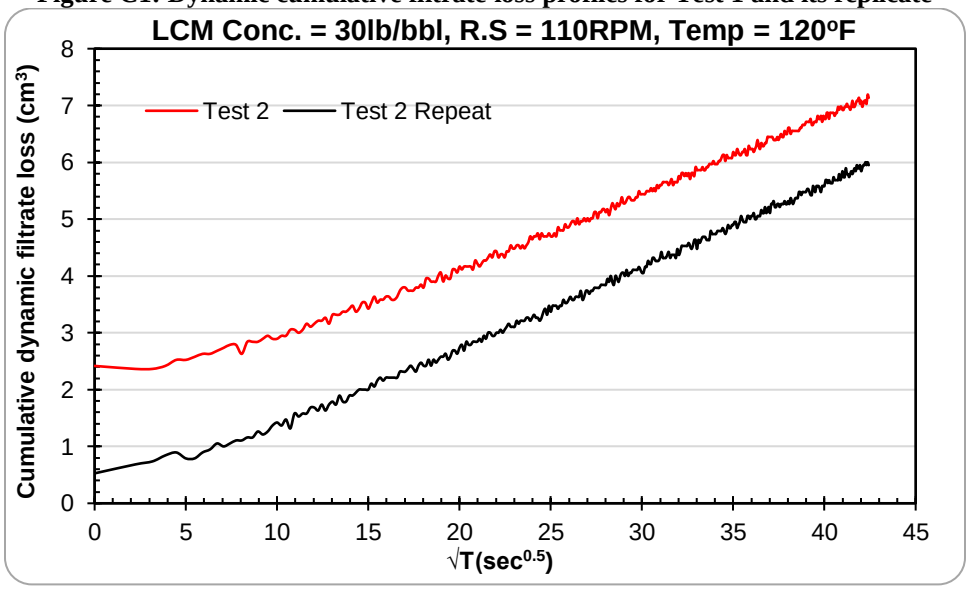

Figure C2: Dynamic cumulative filtrate loss profiles for Test 2 and its replicate

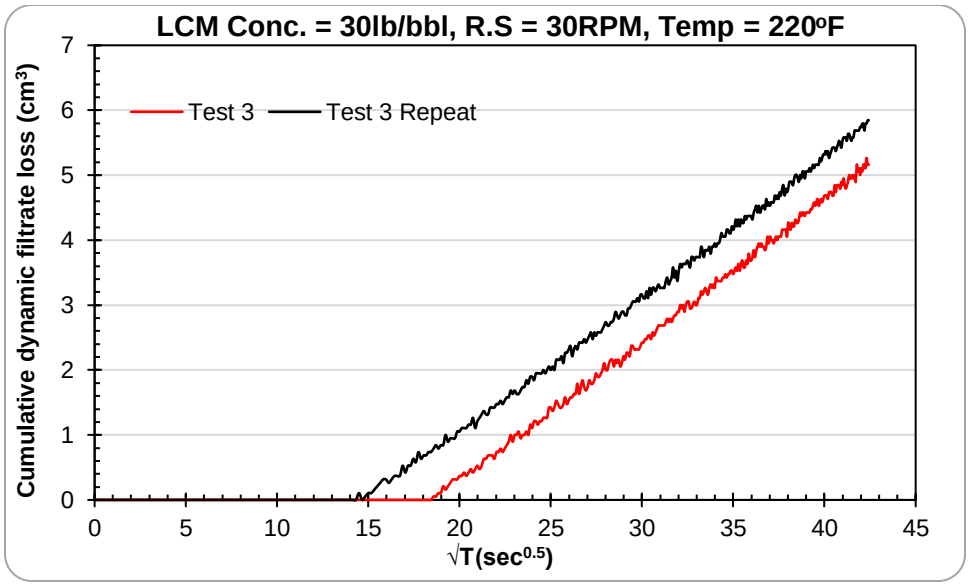

Figure C3: Dynamic cumulative filtrate loss profiles for Test 3 and its replicate

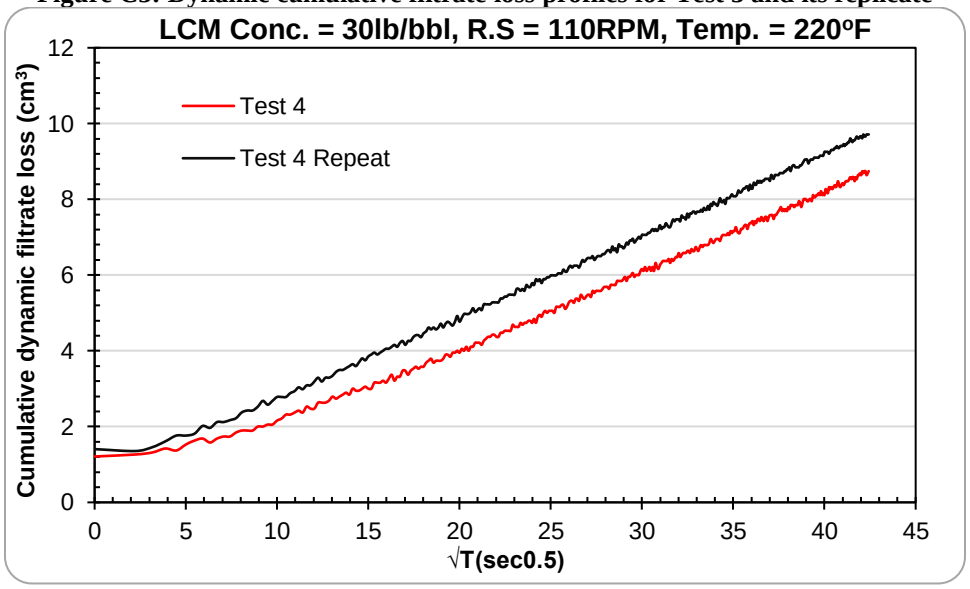

Figure C4: Dynamic cumulative filtrate loss profiles for Test 4 and its replicate

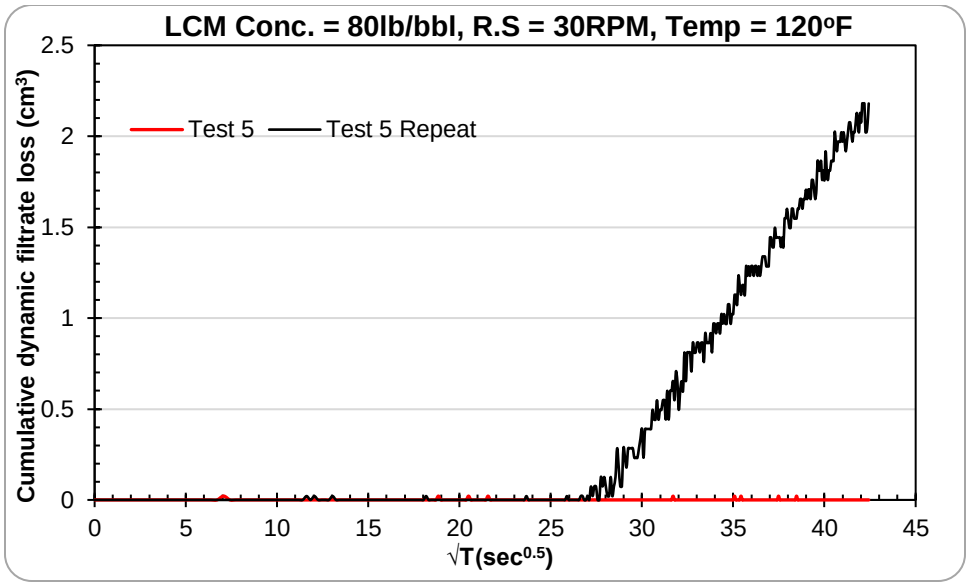

Figure C5: Dynamic cumulative filtrate loss profiles for Test 5 and its replicate

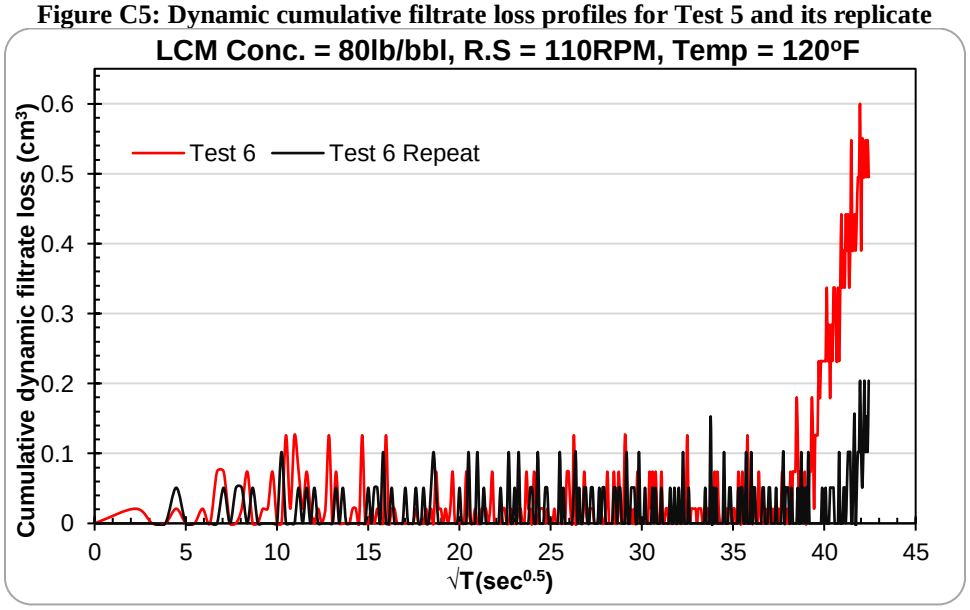

Figure C6: Dynamic cumulative filtrate loss profiles for Test 6 and its replicate

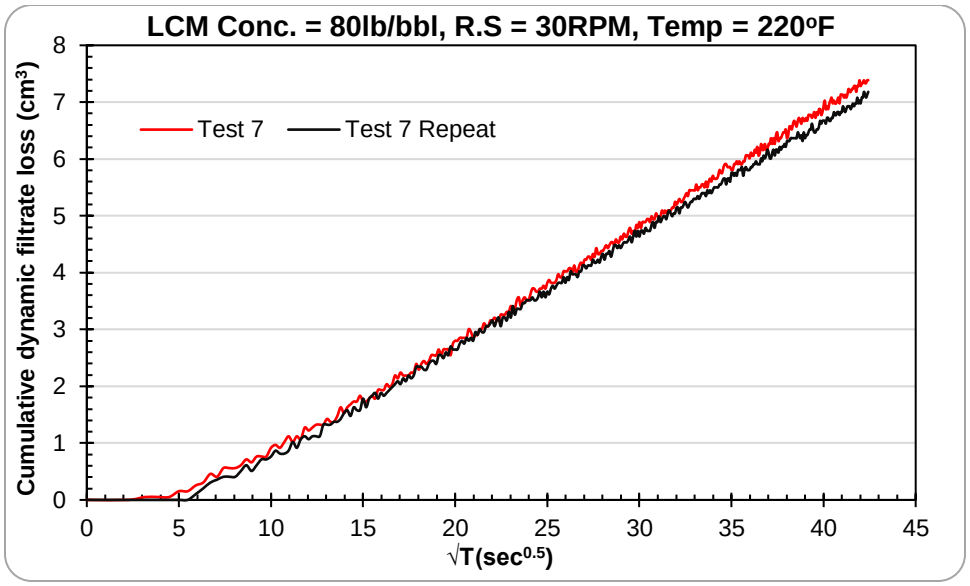

Figure C7: Dynamic cumulative filtrate loss profiles for Test 7 and its replicate

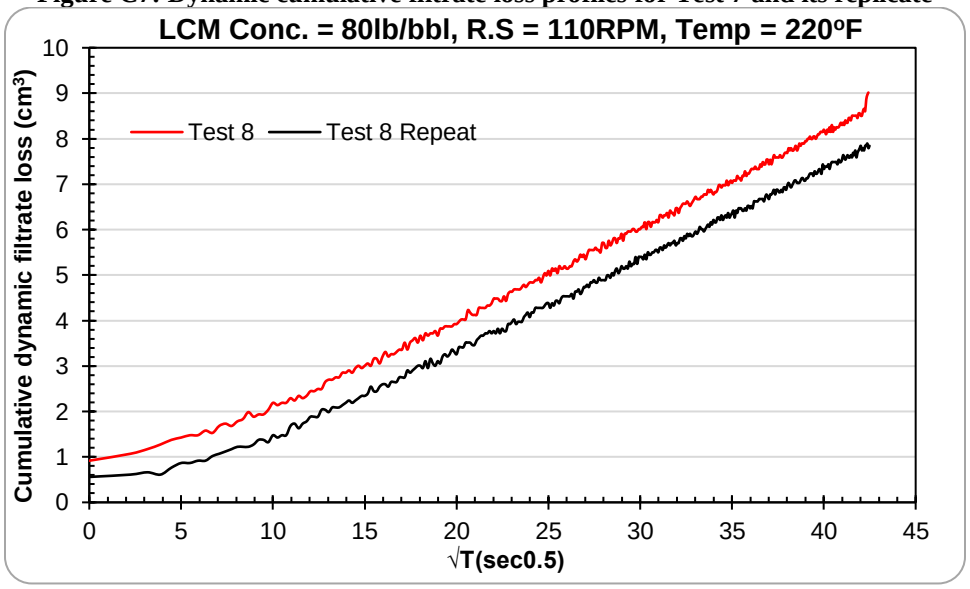

Figure C8: Dynamic cumulative filtrate loss profiles for Test 8 and its replicate

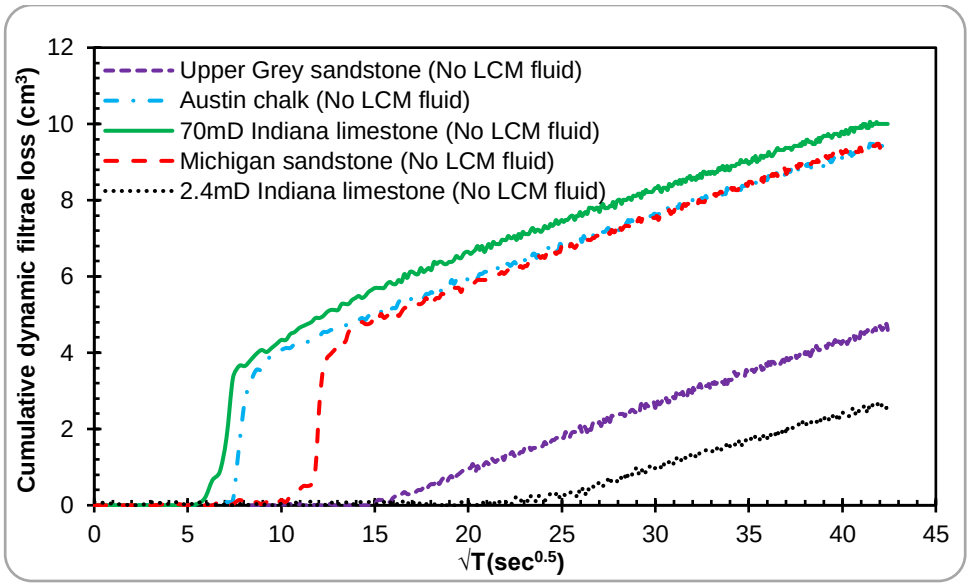

Figure C9: Dynamic cumulative filtrate loss profiles from a base fluid (no LCM) on different

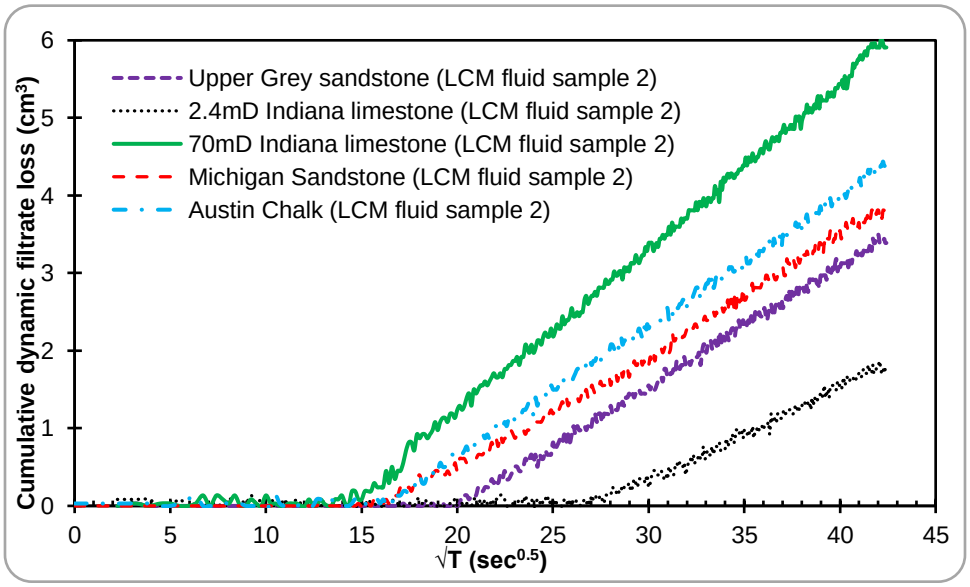

Figure C10: Dynamic cumulative filtrate loss profiles from a $CaCO_3$ fluid on different lithologies at 120°F, 70RPM, and 100 psi

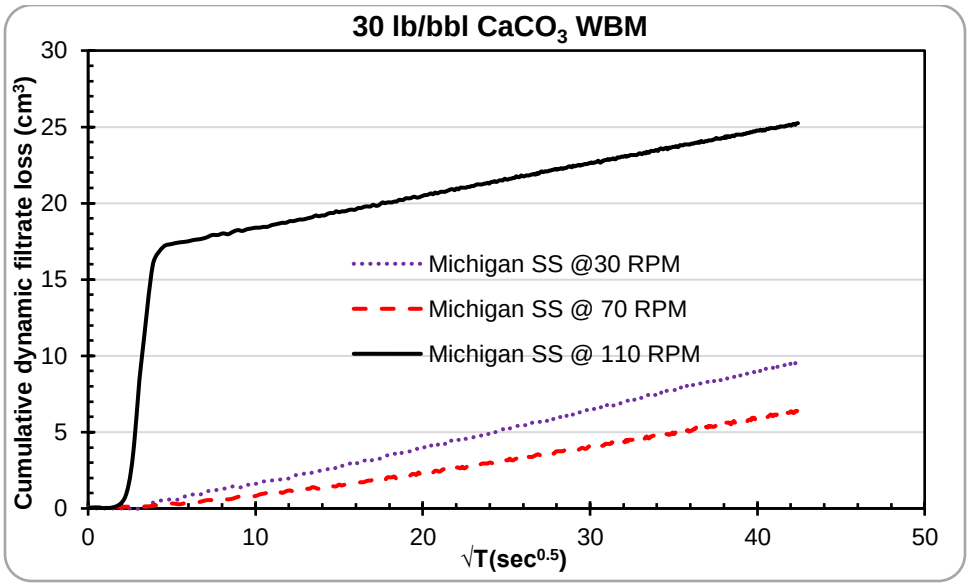

Figure C11: Dynamic filtrate loss profiles in Michigan sandstone for 30 lb/bbl $CaCO_3$ WBM

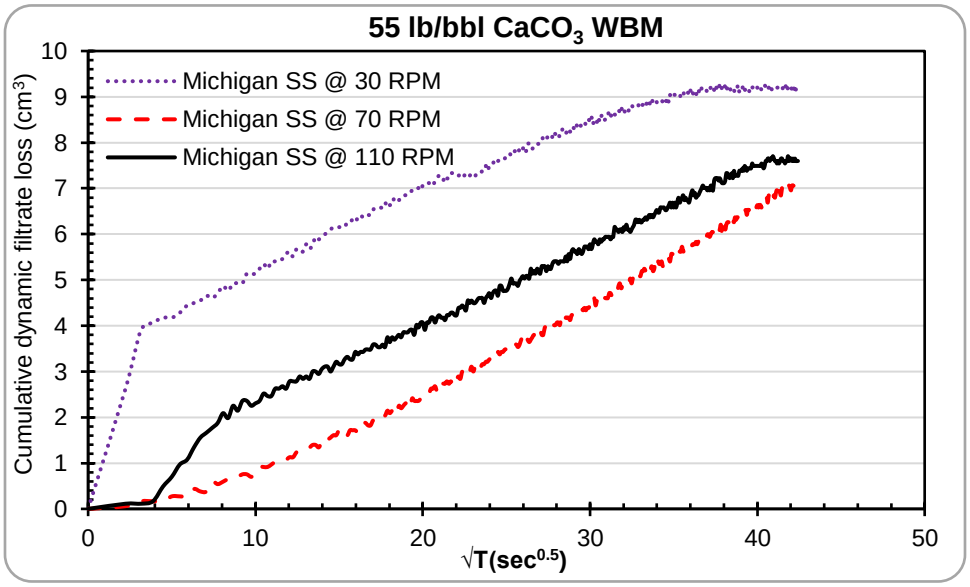

Figure C12: Dynamic filtrate loss profiles in Michigan sandstone for 55 lb/bbl $CaCO_3$ WBM

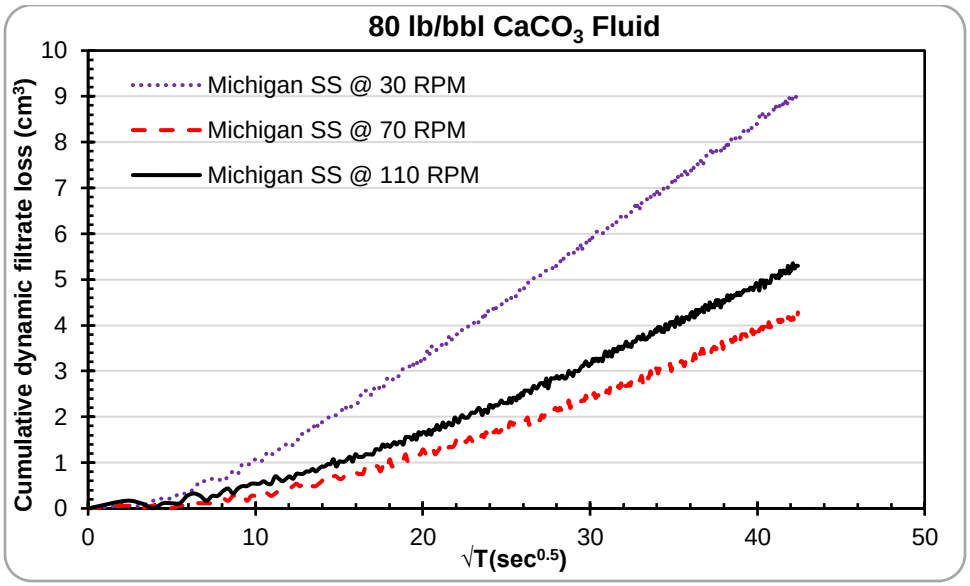

Figure C13: Dynamic filtrate loss profiles in Michigan sandstone for 80 lb/bbl $CaCO_3$ WBM

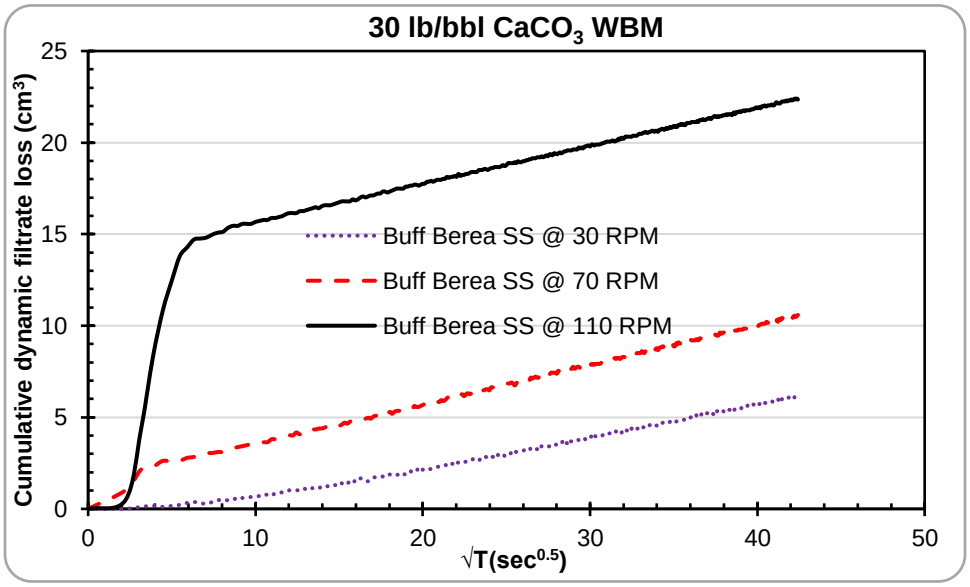

Figure C14: Dynamic filtrate loss profiles in Buff Berea sandstone for 30 lb/bbl $CaCO_3$ WBM

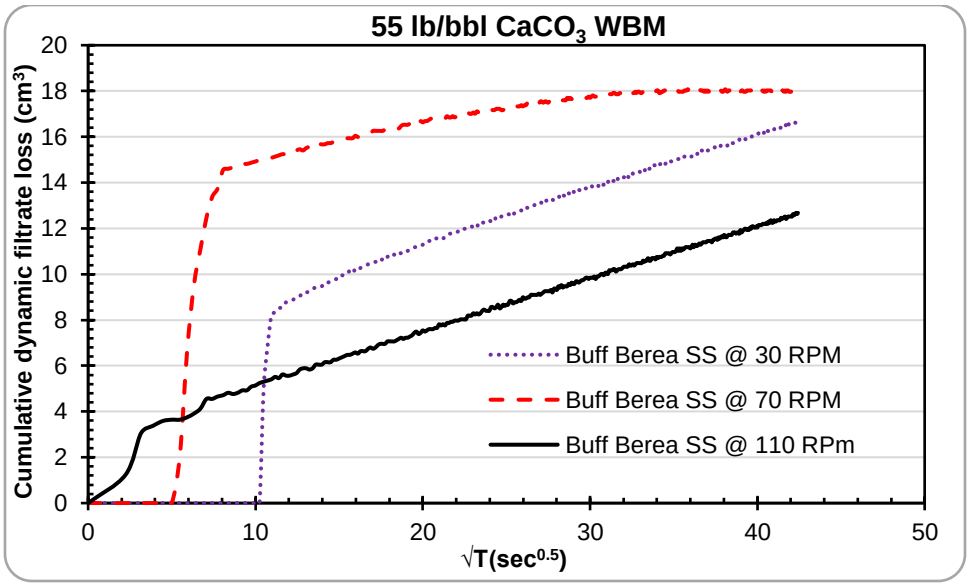

Figure C15: Dynamic filtrate loss profiles in Buff Berea sandstone for 55 lb/bbl $CaCO_3$ WBM

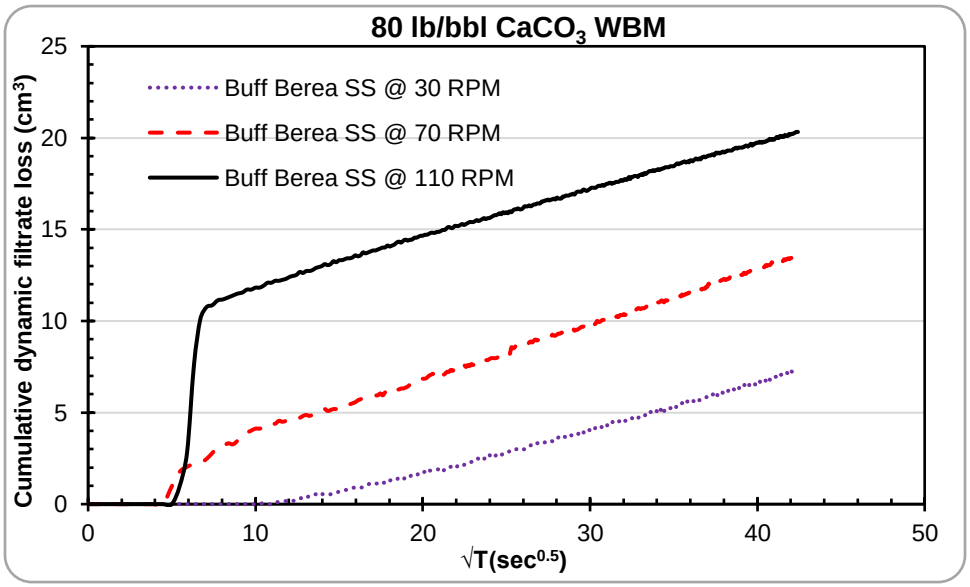

Figure C16: Dynamic filtrate loss profiles in Buff Berea sandstone for 80 lb/bbl $CaCO_3$ WBM

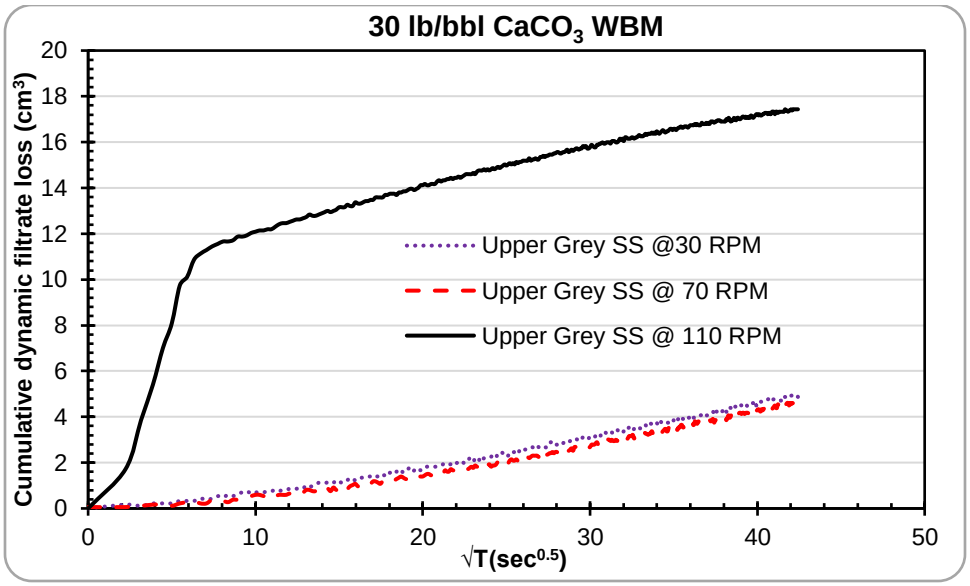

Figure C17: Dynamic filtrate loss profiles in Upper Grey sandstone for 30 lb/bbl $CaCO_3$ WBM

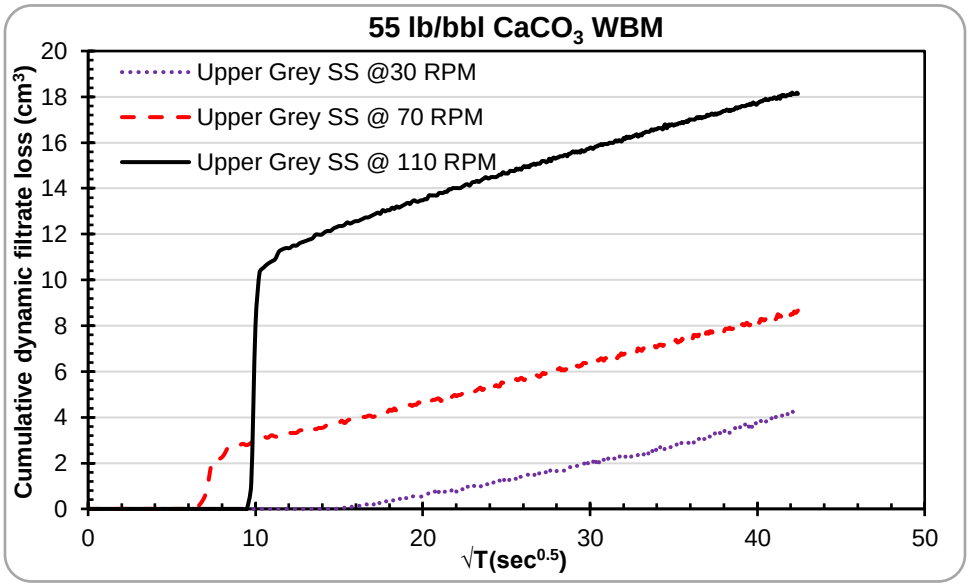

Figure C18: Dynamic filtrate loss profiles in Upper Grey sandstone for 55 lb/bbl $CaCO_3$ WBM

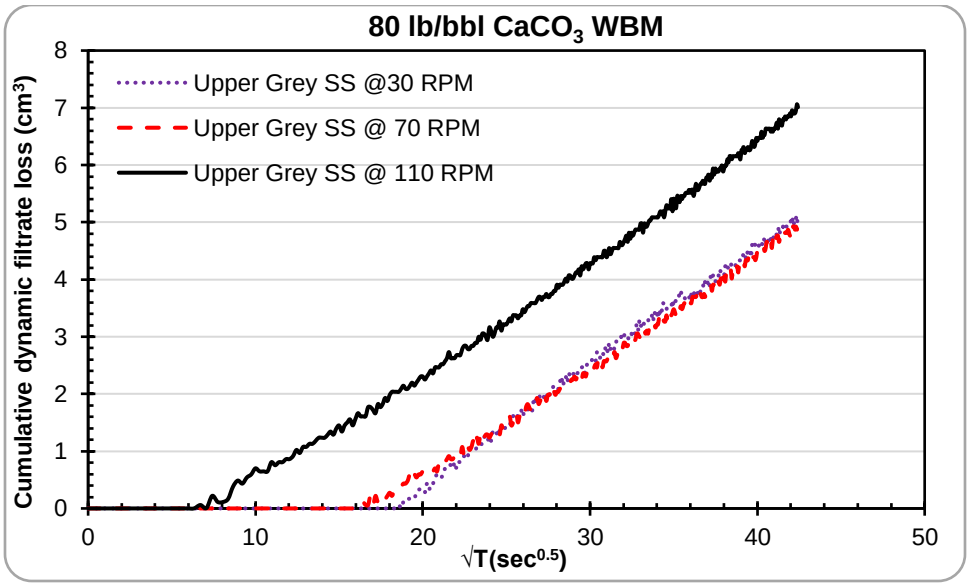

Figure C19: Dynamic filtrate loss profiles in Upper Grey sandstone for 80 lb/bbl $CaCO_3$ WBM

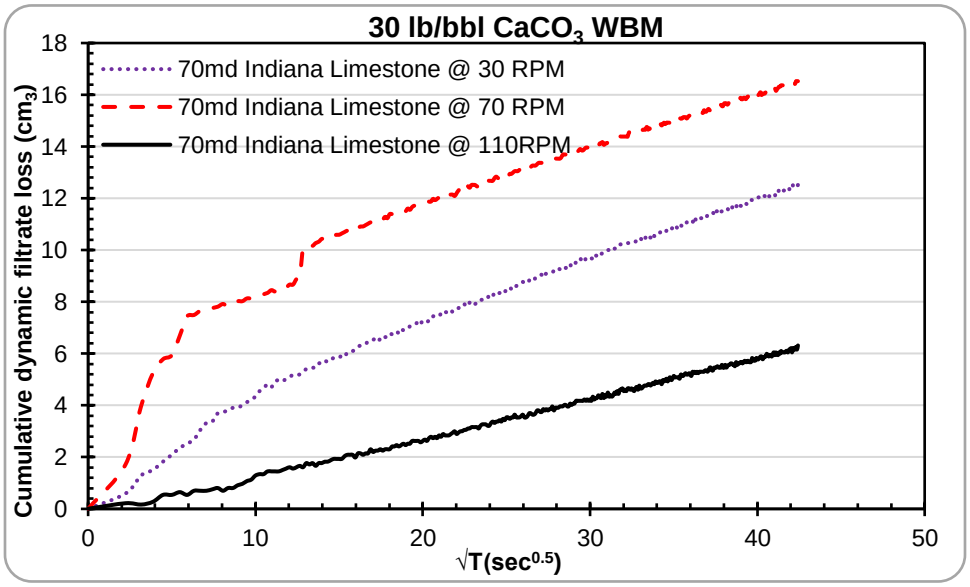

Figure C20: Dynamic filtrate loss profiles in Indiana limestone for 30 lb/bbl $CaCO_3$ WBM

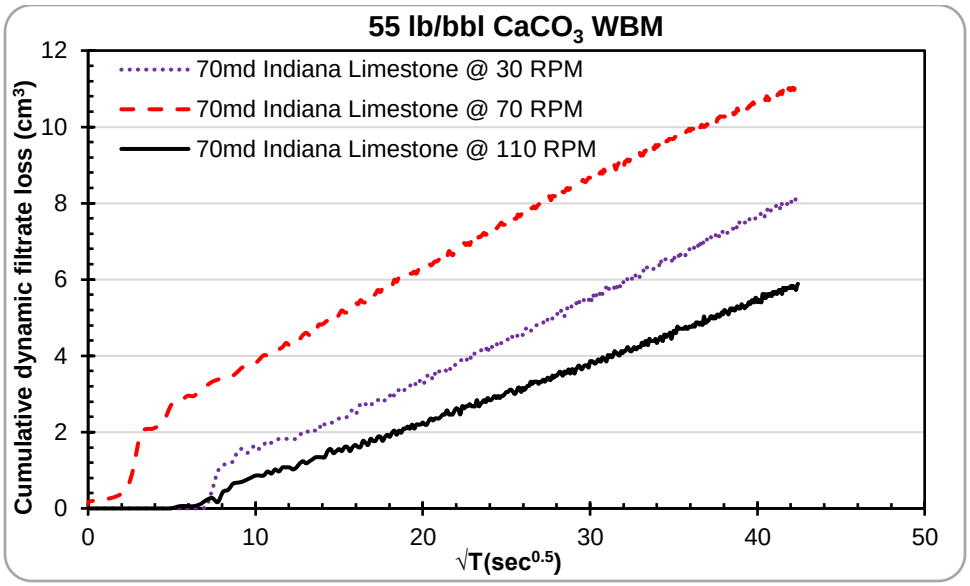

Figure C21: Dynamic filtrate loss profiles in Indiana limestone for 55 lb/bbl $CaCO_3$ WBM

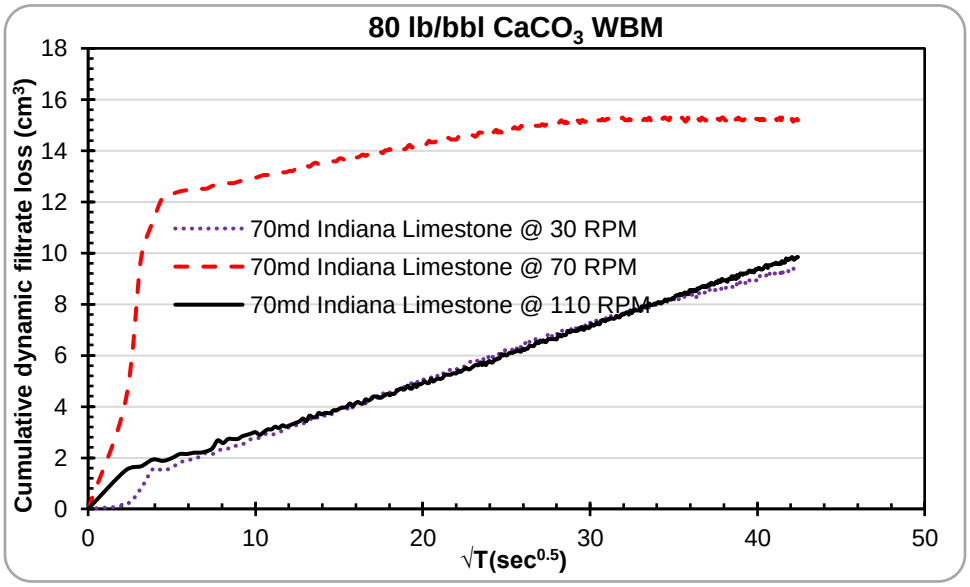

Figure C22: Dynamic filtrate loss profiles in Indiana limestone for 80 lb/bbl $CaCO_3$ WBM

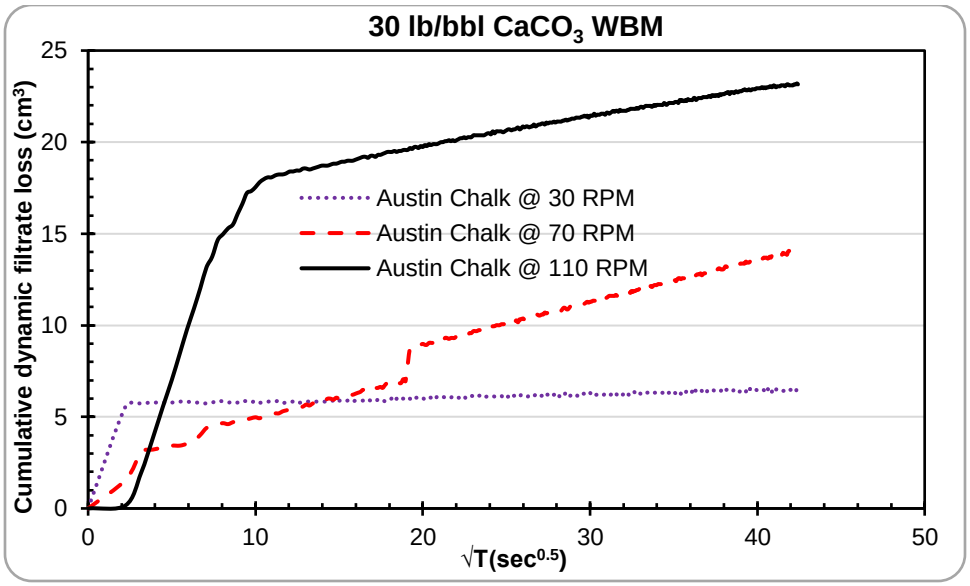

Figure C23: Dynamic filtrate loss profiles in Austin chalk for 30 lb/bbl $CaCO_3$ WBM

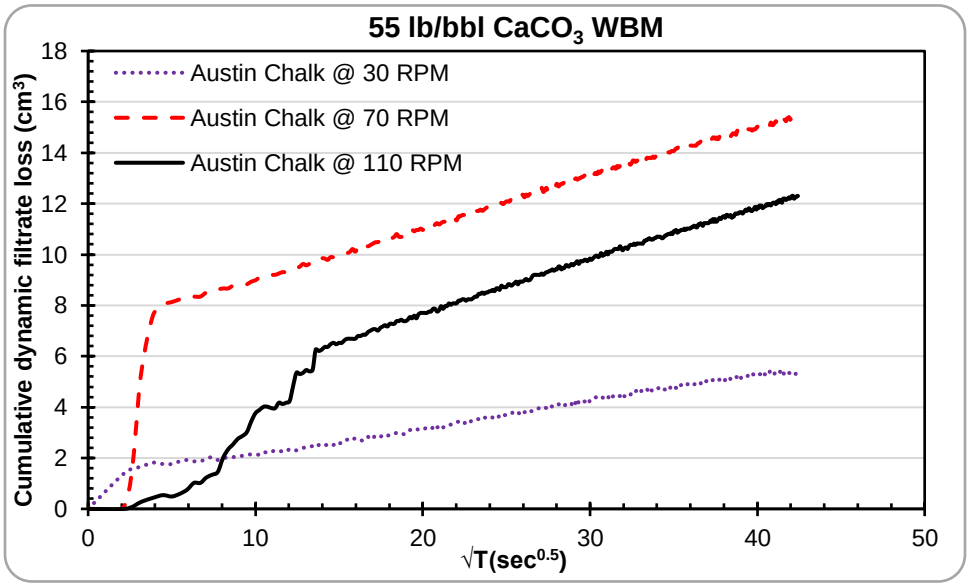

Figure C24: Dynamic filtrate loss profiles in Austin chalk for 55 lb/bbl $CaCO_3$ WBM

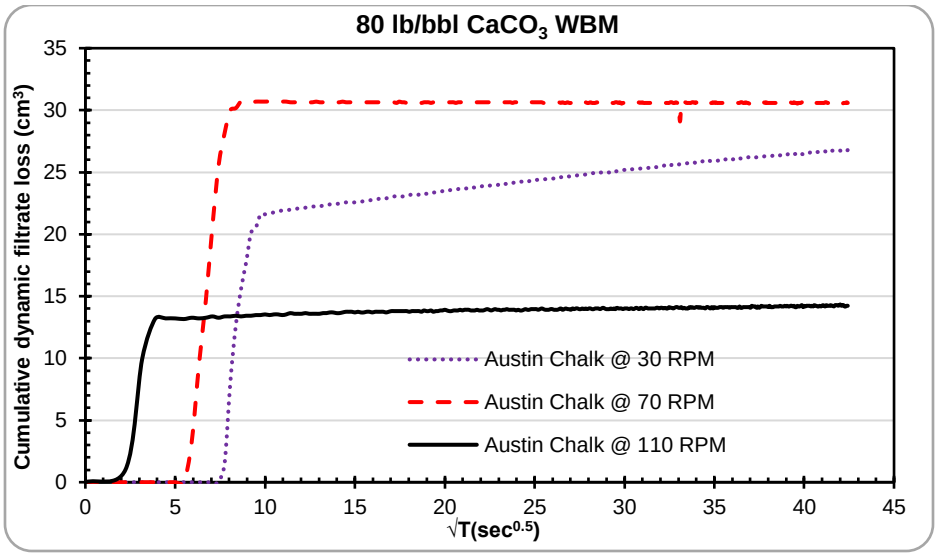

Figure C25: Dynamic filtrate loss profiles in Austin chalk for 80 lb/bbl $CaCO_3$ WBM

Appendix D: List of Publications, Accepted Manuscripts, Manuscripts Under Review from the Results of this Research

Peer-Reviewed Journal Publications

1. Ezeakacha, C.P. and Salehi, S. 2018. Experimental and Statistical Investigation of Drilling Fluids Loss in Porous Media-Part 2 (Fracture-scale). Journal of Natural Gas Science and Engineering. *Manuscript Under Review*.

2. Ezeakacha, C.P. and Salehi. 2018. "A Holistic Approach to Characterize Mud Loss Using Dynamic Mud Filtration Data." ASME Journal of Energy of Resources. Acc *Manuscript in Press*.

3. Ezeakacha, C.P. and Salehi, S. 2018. "An Advanced Coupled Rock-fluid Computational Model for Dynamic-radial Mud Filtration with Experimental Validation." Springer Journals Rock Mechanics and Rock Engineering. *Manuscript Under Review*.

4. Ezeakacha, C.P., Salehi, S. Kiran, R. 2018. "Lost Circulation and Filter Cake Evolution: Impact of Dynamic Wellbore Conditions and Wellbore Strengthening Implications." Journal of Petroleum Science and Engineering 171: 1326-1337. https://doi.org/10.1016/j.petrol.2018.08.063.

5. Mansour, A., Dahi Taleghani, A., Salehi, S. Li, G. and Ezeakacha, C.P. 2018. Smart Lost Circulation Materials for Productive Zones. Journal of Petroleum Exploration Production Technology. https://doi.org/10.1007/s13202-018-0458-z.

6. Ezeakacha, C.P. and Salehi, S. 2018. Experimental and Statistical Investigation of Drilling Fluids Loss in Porous Media-Part 1. Journal of Natural Gas Science and Engineering 51: 104-115. https://doi.org/10.1016/j.jngse.2017.12.024.

Conference Proceedings

1. Ezeakacha, C.P., Salehi, S. Kiran, R. 2018. "Quantification of Multiple Factors and Interaction Effects on Drilling Fluid Invasion." Presented at the 37th International Conference on Ocean, Offshore & Artic Engineering, Madrid, Spain, 17-22 June 2018. OMAE2018-78722. https://doi.org/10.1115/omae2018-78328.

2. Ezeakacha, C.P., Salehi, S. Kiran, R. 2018. "Pore-Scale Mud Invasion in Different Rock Samples and Wellbore Conditions: Implications for Lithology Dependent Wellbore Strengthening." Presented at the 52nd US Rock Mechanics/Geomechanics Symposium, Seattle, Washington, 20-22 June 2018. ARMA 18-544.

3. Ezeakacha, C.P., Salehi, S., and Bi, H. 2018. "A New Approach to Characterize Dynamic Drilling Fluids Invasion Profiles in Application to Near-Wellbore Strengthening Effect." IADC/SPE Drilling Conference and Exhibition, Fort Worth, Texas. March 6-8. IADC/SPE-189596-MS. http://dx.doi.org/10.2118/189596-MS.

4. Ezeakacha, C.P., Salehi, S., Ghalambor, A., and Bi, H. 2018 "Investigating Impact of Rock Type and Lithology on Mud Invasion and Formation Damage." SPE International Symposium and Exhibition on Formation Damage Control, Lafayette, Louisiana. February 7-9. SPE 189471-MS. http://dx.doi.org/10.2118/189471-MS.

5. Ezeakacha, C.P., Rabbani, A., Salehi, S., and Ghalambor, A. 2018. "Integrated Image Processing and Computational Techniques to Characterize Formation Damage." SPE International Symposium and Exhibition on Formation Damage Control, Lafayette, Louisiana. February 7-9. SPE 189509-MS. http://dx.doi.org/10.2118/189509-MS.

6. Mansour, A., Ezeakacha, C.P., Dahi Taleghani, A., Li, G., Salehi, S., 2017. "Smart Lost Circulation Materials for Productive Zones". SPE Annual Technical Conference and Exhibition, San Antonio, Texas. 9-11 October. SPE 187099-MS. http://dx.doi.org/10.2118/187099-MS.

7. Ezeakacha, C.P., Salehi, S., Bi, H, 2017, "How does Rock Type and Lithology Affect Drilling Fluids Filtration and Plastering". AADE National Technical Conference and Exhibition, Houston Texas, 11-12 April, AADE-NTCE-094.

Appendix E: Biography

Chinedum Peter Ezeakacha is a native of Umuchu in Aguata local government area of Anambra state, Nigeria. He holds a bachelor's degree in chemical engineering (2009). After his bachelors' program, he worked with ExxonMobil in Nigeria for a year (2010 to 2011) as a petroleum engineer (trainee). Before commencing his graduate studies in 2013, he worked with NG Equipment and Systems Ltd. (2011 to 2012) as an assistant field system engineer. In December 2014, he earned a Master of Science in Engineering with concentration in Petroleum Engineering from the University of Louisiana at Lafayette. In Chinedum received his PhD in Petroleum Engineering from the Mewbourne School of Petroleum and Geological Engineering at The University of Oklahoma in December 2018. During his 6-year graduate program, Chinedum had 4 scholarships and 3 travel grants/support, participated in 12 graduate student research paper contests (three 1st place awards, one 2nd place award, and two 3rd place awards), participated in three petrobowl competitions as player/coach/mentor and placed 5th in 2014, 4th in 2015, and 2nd in 2016. He presented more than 10 papers at several national and international conferences and published 24 scholarly journal and conference papers. After his graduation, he accepted a post-doctoral research associate position at the Mewbourne School of Petroleum and Geological Engineering, The University of Oklahoma.